General Physical Characteristics of γ-ray Emitting Beamed AGNs in *Fermi* Era

by

Vaidehi Sharan Paliya
Indian Institute of Astrophysics, Bangalore

A thesis submitted in partial fulfillment for the
degree of Doctor of Philosophy to the

Department of Physics
University of Calicut
Calicut, Kerala

February 2016

Certificate

This is to certify that the thesis titled '**General Physical Characteristics of γ-ray Emitting Beamed AGNs in *Fermi* Era**' is a bonafide record of the work done by Vaidehi Sharan Paliya under our joint supervision and that no part of it has been included any where previously for the award of any degree, either in this university or any other institution.

Prof. C. S. Stalin,
Associate Professor,
Indian Insitute of Astrophysics,
Bangalore.

Dr. C. D. Ravikumar,
Assistant Professor,
Department of Physics,
University of Calicut, Kerala.

Declaration of Authorship

I hereby declare that the thesis titled **'General Physical Characteristics of γ-ray Emitting Beamed AGNs in *Fermi* Era'** is an authentic record of the research work carried out by me under the supervision of Prof. C. S. Stalin, IIA and Dr. C. D. Ravikumar, Department of Physics, University of Calicut. No part of this work has formed the basis for award of any other degree or diploma in any university or institution.

Vaidehi Sharan Paliya

Abstract

The research work presented in this thesis is aimed to provide a detailed understanding of the radiative processes powering the jets of the blazars, a class of AGNs with jet pointed towards the line of sight to the observer. Another important aim of this work is to study the multi-frequency properties of a new class of γ-ray emitting narrow-line Seyfert 1 (γ-NLSy1) galaxies using various observational tools and to compare them with that known from powerful blazars.

The goal of understanding the physical characteristics of blazars is achieved by studying the broadband flux variability and spectral energy distribution (SED) modeling of a carefully selected sample of blazars. The aim of the broadband variability study is to provide a general physical scenario, which allows one to put the observed variation from blazars across several decades of frequencies in a coherent context. Extremely fast hr scale flux variations are observed from all the sources studied here, including nearby BL Lac object Mrk 421 ($z = 0.03$) which showed minute scale hard X-ray ($3-79$ keV) flux variability during its 2013 April X-ray outburst. Moreover, by adopting a SED modeling approach, attempts are made to understand the causes of high amplitude γ-ray flux variations observed from these objects. To do this, a simple one zone leptonic emission model was also developed during the course of the thesis. The main reason of the 2014 April and 2015 June γ-ray outbursts of 3C 279 ($z = 0.536$) and 2011 December γ-ray flare of distant blazar S5 0836+71 ($z = 2.17$) is found to be due to sudden acceleration of the jet. On the other hand, minute scale variability seen from Mrk 421 is explained on the basis of magnetic energy dissipation and reconnection events. The multi-wavelength observations of 3C 279 revealed that a single zone leptonic emission model successfully reproduces the γ-ray flares of 2014 April and 2015 June, however, it fails to explain the uncorrelated flux variations and a hard γ-ray spectrum seen during 2013 December event. A two zone leptonic emission model is used to match the observations. All these observations hint for the presence of a

variety of the radiative processes working in the 3C 279 jet (and possibly in other sources as well) and their dominance over each other, as seen during different high activity periods.

The launch of the *Fermi* Gamma-ray space telescope in the year 2008 led to the first detection of γ-ray emission with high confidence from about half-a-dozen radio-loud NLSy1 galaxies. This discovery clearly indicates the presence of relativistic jets in these sources similar to that of blazars. With the motivation to understand the nature of γ-NLSy1 galaxies vis-a-vis blazars, few diagnostic tests are carried out, namely, intranight optical variability (INOV), γ-ray spectral properties, and broadband SED modeling. It is found that: (1) these sources show large amplitude ($>$3%) INOV with a duty cycle of about 80%, (2) their γ-ray spectra exhibit a significant curvature, and (3) their broadband SEDs have the typical double hump structure and the high energy hump can be explained due to external Compton process. Thus, based on the observations covering a wide range of the electromagnetic spectrum, it can be concluded that γ-NLSy1 galaxies have all the properties similar to blazars and could well be the low black hole mass counterparts of flat spectrum radio quasars.

Acknowledgements

I thank my supervisor Prof. C. S. Stalin for a continuous guidance, support, and encouragement and also my co-supervisor Dr. C. D. Ravikumar for his guidance and assistance during the course of the thesis. I am also grateful to Dr. Sunder Sahayanathan of Astrophysical Sciences Division, BARC, Mumbai, for teaching the basics of radiative processes and pointing out the shortcomings during various stages of the work. I am thankful to the Director, Indian Institute of Astrophysics (IIA) for providing all the basic research requirements in the form of computational, library, and other resources. Board of Graduate Studies at IIA is gratefully acknowledged for facilitating the registration process and all subsequent formalities. I acknowledge the support received from the observing staffs at the Indian Astronomical Observatory, Hanle and CREST and the staff members at the Vainu Bappu Observatory, Kavalur, for taking care of all the necessary requirements, during the period of thesis writing. I thank my colleague Avinash Surendran at IIA for various lengthy discussion sessions that worked as a stress reliever during tough times. Needless to say, I am indebted to my beloved family for their continuous support and strength, without which this work was simply not possible.

This research has made use of data, software and/or web tools obtained from NASAs High Energy Astrophysics Science Archive Research Center (HEASARC). Part of this work is based on archival data, software, or online services provided by the ASI Science Data Center (ASDC). This research has made use of the XRT Data Analysis Software (XRTDAS) developed under the responsibility of the ASDC, Italy. This research has also made use of the NuSTAR Data Analysis Software (NuSTARDAS) jointly developed by the ASI Science Data Center (ASDC, Italy) and the California Institute of Technology (Caltech, USA). Steward Observatory spectropolarimetric monitoring project is supported by Fermi Guest Investigator grants NNX08AW56G, NNX09AU10G, and NNX12AO93G. This research has made use of up-to-date SMARTS optical/near-infrared light curves. This research has made use of data from the OVRO 40-m monitoring program (Richards et al. 2011) which is supported in part by NASA grants NNX08AW31G and NNX11A043G, and NSF grants AST-0808050 and AST-1109911. The CRTS survey is supported by the U.S. National Science Foundation under grants AST-0909182 and AST-1313422. This research has made use of the Palermo BAT Catalogue and database operated at INAF − IASF Palermo.

Funding for SDSS-III has been provided by the Alfred P. Sloan Foundation, the Participating Institutions, the National Science Foundation, and the U.S. Department of Energy Office of Science. The SDSS-III web site is `http://www.sdss3.org/`.

SDSS-III is managed by the Astrophysical Research Consortium for the Participating Institutions of the SDSS-III Collaboration including the University of Arizona, the Brazilian Participation Group, Brookhaven National Laboratory, Carnegie Mellon University, University of Florida, the French Participation Group, the German Participation Group, Harvard University, the Instituto de Astrofisica de Canarias, the Michigan State/Notre Dame/JINA Participation Group, Johns Hopkins University, Lawrence Berkeley National Laboratory, Max Planck Institute for Astrophysics, Max Planck Institute for Extraterrestrial Physics, New Mexico State University, New York University, Ohio State University, Pennsylvania State University, University of Portsmouth, Princeton University, the Spanish Participation Group, University of Tokyo, University of Utah, Vanderbilt University, University of Virginia, University of Washington, and Yale University.

Use of the *Hydra* cluster at Indian Institute of Astrophysics is acknowledged.

List of Publications

Refereed Publications:

1. *Broadband Observations of the Gamma-Ray Emitting Narrow Line Seyfert 1 Galaxy SBS 0846+513*
   Paliya, Vaidehi S., Bhoomika Rajput, C. S. Stalin, and S. B. Pandey, **The Astrophysical Journal**, in press

2. *A Hard Gamma-ray Flare from 3C 279 in 2013 December*
   Paliya, Vaidehi S., Chris Diltz, Markus Böttcher, C. S. Stalin, and David Buckley, 2016, **The Astrophysical Journal**, 817, 61

3. *Violent Hard X-ray Variability of Mrk 421 Observed by NuSTAR in 2013 April*
   Paliya, Vaidehi S., Markus Böttcher, Chris Diltz, C. S. Stalin, S. Sahayanathan, and C. D. Ravikumar, 2015, **The Astrophysical Journal**, 811, 143

4. *Fermi-Large Area Telescope Observations of the Exceptional Gamma-ray Flare from 3C 279 in 2015 June*
   Paliya, Vaidehi S., 2015, **The Astrophysical Journal Letters**, 808, L48

5. *The High Redshift Blazar S5 0836+71: A Broadband Study*
   Paliya, Vaidehi S., 2015, **The Astrophysical Journal**, 804, 74

6. *Awakening of the High Redshift Blazar CGRaBS J0809+5341*
   Paliya, Vaidehi S., M. L. Parker, C. S. Stalin, A. C. Fabian, S. Ramya, S. Covino, G. Tagliaferri, S. Sahayanathan, and C. D. Ravikumar, 2015, **The Astrophysical Journal**, 803, 112

7. *Multi-Wavelength Observations of 3C 279 during the Extremely Bright Gamma-ray Flare in 2014 March-April*
   Paliya, Vaidehi S., S. Sahayanathan, C. S. Stalin, and C. D. Ravikumar, 2015, **The Astrophysical Journal**, 803, 15

8. *Fermi Monitoring of Radio-loud Narrow Line Seyfert 1 Galaxies*
   Paliya, Vaidehi S., C. S. Stalin, and C. D. Ravikumar, 2015, **The Astronomical Journal**, 149, 41

9. *The Peculiar Radio-loud Narrow Line Seyfert 1 Galaxy 1H 0323+342*
   Paliya, Vaidehi S., S. Sahayanathan, M. L. Parker, A. C. Fabian, C. S. Stalin, Ayesha Anjum, and S. B. Pandey, 2014, **The Astrophysical Journal**, 789, 143

10. *The Nature of γ-Ray Loud Narrow-line Seyfert I Galaxies PKS 1502+036 and PKS 2004-447*
    Paliya, Vaidehi S., C. S. Stalin, Amit Shukla, and S. Sahayanathan, 2013, **The Astrophysical Journal**, 768, 52

11. *Intranight Optical Variability of γ-ray Loud Narrow-Line Seyfert 1 Galaxies*
    Paliya, Vaidehi S., C. S. Stalin, Brijesh Kumar, Brajesh Kumar, V. K. Bhatt, S. B. Pandey, and R. K. S. Yadav, 2013, **Monthly Notices of the Royal Astronomical Society**, 428, 2450

Refereed Conference Proceedings:

1. *Lepto−Hadronic Origin of γ-ray Outbursts of 3C 279*
   Paliya, Vaidehi S., Chris Diltz, Markus Böttcher, C. S. Stalin, and David Buckley, Refereed proceedings of the RETCO-II meeting held at ARIES, Nainital, India from 2015 May 6−8, published in the ASI Conference Series. Edited by I. Chattopadhyay, A. Nandi, S. Das, and S. Mandal, 2015, ASInC, 12, 113

Contents

List of Figures

List of Tables

Chapter 1

Introduction

Active Galactic Nuclei (AGN) are commonly attributed to a class of center of galaxies, which are active. This activity is manifested in the presence of broad emission lines in their optical/infra-red (IR) spectra. This distinguishes them from other normal galaxies whose optical/IR spectra are usually dominated by absorption lines. The host of an AGN is called an active galaxy. AGN produce extremely luminous radiation from a very compact region, through accretion of mass onto a supermassive black hole (SMBH, $M_{\rm BH} \sim 10^6 - 10^{10} M_{\odot}$) at the center of the galaxy. The emitted radiation generally outshines the total emission from its host galaxy and spans the entire accessible electromagnetic spectrum from low frequency radio waves to high energy γ-rays. They are among the most luminous extragalactic sources. A detailed investigation of AGN can provide insights into physics of accretion flow onto SMBH, their influence on star formation properties of the host, heating of the interstellar and intergalactic medium, etc. A survey study of a large sample of AGN in IR, optical, and X-ray bands can provide the hints on their formation and evolution. AGN are also excellent laboratories to understand particle acceleration processes happening close to the central SMBH.

1.1 Historical Background

The first evidence that some galaxies show strong emission line component from their centers was found by Carl Seyfert in the 1940s. He obtained spectra of six galaxies, showing high-excitation nuclear emission lines superposed on a normal star-like spectrum (Seyfert 1943). They were named as *Seyfert galaxies*. Subsequently, with the advancement of radio astronomy in the 1950's a new class of energetic sources, the radio galaxies, were discovered.

The lunar occultation of the radio source 3C 273, in 1962, allowed the precise measurement of its radio position and consequently the identification of its optical counterpart. 3C 273 appeared like a star in optical images, however, its optical spectrum exhibited several broad emission lines unlike stellar spectrum where mostly absorption lines are detected. For this reason 3C 273 and similar objects were called quasi-stellar radio sources or quasars in short. In 1963, Maarten Schmidt calculated the distances of quasars using their optical spectra, in terms of cosmological redshift, and these sources were then recognized to be extragalactic in nature (Schmidt 1963). The measurement of the redshift of 3C 273 and other similar sources coupled with their large luminosities led to the idea of these sources being powered by accretion onto SMBH. The idea of SMBH powered AGN seems to be emerged by the discovery of SMBH at the center of our own Milky way (e.g., Gillessen et al. 2009) and other nearby galaxies. A large fraction of the known quasar population ($\sim$85%) are known to emit no or little radio emission, hence termed as radio-quiet quasars. A minority of about 15% quasars emit copiously in the radio band and called as radio-loud quasars. The radio-loud quasars exhibit large scale relativistic jets extending upto Mpc scales.

With the advent of high energy astronomy covering X-rays to very high energy (VHE; $E > 100$ GeV) emissions, broadband emission features of AGN have been studied for a few sources and various sub-classes were named accordingly. It has been proposed that the emission from AGN is dominated by the non-thermal processes over the entire electromagnetic spectrum, contrary to normal galaxies where the spectrum is composed mainly from the integrated thermal light of stars.

1.2 The physical picture of AGN

Over the last three decades, there has been considerable progress in our understanding of AGN (e.g. Blandford & Königl 1979; Urry & Padovani 1995, and references therein). The current paradigm ascribes the accretion process of matter onto a SMBH, residing at the center of the host galaxy, as a primary cause of the observed luminous radiation. Matter infalling the black hole forms a disk, called the accretion disk, and loses angular momentum through turbulent and/or viscous processes in the accretion disk. Due to these processes, the accretion disk is heated to extremely high temperatures and dissipates the stored energy primarily at ultraviolet (UV) and X-ray frequencies. The enormous energy release of this central accretion process then affects the environment and matter in the immediate vicinity, that contribute to the emission over the entire electromagnetic spectrum. In this sense, a SMBH represents the “central engine” of the AGN emission. Apart from this, a small fraction of AGN are found to produce large scale jets along the polar axis of the accretion disk. One of the widely accepted theories of jet production asserts that the jet plasma follows twisted magnetic field lines threading the accretion disk or the black hole’s ergosphere, with the flow being collimated and accelerated along the poles (e.g., Blandford & Königl 1979; Blandford & Payne 1982). Thus, the transfer of energy powering the outflow is derived from gravitational energy of the infalling matter. It is then converted to kinetic energy of rotation, and from there via the magnetic field to an outflow, which transports the energy in the form of kinetic jet power (Meier et al. 2001; Spruit 2010). How the gravitational energy is converted into radiative and kinetic energy, though, is poorly understood.

1.2.1 The Accretion Disk

In the standard model of the AGN, cold matter close to the central black hole forms an accretion disk. Many models have been proposed to explain the accretion process, describing both high and low accretion rates. In general, at high accretion rates the commonly accepted model is the geometrically thin, optically thick accretion disk, proposed by Shakura & Sunyaev (1973). According to this model, the matter moves in quasi−Keplerian motion, induced by the gravitational pull of the SMBH, and approaches the center of the disk by losing angular momentum due to the presence of a magnetic field and turbulent motion. The spectrum of an accretion disk around a SMBH peaks at optical-UV frequencies. Additionally, a corona of hot material forms above the accretion disk and can scatter photons up to X-ray energies via inverse Compton (IC) mechanism.

1.2.2 Broad Line Region

The broad line region (BLR) is believed to be formed by clouds of dust and gas which are photo-ionized by the radiation from the accretion disk. The plasma clouds that form this structure are relatively close to the central black hole ($\lesssim 0.1-1$ pc), and therefore move around the central engine with a very high velocity (10^3-10^4 km s^{-1}). The BLR produces strong emission lines by recombination, following the ionization by photons emitted primarily by the accretion disk. The luminosity emitted from the BLR is thus a very good tracer of the ionizing luminosity of the accretion disk, and of its overall luminosity. The emission lines are broadened due to the high rotational velocity of the moving clouds and can be used to derive their average distance from the central engine.

1.2.3 Dusty Torus

The dusty torus lies considerably far from the central black hole ($1-10$ pc) and re-emits the absorbed accretion disk radiation in the IR band. By obscuring the optical-UV emission from the innermost components (i.e. BLR, accretion disk radiation) at specific orientation angles, the torus is believed to be responsible for the various spectral features observed from the different AGN sub$-$classes. The latest models, however, predict different shapes for the torus. The widely accepted model describes a clumpy distribution of dust all around the nucleus (Nenkova et al. 2002).

1.2.4 Narrow Line Region

The narrow line region (NLR) is analogous to the BLR, formed by clouds of ionized plasma, but located at a larger distance ($\sim$100 pc) from the central black hole. The rotational velocity of the NLR clouds is comparatively smaller than that of the BLR clouds ($\sim 100-500$ km s^{-1}). The smaller velocity can be easily derived from the definitely narrower emission lines originated from the plasma in this region. The lines emitted by NLR clouds can be clearly distinguished from those emitted by the BLR, because along with the narrower width, they also exhibit “forbidden” lines, that can be produced only in lower density conditions of NLR so that recombination can happen by spontaneous de−excitation and not by collision events.

1.2.5 The Relativistic Jets

The relativistic jets are the flow of radiation and extremely energetic particles that occurs along the poles of the accretion disk. They form giant radio structures extending from a few hundreds of kpc to several Mpc. They are found to be associated only with radio-loud AGN and are responsible for their radio-loudness. The motion of the plasma inside the jets is relativistic (Rees 1966), as can be inferred from the superluminal motion observations (e.g., Jorstad et al. 2001). The main composition of the jet is normal plasma (electron-protons) and/or pair plasma (electron-positron). Jets extend up to Mpc scales and usually terminate by producing giant structures called lobes where the jets decelerate mainly because of their interaction with the surrounding matter. While the jet emission is highly anisotropic, because of relativistic beaming effect, the lobes emit a strong, isotropic radio emission due to the plasma deceleration. How the relativistic jets are launched from the central part of the AGN, i.e., their production mechanism, is still unknown and is a matter of active debate. The two leading theories are the electromagnetic extraction of energy and angular momentum from an accretion disk and the extraction of rotational energy from the spinning SMBH (Blandford & Znajek 1977; Blandford & Payne 1982). A schematic picture of a standard radio-loud AGN is shown in Figure 1.1.

1.3 AGN Types and Unification Scheme

Different types of AGN form a zoo of different names. Nevertheless, two major classes have been established, i.e., radio-loud AGN and radio-quiet AGN. This classification is based on a parameter called *radio-loudness factor*, defined as the ratio of 5 GHz radio flux density ($f_{5\mathrm{GHz}}$) and the optical B band (λ = 4400 Å) flux density (f_{B}):

$$R = \left(\frac{f_{5\mathrm{GHz}}}{f_{\mathrm{B}}}\right) \tag{1.1}$$

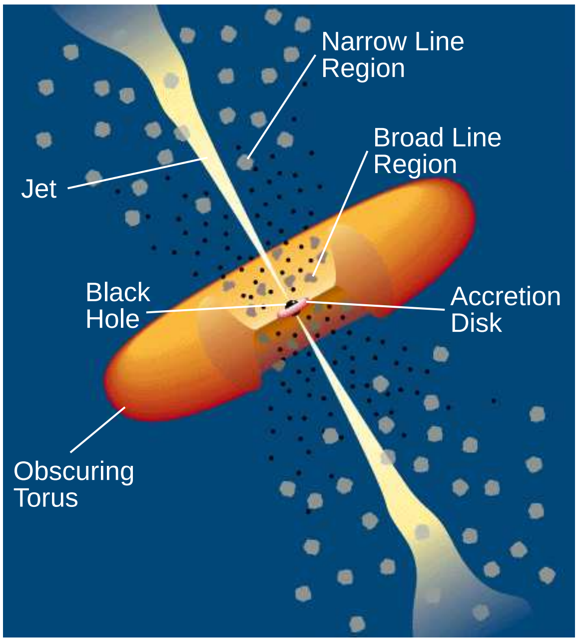

Figure 1.1: A schematic diagram of radio-loud AGN. The SMBH is surrounded by an accretion disk. The nearby clouds orbiting the disk produces the broad emission lines. A doughnut shaped dusty torus obscures the BLR and the inner portion of the jet. Narrow lines are produced by the clouds much farther from the central engine (Urry & Padovani 1995).

Approximately 10−15% of AGN are found to be radio-loud ($R \gtrsim 10$; Kellermann et al. 1989). Generally, the radio emission in radio-loud AGN is dominated by powerful relativistic radio jets and lobes, which are absent in radio-quiet AGN (e.g., Miller et al. 1993).

1.3.1 Types of AGN

Both the radio-loud and radio-quiet AGN are further sub-classified as *Type 1* and *Type 2* objects depending on the strength of the optical emission lines in their spectrum. The optical spectrum of a *Type 2* AGN is characterized by mainly narrow emission lines (FWHM$\sim$1000 km s^{-1}), while, *Type 1* objects exhibit both narrow and broad emission lines. In *Type 1* sources, the line width of broad emission lines can extend up to 10000 km s^{-1}. The orientation of the AGN with respect to an observer highly affects its phenomenology. *Type 1* sources are believed to be viewed at a smaller angle from the polar axis of the accretion disk ($\theta_{\rm v} \lesssim 60°$) and, thus, both the BLR and the NLR are visible, resulting in the observation of both broad and narrow emission lines, as discussed above. However, due to large viewing angle in *Type 2* sources, the BLR emission lines are obscured by the dusty torus and hence only narrow emission lines, emitted by the NLR located farther from the central region, are present in their optical/IR spectra.

Seyfert 2 galaxies: They belong to the category of *Type 2* AGN. Their optical spectrum is characterized by narrow emission lines and they are hosted in nearby spiral galaxies. The Narrow Emission Line Galaxies (NELGs), also called as Narrow Line X-ray Galaxies (NLXGs), belong to this subclass. The optical spectrum of NELGs is similar to *Seyfert 2* galaxies, but the hard X-ray emission is relatively stronger in them.

Seyfert 1 galaxies: They belong to *Type 1* AGN. Their optical spectra are similar to the *Seyfert 2* galaxies with additional broad emission lines. A major fraction of the Seyfert galaxies ($\sim 93\%$) are radio-quiet in nature. Further, Broad Absorption Line Quasars and Low Ionization Nuclear Emission Line Region galaxies (LINERs) also belong to this category.

Radio galaxies: According to the definition introduced by Fanaroff & Riley (1974), the radio-loud AGN, whose radio emission can be resolved, were historically divided in two classes namely: Fanaroff-Riley class I (FR I) and Fanaroff-Riley class II (FR II). The FR II galaxies have radio morphologies characterized by powerful edge-brightened double lobes with prominent hotspots and tend to be found in less dense environments, while, the FR I have radio emission peaking near the nucleus, have rather diffuse edge-darkened lobes, and frequently inhabit more dense environments. FR I sources are less luminous with $P_{178\mathrm{MHz}} < 10^{24}$ W/Hz, while FR II are the strongest radio source with $P_{178\mathrm{MHz}} > 10^{24}$ W/Hz (Fanaroff & Riley 1974).

Blazars: The radio-loud AGN whose radio emission cannot be resolved are classified as radio compact objects. The lack of extended emission is often ascribed to the peculiar orientation of the jet with respect to the line of sight to the observer, even though true compact objets have been observed. Those AGN that are thought to have their relativistic jets directed towards the observer are classified as blazars. Radio galaxies are, therefore, thought to be the parent population of blazars.

1.3.2 The AGN Unification

The idea of AGN unification came when it was realized that orientation effects can play a major role in the interpretation of the observations from some of these sources. With the improvement in optical spectroscopic capabilities, features of both *Type1* and *Type2* objects were discovered from some Seyfert galaxies. Moreover, optical polarization monitoring also revealed similar properties for the two classes of Seyfert galaxies (Smith et al. 2004). Since then, numerous efforts have been made in determining to what extent different types of AGN are simply different manifestations of the same object viewed from different angles.

Rowan-Robinson (1977) reported that the central region in many AGN is contaminated by obscuring material in the form of gas and dust. Further, it was also proposed that the gas or dust is either distributed in the form of a torus (Pier & Krolik 1992a,b) or like a wrapped disk (Sanders et al. 1989). Also, radiation from AGN is anisotropic in nature. The emission is strongly Doppler boosted along the jet direction. So, there are certain other phenomena like relativistic beaming and superluminal motion which play a key role in modifying the appearance of an AGN, apart from obscuration by the torus. Altogether, these effects cause AGN to appear markedly different from different viewing angles.

The basic concept of unification scheme is based on the orientation of the nuclear zone, of the torus, and of the jet with respect to the observer. If the AGN is orientated more edge-on then the torus hides the central region and at large angles it would obscure the BLR completely. In this case, the observed optical spectrum of an AGN is featured by narrow emission lines, while the observer who is looking face-on at the AGN, is able to see the BLR and related features of the central engine along with the NLR emission. The observed properties of the radio-loud AGN are characterized by relativistic jets, which are absent in the radio-quiet AGN. When the line of sight is close to the radio jet, relativistic beaming strongly amplifies the luminosity and produces strong variability, polarization, superluminal motion, and all the other effects described for the class of blazars.

According to the current unification model proposed by Urry & Padovani (1995), narrow line radio galaxies (NLRGs), broad line radio galaxies (BLRGs), radio-loud quasars, and blazars belong to the category of the radio-loud AGN, in which, NLRGs are seen at large angles along the line of sight to the observer, radio-loud

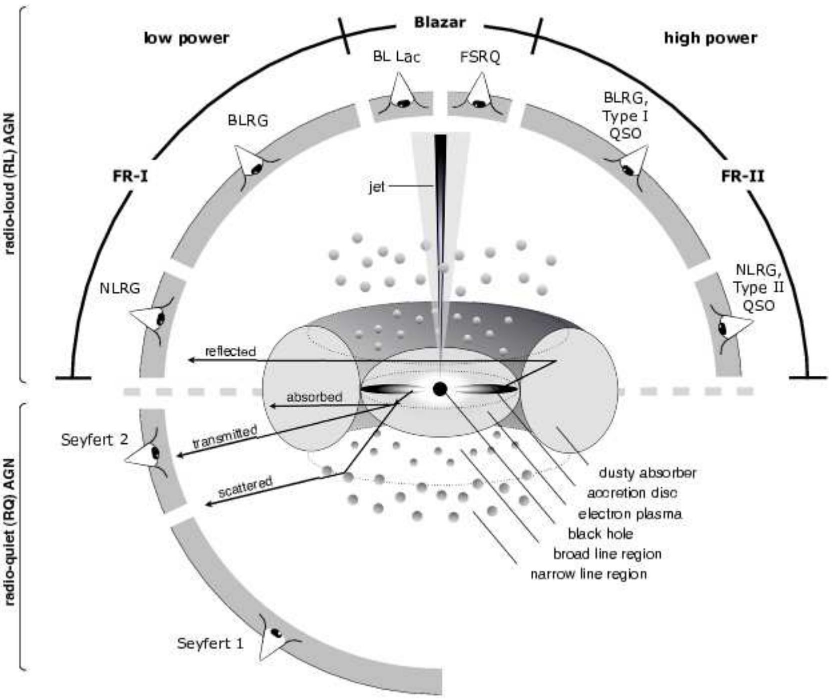

Figure 1.2: A schematic representation of the current understanding the AGN unification scheme. The radio-loud AGN are shown in the upper part and radio-quiet in the lower part (from Beckmann & Shrader 2012).

quasars and BLRGs at modest angles, and blazars are observed close to the line of sight to the observer. Radio-quiet quasars, Seyfert galaxies, LINERs etc. belong to radio-quiet AGN. A basic schematic of AGN unification is presented in Figure 1.2.

1.4 Blazars

A small subset of radio-loud quasars have compact radio morphology with flat radio spectra ($\alpha_r < 0.5$, $S_\nu \propto \nu^{-\alpha}$; Urry & Padovani 1995), show rapid variability at all wavelengths, and their optical and radio emission are also polarized (e.g., Fan et al. 1997; Jorstad et al. 2005). They also exhibit superluminal motion in the radio band (Rees 1966; Gubbay et al. 1969). It is now thought that such observational manifestation of these objects are due to large scale relativistic jets emitted by them which are aligned closely to the observer and thus are subjected to relativistic beaming. These sources are called blazars.

Blazars are classified as BL Lac objects and Flat Spectrum Radio Quasars (FSRQs). FSRQs are known to exhibit broad optical emission lines (rest-frame equivalent width EW>5Å) whereas the optical spectra of BL Lac objects consist of weak or no emission lines (EW<5Å). This EW based classification, beside being easy to apply, could be ascribed to the different accretion mechanisms. The ionizing photons responsible for the broad line emission are produced by the accretion disk, and therefore a difference in the strength of broad emission lines reflects a difference in the accretion process. In the case of an efficient accretion, the BLR produces extremely luminous emission lines. On the other hand, a radiatively inefficient accretion mechanism would not induce the BLR to produce broad emission lines. Since the EW can be considered as a good measure of the line emission dominance over the underlying continuum, the descriptive EW based classification could corresponds to an intrinsic difference between the two classes. FSRQs show strong emission lines, being therefore linked to a radiatively efficient accretion process, such as Shakura & Sunyaev (1973) disk, while the lineless BL Lac objects were connected to inefficient accretion, like the advection−dominated accretion flow (e.g., Narayan et al. 1998).

It is known since the EGRET (Energetic Gamma-Ray Experiment Telescope; Thompson et al. 1993) era that blazars emit bulk of the radiation in the γ-ray band. Since the launch of *Fermi* Large Area Telescope (*Fermi*-LAT; Atwood et al. 2009), it became very clear that blazars dominate the extragalactic high energy γ-ray sky. As of now, more than $\sim$3000 blazars are found to be γ-ray emitter (Acero et al. 2015). This suggests that powerful γ-ray emission is another characteristic property of blazars.

The broadband spectral energy distribution (SED) of a blazar has two broad peaks, the first between mm and soft X-ray wavelengths, and the second in the MeV−GeV range (see Figure 1.3). In general, FSRQs exhibit lower peak energies and higher bolometric luminosities than BL Lac objects and the observed anti-correlation of peak frequencies with bolometric luminosities is termed as 'blazar sequence' (Figure 1.3; Fossati et al. 1998). Various models have been proposed to explain the broadband emission from blazars. The origin of the low energy peak is understood to be associated with synchrotron radiation from relativistic electrons, thanks to the observations of high degree of polarization. The high energy peak in the SED, on the other hand, can be explained by the IC scattering of low energy

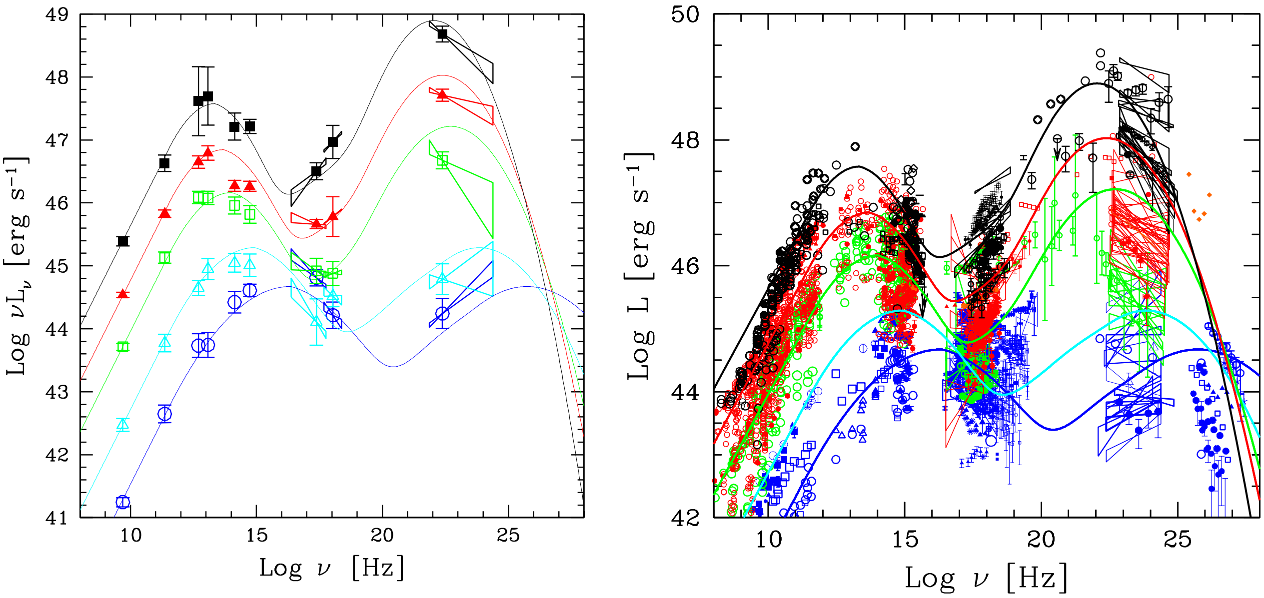

FIGURE 1.3: Left Panel: The typical SED of blazars and the 'blazar sequence' as given by Fossati et al. (1998) and Donato et al. (2001). Right panel: SED of the blazars detected by *Fermi*-LAT in the first 3 months of operation (Ghisellini 2011). Different colors indicates different γ-ray luminosities. The solid lines are the same as the left panel.

photons. In general, most models agree on the fact that the IC scattering involves the same population of electrons that is emitting synchrotron radiation (so called one zone leptonic models). Depending on the reservoir of the seed photons for IC scattering to lie inside or outside the jet, the models are divided into two classes: Synchrotron self Compton (SSC) and External Compton (EC) models. In SSC, synchrotron photons from the jet are scattered by the same electron population that emits them (Konigl 1981; Marscher & Gear 1985; Ghisellini & Maraschi 1989). Thus, SSC models connect synchrotron and IC emission processes directly. Alternatively, the seed photons for IC scattering can be external to the jet (Begelman & Sikora 1987; Melia & Konigl 1989; Dermer et al. 1992). The plausible reservoir of the seed photons for EC can be the accretion disk (Dermer & Schlickeiser 1993; Böttcher et al. 1997), the BLR (Sikora et al. 1994; Ghisellini & Madau 1996), and the dusty torus (Błażejowski et al. 2000). Both SSC and EC mechanisms are likely to be working in blazar jets, however their dominance varies among various subclasses of blazars. For example, FSRQs show prominent thermal components that can act as the source of seed photons for the EC process. Thus, in these objects, the high energy emission is likely to be dominated by EC mechanism. The absence of any evident thermal emission in BL Lac objects suggests that in these objects there are less sources of external photons to be used as seeds for IC scattering process. Hence, γ-ray emission in BL Lac objects is more likely produced by SSC mechanism. Moreover, the existence of the 'blazar sequence' is also explained on the basis of the above discussed models. The presence of dense thermal photon field surrounding the jet in FSRQs implies a severe cooling of the jet electrons and consequently electrons looses their energies before attaining very high energies, thus peak at low frequencies. On the other hand, the presence of almost 'clean' environment in BL Lac objects means less severe cooling and electrons can reach to very high energies before getting cooled and therefore their SED peak lie at GeV−TeV energies. Based on the location of the rest-frame synchrotron peak frequency ($\nu_{\rm syn}^{\rm peak}$), Abdo et al. (2010d) have classified the blazars in various categories. They are considered as low synchrotron-peaked (LSP), intermediate synchrotron-peaked (ISP), and high synchrotron-peaked (HSP) with $\nu_{\rm syn}^{\rm peak} < 10^{14}$ Hz, 10^{14} Hz $< \nu_{\rm syn}^{\rm peak} < 10^{15}$ Hz, and $\nu_{\rm syn}^{\rm peak} > 10^{15}$ Hz, respectively. Almost all *Fermi*-LAT detected FSRQs are LSP blazars, whereas, HSP blazars are major constituent of BL Lac objects.

1.4.1 Narrow Line Seyfert 1 Galaxies

NLSy1 are a subclass of Seyfert galaxies first classified as a separate entity by Osterbrock & Pogge (1985). They are generally hosted by spiral galaxies. NLSy1 galaxies are believed to be rather young AGN in the early stages of their evolution (Mathur et al. 2001). Their optical spectra have narrow Balmer lines (FWHM ($\rm H_\beta$) < 2000 km s^{-1}), weak [O III] ([O III]/$\rm H_\beta$ < 3), and strong optical Fe II lines (Osterbrock & Pogge 1985; Goodrich 1989). They also have steep soft X-ray spectra (Boller et al. 1996; Wang et al. 1996; Leighly 1999b) and show rapid X-ray flux variations (Pounds et al. 1995; Leighly 1999a). These observational characteristics are attributed to them having low mass black holes ($\sim 10^6 - 10^8 M_\odot$) accreting close to the Eddington limit (Peterson et al. 2000; Hayashida 2000; Grupe & Mathur 2004; Zhou et al. 2006; Xu et al. 2012). Similar to quasars, NLSy1 galaxies also exhibit radio-loud/radio-quiet dichotomy but at a lesser extent. About 7% of NLSy1 galaxies are found to be radio-loud (Komossa et al. 2006), compared to ∼15% known for quasars. These RL-NLSy1 galaxies exhibit compact core-jet structure, flat/inverted radio spectra, high brightness temperature, and superluminal patterns (Komossa et al. 2006; Doi et al. 2006). Recently, kiloparsec-scale radio structures have been found in six RL-NLSy1 galaxies (Doi et al. 2012). Along with a larger number of blazars, *Fermi* has also detected significant γ-ray emission from some RL-NLSy1 galaxies (e.g., Abdo et al. 2009b). Subsequent multi-wavelength monitoring using both space and ground based observation facilities confirmed their similarity with blazar class of AGN.

1.4.2 Beamed AGN

The extreme properties shown by blazars and γ-ray emitting NLSy1 (γ-NLSy1) galaxies are now widely believed to be due to relativistic effects. Therefore, in this thesis, both blazars and γ-NLSy1 galaxies are collectively called as beamed AGN.

1.5 Beaming Effects

A series of relativistic effects take place when a source of radiation moves with relativistic velocity towards the observer. If an emission region is moving at a velocity close to the speed of light along a direction which forms a small angle with the observer's line of sight, the time interval between the emission of two successive photons, as measured in the observer's frame, is reduced, and the source appears to move faster than its actual velocity (Blandford & Königl 1979). This effect is known as *superluminal motion.* The apparent velocity of the emitting source in this case is given by

$$v_{\rm app} = \frac{\beta c \sin\theta_{\rm v}}{1-\beta\cos\theta_{\rm v}} \tag{1.2}$$

where $\theta_{\rm v}$ is the angle between the direction of motion of the source and the observer line of sight, $\beta = v/c$, where v is the velocity of the emission region and c is the velocity of light in vacuum. The emitted radiation will be collimated in the direction of motion into a cone with opening angle $\theta_{\rm j} \sim 1/\Gamma$, where $\Gamma = (1-\beta^2)^{-1/2}$, is the bulk Lorentz factor, and the intensity of the radiation will be amplified by Doppler boosting in the direction of motion. These effects are the consequence of special relativity and known as *relativistic beaming.* The relativistic beaming is quantified in terms of Doppler factor (δ):

$$\delta = \frac{1}{\Gamma(1-\beta\cos\theta_{\rm v})} \tag{1.3}$$

Due to relativistic beaming, the observed flux density from a moving emission region is modified as (e.g., Rybicki & Lightman 1979)

$$f(\nu) = \delta^{3+\alpha} f'(\nu') \tag{1.4}$$

where primed quantities are in the comoving frame and α is the spectral index. It is clear that the observed radiation is not the same as emitted by the source. Hence, relativistic effects play a key role in the appearance of an AGN and form the backbone of the unification model.

1.6 Main Goals of the Work

Beamed AGN are excellent laboratories to study the radiative environment within the jets of AGN, as dominant part of the observed non-thermal emission from AGN originates from jets. A very important challenge in understanding the physics of AGN lies in the accumulation of densely sampled data both in time and energy. Due to this constraint of simultaniety in observations, in spite of the progress that has been made to understand the AGN jets, several key questions are still unanswered. Some of the open problems are (i) the jet composition, i.e., whether the jets are composed of electron-proton plasma or electron-positron plasma, or both; (ii) the location and structure of the γ-ray emitting zone; (iii) the origin of observed variability on timescales from minutes to years; (iv) the role of the external photon fields in γ-ray production; (v) the energy distribution of the particles responsible for the observed radiation and their acceleration mechanism; and (vi) the role of magnetic fields in the origin, confinement and propagation of relativistic jet. Moreover, the *Fermi*-LAT detection of γ-rays from about half-a-dozen NLSy1 galaxies have raised the questions on our understanding of the jet production in a completely different class of AGN. One of the primary reasons behind these unsolved mysteries is the lack of good quality data. Such collection of multi-wavelength data sets (as never before) from low energy radio to high energy γ-ray band is now possible due to the recent advances in the observational astronomy. As excellent quality data are now publicly available, an effort has been made in this work to tackle some of the above mentioned problems.

This thesis is aimed at understanding the general physical properties of γ*-ray emitting beamed AGN and it consists of two parts: the first part mainly focuses on constraining the various radiative processes happening in the central regions of blazars and the location of the* γ*-ray emitting region using temporal and spectral studies, while the second part comprises of the study of the physical properties of* γ*-NLSy1 galaxies and their similarities or lack of it with blazars by adopting various observational approaches.*

Chapter 2

Multi-wavelength Observations: Data Reductions and Theoretical Modeling

To understand the physical properties of beamed AGN, it is important to use both observational and theoretical tools. In the thesis, the broadband data (radio to γ-rays) from various ground and space based telescopes are used to cover the observational aspects of the study. The ground based optical telescopes used are the 2 m Himalayan Chandra Telescope (HCT) and the 1.3 m Devasthal Telescope located at Hanle and Nainital, respectively. On the other hand, optical-UV, X-ray and γ-ray data from space telescopes such as *Swift*, *Nuclear Spectroscopic Telescope Array* (*NuSTAR*), and *Fermi* telescopes are also used to carry out the analysis. A theoretical leptonic emission model is developed by incorporating various radiative processes, to describe the observed emission from beamed AGN. Throughout, a ΛCDM cosmology with the Hubble constant $H_0 = 71$ km s^{-1} Mpc^{-1}, $\Omega_m = 0.27$, and $\Omega_\Lambda = 0.73$ is adopted.

2.1 Observations and Data Reduction

2.1.1 *Fermi Gamma-ray Space Telescope*

The *Fermi Gamma-ray Space Telescope*, formerly known as the Gamma-ray Large Area Space Telescope (GLAST), was launched on a Delta II Heavy launch vehicle on 2008 June 11. It has a low Earth orbit at an altitude of ∼550 km with orbital period of ∼96 min. This space telescope covers the photon energy range of 8 KeV to ∼500 GeV. There are two instruments onboard *Fermi*:

1. GLAST Burst Monitor (GBM), and
2. Large Area Telescope (LAT).

LAT and GBM are the primary and secondary instruments of the telescope, respectively. The primary function of GBM (Meegan et al. 2007) is to detect sudden flares of γ-rays produced by Gamma Ray Bursts (GRBs) and solar flares. It includes two sets of detectors: twelve Sodium Iodide (NaI) scintillators, and two cylindrical Bismuth Germanate (BG) scintillators. The NaI detectors cover the lower end of the energy range, from a few KeV to about 1 MeV, while the BG detectors are sensitive to the energy range between 150 KeV to 30 MeV.

2.1.1.1 Large Area Telescope

LAT detects γ-rays by tracking the electron-positron pairs produced by an incident γ-ray photon and it also measures direction and energy of the incident photon. The optimum working energy range of the instrument is from 20 MeV to greater than 300 GeV(Atwood et al. 2009). It has a large field of view (FoV) of 2.4 sr which implies that, at any point of time, LAT covers ∼20% of the sky. Due to LAT's large FoV, the primary observing mode of *Fermi* is the sky survey mode and in the default operating mode it continuously scans the entire sky every 3 hr (∼2 orbits).

The LAT point spread function (PSF), angular resolution, and effective area are the functions of the incident photon's energy, inclination angle, and the event class. The PSF of LAT for an on-axis γ-ray photon is about 3° (68% containment radius) at 100 MeV and 0.04° at around 100 GeV. Systematics on the measured fluxes, governed by the uncertainty in the effective area, are of around 10% below 100 MeV, 5% between 316 MeV to 10 GeV and 10% above 10 GeV. Details of the performance of LAT can be found at Atwood et al. (2009).

2.1.1.2 LAT Data Reduction Procedure

The LAT data are analyzed using the software/tools provided by the *Fermi*-LAT team which is based on maximum likelihood technique (e.g., Mattox et al. 1996). The details of the data reduction procedure can be found at `http://fermi.gsfc.nasa.gov/ssc/data/analysis/`, however, for the purpose of quick reference, it is described here in brief.

Two types of likelihood analysis techniques, binned and unbinned, are used to analyze the *Fermi*-LAT data. The unbinned likelihood method is recommended for short timescale or low source count data. However, binned analysis is preferred for long timescale or high-density data (such as in the Galactic plane) which can cause memory errors in the unbinned analysis. The binned and unbinned likelihood analyses are performed by the set of tasks, fully compatible with Python, provided with the LAT data analysis package `ScienceTools`.

To perform a standard analysis, a circular region of interest (ROI), centered at the source of interest, is chosen for event reconstruction. The size of the ROI should be large enough to take into account the large PSF of LAT. Sources from a region larger than ROI can be included while modeling. This large region is called the "Source Region". The "Source Region" is centered at the target source, with a radius that is larger than the ROI radius by several PSF length scales. In general, the ROI with a radius of 10° and a "Source Region" radius of 15° is reasonable while fitting a point source using unbinned likelihood method. However, while performing binned likelihood technique, one should consider a larger ROI ($\approx$15°). This is due to the fact that the ROI used by the binned likelihood analysis is defined by the 3D counts' map boundary. The region selection used in the data extraction step, which is conical, must fully contain the 3D counts' map spatial boundary, which is square. Furthermore, a model file is used to supply the best guess of the locations and spectral information of all the sources lying within the "Source region". This can be generated using "Modeleditor", a GUI-tool, or by running a user contributed python script[1]. This generates an XML file which contains the information regarding all the sources present in the ROI and "Source Region" from the *Fermi* catalog (e.g., Acero et al. 2015).

In the LAT data analysis, the maximum likelihood (ML) test statistic TS=$2\Delta\log(\mathcal{L})$, where $\mathcal{L}$ represents the likelihood function between models with and without a point source at the position of source of interest, is calculated to determine the significance of the γ-ray signal. While performing the likelihood fitting, the spectral parameters of all the sources lying within the ROI are allowed to vary. For the sources lying outside the ROI, but present within the "Source Region", the parameters are kept fixed to the catalog values. A first run of the ML analysis is performed over the period of interest and all the sources with TS < 25 are removed[2]. This updated model is used for further temporal and spectral analysis.

Following are the steps to perform standard unbinned likelihood analysis for a γ-ray point source.

1. All the events that are not within the extraction region used for the analysis are filtered out. This is done by the task `gtselect`.

2. After the data selection is made, the periods in which the satellite was working in standard data taking mode (also referred as good time intervals or GTI) are selected. The task `gtmktime` is used for this purpose.

3. The next step after selecting GTI is the generation of exposure maps, which is done in two steps. As the LAT mostly operates in the survey mode, it makes an angle with the position of a source in the sky. The number of the events detected by LAT from a position of the sky or source depends on the amount of time that the source spent at a given inclination angle during an observation. The response function of the LAT also depends upon inclination angle between the observed position of the sky (source) and the z-axis of the LAT. The livetime is the time that the LAT observed a given position on the sky at a given inclination angle. Livetime cubes are calculated by the `gtltcube` task.

---

[1] `http://fermi.gsfc.nasa.gov/ssc/data/analysis/user/`

[2] TS = 25 corresponds to $\sim 5\sigma$ detection (Mattox et al. 1996).

4. The tool `gtexpmap` is used to create an exposure map based on the event selection used on the input photon file and the livetime cube. The exposure map is defined as the total exposure for a given source in the sky in the ROI during observations and are essentially integrals of effective area over time.

5. The diffuse source responses are computed by the `gtdiffrsp` tool. For this purpose, the source model file must contain all the diffuse sources to be fit. This tool adds one column to the event data file for each diffuse source present in the ROI. The diffuse response depends on the instrument response function (IRF).

6. The final step of the LAT data analysis is the likelihood fitting. The tool `gtlike` is used to find the best fit model parameters between the given input model and the observed data. The input model contains the spectral parameters and the position of the sources present in the "Source Region". The optimizing algorithm DRMNFB is used to find initial values of the parameters by performing a crude fitting and then more accurate set of parameters are obtained using the NEWMINUIT algorithm.

2.1.2 *Nuclear Spectroscopic Telescope Array*

NuSTAR is a hard X-ray focusing telescope which works in 3−79 keV energy range. It was launched on a Pegasus XL vehicle from the Reagan Test Site on the Kwajalein Atoll in the South Pacific in 2012. The science instrument onboard *NuSTAR* consists of two depth-graded multilayer-coated Wolter-I conical approximation X-ray optics, which focus onto two independent solid-state focal plane modules (FPMA and FPMB) separated from the optics by ∼10 m focal length. Each module contains 133 nested multilayer-coated grazing incidence shells in a conical approximation to a Wolter-I geometry. The *NuSTAR* has an excellent energy resolution with FWHM response of 0.4 keV at 6 keV and 0.9 keV at 60 keV. The instrument is designed to achieve a temporal resolution as short as ∼0.1 ms. The FoV of each focal plane module is 12 × 12 arcmin^2. Further details of the instrument can be found in Harrison et al. (2013).

2.1.2.1 *NuSTAR* Data Reduction Procedure

The *NuSTAR* data reduction software is distributed within the commonly used X-ray reduction package HEASOFT. In the energy range of 3−79 keV, the *NuSTAR* data is first cleaned and filtered for background events using the *NuSTAR* Data Analysis Software (NUSTARDAS) and calibration files included in the *NuSTAR* CALDB are used as instrument responses. This is done using the task `nupipeline`. The cleaned and calibrated event files are then used to extract the light curve and spectrum of the source of interest, using the tool `nuproducts`. For this purpose, the source region is defined as a circle of $30''$, whereas, the background is taken from a nearby source-free region of $70''$, preferably on the same chip. The source spectra are binned to have at least 20 counts per bin to perform spectral fitting. Moreover, light curves are generated by summing FPMA and FPMB count rates, subtracting background, and using appropriate time binning.

2.1.3 *Swift Gamma Ray Burst Explorer*

Swift Gamma Ray Burst Explorer (Gehrels et al. 2004) is a multi-wavelength observatory primarily devoted to the study of GRB science. *Swift* is part of NASA's medium explorer (MIDEX) program and was launched into a low-Earth orbit on a Delta 7320 rocket in 2004. The *Swift* telescope payload is comprised of three instruments, as mentioned below.

1. Burst Alert Telescope (BAT, 15−150 KeV),
2. X-Ray Telescope (XRT, 0.2−10 KeV), and
3. Ultra Violet and Optical Telescope (UVOT, 170−650 nm).

2.1.3.1 Burst Alert Telescope

The BAT is a survey instrument with a large FoV (1.4 sr, half coded). It operates in the energy range of 15−150 keV. Further details of the instrument can be found in Barthelmy et al. (2005). It works on the principle of coded aperture imaging using CdZnTe detector. The energy range is 15−150 keV for imaging with a non-coded response up to 500 keV.

2.1.3.2 X-Ray Telescope

The XRT is a grazing incidence Wolter Type I focusing X-ray telescope. It can be used in image, photodiode, window timing (WT), and photon counting (PC) mode. PC mode is the primary and most sensitive mode of XRT. It retains full imaging and spectroscopic resolution, but the time resolution is only 2.5 sec. The XRT is operated in this mode only at low fluxes (usually below 1 mCrab). On the other hand, for extremely bright sources, WT mode is used. It is a high gain mode to achieve high resolution timing (2.2 ms) with 1-D position information and spectroscopy. Further details about the instrument can be found in Burrows et al. (2005).

The data acquired from *Swift*-XRT are analyzed using XRT data analysis software (XRTDAS) included in the X-ray reduction package HEASOFT. Event files are first cleaned and calibrated using the tool `xrtpipeline` and the latest calibration database. Further, standard grade selections of 0−12 in the photon counting mode are used to carry out the analysis. Event files are summed to extract the energy spectrum. In general, source region is selected as a circle of 20 pixel radius ($\sim 47''$) which encloses about 90% of the PSF, centered on the source position. The background events are collected from a circular region of about 50 pixel radius. However, when the source becomes extremely bright (count rate >0.5 counts s^{-1}), annular regions should be selected to avoid pile-up effects. The size of the annular region depends on the brightness of the source (see, Stroh & Falcone 2013, for details). Once extracted, source spectrum is binned to 15-20 counts per bin, based on the flux strength, and fitting is performed with XSPEC (Arnaud 1996), the X-ray spectral fitting package included in HEASOFT.

2.1.3.3 Ultra Violet and Optical Telescope

The Ultra Violet and Optical Telescope (UVOT) is a diffraction-limited 30 cm Ritchey-Chrétien reflector. The telescope is having a f/2 primary mirror that is re-imaged to f/13 by the secondary. This results in pixels that are $0.502''$ over its $17'$ square FoV. The detectors are two micro-channel plate intensified CCD (MIC) detectors. These are photon counting devices capable of detecting very low signal levels, allowing the UVOT to detect faint objects over 170−650 nm. The UVOT is sensitive to 22.3 mag in a 17 min exposure.

The data from *Swift*-UVOT are processed using the standard tasks `uvotimsum` and `uvotsource`. The source region is chosen as a circle of $5''$ centered at the source location, while the $1'$ sized background region is extracted from the nearby source-free region. The extracted magnitudes are corrected for the galactic extinction given by Schlafly & Finkbeiner (2011) and then converted to flux units using the zero points and conversion factors of the *Swift*-CALDB (Poole et al. 2008; Breeveld et al. 2011).

2.1.4 Himalayan Chandra Telescope

Himalayan Chandra Telescope (HCT) is a 2 m class optical telescope, located at Indian Astronomical Observatory, Hanle, India. The HCT has Ritchey-Chrétien optics with a f/9 beam at the Cassegrain focus. The telescope is equipped with "Hanle Faint Object Spectrograph Camera (HFOSC)", an optical imager cum spectrograph. The detector is a cryogenically cooled 2048 × 4096 chip, of which the central 2048 × 2048 pixels are used for imaging. The pixel size is 15 μm so that the image scale of $0.''29$ pixel^{-1} covers an area of $10' \times 10'$ on the sky. The CCD readout noise is 4.87 e$^-$ pixel^{-1} , and the gain is 1.22 e$^-$ ADU^{-1}. Further details of the instrument can be found at `http://www.iiap.res.in/centers/iao`.

2.1.5 Devasthal Telescope

This is a 1.3 m telescope located at Devasthal and operated by Aryabhatta Research Institute for Observational Sciences (ARIES), Nainital. It is a modified Ritchey Chrétein system with a f/4 beam (Sagar et al. 2010). There are two detectors available for photometric observations. One is a 2k × 2k conventional CCD having a gain of 1.39 e$^-$ ADU^{-1} and readout noise of 6.14 e$^-$. Each pixel in this CCD has a dimension of 13.5 μm. This corresponds to $0.54''$ pixel^{-1} on the sky thereby covering a field of $12' \times 12'$. The second detector is the 512 × 512 electron multiplying charged coupled device (EMCCD). It has very low readout noise (0.02 e$^-$) and a variable gain that can be selected by the observer. The preliminary science results from observations of these CCDs are given by Sagar et al. (2012). A gain of 225 e$^-$ ADU^{-1} is used for observations carried out using EMCCD.

2.1.5.1 Ground based Optical Data Reduction

Preliminary processing of the images and photometry are done using the `IRAF`[3] package. Various steps carried out in the processing of the images are as follows.

Bias Subtraction: Bias in CCDs is a constant value which gets added to all pixels. However, in practice, it is affected by noise and this value also gets changed due to local effects such as temperature and other effects on the electronics and also may not be necessarily uniform across the chip. To account for this effect, several bias frames were taken during the course of the observational night. An average bias frame is then created using the task `zerocombine` in `IRAF` and adopting *minmax* clipping algorithm. The average bias frame is then subtracted from both the science and the flat frames. In this process, enough care is taken, so that the mean bias frame does not have any hits from high energy cosmic ray events. This procedure is justified as in the conventional CCD, the bias counts have a normal distribution and the mean of a set of bias frames can be considered as a good measure of the true bias. However, this may not be true for the case of EMCCD. As have been pointed by Harpsøe et al. (2012), the counts in the bias frames may follow a non-Gaussian distribution. In such a scenario, one cannot use a mean bias from several bias frames. However, in all the observations carried out in this work using EMCCD, the bias counts are found to follow a Gaussian distribution. Therefore, for EMCCD observations too, a mean bias frame is obtained from several bias frames taken during the course of the night.

Dark Subtraction: Both the CCDs used in the work were cooled to very low temperature ($\sim -80°$C). At such a low temperature, the rate of accumulation of thermal charges can be neglected and thus the usual step of subtracting the dark frame from each target frame is not done.

Flat Fielding: An important step in image processing is flat fielding. A feature of the CCD is that its each pixel tends to operate as a nearly perfect linear detector but with a different quantum efficiency from other pixels. Therefore, to treat the observed image as a single entity, various pixel gains need to be normalized relative to others. For this, several twilight flat field frames were taken. These flat frames, after the bias subtraction, are median combined with the task `flatcombine` in

---

[3] Image Reduction and Analysis Facility, distributed by NOAO, operated by AURA, Inc. under agreement with the US NSF.

`IRAF` and adopting *average sigma* clipping algorithm. This combined flat frame is then normalized by average and all the bias subtracted science frames are then divided by the normalized flat field frame.

Photometry: Aperture photometry is performed on both the target and the stars present in the processed science frames. The task `apphot` is used for this purpose. The output of the aperture photometry is the instrumental magnitudes of the sources in the CCD frame. First, the chip coordinates of both the target source and the comparison stars are obtained using the task `daofind` in `IRAF`. Aperture photometry is then performed by fixing apertures around the centers found by `daofind`. A crucial and important parameter to be specified is the radius of the aperture. The optimum aperture is chosen by considering a range of apertures starting from the FWHM over the night for the photometry and selecting the aperture that produces minimum variance in the star-star differential light curve (DLC) of the steadiest pair of the comparison stars. This optimum aperture is then used for the photometry of the target and the comparison stars in all the image frames acquired over the night. DLCs of the AGN relative to the comparison stars (usually two to three) as well as between all pairs of comparison stars are constructed from the derived instrumental magnitudes. The DLCs of the AGN relative to the comparison stars are used to look for the presence of the intra-night optical variability (INOV) in the AGN. The choice of more than one comparison star in the differential photometry enables to reliably identify the AGN variability as any stars that themselves varied during the night can be identified and discarded.

2.1.6 Publicly Available Archival Data

A number of observing programs have been established to provide either regular monitoring or targeted observations specifically designed to support the *Fermi* science effort. Multi-wavelength data of some of the facility are publicly available and are used in this thesis.

2.1.6.1 SMARTS

A sample of γ-ray emitting AGN discovered by *Fermi*-LAT is being monitored by Small and Moderate Aperture Research Telescope System (SMARTS, a 1.3 m telescope) at the Cerro Tololo Inter-American Observatory located at Chile. Optical and near-IR data from SMARTS are routinely available in B, V, R, J, and K bands. The details on data acquisition, reduction, and calibration can be found in Bonning et al. (2012). The data in all the filters are corrected for galactic extinction following Schlafly & Finkbeiner (2011) and then converted to flux units using the zero points of Bessell et al. (1998).

2.1.6.2 Steward Observatory

Optical photometric, spectrophotometric, and spectropolarimetric observations of *Fermi*-LAT detected blazars are being carried out at the Steward observatory at the university of Arizona as part of its monitoring program. Details of the data reduction and calibration procedures can be found in Smith et al. (2009). Optical photometric and polarimetric data of sources of interest are obtained from the publicly available database. Photometric V band observations are corrected for galactic reddening (Schlafly & Finkbeiner 2011) and converted to flux units following Bessell et al. (1998).

2.1.6.3 Ovens Valley Radio Observatory

The Ovens Valley Radio Observatory (OVRO) uses its 40 m telescope to regularly monitor a sample of radio-loud quasars. Calibration of the data is achieved using a temperature-stable diode noise source to remove receiver gain drifts and the flux density scale is derived from observations of 3C 286 assuming a value of 3.44 Jy at 15.0 GHz (Baars et al. 1977). Complete details of the reduction and calibration procedure can be found in Richards et al. (2011). The final data products are publicly available and used in this thesis.

2.2 SED Modeling

The modeling of the observed fluxes in νF_ν vs. ν diagram helps in extracting physical parameters associated with the origin of the radiations in the blazar jets. Majority of the blazar models, available in the literature, are concentrated on the leptonic processes to model contemporaneous multi-wavelength data (e.g., Ghisellini & Tavecchio 2009). Moreover, attempts have been made to incorporate the time evolution of the radiating particles. In the standard time dependent leptonic blazar models, the low- and high-energy components in the SED are simultaneously fit by injecting nonthermal electrons (including positrons) into the jet and allowing the electrons to evolve through radiative and adiabatic cooling (e.g., Böttcher & Chiang 2002; Moderski et al. 2003). These Leptonic models have also been quite successful in explaining many features in the SED and light curves of blazars. Alternatively, the blazar SED can also be reproduced by hadronic models (Mannheim & Biermann 1992; Mannheim 1993; Petropoulou 2014). In the hadronic modeling, the high-energy emission originates from the synchrotron emission from ultrarelativistic protons. The relativistic protons interact with the radiation fields within the emission region, producing high-energy pions, which then decay to produce muons, electrons, positrons, and neutrinos. The pions and their decay products emit their own radiation (primarily synchrotron) which adds to the broadband spectral components in the SED of blazars (e.g., Mücke et al. 2003). Recently, there has been considerable effort in reproducing the blazar SED using a combination of leptonic and hadronic processes (Böttcher et al. 2013; Diltz et al. 2015).

In this thesis, a time independent leptonic emission model is developed using the formalism provided in the literature (Finke et al. 2008; Dermer et al. 2009; Ghisellini & Tavecchio 2009). The full Compton cross section, accurate for relativistic electrons from Thomson to Klein-Nishina regimes, is used in the derivations. The developed model is described here in brief and the details can be seen in Dermer & Menon (2009) and Ghisellini & Tavecchio (2009).

2.2.1 Emission region characteristics

The emission region is assumed to be located at a distance $R_{\rm diss}$ from the central black hole, having spherical size, and filled with electrons having smooth broken power law energy distribution

$$N'(\gamma') \,=\, N'_0\,\frac{(\gamma'_{\rm b})^{-p}}{(\gamma'/\gamma'_{\rm b})^p + (\gamma'/\gamma'_{\rm b})^q}, \tag{2.1}$$

where p and q are the particle indices before and after the break energy ($\gamma'_{\rm b}$), respectively (primed quantities are measured in the comoving frame). The size of the emission region ($R_{\rm blob}$) is adopted by considering it to cover the entire jet cross section with jet semi opening angle assumed as ψ. The emitting region moves with a bulk Lorentz factor Γ which is considered to be either a constant or include an acceleration phase of the kind (see, e.g., Ghisellini & Tavecchio 2009; Vlahakis & Königl 2004):

$$\Gamma \,=\, \min\left[\Gamma_{\rm max}, \left(\frac{R}{3R_{\rm Sch}}\right)^{1/2}\right] \tag{2.2}$$

where $\rm R_{Sch}$ is the Schwarzschild radius.

2.2.2 Energy Densities

2.2.2.1 Direct Accretion Disk Radiation

Thermal emission from the accretion disk is evaluated assuming a standard optically thick, geometrically thin disk (Shakura & Sunyaev 1973). The inner and outer radii of the accretion disk are adopted as $R_{\rm in} = 3R_{\rm Sch}, R_{\rm out} = 500R_{\rm Sch}$, respectively. The accretion disk luminosity can be expressed as $L_{\rm disk} = \eta_{\rm acc}\dot{M}c^2$, where $\dot{M}$ is the accretion rate and $\eta_{\rm acc}$ is the accretion efficiency. Locally, the accretion disk is assumed to be composed of annular rings with each ring acting like a blackbody at a particular temperature. Thus, the radiative profile of the accretion disk is considered as a multi-temperature blackbody of the following form (e.g., Frank et al. 2002)

$$T^4 \,=\, \frac{3R_{\rm Sch}\,L_{\rm d}}{16\pi\,\eta_{\rm acc}\,\sigma_{\rm MB}\,R^3}\left[1 - \left(\frac{3R_{\rm Sch}}{R}\right)^{1/2}\right] \tag{2.3}$$

Each annulus of the accretion disk is characterized by a different temperature and is viewed under a different angle ϕ (with respect to the jet axis), thus its radiation is amplified in a different way. A stationary observer with respect to the black hole (lab frame) will see a flux, integrated over all annuli, given by (e.g., Ghisellini & Tavecchio 2009)

$$F_{\rm d}(\nu) \;=\; 2\pi \int_{\mu_1}^{\mu_2} I(\nu) d\mu \;=\; 2\pi \int_{\mu_1}^{\mu_2} \frac{2h\nu^3/c^2}{\exp[h\nu/(kT)]-1} d\mu, \qquad (2.4)$$

where $\mu = \cos\phi$, and μ_1 and μ_2 are given by

$$\mu_1 \;=\; [1 + R_{\rm out}^2/R_{\rm diss}^2]^{-1/2} \qquad (2.5)$$

$$\mu_2 \;=\; [1 + R_{\rm in}^2/R_{\rm diss}^2]^{-1/2} \qquad (2.6)$$

Further, in the comoving frame, frequency and solid angles are transformed as:

$$\nu' = b\nu, \qquad b \;\equiv\; \Gamma(1-\beta\mu) \qquad (2.7)$$

and:

$$d\Omega' \;=\; \frac{d\Omega}{b^2} \;=\; 2\pi\frac{d\mu}{b^2}, \qquad (2.8)$$

respectively. The intensities as seen in the comoving frame transform as:

$$I'_{\rm d}(\nu') \;=\; b^3 I_{\rm d}(\nu) \;=\; b^3 I_{\rm d}(\nu'/b) \qquad (2.9)$$

The specific radiation energy density seen in the comoving frame is

$$U'_{\rm d}(\nu') \;=\; \frac{1}{c}\int I'_{\rm d}(\nu') d\Omega' \;=\; \frac{2\pi}{c}\int_{\mu_{\rm d}}^{1} \frac{I'_{\rm d}(\nu')}{b^2} d\mu \qquad (2.10)$$

Integrating Equation (2.10) over all the frequencies gives the total accretion disk energy density as a function of $R_{\rm diss}$.

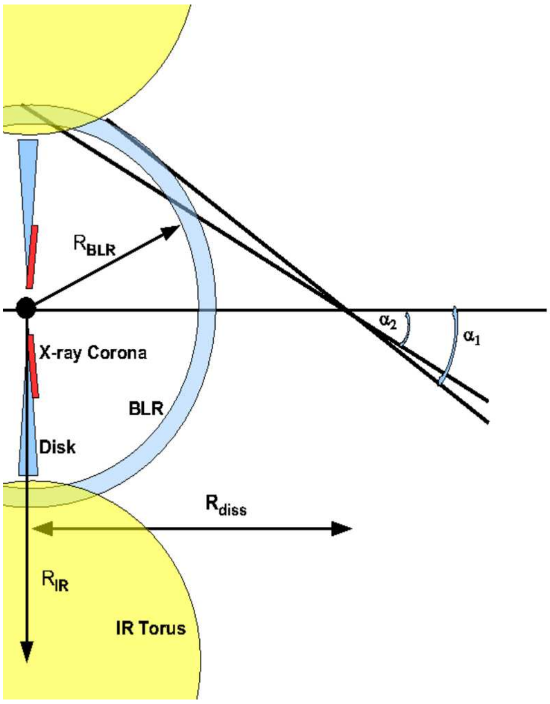

FIGURE 2.1: Cartoon illustrating the accretion disk, its X-ray corona, the BLR, and a schematic representation of the IR torus. At the distance $R_{\rm diss}$, here assumed to be outside the BLR, the relevant angles are lebeled for calculating the contribution of the BLR radiation to the corresponding energy density (Ghisellini & Tavecchio 2009).

2.2.2.2 Radiation from the X-ray Corona

Above and below the accretion disk, the presence of the X-ray corona is also considered (Figure 2.1) which reprocesses $\eta_{\rm cor}$ of the accretion disk luminosity. The inner and outer radii of the corona are assumed to be $3R_{\rm Sch}$ and $30R_{\rm Sch}$, respectively. The spectrum emitted by the corona is a cut-off power law: $L_{\rm cor}(\epsilon) \propto \epsilon^{-\alpha_{\rm cor}} \exp(-\epsilon/\epsilon_{\rm c})$, where ϵ is the dimensionless photon energy (Ghisellini & Tavecchio 2009). Following Ghisellini & Madau (1996), the total radiation energy density $U'_{\rm cor}$ of this component can be expressed as:

$$\begin{aligned} U'_{\rm cor} &= \frac{\eta_{\rm cor}\, L_{\rm disk}\, \Gamma^2}{\pi R_X^2\, c} \left[1 - \mu_X - \beta(1-\mu_X^2) + \frac{\beta^2}{3}(1-\mu_X^3)\right] \\ \mu_X &= [1 + R_X^2/R_{\rm diss}^2]^{-1/2} \end{aligned} \tag{2.11}$$

where R_X is the extension of the X-ray corona.

2.2.2.3 BLR Radiation

The BLR is assumed as a spherical shell located at a distance $R_{\rm BLR} = 10^{17} L_{\rm d,45}^{1/2}$ cm, where $L_{\rm d,45}$ is the accretion disk luminosity in units of 10^{45} erg s^{-1} (Ghisellini & Tavecchio 2009). It reprocesses $\eta_{\rm BLR}$ of the accretion disk luminosity and its spectrum is assumed to be a blackbody peaking at rest-frame Lyman-α frequency (Tavecchio & Ghisellini 2008). The energy density of the BLR radiation field seen in the comoving frame, within $R_{\rm BLR}$, can be approximated as (Ghisellini & Madau 1996):

$$U'_{\rm BLR} \sim \frac{17\,\Gamma^2}{12} \frac{\eta_{\rm BLR}\, L_{\rm disk}}{4\pi R_{\rm BLR}^2\, c} \qquad R_{\rm diss} < R_{\rm BLR} \tag{2.12}$$

At distances much larger than $R_{\rm BLR}$, and calling $\mu = \cos\alpha$ (Figure 2.1),

$$\begin{aligned} U'_{\rm BLR} &\sim \frac{\eta_{\rm BLR}\, L_{\rm disk}}{4\pi R_{\rm BLR}^2\, c} \frac{\Gamma^2}{3\beta} [2(1-\beta\mu_1)^3 - (1-\beta\mu_2)^3 \\ &- (1-\beta)^3)] \qquad R_{\rm diss} \gg R_{\rm BLR} \\ \mu_1 &= [1 + R_{\rm BLR}^2/R_{\rm diss}^2]^{-1/2} \\ \mu_2 &= [1 - R_{\rm BLR}^2/R_{\rm diss}^2]^{1/2} \end{aligned} \tag{2.13}$$

For $R_{\rm diss} \gtrsim R_{\rm BLR}$ the exact value of $U'_{\rm BLR}$ depends on the width of the BLR, which is poorly known. Therefore, in the range $R_{\rm BLR} < R_{\rm diss} < 3R_{\rm BLR}$, a simple power law interpolation is adopted.

2.2.2.4 Radiation from the IR Torus

The IR-torus is assumed as a thin spherical shell, located at a distance of $R_{\rm torus} = 10^{18} L_{\rm d,45}^{1/2}$ cm and reprocesses $\eta_{\rm torus}$ of the accretion disk emission. Its emission profile can be taken as a simple blackbody peaking at temperature $T_{\rm torus}$. The comoving radiation energy density of IR-torus component scales as $U_{\rm BLR}$, but substituting $R_{\rm BLR}$ with $R_{\rm torus}$. With this approach

$$U'_{\rm torus} \sim \frac{\eta_{\rm torus}\, L_{\rm disk}\, \Gamma^2}{4\pi R_{\rm torus}^2\, c} \qquad R_{\rm diss} < R_{\rm torus} \tag{2.14}$$

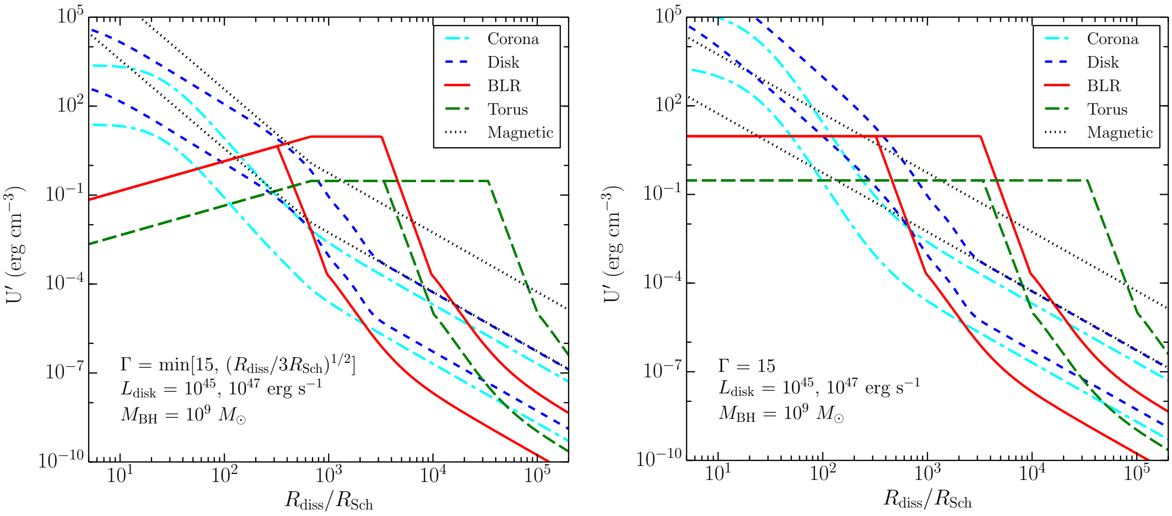

FIGURE 2.2: Left panel: Comparison of different comoving frame energy densities. The bulk Lorentz factor is assumed to scale as $\Gamma = \min[15, (R_{\rm diss}/3R_{\rm Sch})^{1/2}]$. The black hole mass is taken as $M = 10^9 M_\odot$. The two sets of lines correspond to two disk luminosities: 10^{45} and 10^{47} erg s^{-1}. The radius of BLR is assumed to scale with the disk luminosity as $R_{\rm BLR} = 10^{17} L_{\rm disk,45}^{1/2}$ cm. The radius of the IR torus is given by $R_{\rm torus} = 10^{18} L_{\rm d,45}^{1/2}$ cm. The magnetic energy density (dotted lines) is calculated assuming $P_{\rm B} = 0.1 L_{\rm disk}$. Right panel: same as left, but assuming a constant $\Gamma = 15$ all along the jet.

For $R_{\rm diss} > R_{\rm torus}$,

$$\begin{aligned} U'_{\rm torus} &\sim \frac{\eta_{\rm torus}\, L_{\rm disk}}{4\pi R_{\rm torus}^2\, c}\, \frac{\Gamma^2}{3\beta}\, [2(1-\beta\mu_1)^3 - (1-\beta\mu_2)^3 \\ &- (1-\beta)^3)] \qquad R_{\rm diss} \gg R_{\rm torus} \\ \mu_1 &= [1 + R_{\rm torus}^2/R_{\rm diss}^2]^{-1/2} \\ \mu_2 &= [1 - R_{\rm torus}^2/R_{\rm diss}^2]^{1/2} \end{aligned} \tag{2.15}$$

2.2.2.5 Magnetic Energy Density

The magnetic energy density can be expressed as

$$U'_{\rm B} = \frac{P_{\rm B}}{\pi R_{\rm blob}^2\, \Gamma^2\, c} \tag{2.16}$$

where $P_{\rm B}$ is the power carried in the form of Poynting flux. The magnetic field B scales as $1/R_{\rm diss}$ both in the acceleration and in the coasting (i.e. Γ =const) phases, but with a different normalization.

The contributions to the energy density provided by the different components as a function of $R_{\rm diss}$, are shown in Figure 2.2. For this case, a black hole mass

$M = 10^9 M_\odot$, an accretion efficiency $\eta_{\rm acc} = 0.1$, $\eta_{\rm BLR} = 0.1, \eta_{\rm cor} = 0.3$, $\eta_{\rm torus} = 0.5$, and $P_{\rm B} = 0.1 L_{\rm disk}$ are assumed. The results are plotted for two values of $L_{\rm disk}$: 10^{45} and 10^{47} erg s^{-1} with higher disk luminosity resulted in larger comoving frame energy densities. The case of an accelerating jet, whose bulk Lorentz factor is $\Gamma = \min[15, (R_{\rm diss}/3R_{\rm Sch})^{1/2}]$, is presented in the left panel. In the right panel, a constant $\Gamma = 15$ along the entire jet is assumed. As can be seen, the dominance of various radiation energy densities is different at different $R_{\rm diss}$. All the external radiation energy densities drop when $R_{\rm diss}$ is greater than the corresponding typical size of the structure producing the seed photons.

It is important to note the comparison between $U'_{\rm disk}$ and $U'_{\rm BLR}$. The distance above which BLR energy density dominates over disk energy density, depends upon the accretion disk luminosity. This is because the BLR adjusts its radius so to give a constant (in the lab frame) energy density. So, for $L_{\rm disk} = 10^{47}$ erg s^{-1} $U'_{\rm BLR}$ dominates only above $\sim 300 R_{\rm Sch}$, equivalent to 10^{17} cm, while for $L_{\rm disk} = 10^{45}$ erg s^{-1} it starts to dominate about three times closer, when Γ has not reached yet its maximum value (Figure 2.2). Note that, for the shown cases, $U'_{\rm B}$ dominates over the external radiation energy density only at the start of the jet and up to 100–300 $R_{\rm Sch}$, where $U'_{\rm BLR}$ takes over.

2.2.3 Synchrotron Radiation

The synchrotron emissivity from isotropic electrons, moving in a randomly oriented magnetic field is given by following expression (Crusius & Schlickeiser 1986; Ghisellini et al. 1988)

$$\epsilon' J'_{syn}(\epsilon) = \frac{\sqrt{3}\,\epsilon' e^3 B}{h} \int_1^\infty d\gamma' \; N'_e(\gamma') \; R(x) \tag{2.17}$$

where $N'_e(\gamma')$ is the comoving frame electron energy distribution, e is the electronic charge, h is Planck's constant,

$$x = \frac{4\pi\epsilon' m_e^2 c^3}{3eBh\gamma'^2} \; ,$$

$$R(x) = \frac{x}{2} \int_0^\pi d\theta \;\; \sin\theta \; \int_{x/\sin\theta}^\infty dt \;\; K_{5/3}(t),$$

and $K_{5/3}(t)$ is the modified Bessel function of the second kind of order 5/3. An approximation for the function $R(x)$ can be taken as follows (e.g., Dermer & Menon 2009):

$$R(x) \cong 1.78\, x^{0.297} \exp(-x). \tag{2.18}$$

The synchrotron flux is then given by (Finke et al. 2008)

$$f_\epsilon^{\rm syn} = \frac{\delta_{\rm D}^4\, \epsilon' J'_{\rm syn}(\epsilon')}{4\pi d_L^2} = \frac{\sqrt{3}\, \delta_{\rm D}^4 \epsilon' e^3 B}{4\pi h d_L^2} \int_1^\infty d\gamma'\; N'_e(\gamma')\; R(x) \tag{2.19}$$

2.2.3.1 Synchrotron Self Absorption

The frequency dependent synchrotron self absorption (SSA) coefficient is calculated as follows (Dermer & Menon 2009)

$$\kappa'(\epsilon') = -\frac{1}{8\pi\, m_e\, \epsilon'^2} \left(\frac{\lambda_{\rm C}}{c}\right)^3 \left(\frac{\delta_{\rm D}}{(1+z)}\right)^2 \int_{\gamma'_{\rm min}}^{\gamma'_{\rm max}} d\gamma' P^{\rm syn}(\epsilon';\gamma') \left[\gamma'^2 \frac{\partial}{\partial\gamma'} \left(\frac{n'_e(\gamma')}{\gamma'^2}\right)\right], \tag{2.20}$$

where $\lambda_{\rm C} = h/(m_e c)$ is the Compton wavelength and $n'_e(\gamma') = N'_e(\gamma')/V'_{\rm blob}$. The optical depth for SSA is $\tau_{\epsilon'} = 2\kappa'(\epsilon')R'_{\rm blob}$. The unabsorbed spectrum is multiplied by a factor $3u(\tau)/\tau$, to give the absorbed spectrum (Gould 1979). The term $u(\tau)$ can be expressed as follows

$$u(\tau) = \frac{1}{2} + \frac{\exp(-\tau)}{\tau} - \frac{1-\exp(-\tau)}{\tau^2}, \tag{2.21}$$

with $\tau = \tau_{\epsilon'}$.

2.2.4 Synchrotron Self Compton Radiation

The single particle SSC emissivity, integrated over volume, for isotropic and homogeneous photon and electron distributions is given by (e.g., Finke et al. 2008)

$$\epsilon'_s J'_{\rm SSC}(\epsilon'_s) = \frac{3}{4} c\, \sigma_{\rm T}\, \epsilon'^2_s \int_0^\infty d\epsilon'\, \frac{u'(\epsilon')}{\epsilon'^2} \int_{\gamma'_{\rm min}}^{\gamma'_{\rm max}} d\gamma'\, \frac{N'_e(\gamma')}{\gamma'^2}\, F_{\rm C}(q, \Gamma_e)\;, \tag{2.22}$$

where ϵ'_s is the scattered photon's dimensionless energy in the blob frame. The synchrotron radiation energy density $u'(\epsilon')$ is expressed as follows

$$u'(\epsilon') = \frac{3\, d_L^2\, f_\epsilon^{\rm syn}}{c\, R_B'^2\, \delta_{\rm D}^4\, \epsilon'} . \tag{2.23}$$

Combining Equation (2.22) and (2.23) gives

$$\epsilon'_s J'_{\rm SC}(\epsilon'_s) = \frac{9\, \sigma_{\rm T}\, d_L^2\, \epsilon_s'^2}{4\, \delta_{\rm D}^4\, R_{\rm blob}'^2} \int_0^\infty d\epsilon'\, \frac{f_\epsilon^{\rm syn}}{\epsilon'^3} \int_{\gamma'_{\rm min}}^{\gamma'_{\rm max}} d\gamma'\, \frac{N'_e(\gamma')}{\gamma'^2} F_C(q, \Gamma)\ , \tag{2.24}$$

The Compton scattering kernel, $F_{\rm C}(q, \Gamma_e)$, which takes into account both the Thomson and Klein-Nishina scattering, for isotropic electron and photon distributions, is (Jones 1968; Blumenthal & Gould 1970)

$$F_{\rm C}(q, \Gamma_e) = \left[2q \ln q + (1+2q)(1-q) + \frac{1}{2} \frac{(\Gamma_e q)^2}{(1+\Gamma_e q)} (1-q) \right] H\ \left(q; \frac{1}{4\gamma'^2}, 1 \right), \tag{2.25}$$

where

$$q \equiv \frac{\epsilon'_s/\gamma'}{\Gamma_e (1 - \epsilon'_s/\gamma')} \quad \text{and} \quad \Gamma_e = 4\epsilon'\gamma'\ . \tag{2.26}$$

The limits on q are

$$\frac{1}{4\gamma'^2}\ \le\ q\ \le 1\ , \tag{2.27}$$

which imply the limits of the integration over γ':

$$\gamma'_{\rm min} = \frac{1}{2} \epsilon'_s \left(1 + \sqrt{1 + \frac{1}{\epsilon' \epsilon'_s}} \right) \tag{2.28}$$

and

$$\gamma'_{\rm max} = \frac{\epsilon' \epsilon'_s}{\epsilon' - \epsilon'_s} H(\epsilon' - \epsilon'_s)\ +\ \gamma'_2 H(\epsilon'_s - \epsilon') \tag{2.29}$$

Here, two versions of the Heaviside function are used: $H(x) = 0$ for $x < 0$ and $H(x) = 1$ for $x \ge 0$; as well as $H(x; x_1, x_2) = 1$ for $x_1 \le x \le x_2$ and $H(x; x_1, x_2) = 0$ everywhere else. Further, the upper limit (Equation 2.29) takes into account of both Compton up and downscattering. The maximum electron energy γ'_2, in principle, can be calculated from particle acceleration theory.

The νF_ν SSC spectrum is given by

$$f_{\epsilon_s}^{\rm SSC} = \frac{\delta_{\rm D}^4 \epsilon'_s J'_{\rm SSC}(\epsilon'_s)}{4\pi d_L^2} \ . \tag{2.30}$$

Inserting Equation (2.24) into (2.30) gives final SSC spectrum in the observer's frame (Dermer & Menon 2009; Finke et al. 2008)

$$f_{\epsilon_s}^{\rm SSC} = \frac{9}{16}\frac{\sigma_{\rm T}\,\epsilon_s'^2}{\pi R_{\rm blob}'^2}\int_0^\infty d\epsilon' \ \frac{f_\epsilon^{\rm syn}}{\epsilon'^3}\ \int_{\gamma'_{\rm min}}^{\gamma'_{\rm max}} d\gamma' \ \frac{N'_e(\gamma')}{\gamma'^2}F_C(q,\Gamma_e) \tag{2.31}$$

2.2.5 External Compton Radiation

The Compton scattered $\nu F \nu$ spectrum involving isotropic comoving distributions of electrons and external photon fields, under the assumption of head-on collision, is given as (Dermer & Menon 2009)

$$f_\epsilon^{\rm EC} = \frac{3c\,\sigma_{\rm T}\,\epsilon_s'^2\,\delta_{\rm D}^4}{16\pi d_L^2}\int_0^\infty d\epsilon' \frac{u'(\epsilon')}{\epsilon'^2}\int_{\gamma'_{\rm min}}^{\gamma'_{\rm max}} d\gamma' \frac{N'_e(\gamma')}{\gamma'^2}F_C(q,\Gamma_e), \tag{2.32}$$

where $u'(\epsilon')$ is the external specific photon energy density measured in the comoving frame. To calculate EC-disk spectrum, the specific accretion disk energy density can be taken from Equation (2.10). Furthermore, as long as the emission region is inside the BLR, all the external photons appear to come from one direction. In such cases, the formalism of Dermer (1995) can be used to describe the pattern of the scattered radiation. It should be noted that, in this case, if $\theta_v = 1/\Gamma$ (and thus $\delta = \Gamma$), one has the observed luminosity as for radiation isotropic in the rest frame. On the other hand, if the emitting region is outside the BLR, then the arrival directions of the BLR photons are spread, and it is not trivial to reproduce the exact pattern. But, in this case the BLR component is hardly dominant with respect to the IR radiation from the torus. Therefore, for simplicity, it is assumed to have $\theta_v \sim 1/\Gamma$, and to treat the emitted radiation pattern the same way as for an isotropic seed photon distribution. Under this approximation, both the BLR and IR-torus external photon energy densities can be written as follows (Rybicki & Lightman 1979)

$$u'_{\rm ext}(\epsilon') = \frac{15 u'_{\rm tot}}{(\pi\Theta')^4}\left[\frac{\epsilon'^3}{\exp(\epsilon'/\Theta') - 1}\right] \tag{2.33}$$

where $\Theta' = k_B T'/m_e c^2$ is dimensionless temperature, and k_B is the Boltzmann constant. Inserting Equation (2.33) in (2.32), the EC spectrum in the observer's frame would be (Cao & Wang 2013; Finke & Dermer 2012)

$$f_{\epsilon}^{\mathrm{EC}} = \frac{3c\,\sigma_{\mathrm{T}}\,\epsilon_s'^2\,\delta_{\mathrm{D}}^4}{16\pi d_L^2}\frac{15u'_{\mathrm{ext}}}{(\pi\Theta')^4}\int_0^{\infty} d\epsilon' \frac{\epsilon'}{\exp(\epsilon'/\Theta') - 1}\int_{\gamma'_{\mathrm{min}}}^{\gamma'_{\mathrm{max}}} d\gamma' \frac{N'_e(\gamma')}{\gamma'^2} F_C(q, \Gamma_e) \quad (2.34)$$

Note that, in the comoving frame, the soft photon energy is shifted to $\epsilon'_{\mathrm{peak}} \simeq \Gamma\epsilon_{\mathrm{peak}}$, and the external photon energy density is given by $u'_{\mathrm{ext}} \simeq \Gamma^2 u_{\mathrm{ext}}$. The total BLR and IR-torus energy densities (Section 2.2.2.3 and 2.2.2.4) are inserted into Equation (2.34) to derive the final EC-BLR and EC-torus spectrum, respectively.

2.2.6 SED Input Parameters

Having tried to connect the jet emission to the accretion disk luminosity and the black hole mass, and having included many components of external radiation, there are a large numbers of input parameters for the model developed here. They are summarized below in two separate lists. First list contains the parameters which are kept fixed for all the models, based on physical considerations or *a priori* knowledge, or that do not influence the model SED.

1. R_X: the extension of the X-ray corona is fixed to 30 R_{Sch}.
2. R_{out}: the outer radius of the accretion disk. It is fixed to 500 Schwarzschild radii.
3. α_{cor}: the spectral shape of the coronal X-ray flux is fixed to $\alpha_{\mathrm{cor}} = 1$.
4. ϵ_{c}: the high energy cut-off of the X-ray coronal flux. It is fixed at 150 keV.
5. η_{cor}: fraction of the accretion disk luminosity reprocessed by X-ray corona. It is taken as 0.3.
6. η_{BLR}: fraction of L_{disk} intercepted by the BLR and re-emitted in broad lines. It is fixed to $\eta_{\mathrm{BLR}} = 0.1$.
7. η_{torus}: fraction of L_{disk} intercepted by the torus and re-emitted in IR. It is adopted as $\eta_{\mathrm{torus}} = 0.5$.

8. ψ: semi aperture angle of the jet. It is fix to $\psi = 0.1$ rad.

The following are 12 parameters that are allowed to vary during the modeling:

1. $M_{\rm BH}$: the central black hole mass.
2. $L_{\rm disk}$: the accretion disk luminosity.
3. $R_{\rm diss}$: the distance of the emission region from the central black hole, along the jet axis.
4. $\nu_{\rm syn}^{\rm peak}$: the approximate synchrotron peak frequency.
5. $\nu_{\rm syn}^{\rm peak} F\nu_{\rm syn}^{\rm peak}$: the approximate synchrotron peak flux at $\nu_{\rm syn}^{\rm peak}$.
6. B: the magnetic field.
7. $\Gamma_{\rm max}$: the value of bulk Lorentz factor after the acceleration phase, in which the bulk Lorentz factor varies as $[R/(3R_{\rm Sch})]^{1/2}$.
8. $\theta_{\rm v}$: the viewing angle.
9. p: the slopes of the electron energy distribution before the break energy.
10. q: the slopes of the electron energy distribution after the break energy.
11. $\gamma_{\rm min}$: value of the minimum Lorentz factor of the injected electrons.
12. $\gamma_{\rm max}$: value of maximum random Lorentz factor of the injected electrons.

If $\theta_{\rm v} \sim 1/\Gamma$ is assumed, then the number of relevant parameters decrease to 11. The black hole mass and the accretion disk luminosity can be constrained provided the big blue bump is visible at optical-UV energies. Moreover, since the low energy electrons emit synchrotron radiation primarily at the frequencies where SSA effect dominates, determination of $\gamma_{\rm min}$ is difficult. However, if the observed soft X-ray flux is produced via EC process involving same low energy electrons, the $\gamma_{\rm min}$ can be constrained. It is found that it is having a rather low value of few (1-5, e.g., Celotti & Ghisellini 2008). With this idea, $\gamma_{\rm min}$ can be assumed as unity. Moreover, value of $\gamma_{\rm max}$ does not affect the modeling as long as VHE observations are not available (generally the case of FSRQs). Therefore, the total number of free parameters are left as 7.

Chapter 3

Broadband Study of Blazars

Systematic studies of blazars using both broadband variability and SED modeling approach were remained elusive due to limitations in acquiring good quality quasi-simultaneous multi-wavelength observations in the past. However, improvements in the observational capabilities in the last decade, particularly the launch of *Fermi* Gamma Ray Space Telescope in 2008, have revolutionized our understanding about blazars. Observations from *Fermi* have now enabled us to detect γ-ray flux variations from blazars on timescales as short as of the order of minutes. Moreover, contemporaneous observations at other wavelengths have made it possible to study the broadband physical properties of blazars in an unprecedented detail.

3.1 Sample selection

The source selection is done based on the brightness of the sources and also on the availability of the good quality densely sampled data. Keeping this in mind, four blazars have been selected to study their broadband properties, including two low redshift (z <1) and two high redshift blazars (z >1). All of them are included in the recently released third catalog of *Fermi* detected sources (3FGL; Acero et al. 2015). The basic information of all the four sources are presented in Table 3.1. In this chapter, a detail multi-wavelength study of these four blazars are presented.

TABLE 3.1: Basic information of the blazars studied in this thesis.

3FGL name	Other name	RA (hh mm ss)	DEC (dd mm ss)	z	R (mag)
J0841.4+7053	S5 0836+71	08 41 24.3	+70 53 42	2.17	16.5
J0809.5+5342	BZQ J0809+5341	08 09 41.7	+53 41 25	2.14	19.62
J1256.1−0547	3C 279	12 56 11.1	−05 47 22	0.54	14.33
J1104.4+3812	Mrk 421	11 04 27.3	+38 12 32	0.03	12.65

3.2 3FGL J0841.4+7053 (S5 0836+71)[1]

The high redshift blazar S5 0836+71 is a radio-bright source ($F_{5\ \rm GHz} = 1.68$ Jy; Linford et al. 2012). It has a flat radio spectrum ($\alpha = -0.33$; Kuehr et al. 1981) with a one-sided kilo-parsec scale radio jet (Hummel et al. 1992). Its Very Long Baseline Interferometry (VLBI) observations indicated the emergence of a new superluminal knot closely associated with a bright γ-ray state (Otterbein et al. 1998). In a recent study by Perucho et al. (2012), the inner structure of the jet is found to be of helical shape (see also, Lobanov et al. 1998). Moreover, a spine-sheath structure of the jet is also proposed by Asada et al. (2010) on the basis of the Very Long Baseline Array (VLBA) observations. The observed optical-UV spectrum of S5 0836+71 is dominated by thermal emission from the accretion disk and by reproducing it using a standard accretion disk model Ghisellini et al. (2010b) obtained the accretion disk luminosity and the black hole mass as 2.25×10^{47} erg s^{-1} and $3 \times 10^{9}\ M_{\odot}$, respectively. It is a hard X-ray bright source and included in the 70 month *Swift*-BAT catalog (Baumgartner et al. 2013). Furthermore, it is also detected in high energy γ-ray band (Thompson et al. 1993; Acero et al. 2015). As expected from a high redshift blazar its γ-ray spectrum is steep, in accordance with the ‘blazar sequence’.

Recently, Akyuz et al. (2013) have performed a detailed broadband study of S5 0836+71 with a major focus on its variability nature. No significant correlation between radio and γ-ray was observed and it was concluded that the observed radio emission may originate from the regions other than that produce γ-rays. A significant curvature in the flaring state γ-ray spectrum is also reported by them. However, in another study, the emergence of a new radio knot is associated with the γ-ray flaring period in 2011 April by Jorstad et al. (2013). They argue that the γ-ray emission region is located at a distance of $\sim$35 pc from the central engine.

---

[1] The results presented for S5 0836+71 are published in Paliya (2015b).

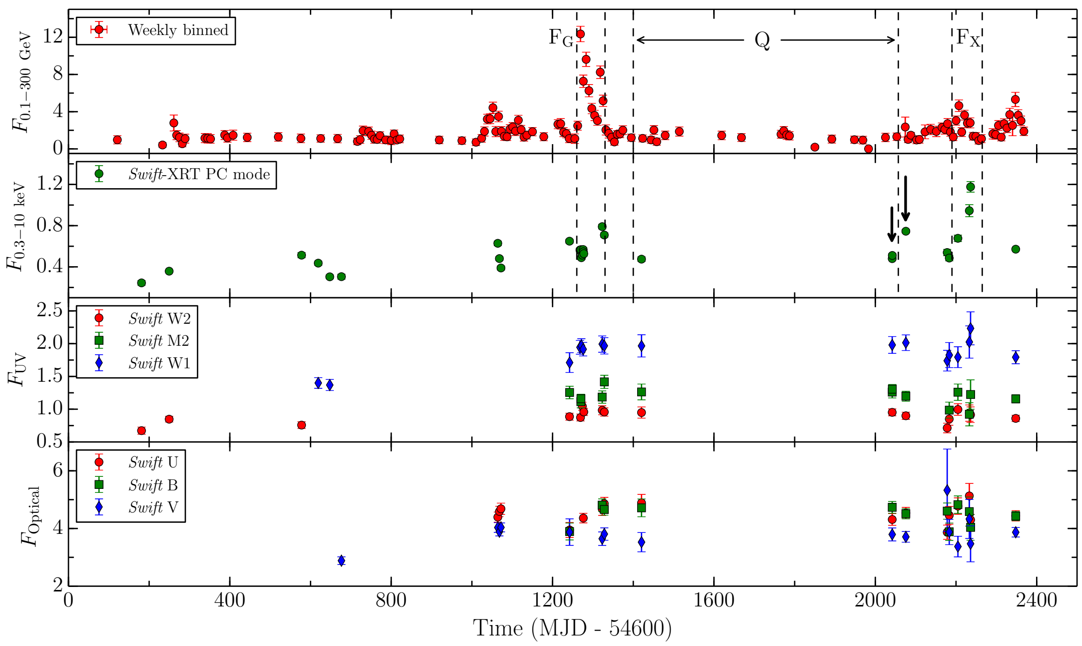

FIGURE 3.1: Multi-frequency light curves of S5 0836+71 since the launch of *Fermi* satellite. *Fermi*-LAT and *Swift*-XRT data points are in units of 10^{-7} ph cm^{-2} s^{-1} and counts s^{-1}, respectively. UV and optical fluxes have units of 10^{-12} erg cm^{-2} s^{-1} . Periods corresponding to high γ-ray and X-ray states and a low activity phase are quoted as $\rm F_G$, $\rm F_X$, and Q, respectively. Black downward arrows represent the time of *NuSTAR* observations.

Publicly available broadband data of S5 0836+71 are analyzed using the prescriptions given in Chapter 2 and the results are presented and discussed below.

3.2.1 Multi-band Temporal Variability

In Figure 3.1, the long term multi-band light curves of S5 0836+71, covering the period 2008 August 5 to 2014 November 15, are shown. As can be seen in this plot, the flaring activities are present both in X-ray and γ-ray bands, however, optical-UV observations show little or no flux variations. This indicates the dominance of the accretion disk radiation at optical-UV energies, even during the flaring periods. This is because the accretion disk is not expected to vary drastically over short time intervals. The fractional rms variability amplitude ($F_{\rm var}$; Vaughan et al. 2003) is calculated and presented in Table 3.2. The $F_{\rm var}$ is found to be highest for γ-rays and decreases with frequency, a trend generally seen in blazars (e.g., Zhang et al. 2005; Vercellone et al. 2010).

Table 3.2: Fractional rms variability amplitude parameter ($F_{\rm var}$) calculated for the light curves shown in Figure 3.1 and 3.4.

Energy band	$F_{\rm var}$
γ-ray (0.1−300 GeV)	0.79 ± 0.02
X-ray (3−79 keV)	0.21 ± 0.01
X-ray (0.3−10 keV)	0.33 ± 0.01
$UVW2$	0.07 ± 0.02
$UVM2$	0.04 ± 0.05
$UVW1$	0.09 ± 0.02
U	0.05 ± 0.02
B	0.04 ± 0.03
V	0.04 ± 0.08

During the period MJD 55860−55930, the largest γ-ray flare is not associated with that in X-rays (Figure 3.1). The X-ray flux amplitude is relatively small at the time of the γ-ray flare, however, when X-ray flux peaks (MJD 56790−56865) the γ-rays increases a little. To understand this peculiar observation, a X-ray flaring period ($\rm F_X$; MJD 56790−56865) and a γ-ray flaring period ($\rm F_G$; MJD 55860−55930) are selected. A low activity state (Q; MJD 56000−56657) is also chosen for comparison. These periods are shown with dashed lines in Figure 3.1.

The availability of good photon statistics during the high γ-ray activity period $\rm F_G$ allows to generate the daily binned γ-ray light curve and shown in the top panel of Figure 3.2. The shorter duration flares are further chosen from the one day binned γ-ray light curve to generate finer time binned light curves. This is required to determine the highest γ-ray flux and the shortest flux variability timescale. The selected periods are annotated by P1, P2, P3, and P4 (Figure 3.2). The largest flux enhancement is observed during the period P1. In the energy range of 0.1−300 GeV, the highest 3 hr binned flux is $(5.22 \pm 1.10) \times 10^{-6}$ ph $\rm cm^{-2}\,s^{-1}$, measured on MJD 55866. The associated photon index is steep and has a value of 2.62 ± 0.27. Accordingly, the observed apparent γ-ray luminosity is $(1.62 \pm 0.44) \times 10^{50}$ $\rm erg\,s^{-1}$. Within error, this equals the recorded highest γ-ray luminosity ever measured from a blazar ($2.1 \pm 0.2 \times 10^{50}$ $\rm erg\,s^{-1}$ for 3C 454.3; Abdo et al. 2011). Further, two rapid flares are selected for flare profile fitting so as to have a better estimate of the fastest rising and decaying timescales. They are quoted as F1 and F2 in the period P1 in Figure 3.2. The function used to carry out the fitting has the following form (see, e.g., Abdo et al. 2010b)

$$F(t) = F_{\rm c} + F_0 \left[\exp\left(\frac{t_{\rm p} - t}{T_{\rm r}}\right) + \exp\left(\frac{t - t_{\rm p}}{T_{\rm d}}\right)\right]^{-1} \quad (3.1)$$

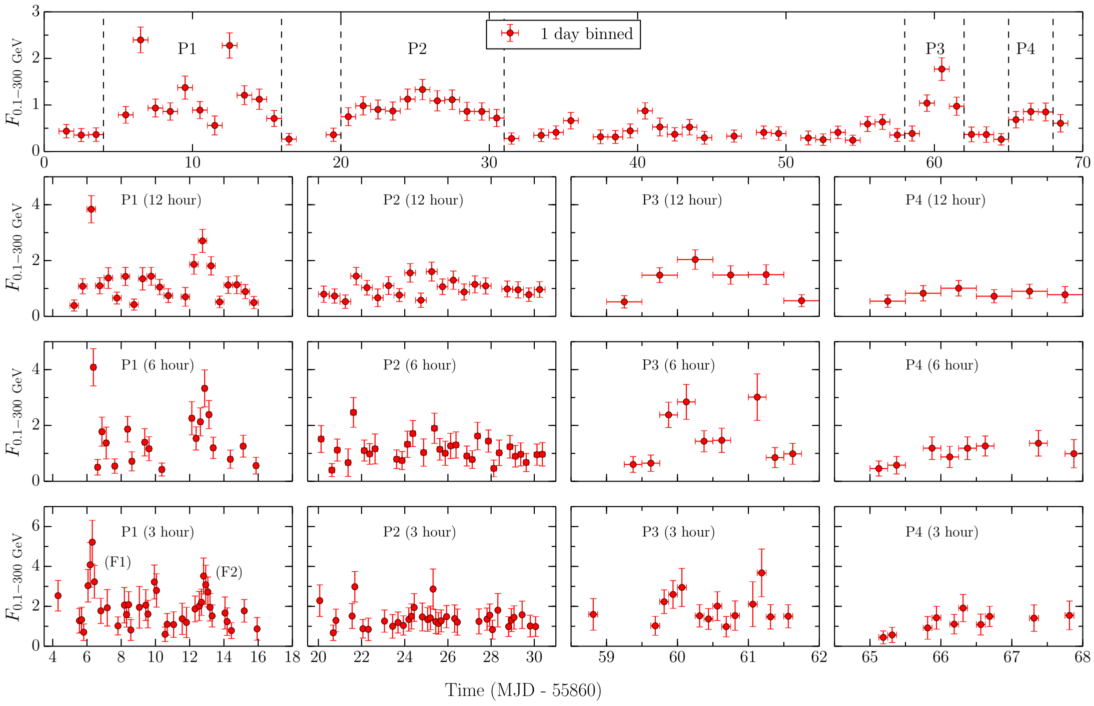

FIGURE 3.2: Gamma-ray light curves of S5 0836+71 covering the period of GeV outburst. Fluxes are in units of 10^{-6} ph cm^{-2} s^{-1}. Good photon statistics during this period allows to go for various time binnings. Top panel represents the daily binned light curve, from which the intervals of higher activities (marked as P1, P2, P3, and P4) are selected to go for 12 hr, 6 hr, and 3 hr binning. In the 3 hr binned light curve of P1 period (bottom left corner), two flares F1 and F2 are selected for profile fitting.

where $F_{\rm c}$ corresponds to the quiescent level flux and F_0 is the amplitude of the flares, $t_{\rm p}$ measures the approximate time of the peak that is kept fixed at the time when the highest flux is observed, and $T_{\rm r}$ and $T_{\rm d}$ decide the rise and decay times. The results of this analysis are presented in Figure 3.3 and the associated parameters are given in Table 3.3. The fastest flux rise and decay times are found to be ∼3 hr and ∼2.5 hr, respectively. This is the first report of hr scale γ-ray variability detected from S5 0836+71. Such hr scale flux variability was also probably not known in any high redshift blazar beyond redshift 2, prior to this work. Furthermore, results of the flare profile fitting indicate that the flare F1 seems to have a symmetric profile and the flare F2 possess an asymmetric shape, i.e., fast rise and slow decay. Such a fast rise of the flare could be associated with the faster acceleration of the injected electrons, probably at shock front, and the slow decay can be attributed to the weakening of the shock.

In the energy range of 0.3−10 keV, the maximum unabsorbed X-ray flux is $4.78^{+0.57}_{-0.38}$ $\times$ 10^{-11} erg cm^{-2} s^{-1}, detected on MJD 56836, i.e., during the period F$_{\rm X}$. The

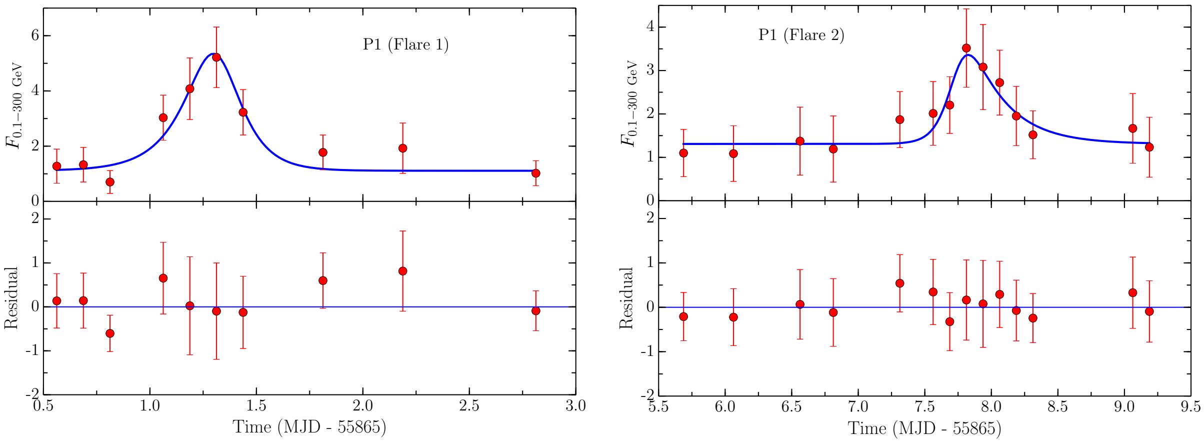

Figure 3.3: Top: 3 hr binned γ-ray flares of S5 0836+71 selected for time profile fitting, during the period of GeV outburst. Fluxes have same units as in Figure 3.2. Blue solid line denotes the best-fit temporal profile assuming an exponential rise and fall. Bottom: The residual of the fitting.

Table 3.3: Parameters obtained from the time profile fitting of two flares.

Name	F_c	F_p	t_p	T_r	T_d	χ^2_r
F1	1.11 ± 0.27	8.41 ± 2.01	55866.31	0.13 ± 0.05	0.10 ± 0.04	0.77
F2	1.31 ± 0.26	3.54 ± 1.29	55872.75	0.08 ± 0.06	0.27 ± 0.13	0.21

Notes. Errors are estimated at 1σ level. Fluxes F_c and F_p are in 10^{-6} ph cm^{-2} s^{-1}, T_r and T_d are in days, and t_p, which is kept fixed, is in MJD.

associated photon index is hard and has a value of $1.47^{+0.11}_{-0.11}$. This corresponds to an isotropic X-ray luminosity of $L_X = 9.43 \times 10^{47}$ erg s^{-1}.

The hard X-ray light curves of S5 0836+71, by applying 4 ksec binning to the *NuSTAR* data, are shown in Figure 3.4. The source has shown flux variations with the variability probability (Abdo et al. 2010b) of 98.33% and 99.86% for 2013 December and 2014 January observations, respectively. A significant change in the flux between the two epochs is also observed.

3.2.2 Spectral Analysis

The γ-ray spectra of powerful FSRQs are known to exhibit a significant curvature (e.g., Abdo et al. 2010c). With this in mind, the presence of curvature in the γ-ray spectra is tested for all the three activity states considered in this work. Two spectral models are used for this purpose: power law ($dN/dE \propto E^{\Gamma_\gamma}$), where Γ_γ is the photon index and log parabola ($\frac{dN}{dE} \propto (\frac{E}{E_o})^{-\alpha-\beta\log(E/E_o)}$, where E_o is an arbitrary reference energy fixed at 300 MeV, α is the photon index at E_o and β

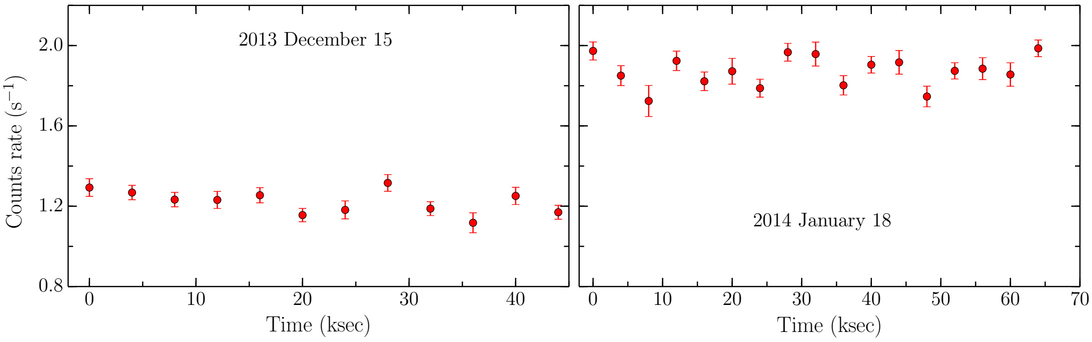

Figure 3.4: Background subtracted 3−79 keV light curves of the two *NuSTAR* observations of S5 0836+71. For this plot, the FPMA and FPMB count rates are summed, and 4 ksec binning is applied.

Table 3.4: Results of the model fitting to the γ-ray spectra of S5 0836+71, obtained for different time periods.

Period [1]	Activity [2]	Model [3]	$F_{0.1-300\ \mathrm{GeV}}$ [4]	$\Gamma_{0.1-300\ \mathrm{GeV}}/\alpha$ [5]	β [6]	TS [7]	$\mathrm{TS_{curve}}$ [8]
55860−55930	$\mathrm{F_G}$	PL	6.25 ± 0.21	2.67 ± 0.04		2621.34	
		LP	5.85 ± 0.22	2.50 ± 0.05	0.29 ± 0.05	2638.81	51.0
56000−56657	Q	PL	0.51 ± 0.04	3.09 ± 0.10		242.03	
		LP	0.49 ± 0.04	3.04 ± 0.11	0.13 ± 0.12	241.75	1.26
56790−56865	$\mathrm{F_X}$	PL	2.22 ± 0.15	2.59 ± 0.06		582.70	
		LP	2.05 ± 0.16	2.40 ± 0.10	0.18 ± 0.07	586.40	8.96

Notes. (1) period of observation (MJD); (2) activity state; (3) model used (PL: power law, LP: log-parabola); (4) integrated γ-ray flux (0.1−300 GeV), in units of 10^{-7} ph cm^{-2} s^{-1}; (5) and (6): spectral parameters (see definitions in the text); (7) test statistic; and (8) test statistic of the curvature.

is the curvature index which defines the curvature around the peak). To quantify the presence/absence of the curvature, the test statistic of the curvature $\mathrm{TS_{curve}} = 2(\log \mathcal{L}(\text{log parabola}) - \log \mathcal{L}(\text{power-law}))$ is calculated. A $\mathrm{TS_{curve}} > 16$ indicates the existence of a significant curvature (Nolan et al. 2012). The resultant fitting parameters are provided in Table 3.4. A significant curvature is noticed only during the γ-ray flare with $\mathrm{TS_{curve}} = 51$. Though at low significance, there is a hint for the presence of curvature in the X-ray flaring period also ($\mathrm{TS_{curve}} \approx 9$), and during the low activity state the power law model represents the spectrum better.

The overall γ-ray spectral behavior is studied by analyzing the variation of the photon index against the photon flux. The obtained results are shown in Figure 3.5. In this plot, the variation of photon indices with fluxes is shown for the weekly binned γ-ray light curve and for the daily binned γ-ray light curve, covering the period of GeV outburst. Visual inspection of the results does not reveal any correlation between daily binned fluxes and photon indices, however,

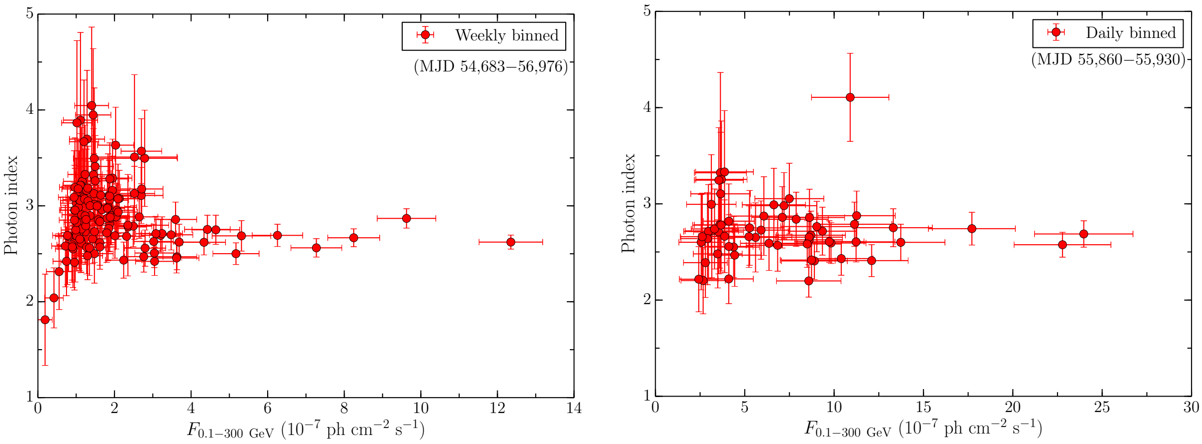

FIGURE 3.5: Left: Weekly scatter plot of the γ-ray flux vs. photon index. Right: Same as left but for daily binned data covering the period of high γ-ray activity.

for weekly binned plot the source seems to show a 'softer when brighter' trend, up to a flux level of $\simeq$1.5 $\times$ 10^{-7} ph cm^{-2} s^{-1}. Above this flux, there is a hint for a 'harder when brighter' behavior. To statistically test these findings, a Monte Carlo simulation is used that takes into account the errors associated with the flux and photon index measurements. In particular, for each observed randomly drawn flux and photon index pair, the data are re-sampled by extracting it from a normal Gaussian distribution centered on the observed value and having standard deviation equal to the error estimate. For lower fluxes of weekly binned data (i.e., $F_\gamma < 1.5 \times 10^{-7}$ ph cm^{-2} s^{-1}), ρ is found to be 0.18 $\pm$ 0.12 with 95% confidence limit of -0.07 $\leqslant \rho \leqslant$ 0.41. For higher flux level ($F_\gamma > 1.5 \times 10^{-7}$ ph cm^{-2} s^{-1}), the correlation coefficient (ρ) is found to be 0.27 $\pm$ 0.11 with 95% confidence limit of 0.02 $\leqslant \rho \leqslant$ 0.48. For daily binned data set, ρ is found to be 0.02 $\pm$ 0.13 with a 95% confidence limit -0.23 $\leqslant \rho \leqslant$ 0.28, clearly suggesting the absence of any correlation between fluxes and photon indices. Hence, based on the Monte Carlo test, no claim can be made for the presence of correlation between fluxes and photon indices in both the weekly binned and daily binned data set.

There were simultaneous observations of S5 0836+71 with *NuSTAR* and *Swift* in 2013 December and 2014 January (shown by black downward arrows in Figure 3.1). This permitted to perform joint spectral fit to the XRT and *NuSTAR* data. To account for the difference in flux calibration between XRT and *NuSTAR*, an inter-calibration constant (CONST in XSPEC) is introduced. This constant is fixed to unity for two *NuSTAR* spectra, since the calibration difference between two modules FPMA and FPMB are of the order of 1% (see, e.g., Marinucci et al. 2014).

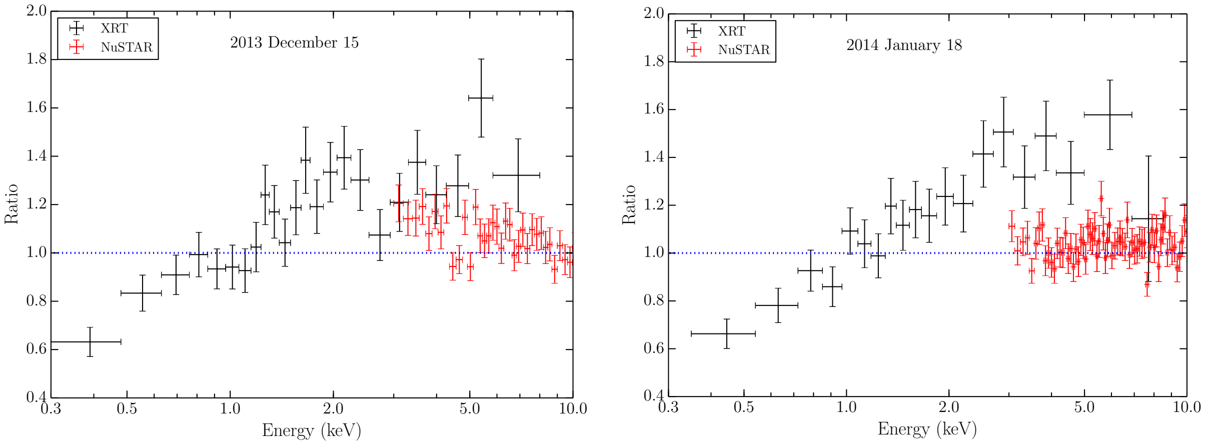

FIGURE 3.6: Data to model ratio of the fit of joint XRT and *NuSTAR* spectra with a power law and fixed galactic absorption. The deficit of soft photons below 1 keV clearly indicates a greater degree of absorption or an intrinsic hardening of the spectrum.

TABLE 3.5: Summary of the joint XRT+*NuSTAR* spectral fitting.

Model (1)	$N_{\mathrm{H}}^{\mathrm{addi.}}$ (2)	CONST (3)	$\Gamma_{\mathrm{X}}/\Gamma_1$ (4)	Γ_2 (5)	E_{break} (6)	Norm. (7)	χ^2/dof. (8)
			2013 Dec 15				
PL+GA	...	0.81 ± 0.03	1.58 ± 0.01	...	...	3.02 ± 0.09	692.30/550
PL+GA+zA	87.25 ± 10.94	0.85 ± 0.03	1.64 ± 0.02	...	...	3.48 ± 0.12	573.44/549
PL+GA+AA	8.31 ± 0.93	0.88 ± 0.03	1.66 ± 0.02	...	...	3.57 ± 0.12	559.43/549
BPL+GA	...	0.93 ± 0.06	1.13 ± 0.10	1.67 ± 0.03	2.07 ± 0.37	2.46 ± 0.18	553.30/548
			2014 Jan 18				
PL+GA	...	0.72 ± 0.02	1.66 ± 0.01	...	...	5.54 ± 0.13	880.74/762
PL+GA+zA	106.51 ± 13.84	0.83 ± 0.03	1.69 ± 0.01	...	...	5.90 ± 0.14	779.32/761
PL+GA+AA	9.58 ± 1.11	0.87 ± 0.03	1.69 ± 0.01	...	...	5.97 ± 0.14	766.55/761
BPL+GA	...	0.98 ± 0.08	1.23 ± 0.10	1.70 ± 0.02	2.83 ± 0.62	3.71 ± 0.33	755.79/760

Notes. (1) Fitted model (PL: power law, BPL: broken power law, GA: galactic absorption, AA: additional galactic absorption, zA: absorption in the intrinsic source frame); (2) additional neutral Hydrogen column density (10^{20} cm^{-2}); (3) intercalibration constant ; (4) photon index of PL model or photon index before break energy in BPL model; (5) photon index after break energy in BPL model; (6) break energy (keV); (7) normalization at 1 keV (10^{-3} ph cm^{-2} s^{-1} keV^{-1}); and (8) statistical parameters.

However, it is left free to vary for the XRT. A first round of fitting is performed with a power law model plus fixed galactic absorption. However, as can be seen in Figure 3.6, where the data to model ratio is plotted against energy, a simple power law clearly does not provide acceptable fitting parameters (see also, Table 3.5). The fit is improved by adding redshifted absorption (`zwabs` in XSPEC) or a broken power law shape for the continuum (F-test probability of null hypothesis $< 10^{-10}$). For the case of redshifted absorption, the level of absorption is higher but with relatively larger uncertainty and the obtained neutral Hydrogen column density N_{H} is similar to that reported by Sambruna et al. (2007). A satisfactory fit is also obtained by applying a broken power law model on joint XRT-*NuSTAR* spectra, while keeping the Galactic absorption fixed. Fitting the data with a power law

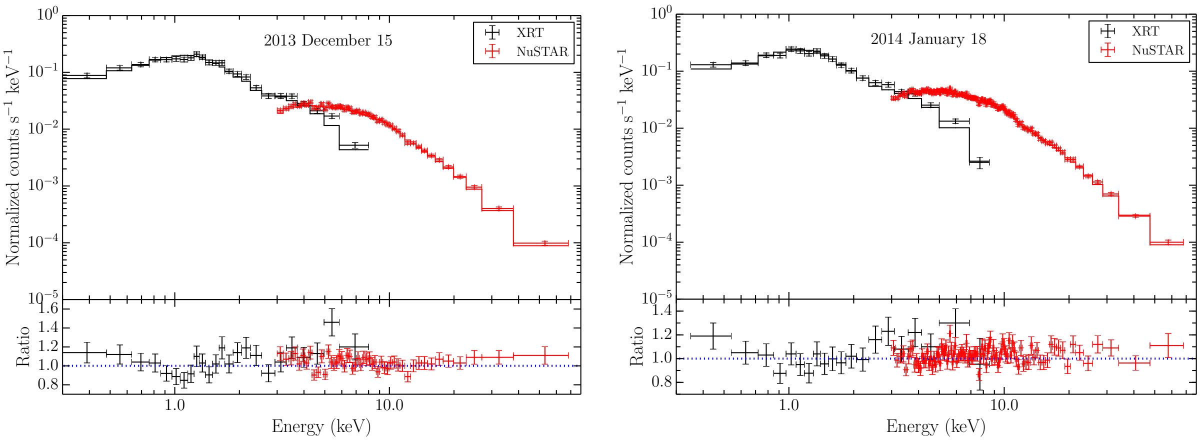

Figure 3.7: Top: Joint XRT (0.3–10 keV) and *NuSTAR* (3–78 keV) spectrum, fit with power law plus two layers of absorption. Bottom: data to model ratio for the obtained fit. Two *NuSTAR* spectra are grouped in XSPEC and rebinned for visual clarity.

plus two layers of galactic absorption (keeping one absorption fixed to the Galactic value and other left to vary) also gives a good fit with statistical parameters similar to that obtained with the use of broken power law model (see a similar approach in Akyuz et al. 2013). However, the additional absorption, in this case, is higher than the Galactic absorption by a factor of ∼3. Comparison of the fitting obtained with broken power law model with that obtained from power law plus two layers of absorption, is inconclusive. The F-test probability of null hypothesis, that the data is better described by the power law plus two layers of absorption, is found to be 0.014 and 0.001 for 2013 December and 2014 January observations, respectively. The results of fitting the power law with two layers of absorption for two simultaneous XRT-*NuSTAR* observations are shown in Figure 3.7. Finally, in the source frame, the Fe-K$_\alpha$ emission line is located at around 6.4 keV, and for S5 0836+71 it is expected to be around 2 keV in the observer's frame. A slight excess emission at ∼2-3 keV can be seen in Figure 3.6, however, due to poor data statistics of the short exposure XRT observations, a strong claim cannot be made.

3.2.3 SED Modeling

The SEDs of S5 0836+71 are generated covering the three different activity states (Figure 3.1). The generated broadband SEDs are modeled using the methodology described in Chapter 2. The results are presented in Figure 3.8 and the associated modeling parameters are given in Table 3.6. Variations of the comoving frame

TABLE 3.6: Summary of the parameters used/derived from the modeling of the SED in Figure 3.8.

	Activity state		
Parameter	F_G	Q	F_X
Slope of particle spectral index before break energy (p)	1.6	1.7	1.6
Slope of particle spectral index after break energy (q)	4.0	4.2	3.8
Magnetic field in Gauss (B)	1.7	1.8	2.5
Equipartition factor*($\eta_{\rm equi.}$)	0.89	2.74	1.43
Bulk Lorentz factor (Γ)	19	10	15
Break Lorentz factor ($\gamma'_{\rm b}$)	84	69	73
Maximum Lorentz factor ($\gamma'_{\rm max}$)	5e4	5e4	2e4
Dissipation distance in parsec ($R_{\rm Sch}$)	0.14 (500)	0.11 (400)	0.07 (250)
Jet power in electrons in log scale ($P_{\rm e}$)	45.83	45.62	45.57
Jet power in magnetic field in log scale ($P_{\rm B}$)	45.88	45.18	45.41
Radiative jet power in log scale ($P_{\rm r}$)	47.84	46.58	47.23
Jet power in protons in log scale ($P_{\rm p}$)	48.17	48.06	47.93

Notes. Viewing angle is taken as 3° and the characteristic temperature of the torus as 900 K. For a disk luminosity of 2.25 × 10^{47} erg s^{-1} and black hole mass of 3 × 10^9 $M_\odot$, the size of the BLR is ~0.5 parsec (1700 $R_{\rm Sch}$).

* Equipartition factor is the ratio of the particle to magnetic energy density ($\eta_{\rm equi.} = U'_{\rm e}/U'_{\rm B}$).

energy densities are also shown in the right column of Figure 3.8. To constrain the accretion disk luminosity and the block hole mass, the optical-UV spectrum of S5 0836+71 is fitted with a standard Shakura & Sunyaev (1973) disk model. This resulted in the disk luminosity and black hole mass of 2.25 × 10^{47} erg s^{-1} and 3 × 10^9 $M_\odot$, respectively. Accordingly, the accretion disk luminosity is ~60% of the Eddington luminosity.

A one zone leptonic synchrotron plus IC model, with the inclusion of thermal emission from the accretion disk, successfully reproduces the observed SEDs of S5 0836+71. However, due to synchrotron self absorption process, it fails to explain the radio data, suggesting that much of the radio emission come from the regions other than that considered here. In all the activity states, the optical-UV part of the SED is dominated by the accretion disk radiation and probably this is the reason of the lack of significant variability seen in the optical-UV band. Furthermore, the X-ray to high energy γ-ray window of the SED is reproduced via IC scattering of the photons originating outside the jet, from the accretion disk and the BLR. The X-ray spectrum is primarily reproduced by EC-disk and γ-ray emission via EC-BLR mechanism, as can be seen in Figure 3.8.

Comparing the low activity state SED parameters with that obtained during the γ-ray flare suggests the enhancement of bulk Lorentz factor as a major cause of the flare. It should be noted, however, that these results can also be reproduced by keeping bulk Lorentz factor fixed and varying the equipartition condition and

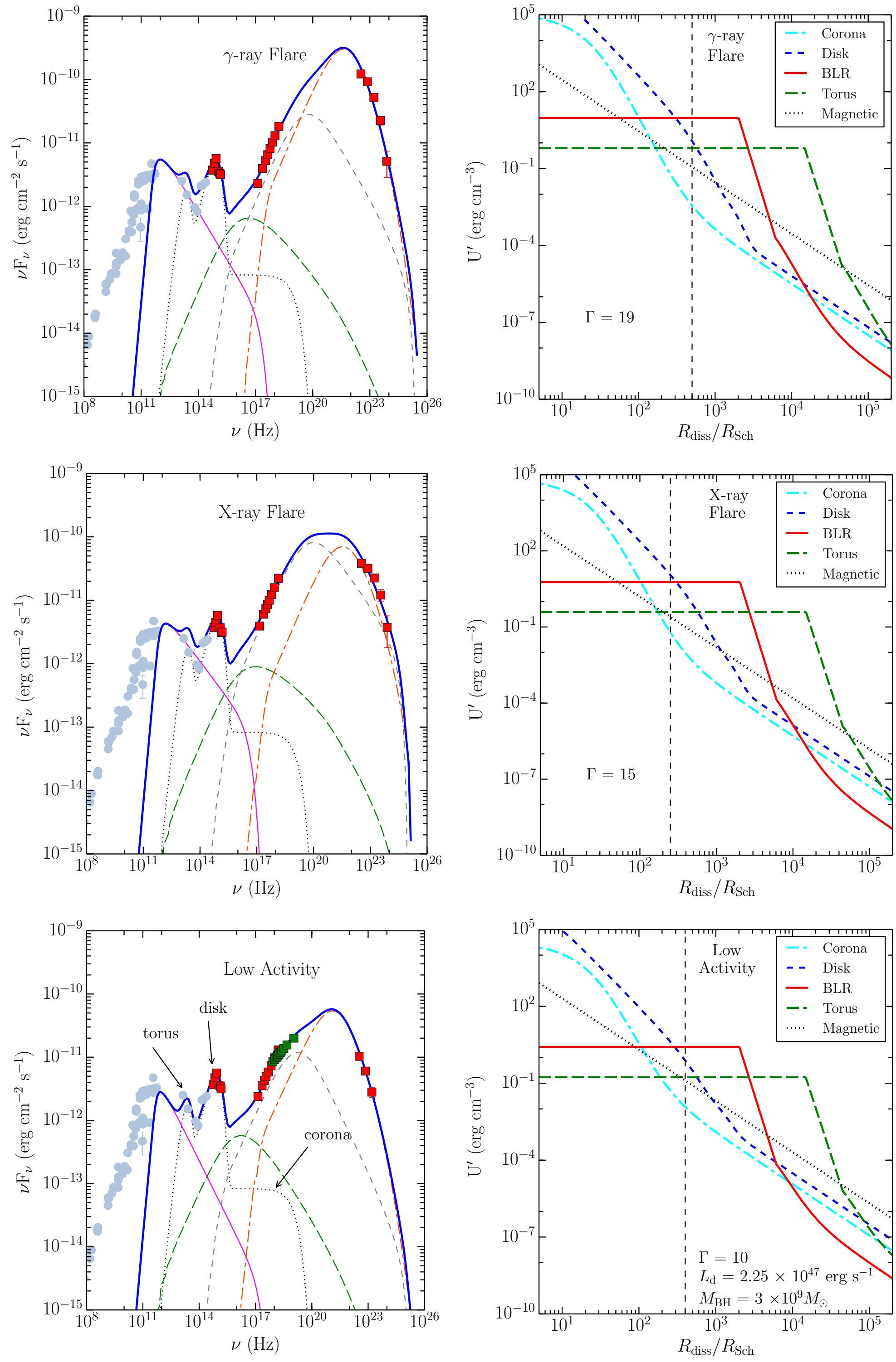

FIGURE 3.8: Left column: Spectral energy distributions of S5 0836+71 during different activity states. Simultaneous *Swift* and *Fermi*-LAT data are shown with red squares and light blue circles represent the archival observations. During the low activity period, the *NuSTAR* data is also available which is shown by green squares. Pink thin solid and green long dashed lines correspond to synchrotron and SSC, respectively. EC-disk and EC-BLR mechanisms are shown by grey dashed and orange dash-dash-dot lines, respectively. Blue thick solid line is the sum of all the radiative contributions. Right column: Variations of the energy densities measured in the comoving frame, as a function of the distance from the black hole, in units of $R_{\rm Sch}$. Vertical line denotes the location of the emission region.

the total jet power. The required jet power, in such a situation, would be less for the low activity state. There are few other modifications in the parameters, such as slight hardening of the spectral shape of the particle energy distribution, location of the emission region (and hence its size), and decrease in the magnetic field. The Compton dominance (the ratio of IC to synchrotron peak luminosities) also increases by about an order of magnitude. Though the synchrotron flux also increases during the flares, its contribution to the observed optical-UV radiation is negligible and thus no major change in the optical-UV spectrum is noted.

Though the modeling is performed in a manner to get the close equipartition between electrons and magnetic fields ($P_{\rm e} \sim P_{\rm B}$), the magnetic power is tiny compared to the proton power, or total jet power. This suggests a very low magnetization of the emission region. Moreover, the radiative efficiency of the jet (expressed as $P_{\rm r}/P_{\rm jet}$) is obtained as 0.23, 0.03, and 0.20 for $\rm F_G$, Q, and $\rm F_X$ periods, respectively. This indicates an efficient conversion of the kinetic jet power to the radiative power during the flaring episodes. However, a major fraction of the jet power remains in the form of proton power and used to produce large scale jets. An interesting point worth noting is that both $P_{\rm e}$ and $P_{\rm B}$ are smaller than $P_{\rm r}$ (see Table 3.6). At first sight, the fact that the electron jet power $P_{\rm e}$ is less than radiative jet power $P_{\rm r}$ appears to be a contradiction since the radiation produced by electrons, in principle, cannot have more power than the emitting electrons. However, this inference may not be correct. This is because the cooling timescale of γ-ray producing electrons is much shorter than $R'_{\rm blob}/c$, and therefore, in order to maintain the emission over the entire flare period, the number of high energy electrons should be replenished continuously. In other words, the electron population continuously gains energy at the expense of bulk jet power and transfers the power to radiation. Hence, $P_{\rm r}$ should be taken as the fraction of bulk luminosity converted to radiation through electrons. On the other hand, since the mean energy of the electrons will be closer to $\gamma_{\rm min}$, $P_{\rm e}$ is primarily decided by the total number of electrons at lower energies which do not emit γ-rays.

Modeling of the SED suggests the emission region to be located inside the BLR, in all the activity states. In such situation, the BLR radiation energy density would dominate over the energy densities of other comoving frame photon fields, and the primary mechanism for the production of γ-rays would be IC scattering of BLR photons (observed energies $\epsilon_0 \simeq$10 eV). Accordingly, the cooling timescale for the electrons responsible for γ-ray production with the energies $\epsilon_\gamma \simeq$1 GeV would be, in the observer's frame

$$\tau_{\rm cool} \simeq \frac{3\, m_e\, c}{4\, \sigma_{\rm T}\, u'_{\rm BLR}} \sqrt{\frac{\epsilon_0 (1+z)}{\epsilon_\gamma}}, \tag{3.2}$$

i.e., ~9 minutes for the comoving BLR photon energy density $u'_{\rm BLR} \simeq 10$ erg cm^{-3}. The calculated cooling time is significantly shorter than the shortest flux decay time of the flares. This implies that the observed flux decrease is governed by not only radiative energy losses but also by a combination of different factors such as particle acceleration or jet dynamics (e.g., Böttcher & Principe 2009; Kushwaha et al. 2014). On the other hand, presence of sub-structures and/or geometry of the emitting region could also led to such observations (Tanihata et al. 2001).

The highest isotropic γ-ray luminosity is measured as ~1.64×10^{50} erg s^{-1}, which corresponds to the total power emitted in the γ-ray band, in the proper frame of the jet, $L_{\gamma,{\rm em}} \simeq L_\gamma/2\Gamma^2 \simeq 2.27 \times 10^{47}$ erg s^{-1}, assuming the bulk Lorentz factor $\Gamma = 19$, obtained from the modeling of the γ-ray flaring SED. This is a good fraction of the kinetic jet power (~15 %, $P_{\rm j,kin} = 1.48 \times 10^{48}$ erg s^{-1}), suggesting that the jet became radiatively efficient and the bulk of the radiative energy released in the form of γ-rays. For a comparison, the $L_{\gamma,{\rm em}}$ is found to be about 60% of the Eddington luminosity (for a black hole mass of $3 \times 10^9 M_\odot$). Moreover, $L_{\gamma,{\rm em}}$ is also a found to be a good fraction of the entire available accretion power ($L_{\rm acc} \simeq L_{\rm disk}/\eta_{\rm disk} = 2.25 \times 10^{48}$ erg s^{-1}; assuming accretion efficiency $\eta_{\rm disk} =$ 10%).

The results of the energetics suggest that both the total jet power (dominated by protons), and $L_{\rm acc}$ exceed the Eddington luminosity. However, there could be few caveats. First, for a given value of $L_{\rm disk}$, a higher $\eta_{\rm disk}$ will reduce the total accretion power. Second, if number density of leptons is higher than that of proton, the budget of the proton jet power will come down. Third and most important factor could be the underestimation of the central black hole mass. This can lead to super Eddington accretion and jet power. The mass of the central black hole used in this work is 3×10^9 $M_\odot$, obtained by fitting the standard accretion disk model to the optical-UV spectrum. However, if the C IV line parameters from Torrealba et al. (2012) are taken to calculate the black hole mass and the empirical relations of Shen et al. (2011) are used, the calculated black hole mass is as large as

$\sim 1.3 \times 10^{10}\ M_{\odot}$. Therefore, these uncertainties and/or their combinations could lead to overestimation of the total jet power and the accretion power, higher than the Eddington luminosity.

A significant curvature is noticed in the γ-ray spectrum of S5 0836+71 during the period of γ-ray outburst (Table 3.4). Many models have been proposed to explain such curvature. One such possibility could be due to attenuation of γ-rays by photon-photon pair production on He II Lyman recombination lines within the BLR (Poutanen & Stern 2010). Cerruti et al. (2013) have proposed an alternative model, in which a combination of log parabolic electron energy distribution and the introduction of Klein-Nishina cross section for the calculation of IC scattering of BLR photons is adopted to explain the observed curvature. In this work, the spectral curvature of S5 0836+71 is reproduced on the basis of Klein-Nishina mechanism and broken power law electron distribution.

An interesting phenomenon observed in the multi-wavelength light curves is the detection of a large X-ray flare with relatively moderate γ-ray counterpart (see period $\mathrm{F_X}$ in Figure 3.1). Since, the X-ray emission is dominated by EC-disk mechanism, a possible cause of the X-ray flare could be due to enhancement in the EC-disk flux. One of the possibilities is the emission region being located close to the central black hole. Since the comoving frame energy density of the accretion disk increases with decrease in the dissipation distance (e.g., Dermer et al. 2009; Ghisellini & Tavecchio 2009), a higher disk energy density reflects in the higher EC-disk flux. This, in turn, causes a larger enhancement in the X-ray flux with respect to γ-rays. To elaborate this hypothesis, the variation of comoving frame energy densities as a function of the distance of the emission region from the central black hole is shown in the right column of Figure 3.8. As can be seen, during the X-ray flaring period, the emission region is located in a jet environment where the accretion disk energy density dominates over the energy densities of the other components. Accordingly, the enhancement of EC-disk radiation will be higher as compared to EC-BLR and the rise in the X-ray flux will be greater.

3.2.4 Summary

The main findings of the broadband study of S5 0836+71 are as follows.

1. The long term multi-frequency light curves show multiple episodes of flaring activities in X-ray and γ-ray bands, while optical-UV fluxes vary little.

2. In the energy range of 0.1−300 GeV, the highest 3 hr binned γ-ray flux is $(5.22 \pm 1.10) \times 10^{-6}$ ph cm^{-2} s^{-1}, measured on MJD 55866. This corresponds to an isotropic γ-ray luminosity of $(1.62 \pm 0.44) \times 10^{50}$ erg s^{-1}. This is the most luminous γ-ray flare ever observed from the blazar class of AGN.

3. The observed γ-ray flux variability of about 3 hr is the shortest flux variability time ever measured from this source, and probably from any high redshift blazar ($z > 2$).

4. A simple one zone leptonic emission model is used to reproduce the SED and the obtained parameters hint the emission region to be located inside the BLR. In all the activity states, the optical-UV spectrum is dominated by the accretion disk radiation.

5. Enhancement in the bulk Lorentz factor is probably a primary factor for the observed giant γ-ray flare. The high activity seen in the X-ray band with less variable γ-ray counterpart can be explained by locating the emission region closer to the central black hole where the comoving frame energy density from the accretion disk dominates over the energy densities of other components, resulting in an enhanced EC-disk flux peaking in X-rays.

3.3 3FGL J0809.5+5342 (BZQ J0809+5341)[2]

BZQ J0809+5341 (hereafter J0809+5341) is a high redshift FSRQ ($z = 2.144 \pm 0.002$; Pâris et al. 2014). It was overlooked for a long time due to its faintness and/or prolonged quiescence. It was included in the list of candidate γ-ray emitters by Healey et al. (2008) but not detected by any earlier γ-ray surveys. It was not detected by *Fermi*-LAT in its first two years of operation and subsequently not present in 2FGL catalog (Nolan et al. 2012). J0809+5341 is radio bright ($F_{8.4\ \mathrm{GHz}} = 183.4$ mJy; Healey et al. 2007) and exhibits a compact core morphology in the Faint Images of the Radio Sky at Twenty centimeters (FIRST) observations.

---

[2] The results presented for J0809+5341 are published in Paliya et al. (2015d).

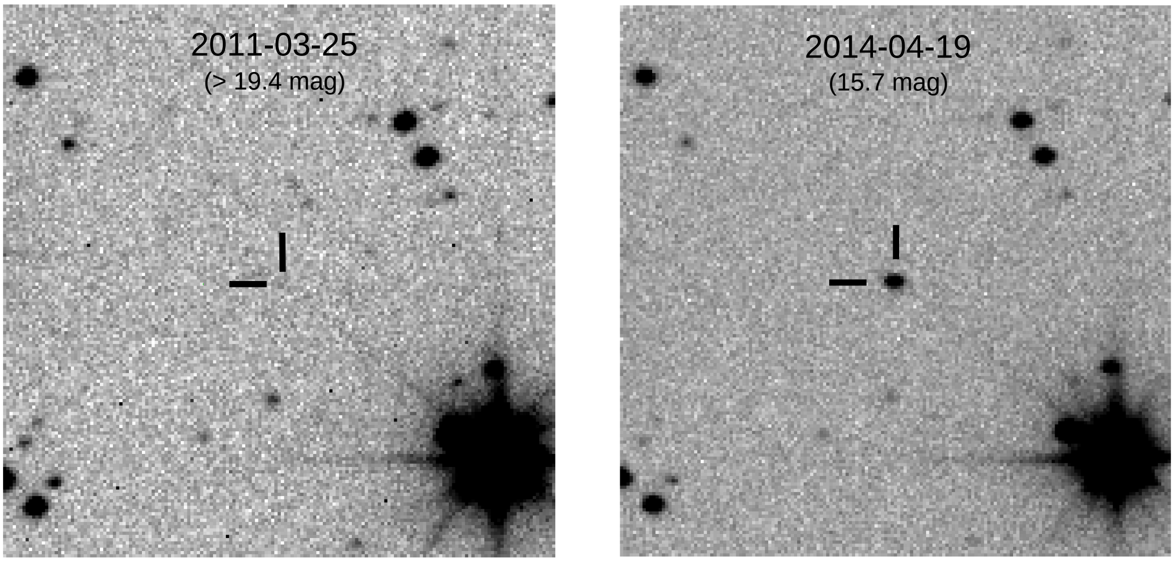

Figure 3.9: Mobile Astronomical System of the TElescope-Robots (MASTER) image of J0809+5341 (field of view of $5'' \times 5''$) taken on 2011 March 25 (left) and on 2014 April 19 (right). An upper limit of 19.4 mag is obtained during 2011 observations, while there is ∼5 mag brightening (with respect to the SDSS observations) during the 2014 optical outburst. North is up and East is left.

J0809+5341 underwent a giant optical outburst on 2014 April 19 (Balanutsa et al. 2014), when its unfiltered apparent magnitude reached 15.7 mag (Figure 3.9). At a redshift of 2.14, this corresponds to an absolute magnitude of −30.5 mag, thereby making it as one of the brightest quasars in the Universe. Also, the source was ∼5 mag brighter on 2014 April 19, compared to the archival Sloan Digital Sky Survey (SDSS) observations. To study this extraordinary event, immediately a multi-frequency campaign was organized, using both space and ground based observational facilities. The hard X-ray mission *NuSTAR* (Harrison et al. 2013) observed the target on 2014 May 8 and was supplemented by a contemporaneous *Swift* target of opportunity (ToO) monitoring. Moreover, optical photometric and polarimetric observations from the *Telescopio Nazionale Galileo*[3] (TNG) and the *Himalayan Chandra Telescope*[4] (HCT) were also carried out. In addition to that, the source was observed on 2014 April 26, 27, and 28 by other *Swift* ToO observations. The entire campaign was complemented by continuous monitoring from the *Fermi*-LAT.

---

[3] `http://www.tng.iac.es`

[4] `http://www.iiap.res.in/centers/iao`

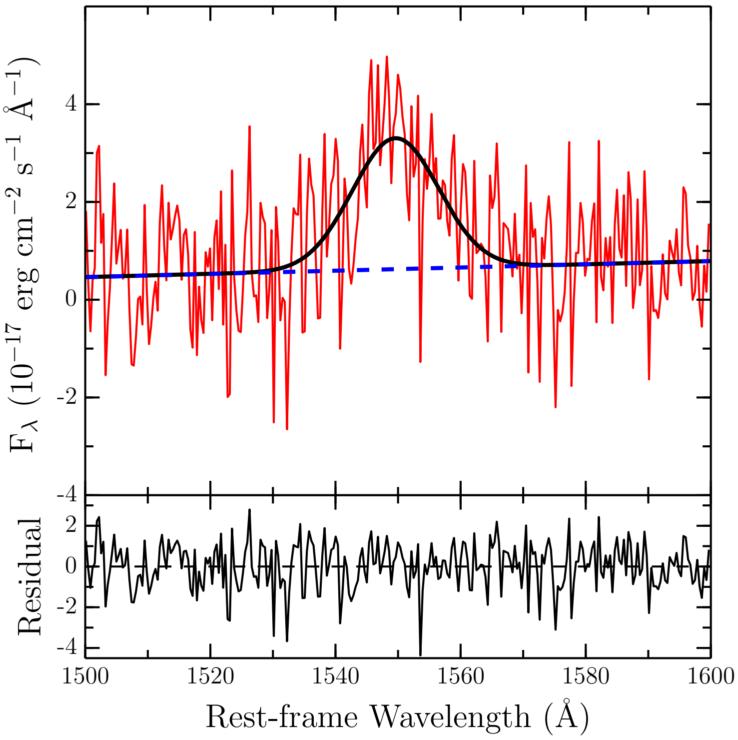

FIGURE 3.10: Top: A fit to the continuum and C IV line in the SDSS spectrum of J0809+5341. Bottom: The residual between the fit and the rest-frame spectrum.

3.3.1 Black Hole Mass And Accretion Disk Luminosity

J0809+5341 has a low signal to noise (S/N) spectrum available from SDSS-DR10 (Pâris et al. 2014) and is used to estimate the black hole mass ($M_{\rm BH}$) and the accretion disk luminosity ($L_{\rm disk}$). The spectrum is brought to the source-frame and then corrected for galactic extinction using E(B−V) of 0.038 (Schlafly & Finkbeiner 2011). A χ^2 minimization technique is adopted to perform the fitting, based on the `MPFIT` package (Markwardt 2009). The continuum is assumed to follow a power law profile and fit to the spectrum using the line free regions [1445, 1465] Å and [1700,1710] Å, i.e. on either side of the C IV line. This fitted continuum is then subtracted from the spectrum. Since Fe emission line is known to be weak compared to C IV line (Shen et al. 2011), it is not subtracted from the spectrum. A single Gaussian function is then used to fit the modified spectrum between the wavelength range [1500, 1600] Å. Since the virial black hole mass estimates using C IV are based on the FWHM of the entire C IV line profile (Vestergaard & Peterson 2006), the narrow component C IV is not considered for the fitting. The resultant fitting is shown in Figure 3.10. The line flux and the σ of the C IV line are obtained as $(46.46 \pm 0.76) \times 10^{-17}$ erg cm^{-2} s^{-1} Å^{-1} and 1338.3 ± 139 km s^{-1}, respectively. The FWHM of C IV is estimated as 3145 ± 327 km s^{-1} by correcting the observed σ for the resolution of the instrument. The mean continuum flux at 1350 Å is calculated as $(4.96 \pm 0.26) \times 10^{-17}$ erg $cm^{-2}\,s^{-1}$ $Å^{-1}$. This, in turn, translates to a continuum luminosity (λL_λ) of $(2.43 \pm 0.14) \times 10^{45}$ erg s^{-1}. The C IV line luminosity is obtained as $L_{\rm C\ iv} = (1.69 \pm 0.03) \times 10^{43}$ erg s^{-1}. Using the measured FWHM and the continuum luminosity, the black hole mass is estimated from the following equation (Shen et al. 2011)

$$\log\left(\frac{M_{\rm BH,vir}}{M_\odot}\right) = a + b\log\left(\frac{\lambda L_\lambda}{10^{44}\,{\rm erg\,s^{-1}}}\right) + 2\log\left(\frac{\rm FWHM}{\rm km\,s^{-1}}\right) \tag{3.3}$$

Following Shen et al. (2011), a and b are taken as 0.66 and 0.53, respectively. This resulted in a black hole mass of $\log\left(\frac{M_{\rm BH}}{M_\odot}\right) = 8.39 \pm 0.21$. Moreover, following Celotti et al. (1997) the total BLR luminosity ($L_{\rm BLR}$) is derived using the flux of the C IV line. This resulted in $L_{\rm BLR} = 1.5 \times 10^{44}$ erg s^{-1}. Assuming 10% of the accretion disk luminosity is reprocessed by the BLR, the accretion disk luminosity is 1.5×10^{45} erg s^{-1}.

3.3.2 Average Gamma-Ray Properties

The LAT data analysis covering the first two years of *Fermi* operation results in TS = 0.5, indicating that the source flux was below $\sim 5\sigma$ detection. This is the reason of its absence in the 2FGL catalog. However, analysis of the third through fifth years of the LAT data gives TS $\approx$185.5 ($\sim 13\sigma$; Mattox et al. 1996), thereby confirming the detection of J0809+5341 in the γ-ray band for the first time. J0809+5341 brightened in γ-rays during the sixth year of *Fermi* operation with TS = 191.3. The derived γ-ray flux and photon index are $(2.78 \pm 0.44) \times 10^{-8}$ ph $cm^{-2}\,s^{-1}$ and 2.15 ± 0.08, respectively. The results of the average analysis of *Fermi*-LAT data covering various time intervals are given in Table 3.7.

3.3.3 Gamma-ray Temporal Variability

The monthly binned γ-ray light curve of J0809+5341, for the first 72 months of *Fermi* operation, is shown in Figure 3.11. Daily scaled γ-ray flux covering the period of high optical activity (MJD 56748−56786 or 2014 April 1 to 2014 May 9)

TABLE 3.7: Details of the power-law model fits to the averaged γ-ray data for various time periods.

Time Period (MJD)	$\Gamma_{0.1-300\ \mathrm{GeV}}$	$F_{0.1-300\ \mathrm{GeV}}$	TS	log L_γ	TS$_{\mathrm{curve}}$
54683−55412	–	–	0.5	–	–
55412−56508	2.26 ± 0.08	1.61 ± 0.26	185.5	47.72	8.70
56508−56873	2.15 ± 0.08	2.78 ± 0.44	191.3	48.00	9.64
54683−56873	2.28 ± 0.06	1.40 ± 0.19	267.6	47.65	9.60

Notes. The quoted flux values are in units of 10^{-8} ph cm^{-2} s^{-1} whereas L_γ is the γ-ray luminosity (erg s^{-1}). The last column quotes the significance of the curvature present in the spectrum.

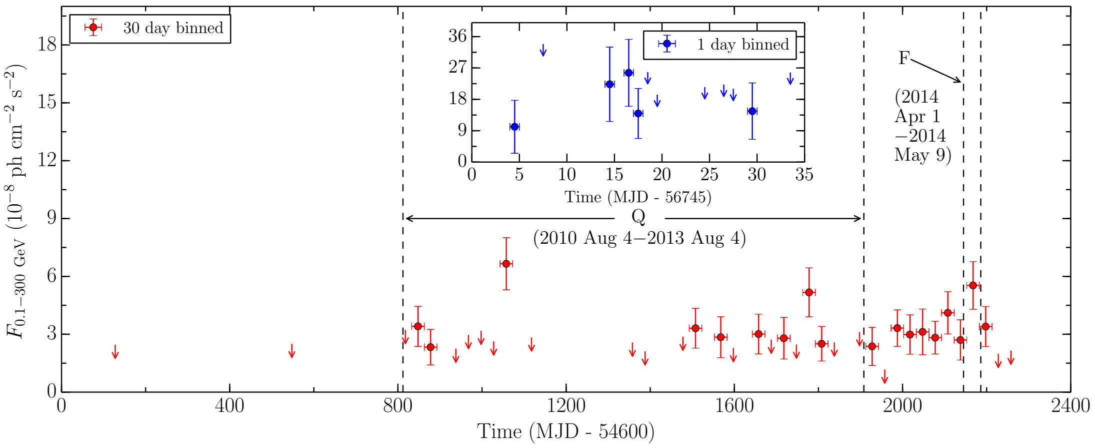

FIGURE 3.11: Flux history of J0809+5341 in the γ-ray band, covering the first 72 months of *Fermi*-LAT operation. Data are in units of 10^{-8} ph cm^{-2} s^{-1}. The 2σ upper limits are shown by downward arrows. Q represents a low activity state, while, F denotes a high activity state selected for the SED modeling. Inset: Daily binned γ-ray light curve covering the period of high activity. The flux units are same as that of the main panel.

are also shown by blue circles in the inset. As can be seen in Figure 3.11, the source was below $\sim 3\sigma$ detection limit in the first two years of *Fermi* operation. It was sporadically detected during the third through fifth years at a low flux level. However, it becomes relatively active in the sixth year. The maximum daily binned γ-ray flux (F_γ), for the flaring period, is obtained as $(2.56 \pm 0.96) \times 10^{-7}$ ph cm^{-2} s^{-1} on 2014 April 14 (MJD 56,761), which coincides with the first report of the high optical activity from the source (Shumkov et al. 2014).

3.3.4 Optical-UV Observations

In Table 3.8, the multi-band apparent magnitudes of J0809+5341 as observed from HCT, are presented. For comparison, the SDSS magnitudes, converted to UBVRI

Table 3.8: Apparent magnitudes of J0809+5341, as observed from HCT.

Filters	2014 Apr 27	2014 May 1	2003 Nov 20 (SDSS)
U	–	18.15 ± 0.07	21.03 ± 0.12
B	18.14 ± 0.04	18.48 ± 0.04	21.19 ± 0.04
V	17.67 ± 0.02	17.99 ± 0.03	20.61 ± 0.04
R	17.17 ± 0.01	17.47 ± 0.03	20.21 ± 0.04
I	16.56 ± 0.02	16.82 ± 0.04	19.69 ± 0.05

Note. For comparison, the ugriz magnitudes from SDSS that are converted to UBVRI magnitudes are also given.

filters using the transformations given by Jordi et al. (2006), are also provided. A significant optical brightening is seen in all filters, as evident from Table 3.8

The optical polarimetric observations of J0809+5341 from TNG were carried out on 2014 May 8 and found it in a highly polarized state. The observed polarization is found to be as high as 9.8 ± 0.5%. The associated polarization angle is 98 ± 1°.

3.3.5 Spectral Analysis

The presence of curvature in the overall γ-ray spectrum of J0809+5341 is tested by fitting a log parabola model. The methodology adopted is similar to that presented in Section 3.2.2. There are hints for the presence of curvature as $\mathrm{TS_{curve}} \approx 10$ ($\sim 3\sigma$; Table 3.7), though a strong claim can not be made as $\mathrm{TS_{curve}}$ is below the threshold of 16 (Nolan et al. 2012).

The joint XRT and *NuSTAR* spectrum is well fit with a simple power law plus a fixed Galactic absorption (C-statistic/d.o.f.= 40/35). The best-fit photon index of 1.4 ± 0.1 is obtained which is typical to that observed from high redshift blazars. The result of the fitting is shown in Figure 3.12, along with the residuals to the model. The difference in flux calibration between *NuSTAR* and XRT spectra is allowed to vary by including a constant (CONST in XSPEC) fixed at one for two *NuSTAR* spectra (e.g., Marinucci et al. 2014) and left free to vary for the XRT. This constant offset is consistent with 1 (1.2 ± 0.3) and the same value of the photon index is obtained irrespective of whether the constant multiplicative factor is allowed to vary or not. The goodness of the fit is calculated using Monte-Carlo simulations with the GOODNESS command in XSPEC, and it is found that 47% of the simulated spectra based on the model have a lower χ^2.

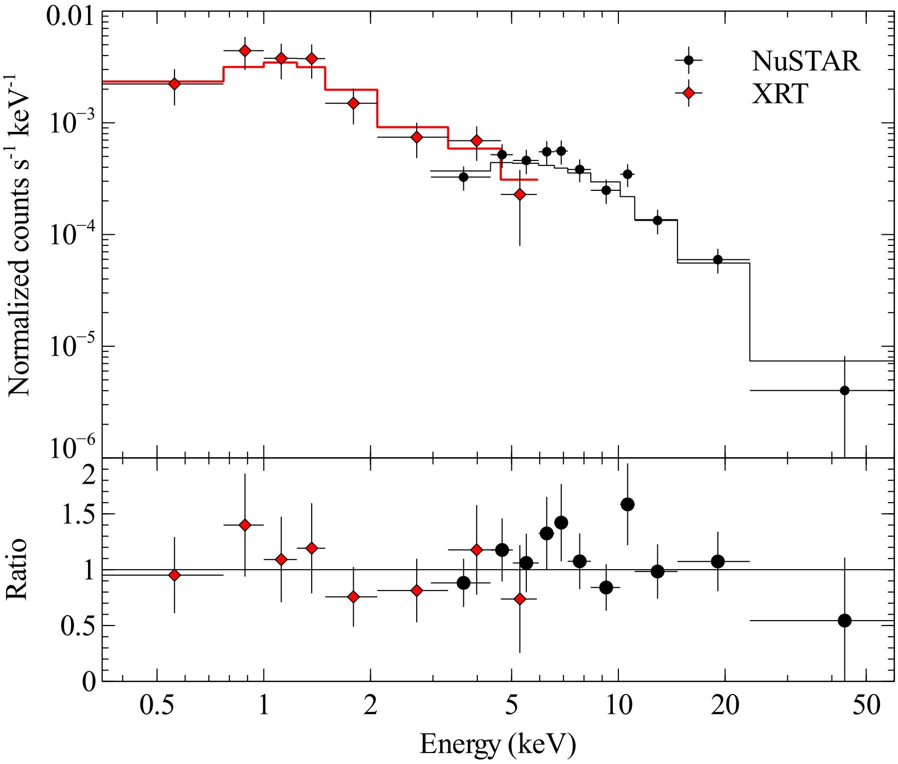

Figure 3.12: Top: Joint XRT (from 0.3–7 keV) and *NuSTAR* (from 3–60 keV) spectrum, fit with an absorbed power-law. Bottom: data to model ratio for this fit. Data are rebinned for clarity, and the two *NuSTAR* spectra are grouped in Xspec but fit separately.

From HCT observations, the $B - R$ colors of J0809+5341 are found to be 0.90 ± 0.04 and 0.94 ± 0.05 for the epochs of 2014 April 27 and 2014 May 1, respectively. Thus, there is no color change between these two epochs. At the time of the SDSS observation, B−R = 0.98 ± 0.06, which clearly indicates the absence of any optical color variation between the epochs in 2003 and 2014, though the source has varied significantly in flux.

3.3.6 Spectral Energy Distributions

The SEDs of J0809+5341 are generated during two different activity states. A high flux state covering the period of the optical outburst (2014 April 1 to 2014 May 9), and a low activity phase for which non-simultaneous archival observations[5] and the LAT data, covering the third through fifth years of *Fermi* operation, are used. In principle, one should not use non-simultaneous observations to constrain

---

[5] `http://www.asdc.asi.it/bzcat`

TABLE 3.9: Summary of the parameters used/derived from the modeling of the SED.

Parameter	Symbol	High Activity
Slope of particle spectral index before break energy	p	1.6
Slope of particle spectral index after break energy	q	5.3
Magnetic field in Gauss	B	2.0
Particle energy density in erg cm^{-3}	$U'_{\rm e}$	0.05
Bulk Lorentz factor	Γ	20
Minimum Lorentz factor	γ'_{min}	1
Break Lorentz factor	γ'_b	1714
Maximum Lorentz factor	γ'_{max}	1e5
Size of the BLR in the units of $R_{\rm Sch}$	$Z_{\rm BLR}$	1570
Distance of the emission region from the black hole in parsec ($R_{\rm Sch}$)	$Z_{\rm diss}$	0.048(1980)
Dusty torus temperature in Kelvin	$T_{\rm IR}$	900
Viewing angle in degrees	θ	3
Jet power in electrons in log scale	$P_{\rm e}$	44.62
Jet power in magnetic field in log scale	$P_{\rm B}$	45.11
Radiative jet power in log scale	$P_{\rm r}$	46.19
Jet power in protons in log scale	$P_{\rm p}$	46.34

the physical parameters, however, it can be justified by the fact that during the recent optical flare, the optical magnitude was brighter by ∼5 mag compared to the archival SDSS measurements (Balanutsa et al. 2014). This means, SDSS observations or the data from earlier epochs can be taken as a representation of the low activity state. Moreover, the source was observed by Mobile Astronomical System of the TElescope-Robots (MASTER; Lipunov et al. 2010) on 2011 March 25, i.e. between the third and fifth years of *Fermi* operation (see Figure 3.9) and only an upper limit of 19.4 mag in the unfiltered magnitude could be obtained. This result also indicates that before the 2014 April outburst, the optical flux level of the source was possibly similar to that observed by the SDSS in 2003. Moreover, as can be seen in Figure 3.11, the source become γ-ray active only very recently. Therefore, the third through fifth years of *Fermi*-LAT observations can be taken as a representative of low activity state.

As discussed above, the low activity state SED is constructed using non-simultaneous data and therefore the modeling is performed only on the flaring state SED, when the source was monitored contemporaneously over a wide energy range. The model spectrum due to different emission mechanisms along with the observed fluxes are presented in Figure 3.13 and the modeling parameters are given in Table 3.9. The variation of the comoving frame radiation energy densities are also shown in the bottom panel of Figure 3.13.

The optical-UV spectrum of J0809+5341 is steep and is interpreted as synchrotron

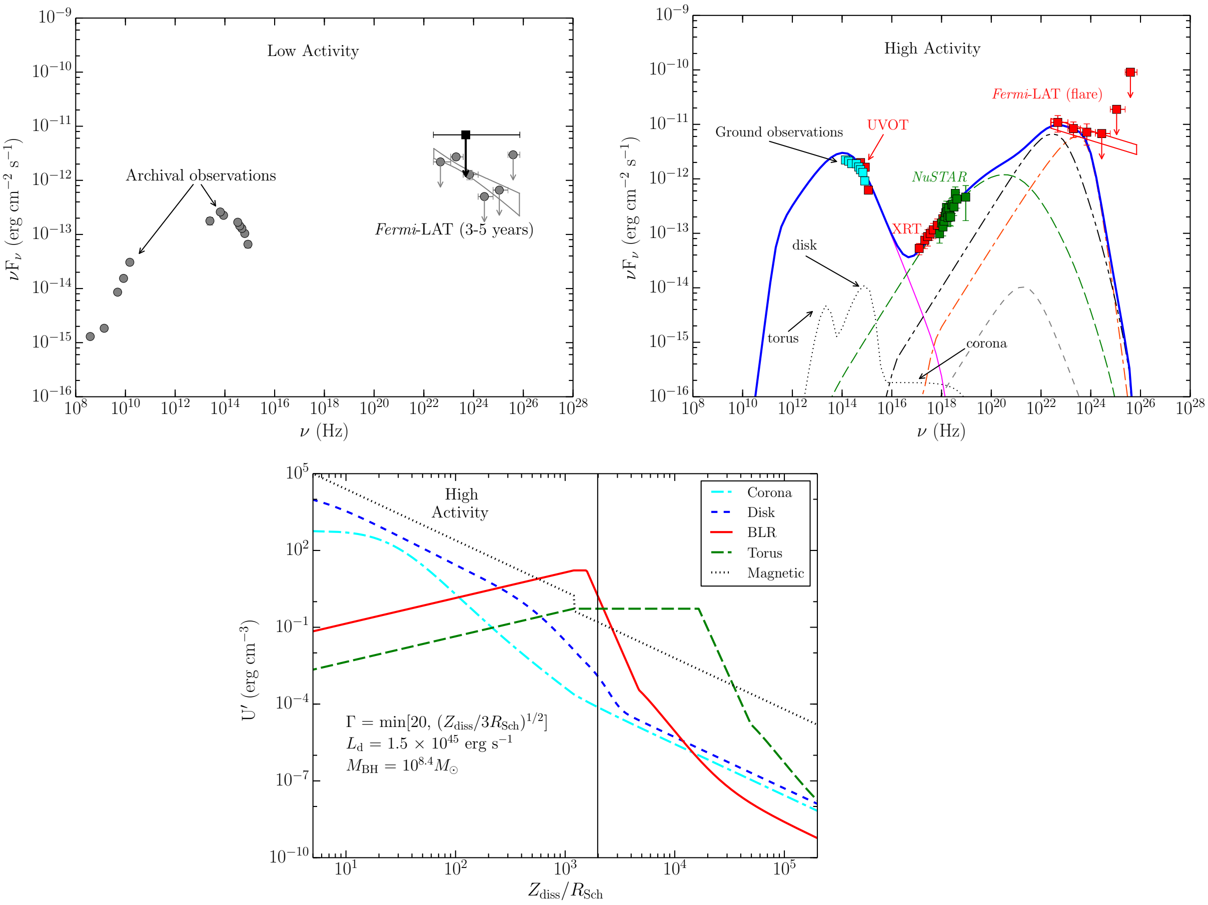

FIGURE 3.13: Top left: Low activity state SED of J0809+5341. Gray bow-tie plot represents third through fifth year of *Fermi* operation. Black downward arrow is the first two years 95% flux upper limit, calculated by assuming the photon index obtained from the analysis of the third through fifth year LAT data. Top right: Modeled high activity state SED. Black dotted line represents thermal contributions from the torus, the accretion disk, and the X-ray corona. Pink thin solid line and green long dashed line are synchrotron and SSC radiation. Grey dashed, red dash-dot, and black dash-dot-dot lines represent EC-disk, EC-BLR, and EC-torus components, respectively. Blue thick solid line refers to the sum of all the radiation components. Bottom panel: Variation of the energy densities measured in the comoving frame, as a function of the distance from the black hole, in units of R_{Sch}. Vertical line denotes the location of the emission region.

emission. Alternatively, it can be associated to the accretion disk emission. However, the large variation seen at optical-UV energies during low and high activity states are difficult to associate with the perturbations in the accretion disk emission. The accretion disk luminosity obtained from the line fitting of the SDSS spectrum also suggests a relatively small contribution of the disk emission to the observed optical-UV radiation (see Section 3.3.1). Additionally, the detection of the high optical polarization during the recent flare also supports the synchrotron origin of the optical-UV spectrum. Moreover, the X-ray spectrum of J0809+5341 is typical of powerful blazars and can be well explained by the SSC process.

It can be seen in Figure 3.13 that the spectral shape at optical-UV energies is relatively steep compared to the γ-ray spectrum. Since the shape of the underlying electron energy distribution is reflected in the synchrotron emission, a steep optical-UV spectrum hints that the spectral shape of the emitting electrons to be soft. Moreover, if the same population of the electrons is contributing to the emission at γ-rays through IC process, then steep γ-ray spectrum, similarly to the optical-UV, is expected. However, the observed γ-ray spectrum is hard. Hence, the most plausible option could be the assumption that the harder γ-ray spectrum is the result of the superposition of different IC emission processes. One of the possibilities is that the SSC is contributing in the hard X-ray to soft γ-rays and an EC component can explain the remaining γ-ray spectra. However, a steeply falling optical spectrum indicates the synchrotron peak to lie at lower energies which in turn causes negligible SSC emission at high energies (e.g., Sahayanathan & Godambe 2012). This implies that, though significant, SSC cannot reproduce the observed γ-ray spectrum. Alternatively, the radiative interplay between various EC mechanisms can also led to a flat γ-ray spectrum. It is found that the inclusion of EC-BLR and EC-torus emission can satisfactorily reproduce the γ-ray spectrum. The relative contribution of the target photons for EC-BLR and EC-torus mechanisms, measured in the comoving frame, depends on the location of the emission region from the central engine. Then, the location of the emission region can be derived under the assumption that the γ-ray spectrum is the superposition of EC-BLR and EC-torus components. The energy densities of various components in the comoving frame are plotted as a function of $R_{\rm diss}$ in the bottom panel of Figure 3.13. The analysis of the flaring SED suggests the emission region to be located at a distance from the central black hole where both the BLR and IR-torus energy densities are contributing almost equally to produce the flat γ-ray spectrum. Moreover, the SED parameters are further constrained by considering near-equipartition between relativistic particles and magnetic field.

Few interesting features are found when comparing the low activity state SED with that representing the flaring phase. The amplitude of the flux variations seems to be higher for optical flux than that for γ-rays. This is also supported by the fact that at the time of the flare, the source was one of the brightest quasars in the optical band, whereas, the γ-ray flux enhancement was relatively moderate.

However, the lack of simultaneous γ-ray observations at the time of low activity state SDSS observations precludes to make a strong claim. A comparison of the accretion disk flux with that of the archival optical observations indicates that even during quiescence the optical-UV emission is synchrotron dominated.

Comparing to the high redshift blazars, the SED and the associated modeling parameters of J0809+5341 are quite different. In general, the optical-UV spectrum of high redshift blazars is dominated by a luminous accretion disk radiation and the peak of IC emission lies in the hard X-ray regime resulting in a steep γ-ray spectrum. They also are known to host more than a billion solar mass black hole at their centers (e.g., Ghisellini et al. 2011, 2013). In contrast, J0809+5341 hosts a relatively less luminous accretion disk and a less massive central black hole. Its optical-UV spectrum is dominated by synchrotron radiation and the IC peak lies at GeV energy regime. Overall, the observed properties of J0809+5341 indicate that this source is, in many ways, different from other high redshift counterparts but show similarities with low redshift blazars.

3.3.7 Summary

The giant optical outburst of J0809+5341 is studied in detail and the main findings of the work are summarized below.

1. Earlier predicted as a candidate γ-ray emitter, J0809+5341 is now detected in the γ-ray band by *Fermi*-LAT, as further confirmed by the 3FGL catalog.
2. Analysis of the SDSS spectrum resulted in the black hole mass and accretion disk luminosity of $10^{8.4} M_{\odot}$ and 1.5×10^{45} erg s^{-1}, respectively.
3. The choice of the synchrotron mechanism over the accretion disk for flaring state optical-UV spectrum is primarily influenced by the observation of high optical polarization during the flare and by the flare itself.
4. The observed γ-ray spectrum of J0809+5341 is relatively flat and the optical-UV spectral shape is found to be steep. The flatness of the γ-ray spectrum can be reproduced by locating the emission region outside the BLR where both the BLR and torus energy densities are required to describe the observed γ-ray spectrum.

5. Many of the observed properties of J0809+5341 are at odds with that generally observed in other high redshift blazars.

3.4 3FGL J1256.1−0547 (3C 279)[6]

The quasar 3C 279 ($z = 0.536$; Lynds et al. 1965) is one of the first blazars found to be a γ-ray emitter by EGRET onboard the *Compton Gamma-Ray Observatory* (Hartman et al. 1992). This is also the first FSRQ detected in the VHE γ-ray band by the Major Atmospheric Gamma-ray Imaging Cherenkov (MAGIC) telescopes (MAGIC Collaboration et al. 2008). 3C 279 is known to show large amplitude variability over the entire electromagnetic spectrum (e.g., Hayashida et al. 2012). 3C 279 is hard X-ray bright and included in the 70 month *Swift*-BAT catalog (Baumgartner et al. 2013). At the radio wavelengths, it exhibits a compact core morphology and VLBA observations have revealed superluminal patterns with apparent speed of ∼21.6c (Lister et al. 2013). Moreover, the bulk Lorentz factor and viewing angle of the jet flow, estimated from the radio studies, are found as $\Gamma_{\rm j} = 15.5 \pm 2.5$ and $\Theta_{\rm j} = 2^{\circ}.1 \pm 1^{\circ}.1$ (Jorstad et al. 2004, 2005).

3C 279 is being continuously monitored by *Fermi*-LAT since 2008 and it was a subject of various multi-wavelength campaigns (e.g., Hayashida et al. 2012). This source is an active γ-ray emitter and multiple episodes of γ-ray outbursts have been detected (see Figure 3.14). In particular, two prominent flares of similar intensity ($\sim 1.2 \times 10^{-5}$ ph cm^{-2} s^{-1}) have been detected by *Fermi*-LAT in 2013 December and 2014 April. Furthermore, in 2015 June also 3C 279 displayed an exceptionally high activity state with the measurement of the highest γ-ray flux ever recorded from the source. For 2014 April and 2015 June flares, target of opportunity (ToO) observations were approved in which *Fermi* observed 3C 279 in a special pointing mode other than its regular sky scanning mode operation. The available multi-frequency data covering various flaring states of 3C 279 have been used in this thesis to study a variety of radiative processes operating in the jet of 3C 279.

The weekly binned γ-ray light curve of 3C 279, covering the period since the launch of *Fermi*-LAT, is presented in Figure 3.14. As can be seen, multiple episodes of

---

[6] The results presented for 3C 279 are published in Paliya et al. (2015b), Paliya (2015a), and Paliya et al. (2016).

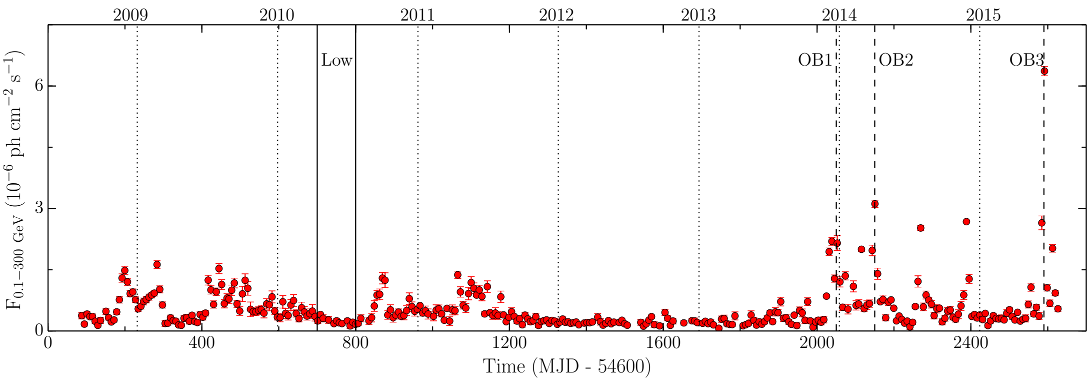

FIGURE 3.14: Gamma-ray flux history of 3C 279, since the launch of *Fermi* satellite. Three γ-ray outbursts, OB1, OB2, and OB3 are shown by dashed lines centered at the peak of the flare, whereas, a seperate low activity period 'Low' is represented by solid lines. Dotted lines correspond to the beginning of the new years.

γ-ray flares have been detected by *Fermi*-LAT. Three outbursts are then selected for further study and they are quoted as OB1, OB2, and OB3. The selection of these flares is based on the availability of the multi-band data. Moreover, a separate low activity state has also been chosen for comparison and is annotated by 'Low' in Figure 3.14. An exhaustive study of all these activity phases has been performed to understand the underlying physical mechanisms responsible for the observed flux variations.

3.4.1 2013 December γ-ray Outburst (OB1)

Multi-band temporal variability:

The period 2013 December 14 to 2014 January 3 (MJD 56640−56660) is selected to study the giant γ-ray outburst in detail. The multi-band light curves for OB1 are shown in Figure 3.15. In this plot, LAT data points are one day binned and the observations at other frequencies correspond to one point per observation. For further deep understanding, the high activity period is divided into three sub-periods; Low activity (MJD 56640−56646), Flare 1 (MJD 56646−56649), and Flare 2 (MJD 56649−56660). The availability of contemporaneous observations in all the energy bands are also taken into account while selecting these sub-periods. It is not possible to study the behavior of 3C 279 in X-rays at the peak of the γ-ray flare due to lack of the observations. However, because of the dense monitoring from *Swift*-XRT during Flare 2, a bright X-ray flare is seen. As cane be seen,

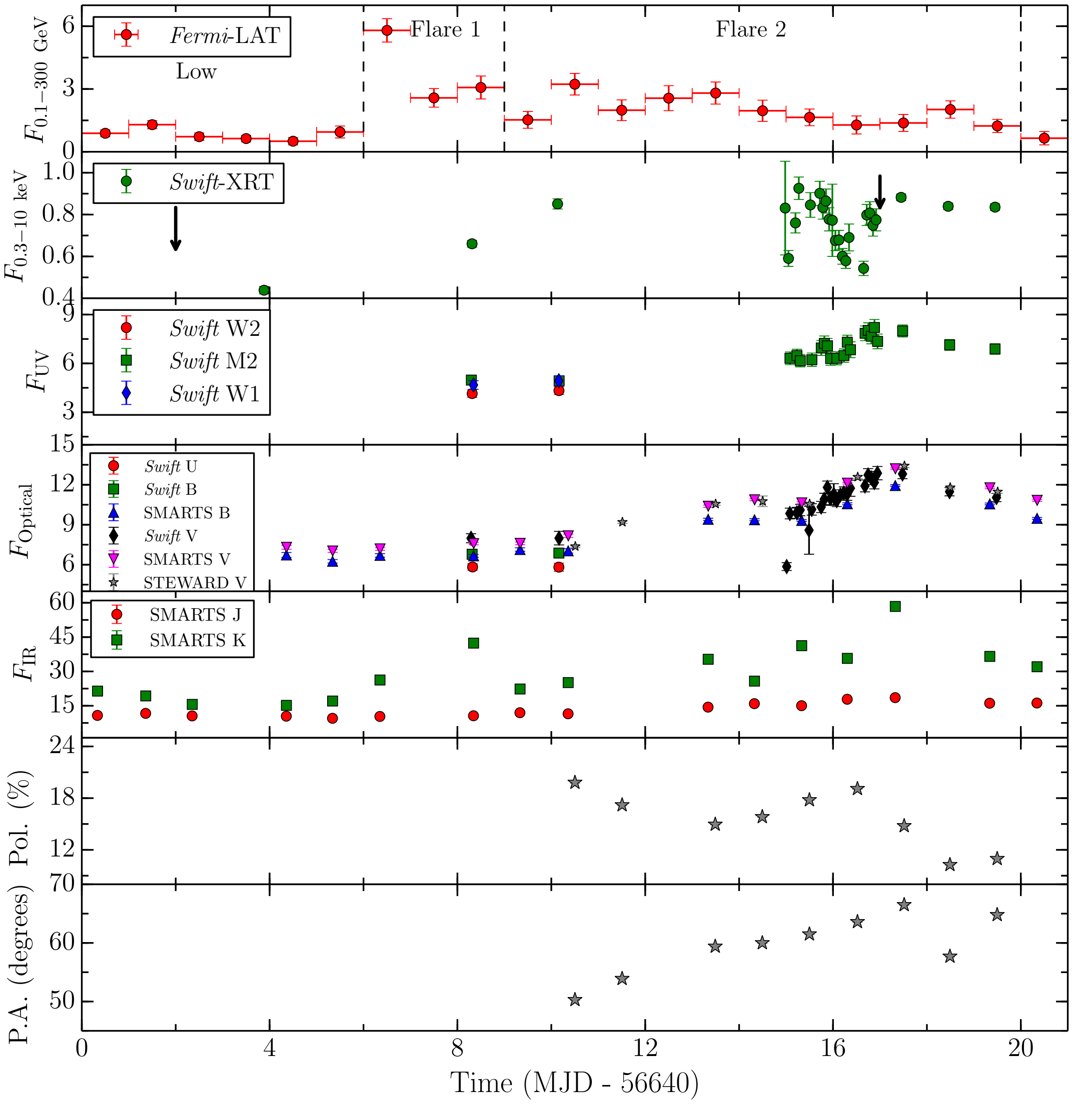

FIGURE 3.15: Multi-frequency temporal behavior of 3C 279 covering the period of high activity in 2013 December. *Fermi*-LAT and *Swift*-XRT data points are in units of 10^{-6} ph cm^{-2} s^{-1} and counts s^{-1}, respectively. UV, optical and IR fluxes have units of 10^{-12} erg cm^{-2} s^{-1}. Black downward arrows in the second panel from the top coprrespond to the *NuSTAR* monitoring epochs.

optical-UV observations seem to show a slow variations, irrespective of the γ-ray flaring activity, and reaches maximum during Flare 2 period. Such uncorrelated variability behavior is difficult to explain on the basis of commonly accepted one zone leptonic emission scenario. Optical polarization and angle of polarization also do not seem to show any correlation/anti-correlation with γ-rays.

The short timescale variability is searched by generating light curves using finer time bins of 12 hr, 6 hr, and 3 hr (see Figure 3.16). The shortest variability is searched by scanning these light curves using the following equation

$$F(t) = F(t_0).2^{(t-t_0)/\tau}, \tag{3.4}$$

where $F(t_0)$ and $F(t)$ are the fluxes at time t_0 and t, respectively, and τ is the characteristic flux doubling/halving timescale. A condition that the difference in flux at the epochs t and t_0 is at least significant at 3σ level, is also met (Foschini et al. 2011). The shortest γ-ray flux doubling time derived is 3.04 ± 0.77 hr with $\sim5\sigma$ significance. Further, analyzing the data using the bins defined as good time intervals (GTI) resulted in the highest γ-ray flux of $(1.22 \pm 0.25) \times 10^{-5}$ ph $\mathrm{cm^{-2}\,s^{-1}}$ and the associated photon index is found to be hard and having a value of 1.70 ± 0.13. The obtained spectral shape is the hardest ever observed from 3C 279 and this suggests that at the peak of the γ-ray flare, it was a probable candidate to detect VHE emission. The hardness ratio (HR) is also calculated with the following definition

$$\mathrm{HR} = \frac{F_{\mathrm{H}} - F_{\mathrm{S}}}{F_{\mathrm{H}} + F_{\mathrm{S}}}, \tag{3.5}$$

where F_{S} and F_{H} are 6 hr binned γ-ray fluxes in 0.1−1 GeV and 1−300 GeV energy ranges, respectively. The temporal evolution of HR is presented in the bottom panel of Figure 3.16 and clearly the HR has the highest value at the peak of the flare.

Swift has performed 22 observations of 3C 279 on 2013 December 30 and 31 (MJD 56656 and 56657). Such a dense monitoring has revealed a fast varying bright X-ray flare (see Figure 3.15). The shortest X-ray flux doubling time, estimated using Equation (3.4), is 2.89 ± 0.67 hr measured on MJD 56656 with $\sim4\sigma$ confidence. Interestingly, this fast X-ray flare is not associated with any γ-ray flaring event, as can be seen in Figure 3.15. This is probably the first report of hr scale X-ray variability measured from 3C 279. In the energy range of 0.3−10 keV, the highest X-ray flux is measured on MJD 56655 and having a value of $3.92^{+0.49}_{-0.44} \times 10^{-11}$ erg $\mathrm{cm^{-2}\,s^{-1}}$ and the associated photon index is $1.50^{+0.17}_{-0.16}$. This implies an isotropic X-ray luminosity of $\sim3.6 \times 10^{46}$ $\mathrm{erg\,s^{-1}}$.

Gamma-ray Spectral Analysis:

The γ-ray spectra are generated for all the three periods, namely Low activity, Flare 1, and Flare 2. Two spectral models: power law and log parabola are used to fit the spectra (see Section 3.2.2). The parameters of the model fitting to the

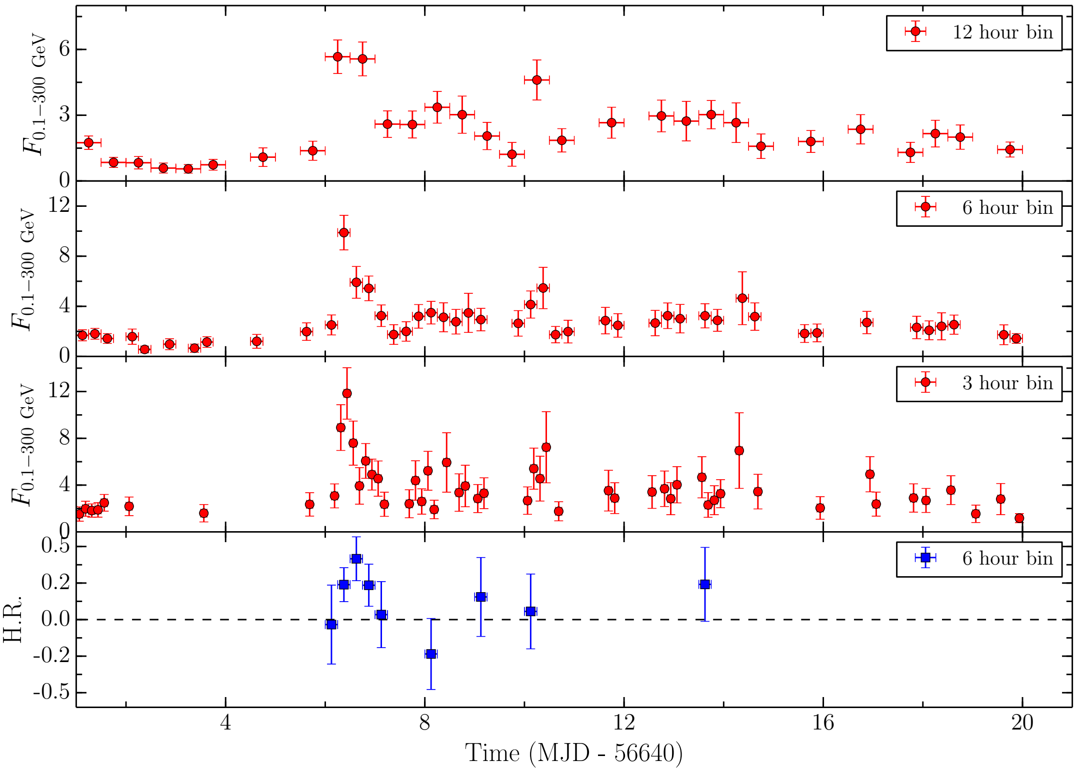

FIGURE 3.16: *Fermi*-LAT light curve of 3C 279 around the period of high activity in 2013 December. The adopted binning sizes are 12 hr, 6 hr, and 3 hr. The bottom panel represents the variation of the hardness ratio (see Equation 3.5) for 6 hr binned data, as a function of time.

TABLE 3.10: Results of the model fitting to the γ-ray spectra of 3C 279, covering 2013 December γ-ray outburst.

Period [1]	Activity [2]	Model [3]	$F_{0.1-300\ \mathrm{GeV}}$ [4]	$\Gamma_{0.1-300\ \mathrm{GeV}}/\alpha$ [5]	β [6]	TS [7]	$\mathrm{TS_{curve}}$ [8]
56640−56645	Low activity	PL	0.84 ± 0.08	2.48 ± 0.09		403.06	
		LP	0.81 ± 0.08	2.38 ± 0.12	0.09 ± 0.08	403.13	1.47
56645−56649	Flare 1	PL	3.76 ± 0.30	1.95 ± 0.05		1245.89	
		LP	3.30 ± 0.33	1.70 ± 0.12	0.09 ± 0.04	1272.25	6.46
56649−56660	Flare 2	PL	1.90 ± 0.14	2.28 ± 0.06		991.19	
		LP	1.79 ± 0.15	2.15 ± 0.10	0.07 ± 0.04	994.27	3.20

Notes. Col.[1]: period of observation (MJD); Col.[2]: activity state; Col.[3]: model used (PL: power law, LP: log parabola); Col.[4]: integrated γ-ray flux (0.1−300 GeV), in units of 10^{-6} ph $\mathrm{cm^{-2}\,s^{-1}}$; Col.[5] and [6]: spectral parameters; Col.[7]: test statistic; and Col.[8]: $\mathrm{TS_{curve}}$.

γ-ray SEDs are presented in Table 3.10 and the results are shown in the left panel of Figure 3.17. As can be seen, no statistically significant curvature is found. At the peak of the γ-ray flare, the derived γ-ray spectral shape is extremely hard and can be well explained by a power law model.

Spectral Energy Distribution and Modeling:

The broadband SEDs of 3C 279 are generated for three sub-periods and shown

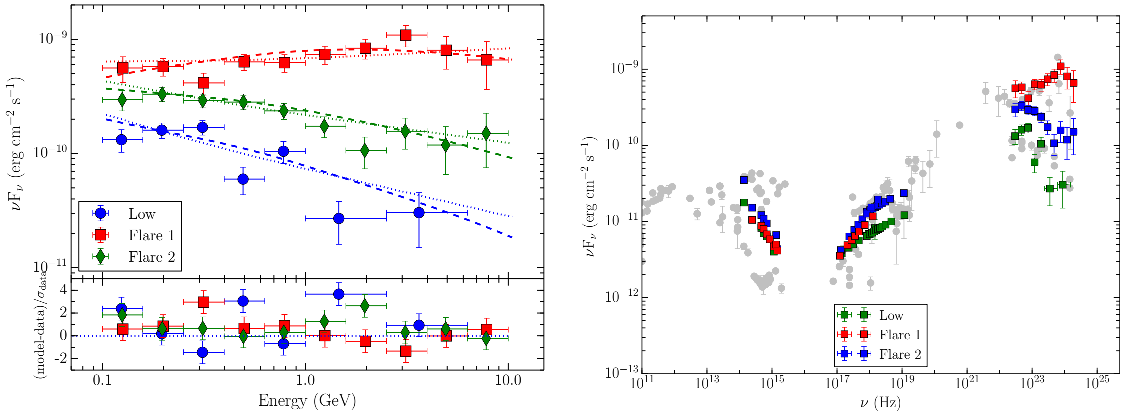

FIGURE 3.17: Left:*Fermi*-LAT SEDs of 3C 279 covering various activity states of 2013 December outburst. Power law and log parabola models are shown with dotted and dashed lines, respectively. Horizontal error bars correspond to the energy range of each bin, whereas, vertical bars represent 1σ statistical error. The residuals in the lower panel refer to the power law model. Right: Broadband SEDs of 3C 279 during different activity states. The green data points represent the SED for the low activity state, whereas, red and blue points show Flare 1 and Flare 2 periods. Silver gray points represent the archival observations.

in the right panel of Figure 3.17. As discussed earlier, the observed uncorrelated variability behavior indicates that a one zone leptonic model may not be able to explain the observed SEDs. Moreover, in one zone leptonic emission modeling, the spectral shape of the synchrotron spectrum reflects the underlying electron energy distribution, which in turn, determines the shape of the high energy γ-ray emission (produced by IC mechanism). This is because, the same population of electrons are responsible for emitting both the radiations. In such a scenario, a declining optical spectrum suggests the γ-ray spectrum to be falling. However, a rising γ-ray spectrum is seen (Figure 3.17), which is difficult to explain in the light of above mentioned hypothesis, since the observed optical spectrum during the flare is falling. This finding also hints that the assumption of single zone leptonic emission to explain the observed phenomena may not be correct. Therefore, these peculiar observations are reproduced by adopting a two-zone leptonic radiation emission scenario.

In two-zone methodology, emission from a large region dominates at IR to X-rays with little or negligible contribution in the γ-ray band, whereas, a small fast moving emission region explains predominantly the γ-ray spectrum. The relatively slow flux variations seen in the IR to X-ray energy bands support their origin from a large emission region. On the other hand, a fast γ-ray flare could be originated from a smaller emitting region. This approach is similar to that

Table 3.11: The SED model parameters obtained by adopting two-zone leptonic emission scenario, to explain 2013 December flare of 3C 279.

Activity	Location	$R_{\rm size}$	Γ	B	$\gamma_{\rm b}$	p	q	$U'_{\rm e}$	$P_{\rm e}$	$P_{\rm p}$	$P_{\rm B}$	$P_{\rm r}$
Low	Blob1 inside BLR	10	9	2.9	579	1.9	5.2	0.27	44.26	46.61	44.35	44.87
Flare 1	Blob1 inside BLR	10	9	2.0	685	1.9	5.2	0.36	44.41	46.76	44.06	44.97
	Blob2 inside BLR	5	40	0.55	1139	1.6	4.8	0.003	43.15	45.02	43.77	44.84
	Blob2 outside BLR	5	45	0.20	3140	1.6	4.8	0.006	43.57	45.26	43.02	44.97
Flare 2	Blob1 inside BLR	10	9	2.9	514	1.6	5.2	0.21	44.22	46.24	44.42	45.05
	Blob2 inside BLR	5	30	0.25	3053	1.6	4.8	0.002	42.54	44.23	42.72	44.00
	Blob2 outside BLR	5	30	0.12	4407	1.6	4.8	0.005	42.98	44.61	42.08	43.90

Notes. Blob1 and blob2 correspond to the large and small emission regions, respectively. The parameters are as follows. $R_{\rm size}$: size of the emission region in 10^{15} cm, Γ: bulk Lorentz factor, B: magnetic field (Gauss), $\gamma_{\rm b}$: the break Lorentz factor , p and q: the slopes of the underlying broken power law electron energy distribution, $U'_{\rm e}$: particle energy density in comoving frame (erg cm^{-3}). The last four columns report the jet power in electrons, protons (assumed to be cold and having equal electron number density), magnetic field, and in radiation, in logarithmic scale. The black hole mass and the accretions disk luminosity are taken as $3 \times 10^8\ M_\odot$ and 2×10^{45} erg s^{-1}, respectively. Viewing angle and characteristic temperature of the IR torus are taken as 1° and 1000 K, respectively. The minimum Lorentz factor of the emitting electrons is taken as unity.

adopted by Tavecchio et al. (2011) to reproduce very fast VHE variations and a hard GeV spectrum observed from FSRQ PKS 1222+216. During the 2013 December flare, though the γ-ray spectrum is hard, VHE monitoring of 3C 279 from the ground based Cherenkov telescopes was not possible due to full moon period. Therefore, unlike PKS 1222+216, the location of the γ-ray emitting region could not be identified. This is due to the fact that the intense optical-UV radiation field of the BLR completely absorbs the VHE radiation. Keeping this in mind, the results according to both inside and outside BLR location of the fast moving small emission region are presented. It should be noted that the precise measurement of the location of the emission region is not very important, since the comoving frame radiation fields of both BLR and IR-torus remain uniform, as long as the emission region is inside the respective components (Ghisellini & Tavecchio 2009). It is also assumed that both emission regions do not interact with each other (see, e.g., Tavecchio et al. 2011). The size of the large emission region is adopted by assuming it to cover the entire jet cross-section with jet semi opening angle of 0.1 rad. The size of the small emission region is derived from the observed fastest γ-ray variability.

The modeling is first performed on the low activity state SED where a single zone approximation successfully reproduces the observations. This is used to constrain the physical parameters associated with the large emission region. Further, to explain both Flare 1 and Flare 2 SED, a two-zone modeling approach is used following the above mentioned procedure. The resultant SEDs along with the

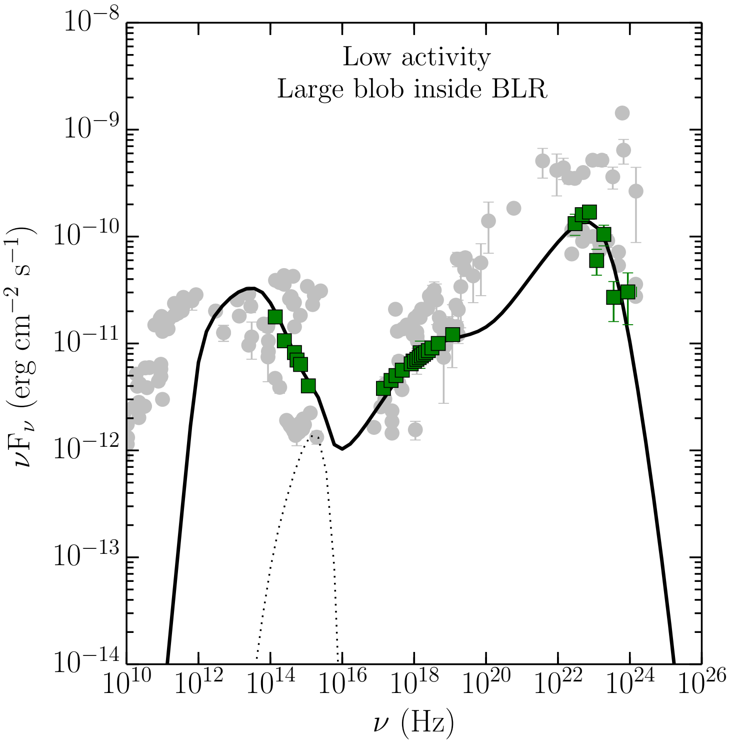

FIGURE 3.18: Broadband SED of low activity period selected from the 2013 December flare of 3C 279. Black dotted line represnts the thermal radiation from the accretion disk, whereas, solid line is the total radiation predicted by the model. As can be seen, a single-zone leptonic emission model successfully reproduces the observations.

models are shown in Figure 3.18 and 3.19. The parameters associated with the modeling are provided in Table 3.11.

In the two zone modeling approach, there is a freedom in choosing the set of parameters due to large number of inputs, however, choice of the parameters is not completely arbitrary and is driven by the following constraints.

Large emission region– The observed optical-UV SED is primarily emitted by the large region and this not only constrains the shape of the electron energy distribution but also the peak of the synchrotron emission, which in turn controls the IC peak location. The parameters of the IC mechanism are further determined by the observed X-ray and γ-ray spectra. Since the contribution of the large region to the observed X-ray flux is significantly higher than that by the small emission region, together with its negligible contribution to the observed MeV-GeV spectrum, both the Doppler factor and the magnetic field are constrained. The large emission region is assumed to be located inside BLR, which is generally the case for FSRQs (Ghisellini et al. 2010a).

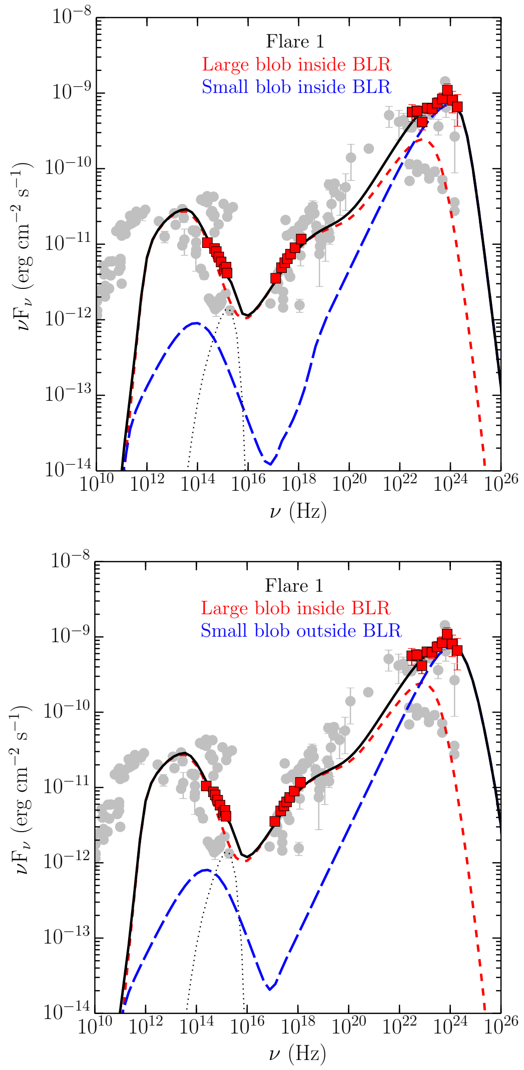

FIGURE 3.19: Two zone leptonic emission modeling of 2013 December flare of 3C 279. Modeling of the Flare 1 is shown in left column, and for Flare 2, in the right column. Symbols have the meaning same as in the right panel of Figure 3.17. Red dashed line represents the total radiation from the large emission region, whereas blue long dahsed line corresponds to that from the small emission region. Solid black line is the sum of all the radiations.

Small emission region– It is assumed to emit primarily at γ-ray energies and its contributions at optical-UV and X-rays are negligible. The magnetic field ($0.1-1$ G) and the Doppler factor ($\delta \gtrsim 50$) values are obtained by noting that the SSC component should lie below the observed X-ray flux. Finally, the electron energy density (and magnetic field also) is determined by the observed γ-ray flux and from the condition that the synchrotron emission lies below the detected optical-UV flux. As discussed earlier, the location of the emission region could not be determined due to lack of VHE observations. As can be seen in Figure 3.19, the

γ-ray spectrum falls sharply for the case of inside BLR scenario, due to Klein-Nishina effect. However, if lying outside BLR, the model predict significant VHE radiation. Remaining parameters, associated with both large and small emission regions, are adopted from the values typically inferred in FSRQs (e.g., Ghisellini et al. 2010a).

3.4.2 2014 April γ-ray Outburst (OB2)

Multi-band temporal variability:

The broadband light curves covering OB2 are shown in Figure 3.20. In this plot, *Fermi*-LAT data points are one day binned, whereas the observations in other wavebands are one point per observation. The period of high activity is further divided into three sub-periods; Flare 1 (MJD 56741−56749), Flare 2 (MJD 56749−56755), and post−flare (MJD 56755−56760). Like 2013 December flare, these sub-periods are selected taking into account the availability of near simultaneous observations in other energy bands. From low-cadence multi-band light curves, the flux variations at different frequencies appear to be correlated. This supports the single-zone origin of the radiation that are emitted by same population of electrons.

The variability amplitude of 3C 279 at various wavelengths is calculated using the fractional rms variability amplitude parameter $F_{\rm var}$ (e.g., Vaughan et al. 2003). It is calculated as follows

$$F_{\rm var} = \frac{(S_v^2 - \Delta^2)^{1/2}}{\langle r \rangle}, \tag{3.6}$$

where S_v^2 is the sample variance, $\langle r \rangle$ is the unweighted mean count rate, and Δ^2 is the mean square value of the uncertainties associated with each individual observation. The error in $F_{\rm var}$ is calculated following Vaughan et al. (2003):

$$\sigma_{F_{\rm var}} = \sqrt{\left(\sqrt{\frac{1}{2N}} \cdot \frac{\Delta^2}{\langle r \rangle^2 F_{\rm var}}\right)^2 + \left(\sqrt{\frac{\Delta^2}{N}} \cdot \frac{1}{\langle r \rangle}\right)^2} \tag{3.7}$$

where N is the number of data points. The resultant $F_{\rm var}$ values are quoted in Table 3.12. The maximum $F_{\rm var}$ is found for the γ-ray band and it decreases with energy (see Table 3.12), a trend generally found in blazars (e.g., Zhang et al. 2005; Vercellone et al. 2010). The unusual high K-band $F_{\rm var}$ could be due to the

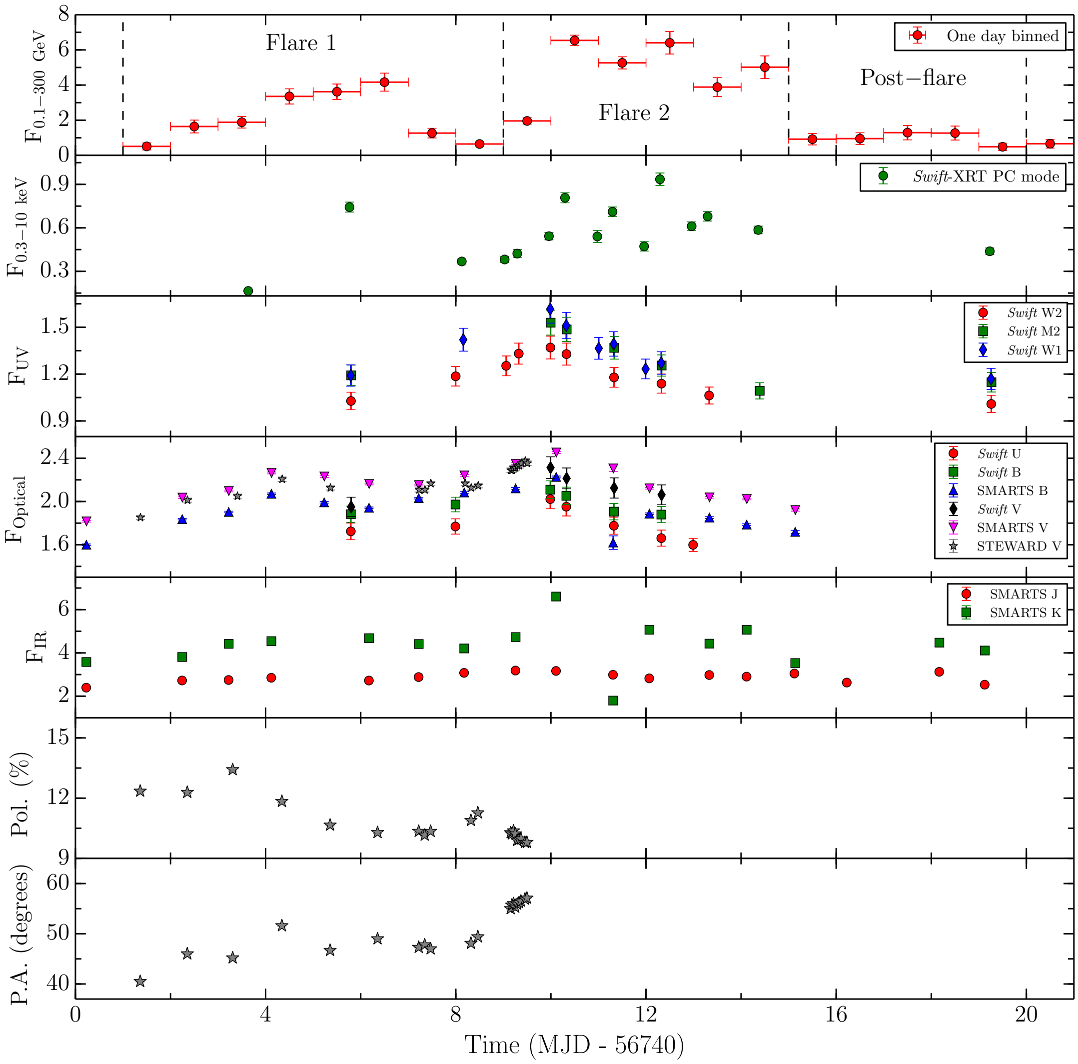

Figure 3.20: Multi-frequency light curves of 3C 279 covering the period of high activity in 2014 April. *Fermi*-LAT and *Swift*-XRT data points are in units of 10^{-6} ph cm^{-2} s^{-1} and counts s^{-1}, respectively. UV, optical and IR fluxes have units of 10^{-11} erg cm^{-2} s^{-1}.

presence of two adjacent points where flux is varying abruptly (MJD 56750 and 56751). Such abrupt flux variations are possibly due to bad weather conditions present during the observing run (SMARTS team 2015, private communication).

The good γ-ray photon statistics during this outburst permitted to search for short timescale variability by generating fine time binned light curves. The selected time bins are 12, 6, and 3 hr and the result of this analysis are shown in Figure 3.21. In this plot, the black data points refer to the observations taken during the pointed mode observations from *Fermi*-LAT (ToO monitoring). These light curves are then scanned to search for short time variability using Equation (3.4). The derived

TABLE 3.12: Fractional rms variability amplitude (F_{var}) values calculated for the light curves shown in Figure 3.20.

Energy band	F_{var}	Time period	Number of observations
K (SMARTS)	0.227 ± 0.001	56742−56760	15
J (SMARTS)	0.067 ± 0.002	56742−56760	16
V (Steward)	0.062 ± 0.002	56741−56749	20
V (SMARTS)	0.074 ± 0.001	56742−56760	16
V (UVOT)	0.083 ± 0.020	56745−56760	6
B (SMARTS)	0.089 ± 0.002	56742−56760	16
B (UVOT)	0.072 ± 0.016	56745−56760	7
U (UVOT)	0.081 ± 0.016	56745−56760	8
$UVW1$	0.097 ± 0.020	56745−56760	9
$UVM2$	0.119 ± 0.021	56745−56760	7
$UVW2$	0.096 ± 0.018	56745−56760	10
X-ray (0.3−10 keV)	0.347 ± 0.014	56743−56760	15
γ-ray (0.1−300 GeV)	0.739 ± 0.034	56741−56760	19

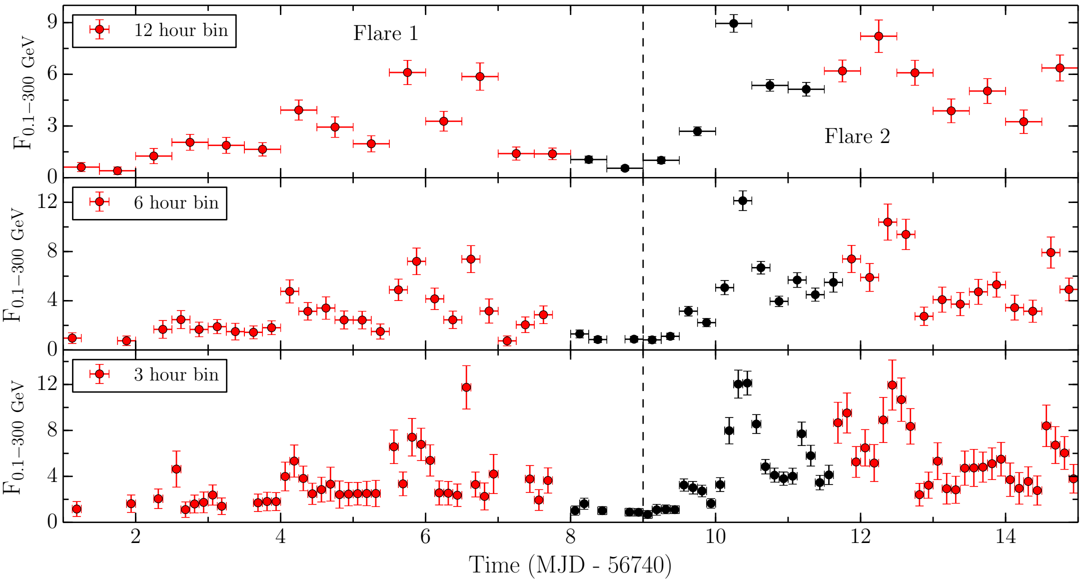

FIGURE 3.21: *Fermi*-LAT light curve of 3C 279, covering the 2014 April outburst, binned in the interval of 12, 6, and 3 hr (upper, middle, and lower panel, respectively). Black data points represent *Fermi* ToO observations. The fluxes are in units of 10^{-6} ph cm^{-2} s^{-1}.

results are presented in Table 3.13. The shortest flux doubling time recorded is 1.19 ± 0.36 hr. The data are also analyzed using the time bins defined as GTI. The shortest flux doubling time, using GTI binning, is obtained as 1.27 ± 0.36 hr on MJD 56746, with $\sim 4\sigma$ significance. This is the first detection of hr scale γ-ray variability detected from 3C 279 since the launch of *Fermi* and similar to that seen during its 1996 outburst (Wehrle et al. 1998). The highest one day binned γ-ray flux measured is $(6.54 \pm 0.30) \times 10^{-6}$ ph cm^{-2} s^{-1} in the bin centered at MJD 56750.5. The corresponding photon index is soft and has a value of 2.22 ±

TABLE 3.13: Summary of the search for the shortest timescale of variability using 3 hr binned γ-ray light curve for 2014 April γ-ray flaring event.

t	t_0	$F(t)$	$F(t_0)$	$\lvert\tau\rvert$	Signif.	R/D
56746.4376	56746.5626	1.91 ± 0.94	10.95 ± 1.92	1.19 ± 0.36	4.225	R
56746.5626	56746.6876	10.95 ± 1.92	2.94 ± 1.12	1.58 ± 0.51	3.599	D
56749.4376	56749.5626	1.03 ± 0.37	3.33 ± 0.57	1.78 ± 0.60	3.400	R
56750.0626	56750.1876	3.29 ± 0.65	7.57 ± 1.16	2.49 ± 0.75	3.219	R
56750.5626	56750.6876	8.34 ± 0.85	4.50 ± 6.26	3.37 ± 0.94	3.636	D

Notes. Times t and t_0 are in MJD; fluxes are in units of 10^{-6} ph cm^{-2} s^{-1}; the absolute values of the observed characteristic timescale $\lvert\tau\rvert$ are in hours; the significance of the flux differences is in σ; and R and D denote the rise or decay time.

0.04. The peak flux and the associated photon index, from the 3 hr binned γ-ray light curve, are found to be $(1.21 \pm 0.10) \times 10^{-5}$ ph cm^{-2} s^{-1} and 2.19 ± 0.09, respectively, again on the same day, i.e., MJD 56750 (Figure 3.21).

The high temporal resolution γ-ray light curves generated during the flaring period reveal the existence of various shorter timescale flaring events (see Figure 3.21). This suggests the possible existence of multiple sub-structures, emitting primarily in γ-rays, inside a larger region responsible for the observed broadband radiation. Further, two major flares are observed in 12 hr binned γ-ray light curve, (one before MJD 56746 and other after 12 hr, see Figure 3.21). Interestingly, the former appears to be resolved in 6 and 3 hr bins, whereas the latter is non-resolvable down to 3 hrs. Further, to understand the nature of the flares that detected during *Fermi* ToO observations (where the data are having better signal-to-noise than other periods), a flare profile fitting method is adopted (see, e.g., Abdo et al. 2010b). The results of the fitting of three selected flares (F1, F2, and F3) are shown in Figure 3.22 and the parameters of the fitting are provided in Table 3.14. A reliable set of parameters could not be obtained for third flare (F3). However, first two flares display a trend of fast rise and slow decay that can be interpreted as a result of particle acceleration process. A fast rise of the flare could be due to the fast injection of the accelerated electrons at the shock front, and the slow decay can be attributed to the weakening of the shock.

Optical polarization observations indicate its anti-correlated behavior with respect to the γ-ray flux variations (Figure 3.20). During Flare 1 period, an enhancement in the γ-ray flux is followed by a decrease in the optical polarization. At the same time, pattern of the variation of the polarization angle is similar to that seen in the γ-rays. Similar features were observed from 3C 279 during its 2009 flare (Abdo

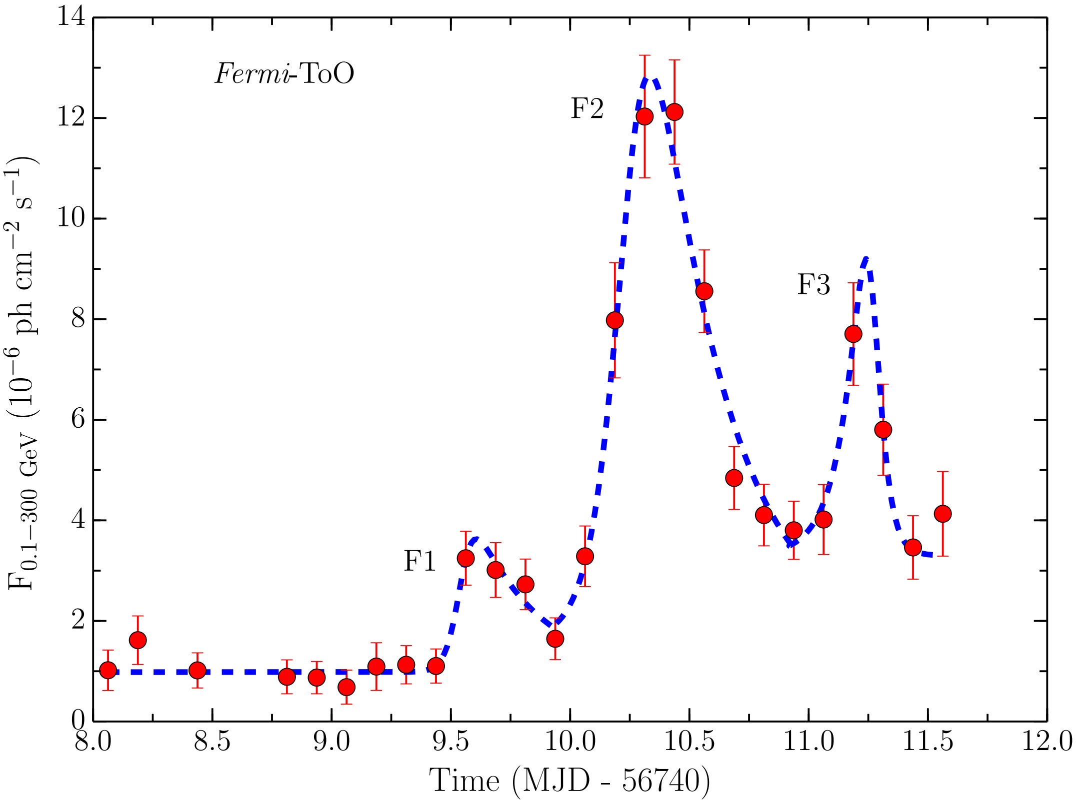

FIGURE 3.22: Three hour binned γ-ray light curve of 3C 279 using the data taken during ToO observations. Dashed blue line represent the best-fit temporal profile.

et al. 2010a). Interestingly, though the amplitude of the γ-ray flux enhancement is much higher in 2014 April than that seen during the 2009 flare, the change in the optical polarization and polarization angle is relatively smaller. One of the possibility could be that the γ-ray flare may be associated with the change in the optical polarization, not to a single coherent event but due to the superposition of multiple shorter duration events. In such a scenario, the overall polarization gets averaged out, irrespective of the γ-ray flux enhancement, resulting in lesser degree of change in polarization. This is supported by the short duration flares observed in the 3 hr binned γ-ray light curve. Alternatively, as discussed below, the primary cause of the flare is found to be sudden increase in the bulk acceleration of the jet, which may not be directly related to the optical polarization. Hence, though there is significant change in the γ-ray flux level, it is not reflected in the polarization observations.

The shortest 0.3$-$10 keV X-ray flux doubling time, calculated using Equation (3.4), is 8.11 ± 0.98 hr measured on MJD 56752 ($\sim 9\sigma$ confidence). Interestingly, this

TABLE 3.14: Flare characteristics obtained by fitting the three flares seen during the 2014 April *Fermi* ToO monitoring (Figure 3.22).

Name	F_c	F_p	t_p	T_r	T_f	χ^2_r
F1	0.98 ± 0.13	3.73 ± 1.41	56749.55 ± 0.04	0.033 ± 0.026	0.268 ± 0.153	0.47
F2	1.61 ± 0.70	18.78 ± 2.56	56750.25 ± 0.04	0.078 ± 0.026	0.295 ± 0.062	1.71
F3	3.30 ± 0.24	10.93 ± 6.17	56751.26 ± 0.09	0.085 ± 0.042	0.038 ± 0.073	0.75

Notes. Errors are estimated at 1σ level. Fluxes F_c and F_p are in 10^{-6} ph cm^{-2} s^{-1}, t_p is in units of MJD, and T_r and T_f are in days.

TABLE 3.15: Results of the model fitting to the γ-ray spectra of 3C 279 for various activity states of 2014 April flare.

Period [1]	Activity [2]	Model [3]	$F_{0.1-300\ \mathrm{GeV}}$ [4]	$\Gamma_{0.1-300\ \mathrm{GeV}}/\alpha$ [5]	β [6]	TS [7]	TS$_{\mathrm{curve}}$ [8]
55,300−55,400	Low activity	PL	0.16 ± 0.02	2.48 ± 0.08		315.61	
		LP	0.15 ± 0.02	2.42 ± 0.13	0.04 ± 0.06	315.50	0.01
56,741−56,749	Flare 1	PL	1.64 ± 0.10	2.15 ± 0.05		1276.40	
		LP	1.53 ± 0.10	1.96 ± 0.09	0.10 ± 0.04	1286.53	7.74
56,749−56,755	Flare 2	PL	4.47 ± 0.15	2.23 ± 0.03		4445.66	
		LP	4.24 ± 0.15	2.05 ± 0.05	0.13 ± 0.03	4463.94	29.96
56,755−56,760	Post−flare	PL	0.95 ± 0.16	2.20 ± 0.11		204.39	
		LP	0.83 ± 0.17	1.93 ± 0.23	0.13 ± 0.10	206.04	2.31

Notes. Col.[1]: period of observation (MJD); Col.[2]: activity state; Col.[3]: model used (PL: power law, LP: log-parabola); Col.[4]: γ-ray flux in 0.1−300 GeV energy range, in units of 10^{-6} ph cm^{-2} s^{-1}; Col.[5] and [6]: spectral parameters; Col.[7]: test statistic; and Col.[8]: TS$_{\mathrm{curve}}$.

coincides with a γ-ray flaring event (see Figure 3.21). The derived highest X-ray flux is $4.54^{+0.62}_{-0.49} \times 10^{-11}$ erg cm^{-2} s^{-1} measured on MJD 56752 and the associated photon index is $1.31^{+0.12}_{-0.13}$. This, in turn, corresponds to an isotropic X-ray luminosity of 3.82×10^{46} erg s^{-1}.

Gamma-ray Spectral Analysis:

Similar to 2013 December outburst analysis, the γ-ray spectra are generated for all the four periods, namely Flare 1, Flare 2, post−flare, and a low activity state. The low activity state considered here is same as shown in Figure 3.14. The resultant γ-ray SEDs are presented in Figure 3.23 and the associated fitting parameters are provided in Table 3.15. A statistically significant curvature is noticed during the Flare 2 with TS$_{\mathrm{curve}}$ $\approx$30. There is also a hint of the presence of curvature in the Flare 1 state, though at low significance (TS$_{\mathrm{curve}} \approx 8$).

Spectral Energy Distribution and Modeling:

The broadband SEDs of 3C 279 during a low activity period and three sub-periods covering the flaring event are generated and modeled using the prescription given in Section 2.2.

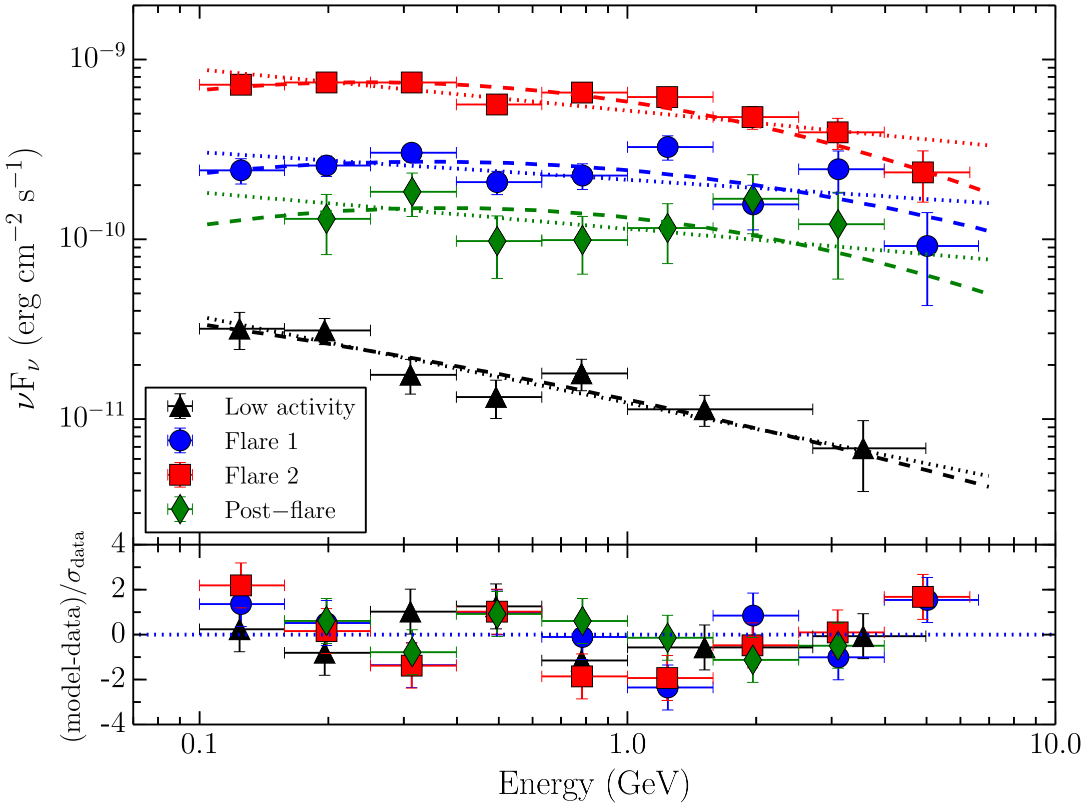

FIGURE 3.23: *Fermi*-LAT SEDs of 3C 279 generated for the various activity states of 2014 April flare. Other information are same as in the left panel of Figure 3.17.

A powerful diagnostic to determine the accretion disk luminosity and the black hole mass is through modeling of the optical−UV part of the SED by accretion disk spectrum (Ghisellini et al. 2010a), provided the optical−UV bump is visible. For the case of 3C 279, the optical−UV spectrum is dominated by non-thermal spectrum. However, there is a good probability that during the low activity states, the signature of the disk radiation could be observed, since non-thermal jetted emission would be less. Therefore, the modeling was started with the low activity state SED. As can be seen in the low activity state SED in Figure 3.24, the optical-UV spectrum shows a turnover at UV energies, though it is not very dominant. This excess could be due to the accretion disk radiation. A combination of synchrotron and the accretion disk radiation is then used to reproduce the observations. This resulted in a black hole mass and disk luminosity of 3 × 10^8 $M_\odot$ and 1 × 10^{45} erg s^{-1}, respectively. The obtained values are in agreement with that obtained in earlier studies using different methods (2 × 10^{45} erg s^{-1}, 3 × 10^8 $M_\odot$; Pian et al. 1999; Woo & Urry 2002). The modeling is performed over the flaring period SEDs using the derived accretion disk luminosity and the black

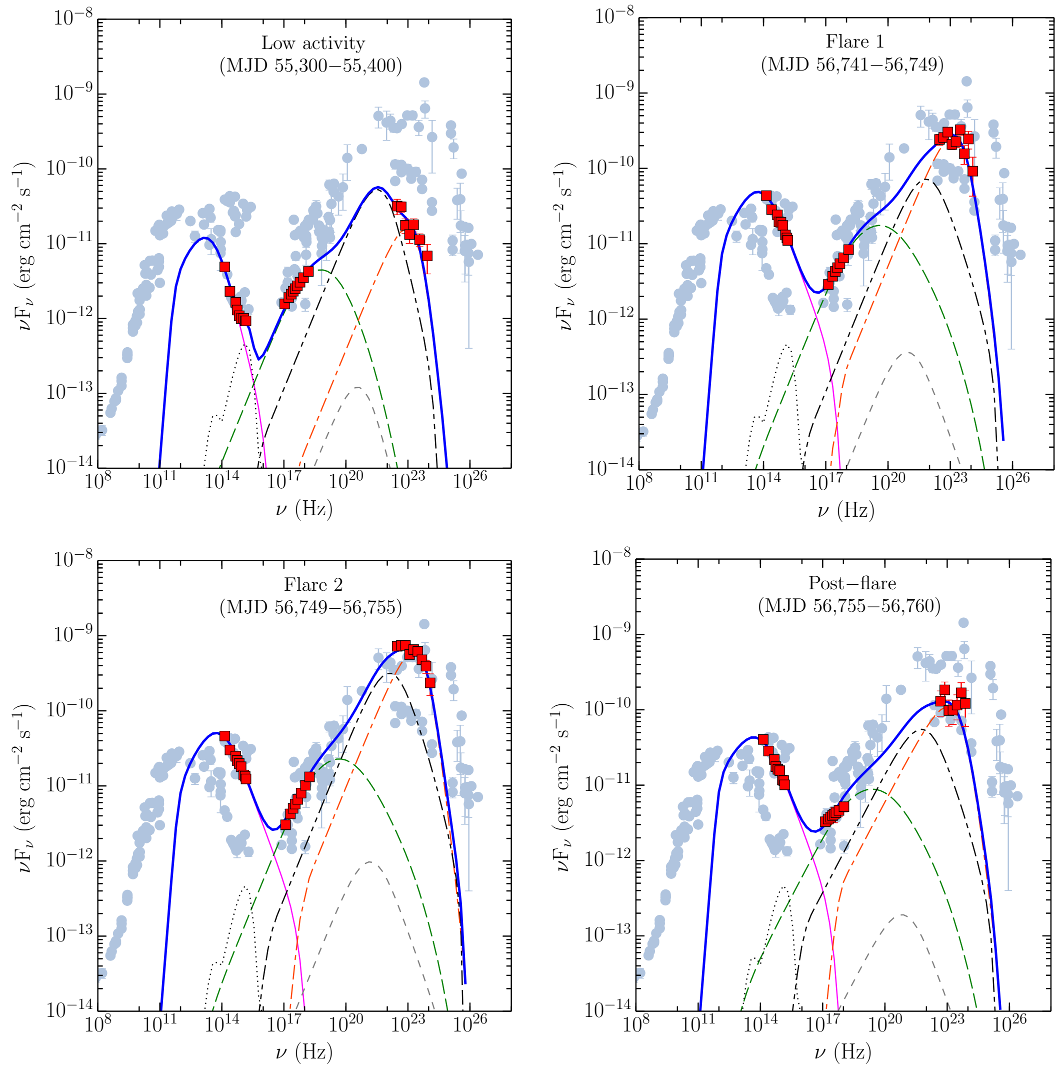

FIGURE 3.24: Spectral energy distributions of 3C 279 during low and high activity states seen during 2014 April flare. Simultaneous data from SMARTS, *Swift* and *Fermi*-LAT are shown with red squares, whereas, light blue circles belong to the archival observations. Black dotted line represents thermal contributions from the torus and the accretion disk. Pink thin solid and green dashed lines correspond to synchrotron and SSC emission, respectively. Grey dashed, red dash-dot, and black dash-dot-dot lines represent EC-disk, EC-BLR, and EC-torus components, respectively. Blue thick solid line is the sum of all the radiative mechanisms.

hole mass. The results are presented in Figure 3.24 and the associated modeling parameters are given in Table 3.16. As can be seen in Figure 3.24, a one zone leptonic emission model successfully explains the observed fluxes.

The size of the emission region, obtained from the SED modeling, is $\sim 1 \times 10^{16}$ cm. This corresponds to a variability time of ∼8 hours in the observer's frame, assuming a Doppler factor $\delta = 19$, obtained from the SED modeling. The derived variability time is quite similar to the shortest X-ray flux doubling timescale. Interestingly,

TABLE 3.16: Summary of the parameters used/derived from the modeling of the SED in Figure 3.24.

Parameter	Low activity	Flare 1	Flare 2	Post−flare
p	1.65	1.65	1.65	1.95
q	5.2	4.5	4.5	4.5
B	1.2	2.6	2.0	3.0
$U'_{\rm e}$	0.15	0.16	0.18	0.16
Γ	10	13	19	14
$\gamma'_{\rm b}$	647	689	758	687
$\gamma'_{\rm max}$	1e4	3e4	5e4	3e4
$R_{\rm diss}$	0.045 (1570)	0.034 (1190)	0.035 (1220)	0.036 (1270)
$P_{\rm e}$	44.44	44.45	44.85	44.57
$P_{\rm B}$	44.00	44.68	44.80	44.92
$P_{\rm r}$	44.86	45.63	46.42	45.49
$P_{\rm p}$	46.48	46.48	46.86	46.97

Notes. . Viewing angle is taken as 3° and the characteristic temperature of the torus as 800 K. For a disk luminosity of 1×10^{45} erg s^{-1} and black hole mass of 3×10^{8} $M_{\odot}$, the size of the BLR is 0.03 parsec (1029 $R_{\rm Sch}$). Other symbols have their usual meanings as given in Table 3.6.

the shortest γ-ray variability time is as short as ∼1 hr (see Table 3.13). This observation indicates for the existence of multiple γ-ray emitting sub-structures within a larger region responsible for the broadband flux enhancement. The detected fast γ-ray variations could originate from these smaller regions. This is also supported from the observations of the short time flaring events seen in the 3 hr binned γ-ray light curve (Figure 3.21). Finally, the SEDs are generated by averaging the fluxes over larger time intervals and therefore the results of the SED modeling should be considered as the representation of the average properties of 3C 279 during the various activity states considered here.

A comparison of the SEDs corresponding to the low and high activity phases reveals that during the flare the flux has substantially increased across the electromagnetic spectrum. However, if the SEDs corresponding to three sub-phases of the 2014 April flare are considered, the major flux enhancement is observed in the γ-ray band. Interestingly, lesser degree of flux variations are seen in the optical−UV and X-ray bands. This is also evident in the multi-frequency light curves (see Figure 3.20). As can be seen in Table 3.16, these changes are reproduced primarily by varying the bulk Lorentz factor, magnetic field, and particle energy density. There are few other minor changes, such as spectral indices of the electron energy distributions and the location of the emission region (and hence its size). These changes are necessary to explain the X-ray spectral variations, particularly the post−flare X-ray spectrum, which is quite softer than other two sub-phases. These modifications, though minor, lead to large variations in the total jet power because the break Lorentz factor $\gamma'_{\rm b}$ and the spectral index before $\gamma'_{\rm b}$, i.e., p, decide the total amount of electrons present in the emitting volume and thus the total number of cold protons (assuming equal number densities of electrons and protons). Interestingly, the derived jet power is maximum during the post−flare state rather than at the peak of the γ-ray flux.

The γ-ray spectral analysis has led to the detection of a significant curvature during Flare 2 (Figure 3.23 and Table 3.15). The observed curvature is reproduced by the Klein-Nishina mechanism and with a broken power law electron distribution. The BLR and torus energy densities are also adjusted in such a manner that the observed curvature can be explained by the superposition of the EC-BLR and EC-torus processes (see a similar approach in Cerruti et al. 2013). Since in the model the radiation energy densities are a function of the distance from the central engine, reproduction of the curvature in the γ-ray window of the SED can constrain the location of the emission region. A similar approach is adopted by Dermer et al. (2014), though they also consider equipartition between various photon fields, particle energy density, and magnetic field. Interestingly, both the studies (i.e., Cerruti et al. 2013; Dermer et al. 2014) concluded the location of the emission region to be at the outer edge of the BLR, akin to results obtained in this work. In the context of the above mentioned discussion, a curvature in the γ-ray spectrum also suggests a significant absorption of the VHE photons by the BLR radiation field. Since a curvature is observed during the Flare 2, the probability of detecting VHE events from 3C 279 during this period is quite low. In fact, preliminary results of the VERITAS observations taken during the Flare 2 also indicate the non-detection of VHE emission from 3C 279 (Errando 2014)[7]. The cut-off at GeV frequencies as hinted by the curved LAT spectrum, upper limits in the VERITAS observations, and the measured short timescale variability, therefore indicate the signature of the BLR on the observed features and thus, the emission region cannot be far outside from the BLR.

During the peak of the flare, *Swift* and SMARTS have monitored 3C 279 almost every day. Such a dense monitoring has allowed to study the time evolution of the flare by generating the SEDs using finer time bins. The one day averaged SEDs covering the duration of Flare 2 are shown in Figure 3.25 and the associated

---

[7] `http://files.aas.org/head14/106-11_Manel_Errando.pdf`

Table 3.17: Summary of the parameters used/derived from the modeling of the SED in Figure 3.25

Parameter	Day 1	Day 2	Day 3	Day 4	Day 5	Day 6
p	1.5	1.7	1.7	1.7	1.7	1.7
q	4.4	4.5	4.5	4.5	4.5	4.5
B	4.6	2.5	2.5	2.5	2.5	2.7
$U'_{\rm e}$	0.09	0.19	0.18	0.18	0.17	0.18
Γ	18	22	20	22	18	20
$\gamma'_{\rm b}$	336	637	634	637	635	526
γ'_{max}	3e4	3e4	3e4	3e4	3e4	3e4
$R_{\rm diss}$	0.034 (1170)	0.034 (1170)	0.034 (1170)	0.034 (1170)	0.034 (1180)	0.034 (1180)
$P_{\rm e}$	44.45	44.97	44.85	44.95	44.76	44.87
$P_{\rm B}$	45.44	45.08	45.00	45.09	44.92	45.08
$P_{\rm r}$	45.97	46.79	46.52	46.77	46.26	46.47
$P_{\rm p}$	46.43	47.07	46.96	47.05	46.86	47.00

Note. Symbols have the same meanings as in Table 3.6.

modeling parameters are given in Table 3.17. In comparison to the optical and X-rays, a greater degree of enhancement in the γ-ray flux is clearly visible. This difference could hint the possible change in the source parameters responsible for the flare, since the optical and X-rays are due to synchrotron and SSC processes, respectively, and γ-rays are due to EC mechanism. The synchrotron emissivity in the comoving frame can be taken as (e.g., Shu 1991)

$$j'_{\rm syn}(\epsilon') \approx \frac{\sigma_{\rm T}\, c\, B^2}{48\pi^2} \epsilon_L^{-\frac{3}{2}} N' \left(\sqrt{\frac{\epsilon'}{\epsilon_L}}\right) \epsilon'^{\frac{1}{2}} \tag{3.8}$$

where $\epsilon_L = (h\nu_L/mc^2)$ is the dimensionless energy corresponding to the Larmor frequency. The EC emissivity, on the other hand, can be approximated as (Dermer 1995; Sahayanathan & Godambe 2012)

$$j'_{\rm ec}(\epsilon') \approx \frac{c\, \sigma_{\rm T}\, u^\star}{8\pi\epsilon^\star} \left(\frac{\Gamma\epsilon'}{\epsilon^\star}\right)^{\frac{1}{2}} N' \left[\left(\frac{\epsilon'}{\Gamma\epsilon^\star}\right)^{\frac{1}{2}}\right] \tag{3.9}$$

where starred quantities are in the black hole frame. Comparing Equation (3.8) and (3.9) indicates that the excess in EC emissivity can be achieved by increasing the jet bulk Lorentz factor without altering the synchrotron emissivity. Moreover, synchrotron and SSC emissivities varies as a function of Γ, whereas EC goes as Γ^2. Therefore, enhancement in the bulk Lorentz factor will result in an additional boosting to the EC fluxes, other than synchrotron and SSC. To illustrate this, the variation of Γ, obtained from the SED modeling, along with the variation of X-ray and γ-ray fluxes is shown in Figure 3.26. As can be seen, the pattern of variability seen in X-rays and γ-rays is similar to that obtained in Γ, thus strengthening the proposed idea of sudden acceleration of the jet as a primary cause of the flare.

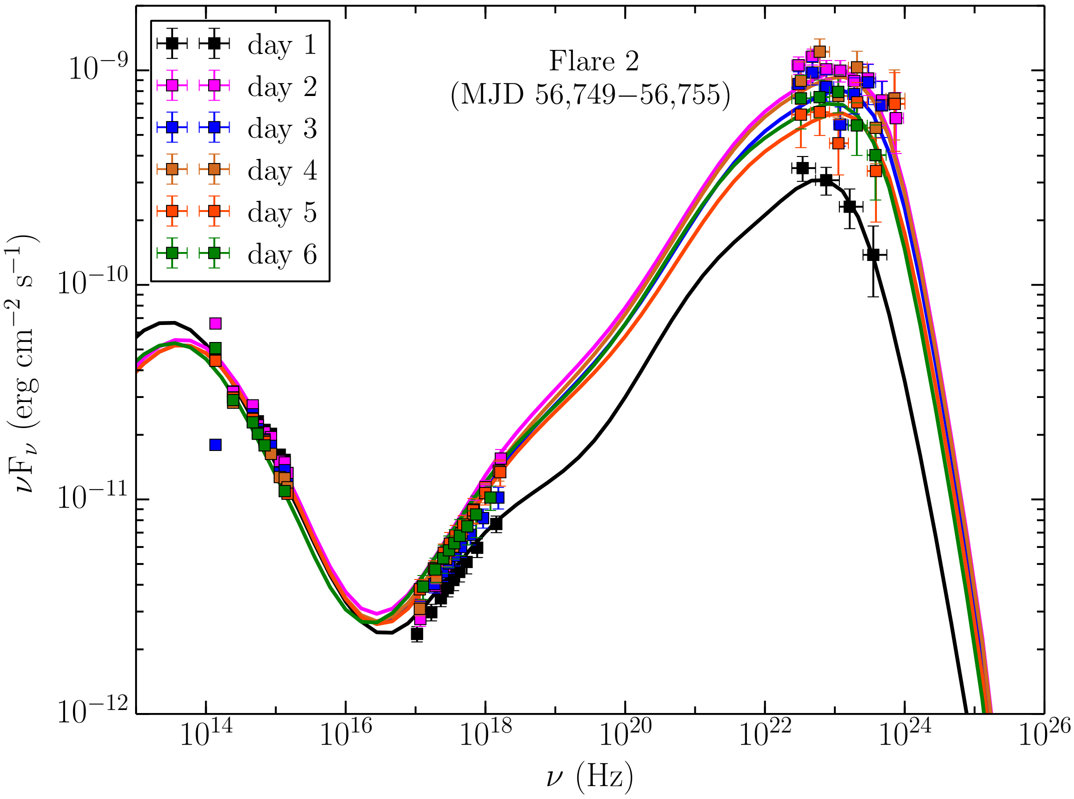

FIGURE 3.25: One day averaged SED of 3C 279 covering the main flaring period of 2014 April outburst of 3C 279.

During the 2014 April flare, the maximum γ-ray flux is obtained as (1.21 ± 0.10) $\times\ 10^{-5}$ ph cm^{-2} s^{-1} and the associated photon index is 2.19 ± 0.09. This implies an isotropic γ-ray luminosity (L_γ) of 1.2×10^{49} erg s^{-1}. The total power emitted in the γ-ray band, in the rest frame of the jet, would be $L_{\gamma,em} \simeq L_\gamma/(2\Gamma^2) \simeq 1.7 \times 10^{46}$ erg s^{-1}, adopting the bulk Lorentz factor $\Gamma = 19$ (obtained from the SED modeling). The emitted power in the the form of high energy γ-rays, thus, is a significant fraction of the kinetic jet power ($\sim$ 23%; $P_{\rm j,kin} = 7.2 \times 10^{46}$ erg s^{-1}). This observation indicates an efficient conversion of the kinetic jet power to the γ-rays. In other words, the jet becomes radiatively efficient during the peak of the flare. This is further supported from the comparison of the jet-frame γ-ray power with the Eddington luminosity ($L_{\rm Edd}$). The $L_{\gamma,em}$ is about $\sim$ 45% of $L_{\rm Edd}$, thus hinting high radiative efficiency of the jet. Moreover, the derived $L_{\gamma,em}$ is 1.7 times larger than the total available accretion power ($L_{\rm acc} \simeq L_{\rm disk}/\eta_{\rm disk} \simeq 1 \times 10^{46}$ erg s^{-1}; assuming accretion efficiency $\eta_{\rm disk}$ = 10%). The radiative jet power (to which the $L_{\gamma,em}$ is a good proxy) is found to be of the same order of the accretion disk luminosity (Ghisellini et al. 2014). The obtained parameters, thus, hint for

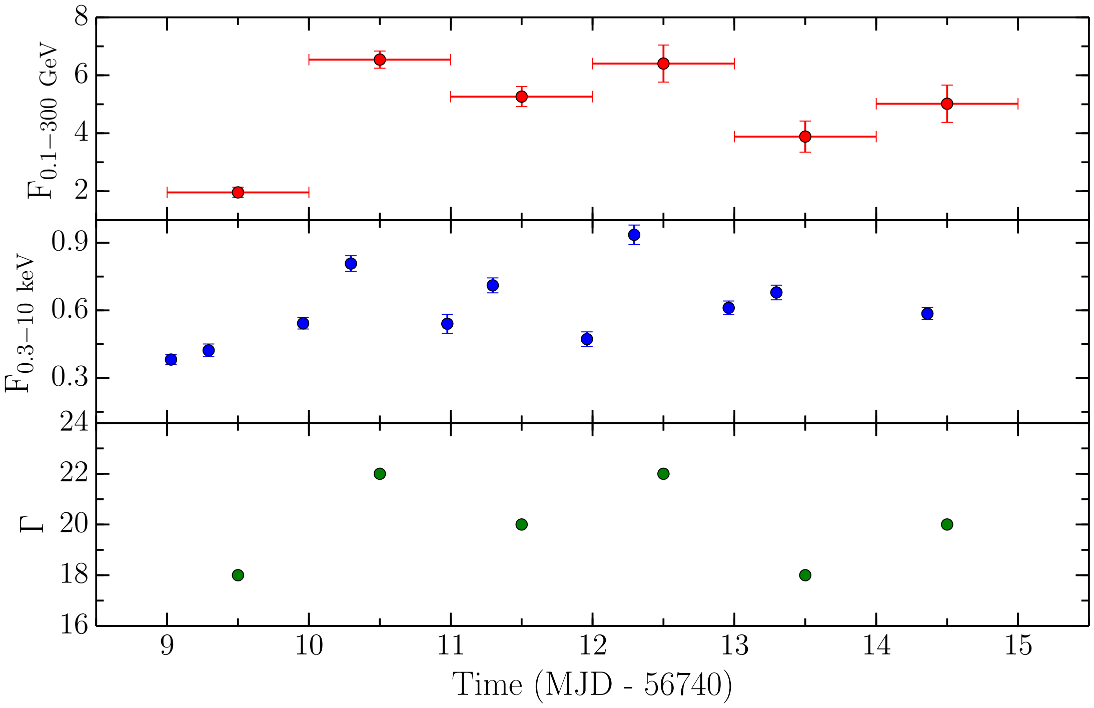

Figure 3.26: Variation of the bulk Lorentz factor Γ as a function of time (bottom panel) for 2014 April γ-ray flare. For comparison, the variation of X-ray and γ-ray fluxes are also shown (top two panels). Units are same as in Figure 3.20. Horizontal errorbar represent the time ranges.

an efficient conversion of the accretion power and/or kinetic jet power to the γ-ray luminosity.

3.4.3 2015 June γ-ray Outburst (OB3)

The 2015 June γ-ray flare of 3C 279 has broken the record of the highest γ-ray flux ever measured from this blazar, exceeding the brightness observed during 2013 December (OB1) and 2014 April (OB2) flares.

Multi-band temporal variability:

Multi-frequency light curves of 3C 279, covering the period of 2015 June outburst, are displayed in the left panel of Figure 3.27. Visual inspection of this plot clearly suggests a simultaneous flux enhancement across the electromagnetic spectrum and thus supports the single zone origin of the observed emission. Furthermore, separate γ-ray light curves are generated with various time binnings (1 day, 12 hr, 6hr, and 3 hr) and are shown in the right panel of Figure 3.27. As can be seen, the source started showing γ-ray brightening around MJD 57184 with flux level

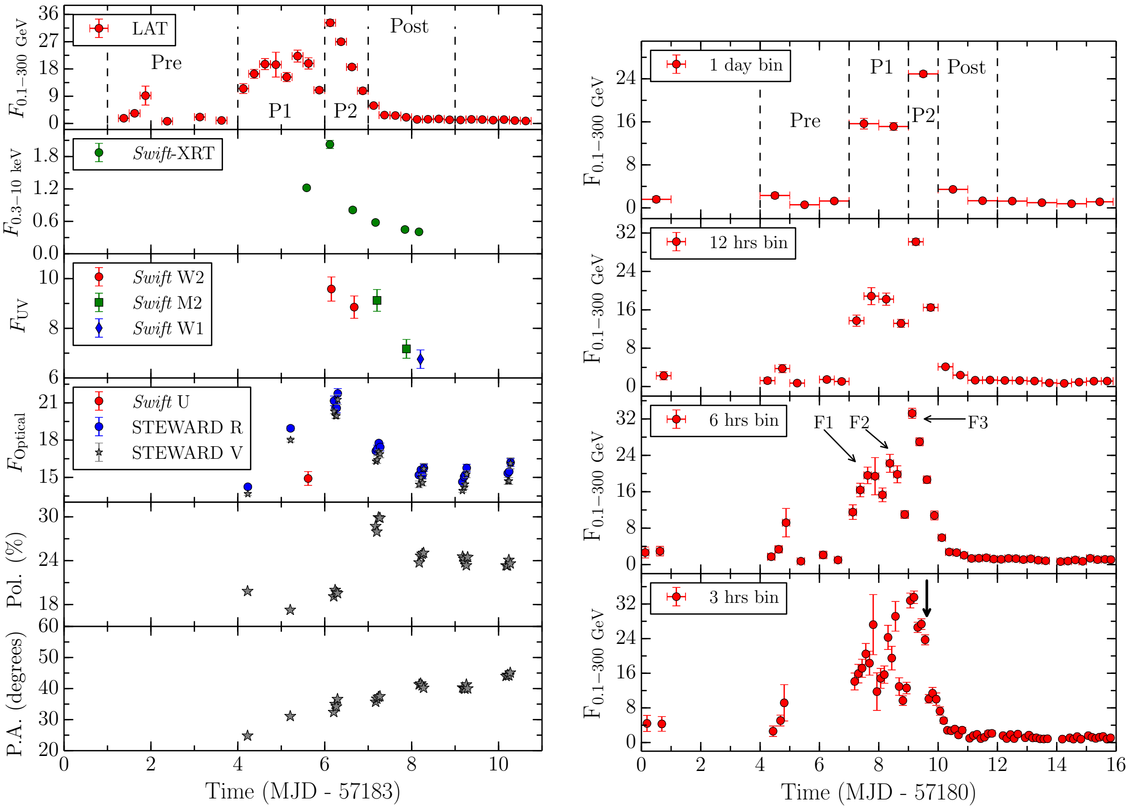

FIGURE 3.27: Left: Multi-wavelength flux variations of 3C 279 during the 2015 June γ-ray flare. *Fermi*-LAT data are 6 hr binned and in units of 10^{-6} ph cm^{-2} s^{-1} and *Swift*-XRT in counts s^{-1}. Optical-UV observations are in units of 10^{-12} erg cm^{-2} s^{-1}. Right: Light curves of 3C 279 focusing on the γ-ray flux variations with various time binnings. The flux units are same as in left panel. The downward arrow in the bottom panel indicate the time of arrival of 52 GeV photon.

of $\sim 1 \times 10^{-6}$ ph cm^{-2} s^{-1} and after a period of 3 days, the γ-ray flux suddenly jumped up by a factor of 10, where it remained steady for 2 days. Another flare of higher amplitude occurred on MJD 57189 when the γ-ray flux reached as high as $(2.45 \pm 0.05) \times 10^{-5}$ ph cm^{-2} s^{-1} which is the highest daily binned γ-ray flux measurement from 3C 279 since the launch of *Fermi*-LAT. The derived photon index is hard and has a value of 2.05 ± 0.02. Immediately after the flare, the flux level returned to a relatively low state where it remained at the level of $\sim 1 \times 10^{-6}$ ph cm^{-2} s^{-1}. Based on the observed activity in the daily binned light curve, the entire flaring period is divided into four states: a pre−flare, two flares, and a post−flare state. These periods are labeled as Pre, P1, P2, and Post, respectively, in Figure 3.27.

A careful inspection of the right panel of Figure 3.27 suggests that the flare of period P1 starts getting resolved in finer bin light curves. In fact, two distinct

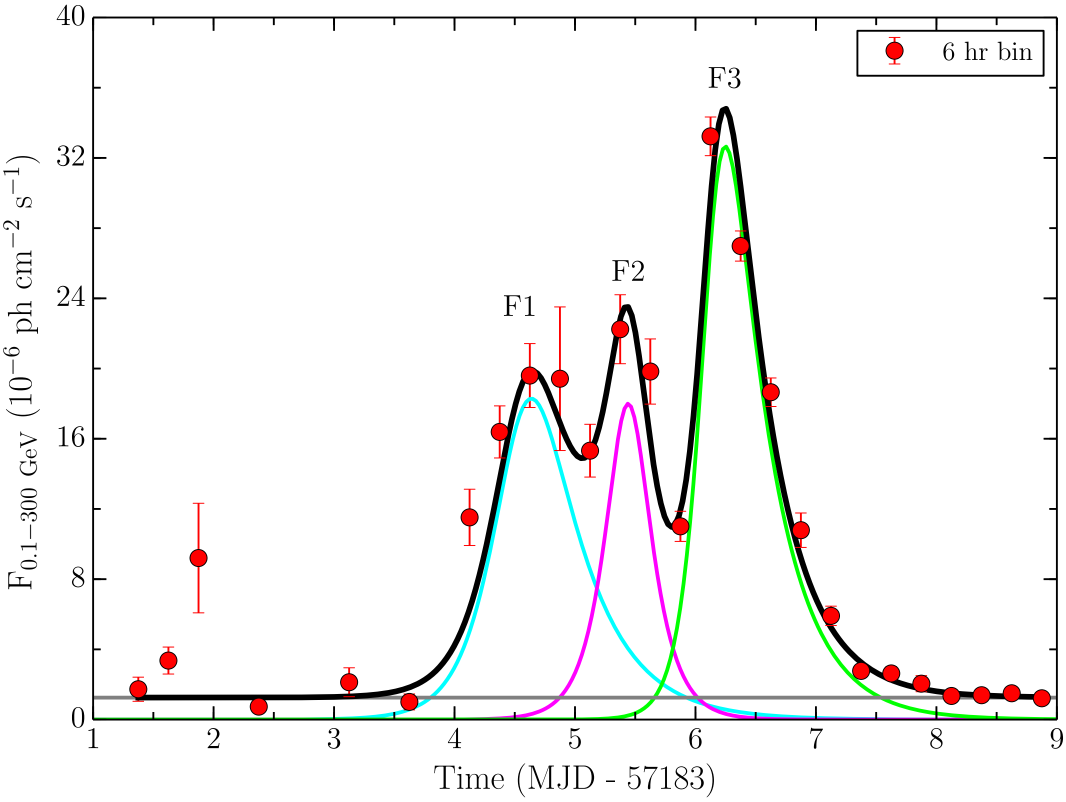

FIGURE 3.28: Temporal profile fitting of 6 hr binned γ-ray light curve of 2015 June outburst of 3C 279. Three flares are shown by cyan, pink, and limegreen colors, whereas, grey line represnts a constant background. Black line is the sum of all the components.

flares are visible in 6 hr binned light curve. There is a third sharp high amplitude flare at MJD 57189, when P1 ends and P2 begins. These three flares are named as F1, F2, and F3 (see Figure 3.27). The rising segment of the brightest flare, F3, is unresolved down to 3 hr, whereas its decaying phase seems to be nicely resolved in 6 hr binning. The flares F1 and F2 appear to be resolved in 6 hr binning, however, the 3 hr binned light curve indicates for the presence of sub-structures consisting of several large amplitude, yet unresolved and chaotic events. The highest 3 hr binned γ-ray flux is derived as $(3.35 \pm 0.14) \times 10^{-5}$ ph cm^{-2} s^{-1}. The data is also analyzed using the time bins defined as GTI. In a GTI of bin size ~14 minutes, the highest γ-ray flux measured is $(3.91 \pm 0.25) \times 10^{-5}$ ph cm^{-2} s^{-1}, with TS = 2407 and 275 counts are registered. This is the highest γ-ray flux recorded from 3C 279 not only since the beginning of *Fermi* operation but also ever. Earlier, the historically brightest flare was detected by EGRET when the derived flux was $\approx 2 \times 10^{-5}$ ph cm^{-2} s^{-1} (Wehrle et al. 1998).

The shortest flux doubling time measured during the flare is 2.2 ± 0.3 hr on MJD

57189 ($\sim 9\sigma$ significance). Moreover, to assess the variability patterns seen during the outburst, all the three flares (F1, F2, and F3) are subjected to temporal profile fitting using 6 hr binned data. The fitting is performed by assuming a constant background and three fast, temporally evolving components. The derived flare rising time for F1, F2, and F3 are 5.40 ± 0.84 hr, 4.05 ± 2.73 hr, and 3.06 ± 0.57 hr, respectively. The associated decay time of the flares, on the other hand, are 9.91 ± 5.04 hr, 4.13 ± 2.02 hr, and 8.68 ± 0.42 hr, respectively. The result of this exercise is shown in Figure 3.28.

LAT γ-ray light curves of 3C 279, in two different energy bands: 0.1−1 GeV and 1−300 GeV, are presented in the top panel of Figure 3.29. In this plot, to compare with the variability patterns seen at low energy 0.1−1 GeV range, 1−300 GeV light curve is scaled appropriately. Though the pattern of the flux variations seen during F3 flare is similar in both the bands, there are very moderate changes in source brightness in 1−300 GeV band compared to 0.1−1 GeV for F1 and F2 events. This observation suggests that F1 and F2 flares are mainly dominated by the emission from low energy electrons. The hardness ratio is also calculated (see Equation 3.5) to study the spectral evolution as a function of time. No significant spectral hardening/softening is seen during F1 and F2 flares, however, the spectrum is clearly hard at the peak of F3 and it softens as the flare decays (see the left bottom panel of Figure 3.29). Recently, Dotson et al. (2012) have proposed that the origin of γ-ray flares that lie inside/outside the BLR should be reflected by the absence/presence of time lag between MeV and GeV emission. A time lag analysis is thus performed using the *z-transformed discrete correlation function* (ZDCF) method of Alexander (2013) to test this hypothesis. The errors are computed by adding a random error at each step to each data from the errors in the light curves and performing a Monte Carlo simulation (Alexander 2013). The result of this analysis is presented in the right panel of Figure 3.29. No significant lead/lag is noticed between the two energy bands (time lag of $0.0^{+0.1}_{-0.1}$ days).

Gamma-ray Spectral Analysis:

The LAT spectra obtained by averaging the four periods are displayed in Figure 3.30. Three models, namely PL (dotted), LP (dashed), and BPL (solid) are used to perform the fitting. The flux data of the periods 'Pre' and 'Post' could not be fitted with BPL model, due to low photon statistics. The presence/absence of the spectral curvature is also substantiated by deriving the TS of the curvature.

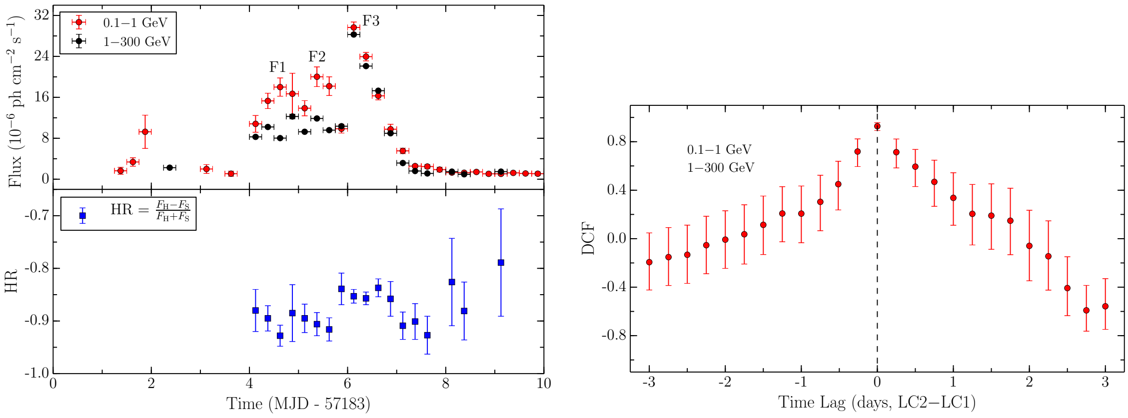

Figure 3.29: Left top: Six hr binned light curves of the fluxes in 0.1−1 GeV (red) and 1−300 GeV (black) energy ranges, multiplied by a factor of 12, covering the 2015 June flare. Left bottom: the variation of HR. Right: DCF calculated for 0.1−1 GeV and 1−300 GeV light curves. The time ordering is T((1−300 GeV)−(0.1−1 GeV)).

Table 3.18: Results of the model fitting to the γ-ray spectra of 3C 279, obtained for different activity periods considered during 2015 June flare.

		power law				
Activity	$F_{\rm GeV}$ (10^{-6} ph cm^{-2} s^{-1})	$\Gamma_{0.1-300\ \rm GeV}$			TS	
Pre	1.41±0.19	2.27±0.11	–	–	274.55	–
P1	15.80±0.55	2.21±0.03	–	–	6553.42	–
P2	24.50±0.49	2.05±0.02	–	–	22673.92	–
Post	2.39±0.13	2.26±0.05	–	–	1690.61	–
		log parabola				
Activity	$F_{\rm GeV}$ (10^{-6} ph cm^{-2} s^{-1})	α	β		TS	$\rm TS_{curve}$
Pre	1.41±0.19	2.27±0.11	0.00±0.00	–	274.55	0.00
P1	15.20±0.55	2.05±0.05	0.11±0.03	–	6572.25	18.83
P2	23.60±0.48	1.84±0.03	0.13±0.02	–	22769.93	96.01
Post	2.34±0.13	2.16±0.08	0.08±0.04	–	1694.40	3.79
		Broken power law				
Activity	$F_{\rm GeV}$ (10^{-6} ph cm^{-2} s^{-1})	Γ_1	Γ_2	$E_{\rm break}$ (GeV)	TS	$\rm TS_{curve}$
P1	15.31±0.55	2.05±0.05	2.60±0.11	$1.00^{+0.35}_{-0.30}$	6571.30	17.88
P2	23.85±0.48	1.88±0.03	2.58±0.07	$1.30^{+0.10}_{-0.15}$	22757.23	83.31

The obtained fitting parameters are given in Table 3.18. Of all the four periods considered here, a significant break/curvature is noticed only during P1 and P2 periods. Moreover, both LP and BPL models reproduce the flux distributions satisfactorily, though LP model gives slightly better fit. The break energy obtained from BPL model fitting does not vary irrespective of the fluctuations seen in the flux levels during both the periods.

Spectral Energy Distribution and Modeling:

The multi-frequency SEDs of 3C 279, covering the high activity period in 2015 June, are generated by averaging the fluxes over the periods of interest. It should be noted that there are no data, other than *Fermi*-LAT, available publicly for the

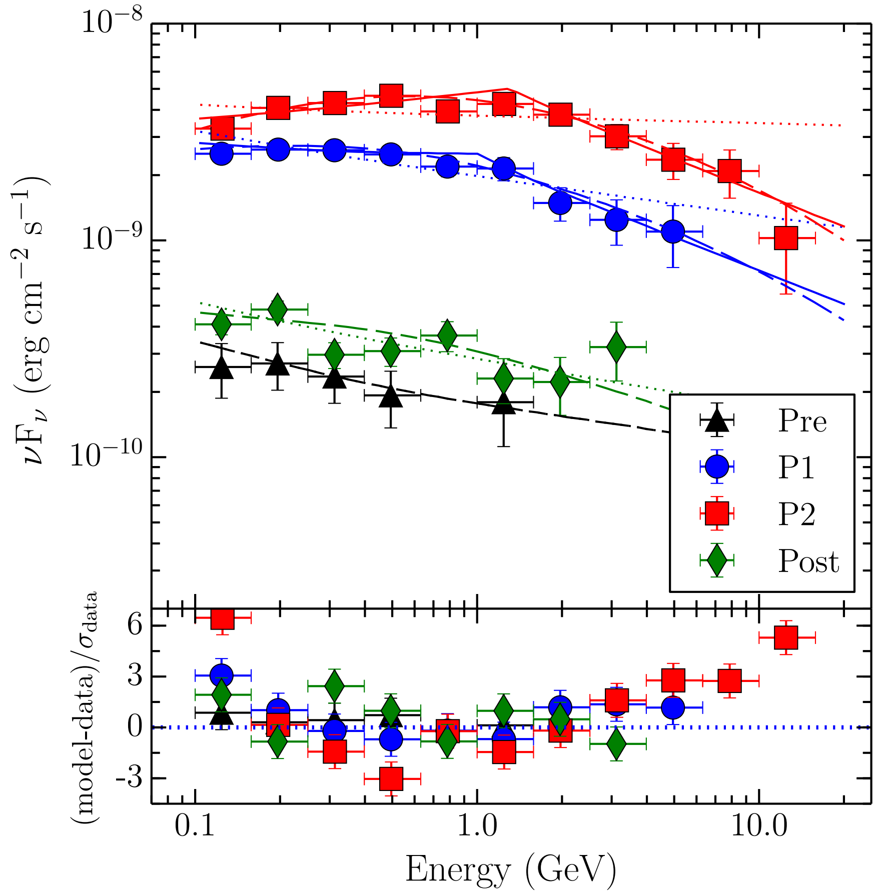

FIGURE 3.30: *Fermi*-LAT SEDs during different activity states of 2015 June flare of 3C 279. PL, LP, and BPL models are shown with dotted, dashed, and solid lines, respectively. Other details are same as in Figure 3.17.

period 'Pre'. Therefore, modeling is performed for the remaining three periods. The procedure adopted to model the broadband SED is similar to that followed to study 2014 April flare (Section 3.4.2). The resultant SEDs, along with the modeled emission mechanisms, are shown in Figure 3.31 and the modeling parameters are provided in Table 3.19.

The minimum Doppler factor $\delta_{\rm min}$ can be calculated numerically from $\gamma\gamma$ opacity arguments and by measuring the energy of the highest energy photon. Assuming that the optical depth $\tau_{\gamma\gamma}(\epsilon_1)$ of a photon with energy $\epsilon_1 = E_1/m_e c^2$ to the $\gamma\gamma$ interaction is $\tau_{\gamma\gamma} = 1$, the minimum Doppler factor can be derived using the following equation (see, e.g., Dondi & Ghisellini 1995; Ackermann et al. 2010)

$$\delta_{min} \cong \left[\frac{\sigma_T\, d_L^2 (1+z)^2 f_{\hat{\epsilon}} \epsilon_1}{4\, t_{var}\, m_e\, c^4}\right]^{1/6}, \tag{3.10}$$

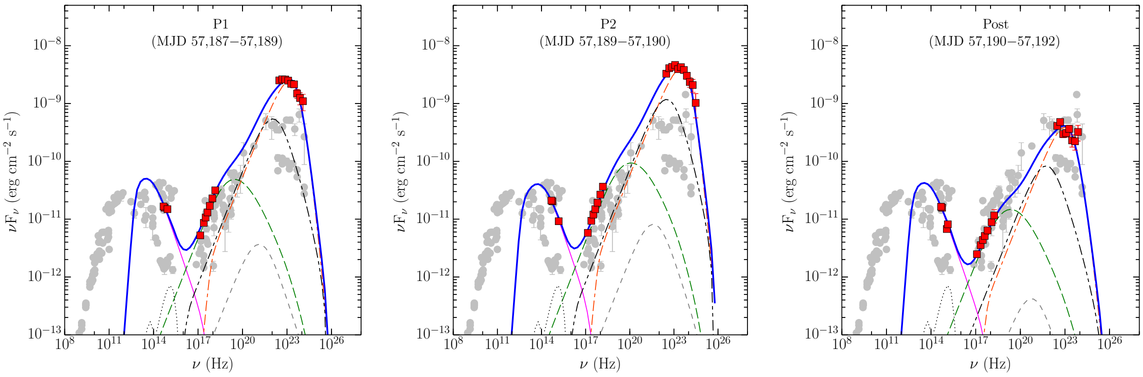

FIGURE 3.31: SEDs of 3C 279 during various activity states observed in 2015 June. Simultaneous data from Steward, *Swift* and *Fermi*-LAT are shown with red squares, whereas, gray circles belong to archival observations. Black dotted line represents thermal contributions from the torus, accretion disk, and X-ray corona (not in the plots). Pink thin solid and green dashed lines correspond to synchrotron and SSC emission, respectively. Grey dashed, red dash-dot, and black dash-dot-dot lines represent EC-disk, EC-BLR, and EC-torus components, respectively. Blue thick solid line is the sum of all the radiative mechanisms.

TABLE 3.19: Summary of the parameters used/derived from the modeling of the SED in Figure 3.31.

Parameter	P1	P2	Post
p	1.7	1.7	1.7
q	4.5	4.5	4.5
B	1.5	0.9	2.5
$U'_{\rm e}$	0.63	0.83	0.23
Γ	19	19	13
$\gamma'_{\rm b}$	649	1130	561
γ'_{max}	5e4	5e4	5e4
$R_{\rm diss}$	0.03 (1050)	0.03 (1050)	0.03 (1150)
$P_{\rm e}$	45.26	45.37	44.58
$P_{\rm B}$	44.41	43.96	44.59
$P_{\rm r}$	46.87	47.11	45.71
$P_{\rm p}$	47.36	47.40	46.71

Notes. Viewing angle is taken as 3° and the characteristic temperature of the torus as 1000 K. For a disk luminosity of 1×10^{45} erg s^{-1} and black hole mass of 3×10^{8} $M_\odot$, the size of the BLR is 0.03 parsec (1029 $R_{\rm Sch}$). Other symbols have their usual meanings as given in Table 3.6.

where f_ϵ is the flux at energy $\epsilon = h\nu/(m_e c^2)$ and $\epsilon = \hat{\epsilon} = 2\delta^2/(1+z)^2\epsilon_1$ (Ackermann et al. 2010). In this calculation, the energy of the highest energy photon (E_1) is used during the period when variability time $t_{\rm var}$ and f_ϵ are measured. The highest energy photon of energy ≈52 GeV is detected on MJD 57189.62 at an angular separation of $0^\circ.09$ from the 3FGL position of 3C 279 (see bold downward arrow in the right panel of Figure 3.27). The simultaneous *Swift*-XRT observation has reveled 0.3−10 keV energy flux as 3.5×10^{-11} erg cm^{-2} s^{-1} and the associated photon index is 1.4 (Pittori et al. 2015). Since the highest energy photon was detected during the decaying part of F3, the variability time can be taken as $t_{\rm var} = \ln(2) \times T_d \approx 6$ hr. This gives $\delta_{\rm min} \approx 14$.

The location of the emission region ($R_{\rm diss}$) can be estimated roughly by assuming bulk Lorentz factor $\Gamma = \delta_{\rm min} = 14$. Then $R_{\rm diss} < 2\,c\,\Gamma^2\,t_{\rm var}/(1+z) \approx 0.05$ pc. Assuming the accretion disk luminosity of 3C 279 as 1×10^{45} erg s^{-1} (Paliya et al. 2015b) and adopting the empirical relation of Kaspi et al. (2007), the size of the BLR comes out to be $\approx 1 \times 10^{17}$ cm, or ≈ 0.03 pc. Therefore, at the time of the 52 GeV photon emission, the γ-ray emitting region must have been located either close to the outer edge of the BLR or beyond it. This is also supported by fact that to avoid severe absorption of high energy photons (having energy >50 GeV) by dense radiation field of the BLR, the emission region has to be farther out from the BLR.

The SED parameters suggest that at the peak of the flare, the bulk Lorentz factor of the jet was high. The particle energy density also increased, causing a dip in the magnetic field. This is because the observed synchrotron fluxes are similar during all the three states (Figure 3.31). Reproducing this flux with increased particle energy density at the peak of the flare (period P2) demands a low magnetic field. The variation in particle energy density during Flare 1 and Flare 2 is required to reproduce the corresponding SSC X-ray fluxes, since SSC flux has a quadratic dependence on particle energy density (Dermer et al. 2009). A combination of the increased injected particle energy and jet bulk Lorentz factor then explains the observed exceptional γ-ray flare. Moreover, from the SED modeling approach too, the location of the emitting region is found to be at the outer edge of the BLR and the Doppler factor is larger than 14, thus supporting the arguments given above (see also Table 3.19).

In Figure 3.32, the SEDs of 3C 279 covering the periods of peak γ-ray activity during all the three epochs, i.e. 2013 December, 2014 April, and 2015 April are presented. For comparison, the low activity fluxes are also shown. As can be seen in this plot, the flux levels at optical-UV band are similar during 2014 April and 2015 June, whereas, it was lower during 2013 December event. The X-ray flux level was similar in 2013 December and 2014 April flares but increases during the 2015 June event. The variations seen both in flux as well as in the spectral

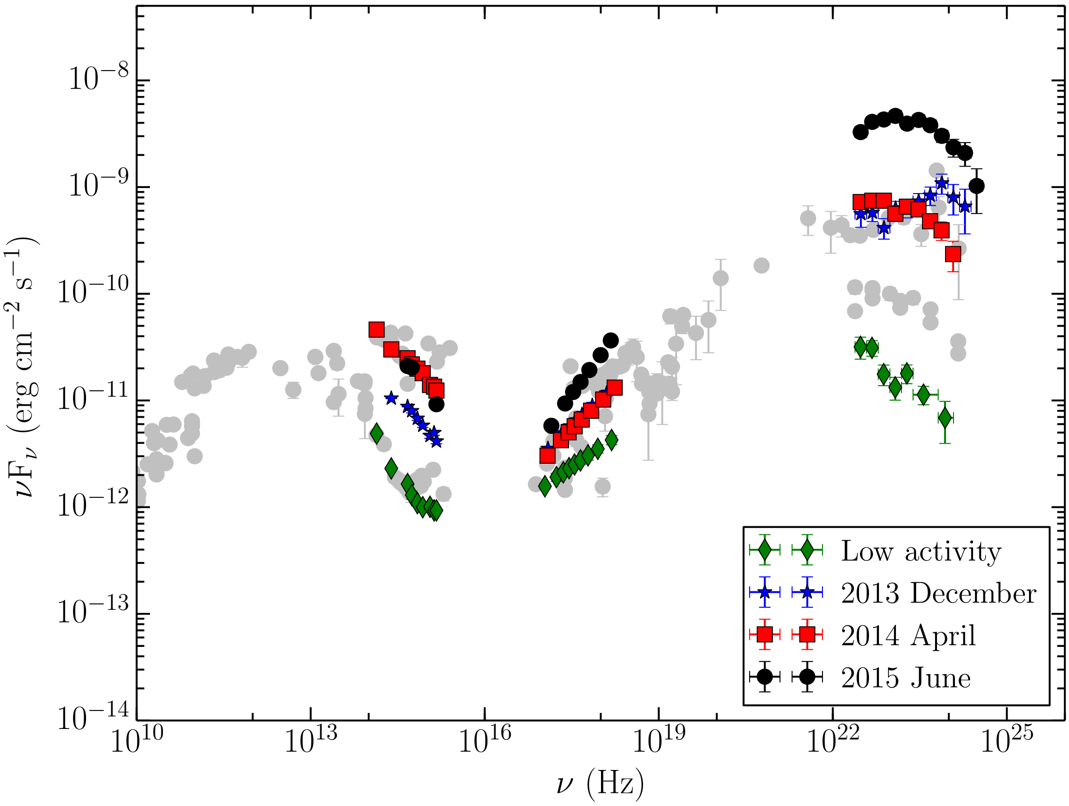

Figure 3.32: Comparison of the broadband SEDs of 3C 279 at the peak of γ-ray activity during the flares in 2013 December, 2014 April, and 2015 June.

shapes are most dramatic for γ-ray band. Among all the bands, the γ-ray flux variations are the largest. Moreover, the γ-ray spectral shape is similar during 2014 April and 2015 June flares, thus suggesting a common factor to be responsible for the observed curvature. As discussed for 2014 April outburst, such a curved γ-ray spectrum could be due to Klein-Nishina effect. However, fitting the broken power law model to the γ-ray spectrum of 2015 June flare suggests the peak of the IC mechanism to be lying in the LAT energy range. Therefore, the observed curvature most likely reflects the energy distribution of the underlying electrons. On the other hand, the shape of the γ-ray spectrum seen during 2013 December flare is extremely hard, thus suggesting a different mechanism or set of various mechanisms to be working. An alternative approach such as multi-zone modeling was required to describe this peculiar γ-ray flare.

3.4.4 Summary

Fermi-LAT has observed multiple episodes of flaring activities from 3C 279 since 2008. Based on the availability of multi-wavelength observations, three high activity periods are selected for a detailed study. The main conclusions are as follows.

1. The γ-ray flux level of 3C 279 during 2013 December and 2014 April flares was comparable to that detected during its historical flare in 1996 by EGRET. However, even higher level of γ-ray activity was detected in 2015 June and the measured flux during this period was the highest ever detected from 3C 279.
2. A significant curvature was observed in γ-ray spectra of 2014 April and 2015 June events, whereas, 2013 December flare exhibited a hard rising spectrum.
3. An hr scale γ-ray flux variability is detected in all the three flares.
4. Multi-wavelength behavior of 3C 279 during 2013 December reveals uncorrelated flux variations.
5. Uncorrelated multi-frequency behavior and the observation of hard γ-ray spectrum ruled out the possibility to explain the observed features using a single zone leptonic emission approach. Therefore, a two-zone leptonic radiative model is used.
6. In two-zone modeling, a large emission region emits in IR to X-rays, whereas, the γ-ray emission is explained by assuming it to be originated from a relatively fast moving small emission region. Due to unavailability of VHE observations the location of the γ-ray emitting region could not be constrained.
7. A simultaneous flux enhancement is seen at all the frequencies during 2014 April and 2015 June activities, thus supporting single zone origin of the flares. A one zone leptonic emission model explains the observed SED well and the location of the emitting region is found to be at the outer edge of the BLR in both the cases.
8. Overall, these three flares are the best examples of the dominance of a variety of radiative processes and this reflects the complexity involves in understanding the physical properties of blazar jets, in general.

3.5 3FGL J1104.4+3812 (Mrk 421)[8]

Markarian 421 (Mrk 421, $z = 0.031$) is a bright BL Lac object that has been studied extensively (see, e.g., Fossati et al. 2008; Shukla et al. 2012; Aleksić et al. 2015a,b). The lack of emission lines in its optical spectrum and a thermal component in the broadband SED suggest that the emission from the jet is dominant over other external sources like the accretion disk. Consistently, the high energy emission is often explained successfully by an SSC process without invoking any additional external Compton component. Moreover, the extension of the synchrotron spectrum up to X-rays reflects an efficient acceleration mechanism that produces a particle spectrum extending up to extremely relativistic energies. Accordingly, the SSC spectrum also extends to VHE band, and hence, Mrk 421 is known as a bright TeV emitter (Punch et al. 1992). It exhibits a flat radio spectrum, compact core morphology, high optical polarization, and large amplitude variability throughout the electromagnetic spectrum (e.g., Aleksić et al. 2015a; Hovatta et al. 2015). In particular, extremely fast VHE outbursts were detected where the shortest doubling times of the flare events were found to be $\sim$15 minutes (Gaidos et al. 1996). A positive correlation between X-rays and VHE radiation is also reported (Aleksić et al. 2015a), thus suggesting that these emissions arise from the same region.

In 2013 April, Mrk 421 underwent a giant X-ray outburst and was extensively monitored by both ground and space based observational facilities (e.g., Cortina & Holder 2013; Paneque et al. 2013). It was also found to be in an extremely bright state by ground based VHE observation facilities. Though in the past too, Mrk 421 has shown such high flaring activities in the VHE regime, the lack of sensitive hard X-ray instruments has prevented from understanding the connection between the observed variability at VHE, corresponding to the tail of SSC spectrum, with that at hard X-rays (synchrotron tail), under the leptonic radiation scenario. During the 2013 April outburst, Mrk 421 was monitored by the hard X-ray mission *NuSTAR*, thus providing a valuable information at hard X-ray energies. Using publicly available *NuSTAR* and *Swift*-XRT data, an exhaustive study of the X-ray emission (0.3$-$79 keV) from Mrk 421 is performed. A major emphasis is given on searching the fastest variations seen in 3$-$79 keV energy band and also on understanding the patterns of X-ray variability.

---

[8] The results presented for Mrk 421 are published in Paliya et al. (2015a).

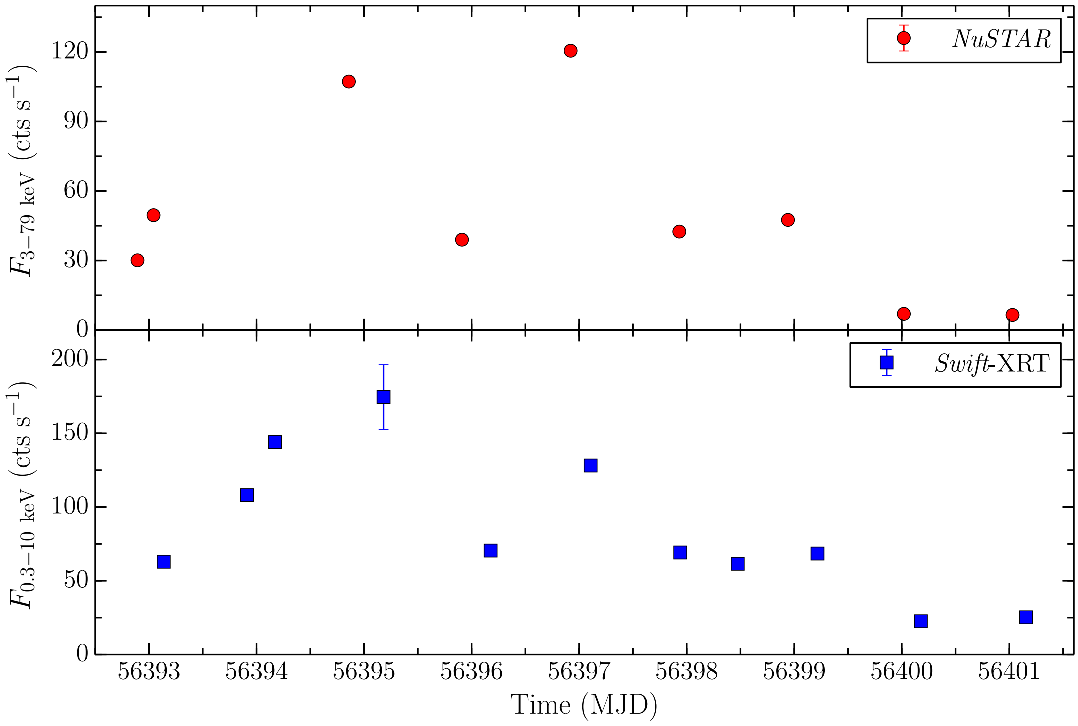

FIGURE 3.33: X-ray light curves of Mrk 421 during the period of high activity in 2013 April, as observed from *NuSTAR* (3−79 keV, top panel) and *Swift*-XRT (0.3−10 keV, bottom panel). Each data point corresponds to one observation ID in both the panels.

3.5.1 X-ray Flux Variability Analysis

The *NuSTAR* and *Swift*-XRT light curves of Mrk 421, covering the period of high activity in 2013 April, are presented in Figure 3.33. Two prominent flares can be easily noticed, one at around MJD 56395 and another at around MJD 56397. The good photon statistics during the outburst has allowed to generate light curves using shorter time binning that is as small as 5 minutes. The generation of such shorter time binned light curves is also useful for searching faster variability and the possible existence of flux variability patterns. The results of this exercise for *NuSTAR* and *Swift*-XRT are shown in the top panels of Figure 3.34 and 3.35, respectively. Furthermore, light curves are also generated in two different energy bands, both for *NuSTAR* (3−10 and 10−79 keV) and *Swift*-XRT (0.3−10 and 1.5−10 keV), and they are presented in the middle panels of Figure 3.34 and 3.35, respectively. These observations hint for the presence of intra-day variability. Multiple episodes of flaring activities can be seen both in the soft and hard X-ray bands. For better visualization of the pattern of flux variations, 5 minute binned *NuSTAR* are also shown in Figure 3.36. As can be seen in this plot, two distinct

Table 3.20: Variability characteristics of Mrk 421 as observed by *NuSTAR* and shown in Figure 3.34.

Date [1]	Obs. Id [2]	$F_{\mathrm{var}}^{3-78\ \mathrm{keV}}$ [3]	$F_{\mathrm{var}}^{3-10\ \mathrm{keV}}$ [4]	$F_{\mathrm{var}}^{10-78\ \mathrm{keV}}$ [5]	$\lvert\tau\rvert$ [6]	Signif. [7]	R/D [8]
2013 Apr 10	60002023024	0.150 ± 0.005	0.149 ± 0.007	0.146 ± 0.024	159.56 ± 40.13	4.17	D
2013 Apr 11	60002023025	0.604 ± 0.002	0.595 ± 0.002	0.642 ± 0.006	14.01 ± 5.03	3.15	R
2013 Apr 12	60002023027	0.140 ± 0.002	0.137 ± 0.003	0.185 ± 0.008	47.97 ± 4.13	11.33	R
2013 Apr 13	60002023029	0.254 ± 0.002	0.223 ± 0.003	0.219 ± 0.007	–	–	–
2013 Apr 14	60002023031	0.320 ± 0.001	0.317 ± 0.002	0.366 ± 0.003	37.87 ± 4.96	7.63	R
2013 Apr 15	60002023033	0.184 ± 0.008	0.186 ± 0.002	0.221 ± 0.006	36.46 ± 9.77	3.73	D
2013 Apr 16	60002023035	0.400 ± 0.002	0.398 ± 0.002	0.451 ± 0.005	28.44 ± 3.76	7.57	R
2013 Apr 18	60002023037	0.186 ± 0.005	0.182 ± 0.005	0.227 ± 0.015	20.26 ± 5.71	3.55	R
2013 Apr 19	60002023039	0.123 ± 0.006	0.121 ± 0.006	0.157 ± 0.018	–	–	–

Notes. Col.[1] and [2]: *NuSTAR* observation date and observation ID; Col.[3], [4], [5]: normalized rms variability amplitude for 3−78 keV, 3−10 keV, and 10−78 keV, respectively; Col.[6] and [7]: the shortest flux doubling/halving time in minutes and its significance; Col.[8]: R: rising flare D: decaying flare.

patterns are visible, a slowly varying flare, and on the top of that, extremely fast flux variations. Though there are also hints of similar behavior at low energy XRT light curves, a strong claim cannot be made due to the short exposures of XRT observations.

The normalized rms amplitude of variability (F_{var}) is calculated to characterize the flux variations. F_{var} is calculated for all of the light curves presented in Figure 3.34 and 3.35. Overall in 3−79 keV energy band, F_{var} is derived as 0.790 ± 0.001, whereas, for 0.3−10 keV it is 0.599 ± 0.007. Moreover, due to the long exposure of each *NuSTAR* pointing, it is possible to derive F_{var} for individual *NuSTAR* observations. The results are presented in Table 3.20. An important result is that the F_{var} for 10−79 keV is found to be higher than that for 3−10 keV in almost all of the observations. Similar behavior is observed for the *Swift*-XRT data where a F_{var} of 0.693 ± 0.006 (1.5−10 keV) and 0.565 ± 0.006 (0.3−1.5 keV) are derived.

The 5 minute binned light curves that are presented in the top panel of Figure 3.34 and 3.35 are scanned to find the fastest flux doubling/halving timescale. For XRT data, the shortest flux doubling time is 64.14 ± 13.78 minutes ($\sim 5\sigma$ significance). On the other hand, the derived fastest flux doubling time for *NuSTAR* observations is 14.01 ± 5.03 minutes. Considering a more conservative 5σ significance, the shortest flux doubling time is 28.44 ± 3.76 minutes. This is the shortest hard X-ray variability ever detected from Mrk 421. The derived parameters of this analysis are presented in Table 3.20.

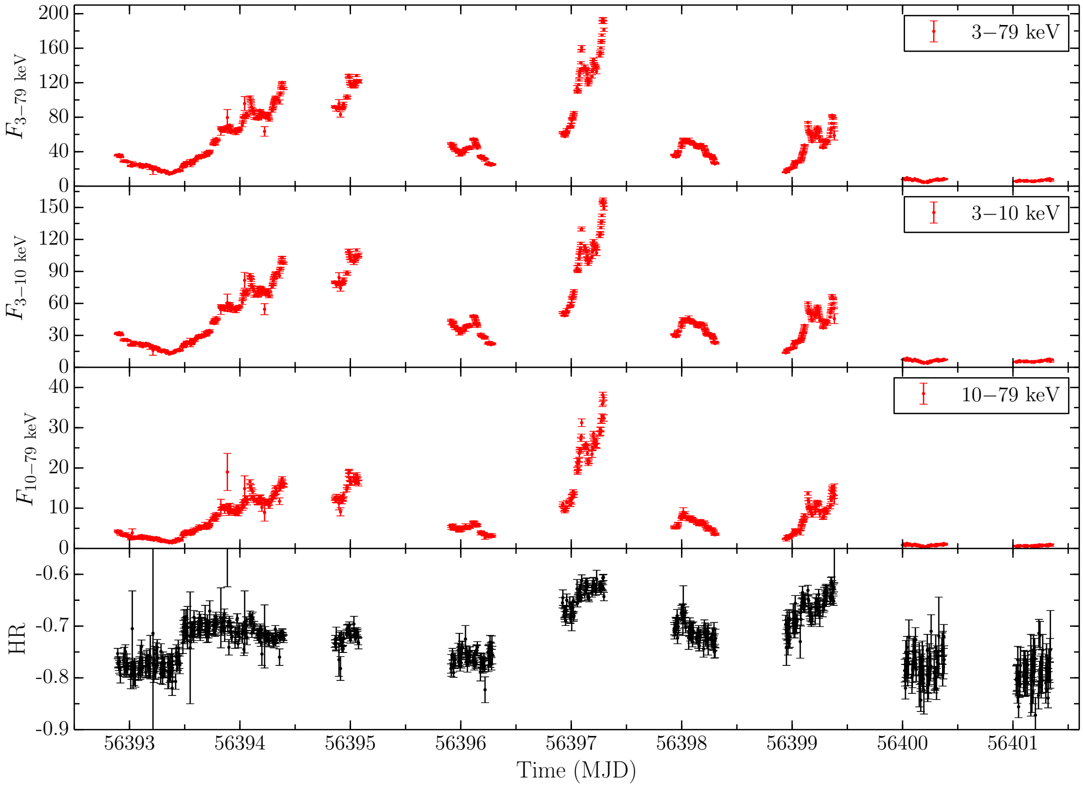

FIGURE 3.34: *NuSTAR* light curves of Mrk 421, adopting 5 minute time binning. The bottom panel referes to the temporal variation of hardness ratio. All the fluxes are in units of counts s^{-1}.

The shortest hard X-ray variability time found is similar to that observed in the VHE energy range by Gaidos et al. (1996). Interestingly, during the 2013 April outburst, Mrk 421 seemed to show fast variations at VHE γ-rays (Cortina & Holder 2013). The simultaneity of hard X-ray and VHE flux enhancements clearly pointed towards a cospatial origin of the observed radiations. Furthermore, if the black hole mass of Mrk 421 is assumed as $1.9 \times 10^8\ M_\odot$ (Barth et al. 2003), the observed variability timescale is similar to the light-crossing time across the black hole's event horizon ($t_{\rm BH} \sim r_{\rm g}/c = GM/c^3 \sim$15 minutes), which is the shortest expected variability timescale of emission powered by accretion onto the black hole. The variability timescales estimated from *NuSTAR* observations are thus, difficult to explain using the conventional blazar emission theories.

In the framework of single-zone jet models, the Doppler factor of the compact emitting region (whose size is constrained from the observed shortest variability time) has to be very high ($\gtrsim$50). This is required to avoid the severe pair production of TeV photons with the synchrotron radiation and also to satisfy the

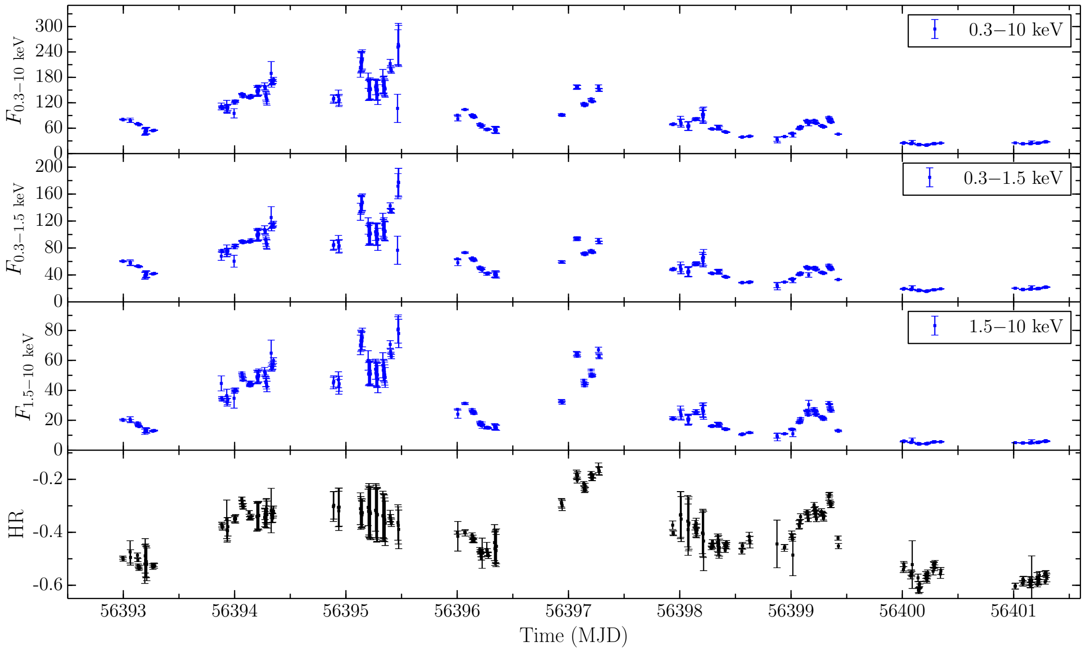

FIGURE 3.35: *Swift*-XRT light curves of Mrk 421, adopting 5 minute time binning. The fluxes are in units of counts s^{-1}. The covered energy ranges are: 0.3−10 keV (top), 0.3−1.5 keV (second from top), and 1.5−10 keV (second from bottom). The variation of the hardness ratio is presented in the bottom panel.

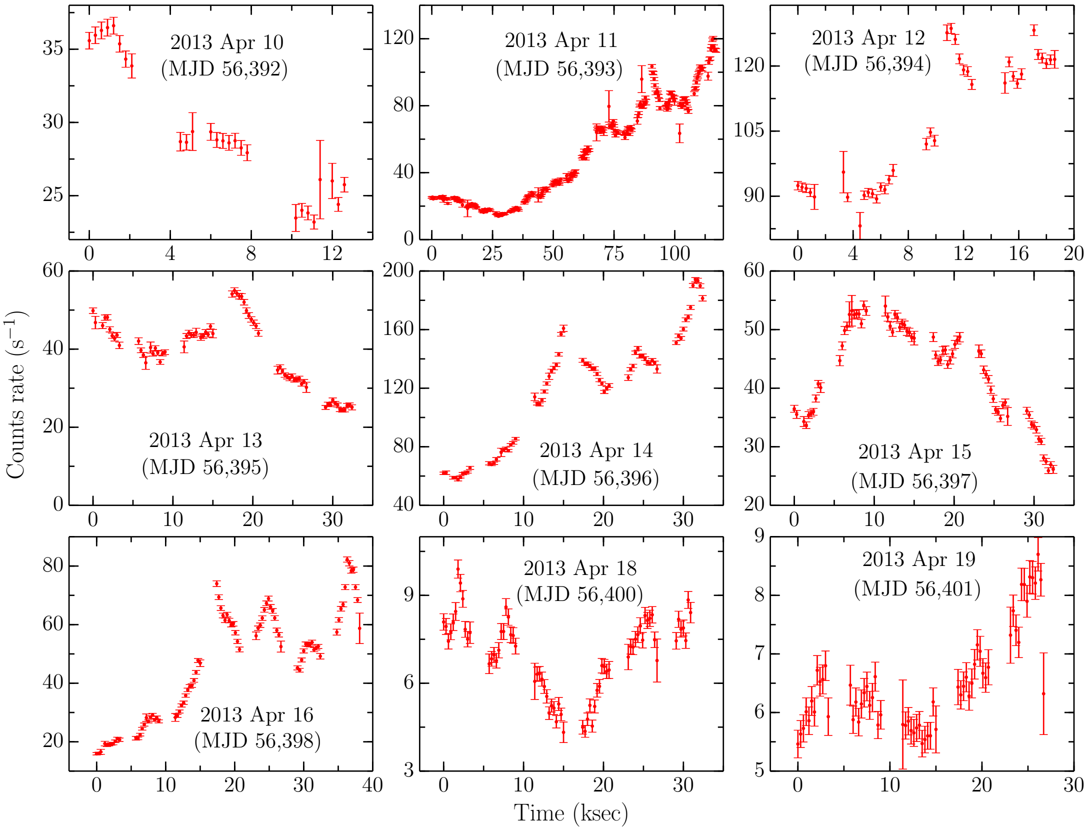

FIGURE 3.36: *NuSTAR* light curves of Mrk 421, adopting 5 min time binning.

condition $t_{\rm var} \lesssim t_{\rm BH}$ (e.g., Begelman et al. 2008). Alternatively, several other models have been put forward to explain such fast variability (of VHE radiations, in particular). Ghisellini & Tavecchio (2008) have invoked the concept of the localized magneto-centrifugal acceleration of the electron beams to explain the fast TeV variability of PKS 2155−304 and Mrk 501. This "needle" model, however, predicts little or no X-ray flux variations. The simultaneous flux enhancement detected both in VHE and X-rays from Mrk 421 clearly disfavors this hypothesis. On the other hand, Giannios et al. (2009) proposed a "jet-in-a-jet" model in which the concept of magnetic reconnection is used to explain the observed fast variability. This model not only reproduces the ultra fast TeV variations, but also predicts the observations of rapid X-ray flares. The 2013 April flaring event of Mrk 421 shows simultaneous variations at X-rays and TeV energies, thus indicating magnetic reconnection to be a possible cause of the flare. Moreover, the model of Giannios et al. (2009) also predicts the presence of a slowly varying flare due to the tearing of a large reconnection region. This leads to the ejection of several small size relativistic plasmoids, which are thought to be responsible for extremely fast variations. Interestingly, a combination of the slowly varying patterns underlying fast flares can be seen in Figure 3.36. The observations thus support the magnetic dissipation hypothesis.

The temporal variation of the hardness ratio (HR) is shown in the bottom panels of Figure 3.34 and 3.35. It is defined as follows

$$\mathrm{HR} = \frac{F_{\rm hard} - F_{\rm soft}}{F_{\rm hard} + F_{\rm soft}}, \tag{3.11}$$

where $F_{\rm soft}$ and $F_{\rm hard}$ are soft (3−10 keV for *NuSTAR* and 0.3−1.5 keV for XRT) and hard (10−79 keV for *NuSTAR* and 1.5−10 keV for XRT) X-ray fluxes, respectively. A 'harder when brighter' behavior is evident for both the *NuSTAR* and XRT light curves, notably at the peak of the flare around MJD 56397.

3.5.2 X-ray Spectral Analysis

The *NuSTAR* spectra are fitted with a log parabola model (see, e.g., Massaro et al. 2004), while keeping the pivot energy fixed to 10 keV, to determine the spectral behavior of the source. The results of the spectral analysis are given in Table 3.21. In addition to this, the variations of both spectral parameters, i.e.,

Table 3.21: Summary of the spectral analysis of the *NuSTAR* data.

OBS ID[1]	Exp.[2]	α[3]	β[4]	$F_{3-79\ \mathrm{keV}}$[5]	Normalization[6]	Stat.[7]
60002023024	5.76	3.011 ± 0.022	0.326 ± 0.057	5.883 ± 0.066	1.250 ± 0.013	634.40/624
60002023025	57.51	2.725 ± 0.005	0.298 ± 0.012	10.460 ± 0.028	2.383 ± 0.006	1799.28/1412
60002023027	7.63	2.735 ± 0.009	0.388 ± 0.024	22.380 ± 0.117	5.217 ± 0.024	1084.49/1014
60002023029	16.51	2.908 ± 0.011	0.338 ± 0.029	7.790 ± 0.055	1.716 ± 0.009	1003.08/911
60002023031	15.61	2.390 ± 0.005	0.360 ± 0.013	28.605 ± 0.106	6.819 ± 0.020	1715.36/1424
60002023033	17.28	2.672 ± 0.009	0.283 ± 0.024	9.088 ± 0.047	2.080 ± 0.010	1036.17/1012
60002023035	20.28	2.466 ± 0.007	0.287 ± 0.019	11.021 ± 0.056	2.570 ± 0.011	1231.30/1188
60002023037	17.80	2.966 ± 0.027	0.290 ± 0.068	1.384 ± 0.015	0.296 ± 0.004	526.60/557
60002023039	15.96	3.031 ± 0.031	0.179 ± 0.076	1.279 ± 0.014	0.259 ± 0.004	515.62/523

Notes.
[1] *NuSTAR* observation ID.
[2] Net exposure, in ks.
[3] Photon index at pivot energy, in the log parabola model.
[4] Curvature index, in the log parabola model.
[5] Energy flux in 3−79 keV energy band and in units of 10^{-10} erg cm^{-2} s^{-1}.
[6] Normalization in units of 10^{-3} ph cm^{-2} s^{-1} keV^{-1}.
[7] tatistical parameters: χ^2/dof.

the photon index (α) at the pivot energy and the curvature index (β) are shown in Figure 3.37 as a function of source brightness. The spectra are found to exhibit more curved behavior during higher flux states, whereas, there is a clear trend of "hardening when brightening". This is also in accordance with the behavior seen in the HR plots.

3.5.3 Constraining Physical Parameters from Observed Variability

The fundamental causes of the origin of the 2013 April outburst of Mrk 421 are uncertain. However, a few model-independent parameter estimates can be derived merely based on the assumption of a synchrotron origin of the hard X-ray emission. If the radiation output of the dominant electron population is primarily from synchrotron emission, electrons of energy $\gamma\, m_e c^2$ lose energy on an observed timescale of $t_c = ([1+z]/\delta)\,(6\pi\, m_e c^2)/(c\,\sigma_T\, B^2\,\gamma)$, where $\delta = 10\,\delta_1$ is the bulk Doppler factor, σ_{T} is the Thomson cross-section, and $B = 1\,B_{\mathrm{G}}$ Gauss is the magnetic field. The electron Lorentz factor can be associated with a characteristic X-ray frequency in the *NuSTAR* energy range, $\nu_{\mathrm{sy}} = 10^{19}\,\nu_{19}\,\mathrm{Hz} = 4.2\times10^{6}\,(\delta/[1+z])\,B_{\mathrm{G}}\,\gamma^2$ Hz. Combining these two identities and requiring that the synchrotron cooling timescale of electrons radiating in the *NuSTAR* energy range has to be shorter than or equal

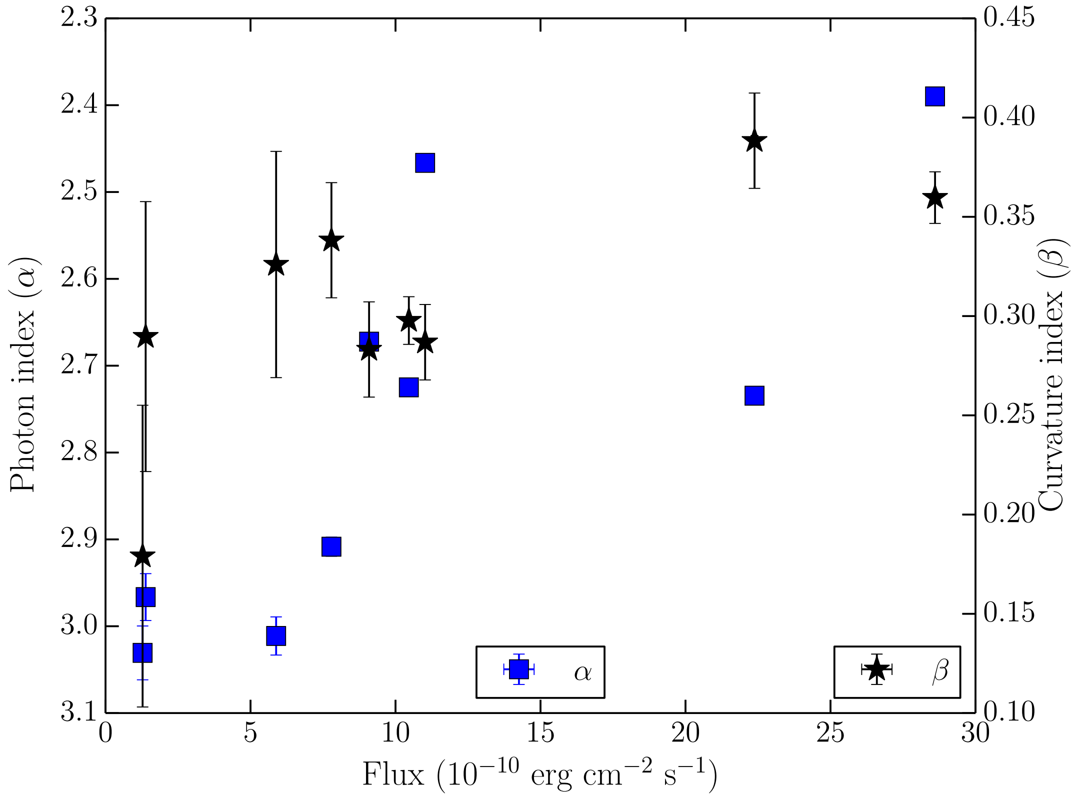

FIGURE 3.37: Variations of log parabolic spectral parameters as a function of energy flux. Left y-axis represents the photon index (α) whereas right y-axis corresponds to curvature index (β).

to the observed minimum variability time scale, the following relation is derived

$$B \geq 0.73\, \delta_1^{-2/3}\, \nu_{19}^{1/3} \text{ G} \tag{3.12}$$

Thus, even for $\delta \sim 30$, the inferred magnetic field of $B \geq 0.35\, \nu_{19}^{1/3}$ G is higher than the values of $B \lesssim 0.1$ G that are typically inferred from SED modeling of high frequency peaked BL Lac objects such as Mrk 421. Assuming values of $B = 0.4$ G and $\delta = 30$, which would be consistent with the above estimates, electrons radiating near the high-energy end of the *NuSTAR* range, have Lorentz factors of

$$\gamma_X \sim 4 \times 10^5 \left(\frac{\delta}{30}\right)^{-1/2} \left(\frac{B}{0.4\,\text{G}}\right)^{-1/2} \nu_{19}^{1/2} \tag{3.13}$$

and can produce γ-rays by Compton scattering in the Thomson regime up to photon energies of $E_{\mathrm{T,max}} \sim (\delta/[1+z])\, \gamma\, m_e c^2$ or

$$E_{\mathrm{T,max}} \sim 6 \left(\frac{\delta}{30}\right)^{1/2} \left(\frac{B}{0.4\,\mathrm{G}}\right)^{-1/2} \nu_{19}^{1/2}\ \mathrm{TeV} \tag{3.14}$$

by scattering target photons of energy $E_t \sim 38\,(\delta/30)^{3/2}\,(B/0.4\mathrm{G})^{1/2}\,\nu_{19}^{-1/2}$ eV, i.e., UV – soft X-ray photons. Hence, the same population of ultra-relativistic electrons can be responsible for both hard X-ray synchrotron and Compton VHE γ-ray emission, varying on comparable timescales, thus providing strong support for a leptonic (plausibly SSC) cospatial origin of the X-ray and VHE γ-ray emission.

The extremely fast variability seen at hard X-rays suggests that the impulsive injection (acceleration) of electrons of the highest energies is the most likely cause of the flux variations, since the highest energy electrons have the shortest cooling timescales. The injection of highly energetic particles is expected to cause not only a flux increase but also a spectral hardening, which is observed.

3.5.4 Summary

1. The 2013 April X-ray outburst of Mrk 421 led to the first time discovery of minute scale (∼14 minutes) hard X-ray (3−79 keV) flux variations ever observed from this blazar and is on the order of the light crossing time of the black hole's event horizon.

2. A pattern of extremely fast variability events superposed on slowly varying flares is found in most of the *NuSTAR* observations. These peculiar variability patterns may be explained by magnetic energy dissipation and reconnection in a fast moving compact emission region within the jet.

3. Based on the fast variability, a lower limit on the magnetic field strength of $B \geq 0.73\delta_1^{-2/3}\,\nu_{19}^{1/3}$ G is derived, where δ_1 is the Doppler factor in units of 10, and ν_{19} is the characteristic X-ray synchrotron frequency in units of 10^{19} Hz.

3.6 Summary of the Chapter

The broadband observations of high redshift blazar S5 0836+71 revealed the presence of an extremely fast hr scale γ-ray variability, which is probably the first report of such a short timescale flux variations from any blazar beyond redshift 2. At the peak of the γ-ray activity, the source was found to emit the most luminous γ-ray flare ever detected from any blazar. The behavior of the optical-UV radiation from S5 0836+71 hint for the dominance of the thermal emission from the accretion disk over non-thermal jetted radiation. This is because the source has shown many high amplitude X-ray and γ-ray flares but the optical-UV flux vary a little. This is further confirmed from the broadband SED modeling where accretion disk component reproduces optical-UV spectra successfully in all the activity states. Moreover, the continuous monitoring from *Swift*-XRT also led to the detection of a bright X-ray flare with a relatively low amplitude γ-ray counterpart. This observation probably reflects the effect of the jet environment on the emission region at various distances from the central engine.

The distant quasar J0809+5341 was not known to be a γ-ray emitter, prior to this work. The giant optical outburst in 2014 April has led to the first time detection of this object in the γ-ray band. The subsequent multi-wavelength analysis and broadband SED modeling indicated that this source, in many aspects, is different from other high redshift blazars. The observed optical-UV spectrum of J0809+5341 is found to be originated from non-thermal synchrotron emission with negligible contribution from the disk. A hard γ-ray spectrum is also observed, which is generally not seen in high redshift blazars. Overall, J0809+5341 could be an exceptional source, or it is also possible that there is a whole population of such sources yet to be discovered.

A dense multi-wavelength monitoring of 3C 279 has revealed many peculiar features of the radiative processes working in the jet of this source. The broadband flux variability behavior show a simultaneous flux enhancement during the two γ-ray flares (2014 April and 2015 June), whereas, during 2013 December flare no such correlation is observed. Moreover, a statistically significant curvature is noticed for the 2014 April and 2015 June event. On the other hand, 2013 December flare displays a hard rising spectrum. The observation of the uncorrelated variability behavior and a rising γ-ray spectrum with falling optical-UV counterpart has ruled out the applicability of commonly accepted one zone leptonic models and therefore a two-zone leptonic modeling is adopted. Interestingly, both the 2014 April and 2015 June γ-ray outbursts can be explained on the basis of single zone leptonic modeling. All these observations hint for the presence of a variety of the radiative processes and their dominance over each other, as seen during different high activity periods of 3C 279.

Ultra-fast flux variations have been observed from a number of BL Lac objects at TeV energies (e.g., Albert et al. 2007). However, due to lack of sensitive hard X-ray instruments, it was not possible to analyze the connection between TeV and hard X-ray energy bands. This becomes more important due to the fact that both radiations are expected to be emitted by the electrons of similar energies (in one zone leptonic scenario). The availability of hard X-ray focusing telescope *NuSTAR* provides a unique opportunity to fill this gap. The 2013 April X-ray outburst of Mrk 421 was contemporaneously monitored by both ground based VHE observation facilities as well as by *NuSTAR*. A detailed analysis of *NuSTAR* data reveals the detection of minute scale hard X-ray flux variations. Prior to this work, such a fast variability in hard X-ray band was never observed from Mrk 421. The subsequent analysis suggests the magnetic reconnection to be a probable origin of such fast varying flaring events.

Chapter 4

Gamma-ray Loud Narrow Line Seyfert 1 Galaxies

The monitoring from *Fermi*-LAT has established the fact that the high energy extra-galactic sky is dominated by blazars (e.g., Acero et al. 2015). Along with blazars, *Fermi* has also discovered variable γ-ray emission from five RL-NLSy1 galaxies (Abdo et al. 2009a,b; D'Ammando et al. 2012). This unambiguously established the presence of closely aligned relativistic jets in these sources. However, it is not clear whether other physical properties of these γ-NLSy1 galaxies are also similar to blazars. In this thesis, a systematic investigation is carried out to understand the nature of these objects along with the comparison of their physical characteristics with blazars.

The sample consists of five γ-NLSy1 galaxies which are known to emit significant emission in the γ-ray band. General information about these five γ-NLSy1 galaxies are given in Table 4.1. The given radio spectral indices are calculated using the 6 cm and 20 cm flux densities found in Véron-Cetty & Véron (2010) ($S_\nu \propto \nu^\alpha$) and the values of radio loudness parameter R are adopted from Foschini (2011).

Table 4.1: Basic information of the γ-NLSy1 galaxies studied in this work

Name	RA (J2000) (h m s)	Dec (J2000) (d m s)	z	V (mag)	α_R	R
1H 0323+342	03:24:41.2	+34:10:45	0.063	15.72	-0.35	318
SBS 0846+513	08:49:58.0	+51:08:28	0.584	18.78	-0.26	4496
PMN J0948+0022	09:48:57.3	+00:22:24	0.584	18.64	0.81	846
PKS 1502+036	15:05:06.5	+03:26:31	0.409	18.64	0.41	3364
PKS 2004−447	20:07:55.1	-44:34:43	0.240	19.30	0.38	6358

4.1 Intra-Night Optical Variability[1]

Blazars show large amplitude optical variability (>3%) and a high duty cycle of about 70% (e.g., Sagar et al. 2004). Among blazars, γ-ray detected objects show more INOV compared to non γ-ray-detected blazars, thus pointing to an association between INOV and relativistic jets that are more aligned to the observer's line of sight (Gopal-Krishna et al. 2011). Therefore, another independent proof of the existence of relativistic jets oriented at small angles to the observer in the γ-NLSy1 galaxies is the detection of INOV on hr to sub-hr timescales. Out of five γ-NLSy1 galaxies, four are in northern hemisphere and one is in southern hemisphere. Therefore, all four northern hemisphere γ-NLSy1 galaxies are selected for night observations. All the observations were carried out using the 1.3 m telescope at Devasthal and 2 m HCT at Hanle. The details of the instruments are given in Chapter 2 and the log of observations are provided in Table 4.2.

The DLCs are generated from the derived instrumental magnitudes, for the given γ-NLSy1 galaxy relative to steady comparison stars. The list of selected comparison stars, consisting the J2000 epoch coordinates and R band apparent magnitudes, are given in Table 4.3. As the radiation from the central nucleus of the γ-NLSy1 galaxy dominates the host galaxy emission, there is negligible host galaxy contribution to the photometry (e.g., Cellone et al. 2000). The obtained intranight DLCs of the four γ-NLSy1 galaxies are presented in Figure 4.1, 4.2, 4.3, and 4.4. To judge the variability nature of the sources, two comparison stars are used A source is considered to be variable only when it shows correlated variations both in amplitude and time relative to both the comparison stars. Selection of comparison stars is done in such a manner that they are in close proximity to the source of

---

[1] The results presented for INOV are published in Paliya et al. (2013a), Paliya et al. (2014), and Paliya et al. (2016, ApJ, in press).

TABLE 4.2: Log of observations.

Source (1)	Date (2)	Telescope (3)	CCD mode (4)
1H 0323+342	12.01.24	1.3 m Devasthal	EM
	12.01.25	1.3 m Devasthal	EM
	12.01.26	1.3 m Devasthal	EM
	12.02.02	1.3 m Devasthal	Normal
	12.11.19	1.3 m Devasthal	Normal
	12.11.20	1.3 m Devasthal	Normal
	12.12.09	2 m HCT	Normal
SBS 0846+513	12.11.20	1.3 m Devasthal	Normal
	12.12.09	2 m HCT	Normal
	12.12.10	1.3 m Devasthal	Normal
	12.12.25	1.3 m Devasthal	Normal
	13.02.12	2 m HCT	Normal
	13.03.11	2 m HCT	Normal
PMN J0948+0022	12.01.26	1.3 m Devasthal	EM
	12.02.02	1.3 m Devasthal	Normal
	12.03.11	1.3 m Devasthal	Normal
	12.04.19	1.3 m Devasthal	EM
PKS 1502+036	12.04.18	1.3 m Devasthal	EM
	12.05.22	1.3 m Devasthal	Normal
	12.05.23	1.3 m Devasthal	Normal
	12.05.24	1.3 m Devasthal	Normal

Notes. Col.[1]: source name; Col.[2]: date of observations (yy.mm.dd); Col.[3] name of the telescope used; Col.[4]: CCD modes used; here "normal" refers to the 2k × 2k pixels^2 CCD and "EM" refers to the 512 × pixels^2 EMCCD.

TABLE 4.3: Positions and apparent magnitudes of the comparison stars from the USNO catalog (Monet et al. 2003).

Source	Star	RA (J2000) (h m s)	Dec. (J2000) (d m s)	R (mag)
1H 0323+342	S1	03:24:44.26	+34:09:31.84	15.17
	S2	03:24:51.24	+34:12:26.53	15.06
	S3	03:24:35.01	+34:09:36.73	15.81
SBS 0846+513	S1	08:49:38.49	+51:07:55.52	16.90
	S2	08:49:41.34	+51:10:57.97	16.90
	S3	08:50:16.73	+51:09:23.36	17.40
PMN J0948+0022	S1	09:49:00.44	+00:22:35.02	16.47
	S2	09:48:57.30	+00:24:18.53	16.15
	S3	09:48:53.69	+00:24:55.14	16.14
PKS 1502+036	S1	15:05:11.30	+03:22:25.57	15.24
	S2	15:05:15.90	+03:19:10.91	15.44
	S3	15:05:26.99	+03:24:37.25	15.71

interest and also have similar brightness. To access the variability nature of the sources, two criteria, *C*-statistics and *F*-statistics, are used.

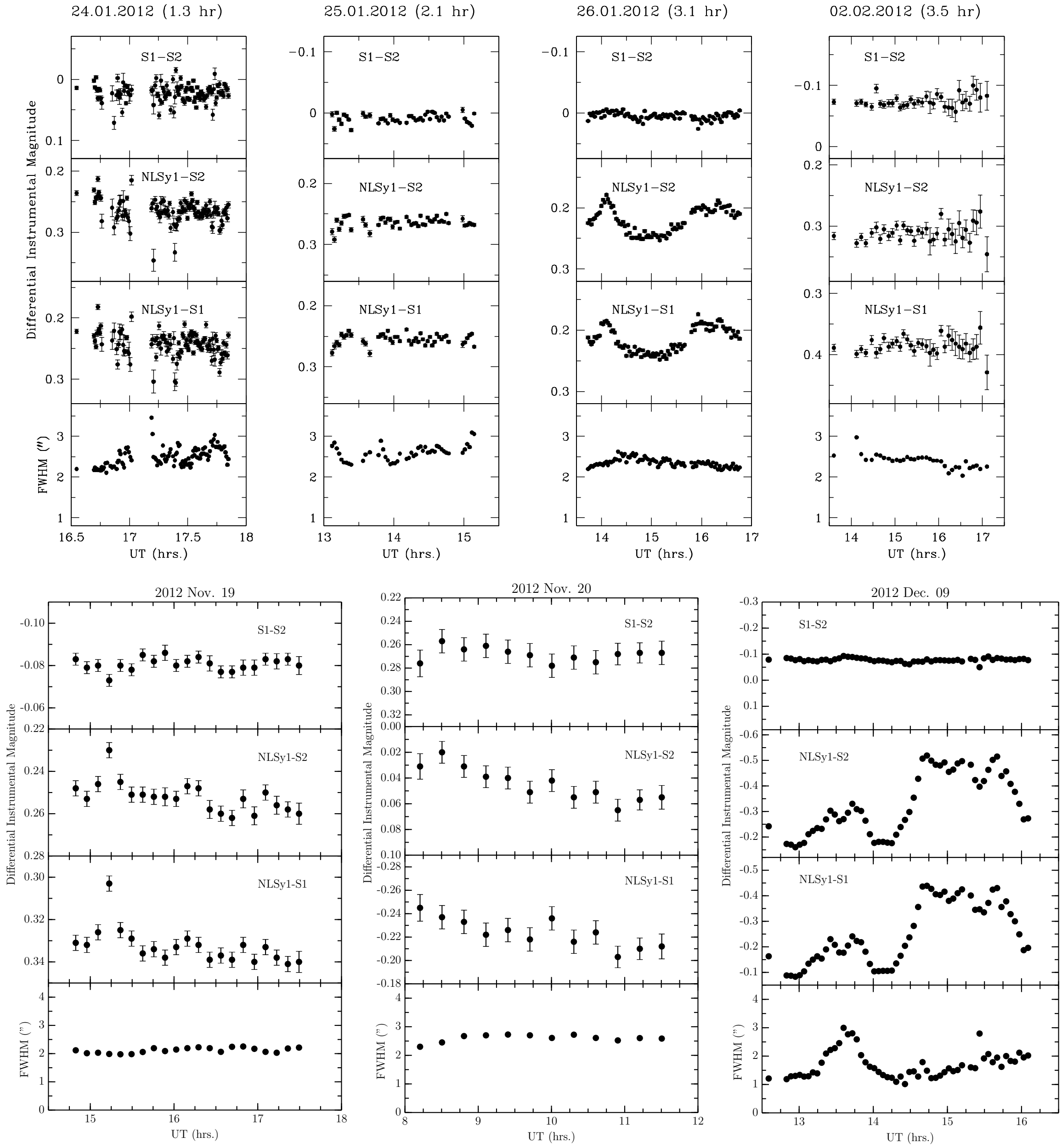

FIGURE 4.1: Intra-night DLCs of the source 1H 0323+342. The date of observation is given on the top of each panel. On the bottom panel of each night is given the variations of the FWHM of the stellar images during the monitoring period.

C-Statistics:

Following (Jang & Miller 1997), C-parameter is defined as

$$C = \frac{\sigma_{\text{target}}}{\sigma_{\text{star}}}, \tag{4.1}$$

where σ_{target} and σ_{star} are the standard deviations of the source and the comparison

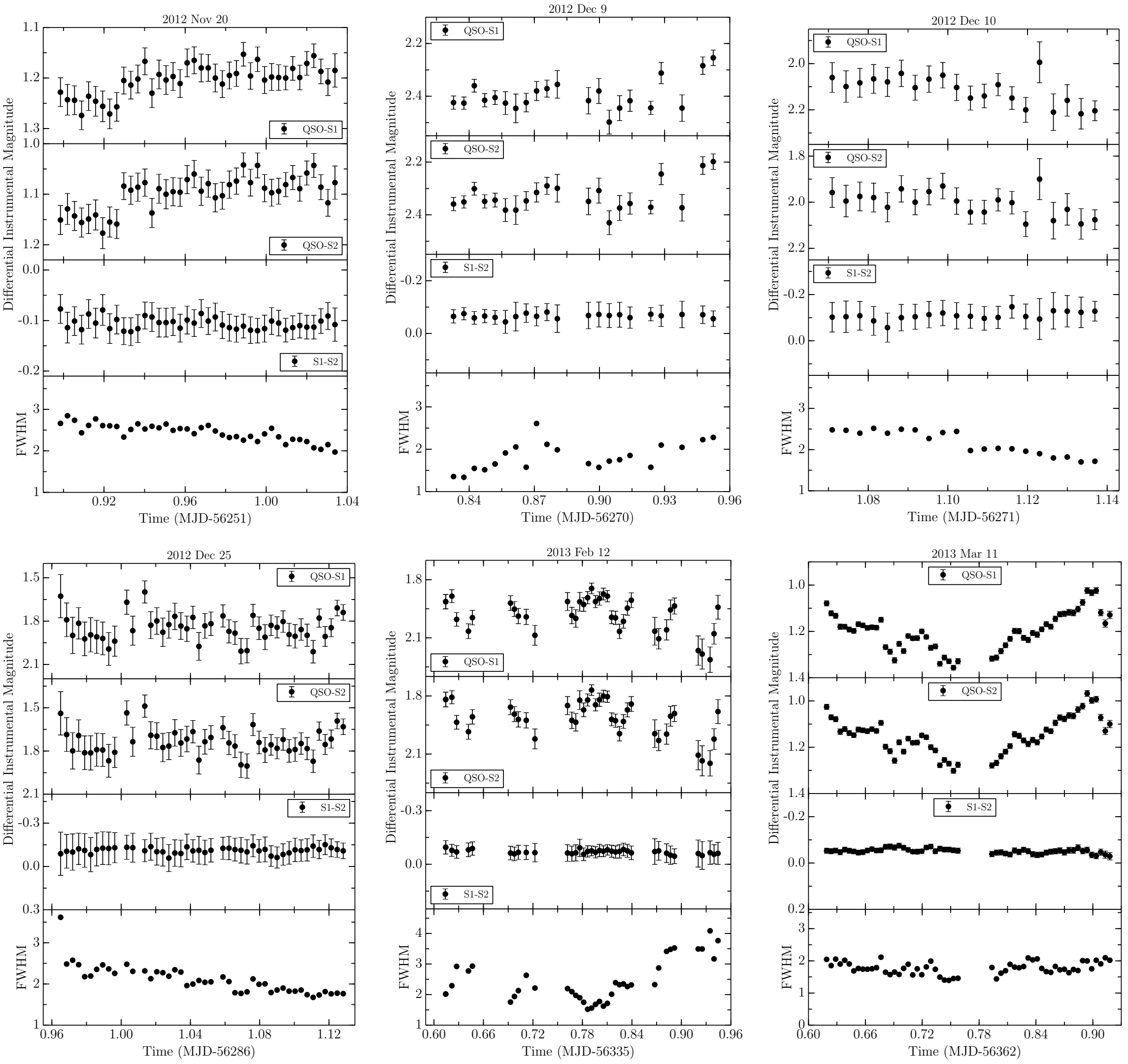

FIGURE 4.2: Intra-night DLCs of γ-NLSy1 galaxy SBS 0846+513. Other information are same as in Figure 4.1.

star DLCs. A source is considered to be variable if C-parameter is greater than 2.576, which corresponds to 99% confidence level (Jang & Miller 1997). Two values of C-parameter are derived, corresponding to two DLCs of the source relative to each of the two comparison stars. Using C-statistics, a source is considered to be variable, when both the calculated C values exceed 2.576. The results of this analysis are presented in Table 4.4.

F-statistics:

According to de Diego (2010), an alternative to C-statistics which can better assess the variations in AGN light curves is the F-statistics. This is defined as the ratio

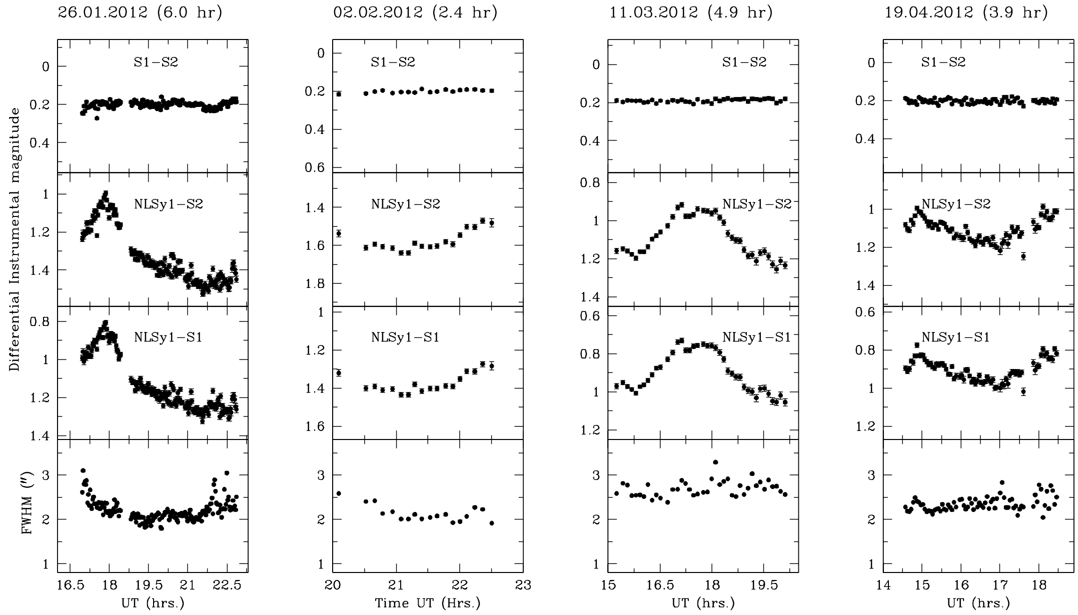

FIGURE 4.3: Intra-night DLCs for the γ-NLSy1 galaxy PMN J0948+0022. Other information are same as in Figure 4.1.

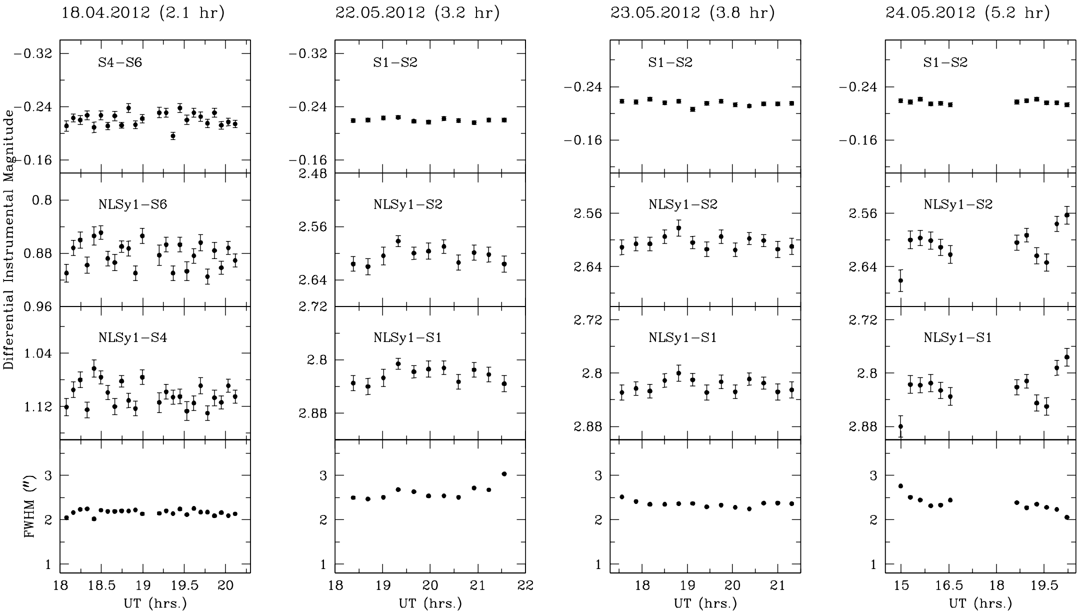

FIGURE 4.4: Intra-night DLCs for the γ-NLSy1 galaxy PKS 1502+036. Other information are same as in Figure 4.1.

of two variances

$$F = \frac{\sigma^2_{\rm target}}{\sigma^2_{\rm star}}, \tag{4.2}$$

where $\sigma^2_{\mathrm{target}}$ is the variance of the source−comparison star DLC and σ^2_{star} corresponds to the variance of the comparison stars DLC. Using Equation (4.2), two values of the F-parameter are derived for the source−star DLCs corresponding to each of the two comparison stars. The computed F-statistics is then compared with the critical F value, F^{α}_{ν} where α is the significance level and ν $(= N_p - 1)$ is the degree of freedom for the DLC. A significance level of $\alpha = 0.01$ is adopted which corresponds to a confidence levels of $> 99\%$. Thus, if both the calculated F values are greater than the critical F value, the source is considered to be variable. The derived results are presented in Table 4.4. It should be noted that the C-statistics might be a more conservative tool to test the presence of variability, particularly when the comparison star light curves are not steady. Also, the fluctuations in the FWHM of the point sources in the observed CCD frames during the course of the night might give rise to fictitious variations in the target NLSy1 galaxies. However, as can be seen, the flux variations of the γ-NLSy1 galaxies do not exhibit any correlation with the FWHM variations, therefore they are the genuine variations of the sources.

Amplitude of Variability (ψ):

The amplitude of variability (ψ), after correcting for the error in the measurements, is determined following the definition of Romero et al. (1999)

$$\psi = 100\sqrt{D_{\mathrm{max}} - D_{\mathrm{min}})^2 - 2\sigma^2}\,\% \tag{4.3}$$

with

D$_{\mathrm{max}}$ = maximum in the γ-NLSy1 DLC,
D$_{\mathrm{min}}$ = minimum in the γ-NLSy1 DLC, and
σ^2 = variance in the star−star DLC involving the steadiest pair of comparison stars.

Using Equation (4.3), the amplitude of variability is calculated for all the observations and reported in Table 4.4. In most of the observations, ψ is found to be greater than 3%, thus, suggesting the presence of significant INOV.

Duty Cycle of Variability:

Following Romero et al. (1999), the duty cycle (DC) is calculated. It is a well known fact that sources may not show variability on all the nights they were observed. Therefore, DC is evaluated by taking the ratio of the time over which the object shows flux variations to the total observing time. With this, DC is defined as

$$DC = 100\frac{\sum_{i=1}^{n} N_i(1/\Delta t_i)}{\sum_{i=1}^{n}(1/\Delta t_i)}\ \%, \tag{4.4}$$

where $\Delta t_i = \Delta t_{i,\mathrm{obs}}(1+z)^{-1}$ is the duration of the monitoring session of a source on the ith night, corrected for redshift. N_i is equal to 1 if INOV is detected, otherwise 0. If only C-statistics is used to judge the presence of INOV, a DC of 55% is obtained for γ-NLSy1 galaxies. However, using F-statistics, an increased DC of 81% is derived. Moreover, ψ is also found to be greater than 3% for all the objects, in most of the observations. Such high amplitude (ψ >3%), high DC (~70%) INOV are generally seen in the BL Lac objects (Stalin et al. 2004). Therefore, it can be concluded that INOV characteristics of γ-NLSy1 galaxies are similar to blazars. The present study, therefore, provides yet another strong argument in favor of the presence of highly beamed relativistic jets in these γ-NLSy1 galaxies, similar to the blazar class of AGN.

4.2 SED of γ-NLSy1 Galaxies[2]

γ-NLSy1 galaxies are found to show INOV properties similar to blazars. It is, therefore, intuitive to expect that the broadband SEDs of these objects should have a typical double hump structure, similar to blazars. If found to be blazar like SED, the modeling of their SEDs will help in comparing their properties both with FSRQs and BL Lac objects. This is because, the requirement of SSC mechanism to explain γ-ray emission will indicate their physical properties similar to BL Lac objects. On the other hand, if the additional EC process is necessary, then it would point towards their similarity more with FSRQs. Using non-simultaneous archival data, Abdo et al. (2009b) have first reported the similarity of the γ-NLSy1 galaxies with blazars. Later, D'Ammando et al. (2012) and Foschini et al. (2012) performed a deeper investigation of two sources, SBS 0846+513 and PMN J0948+0022, and suggested their similarity more with FSRQs. With this information available, in this work, broadband SED modeling of remaining three γ-NLSy1 galaxies (Table 4.1) have been done and the results are described in the following sections.

---

[2] The results presented for SED of γ-NLSy1 galaxies are published in Paliya et al. (2013b), Paliya et al. (2014), and Paliya et al. (2016, ApJ, in press).

Table 4.4: Statistical parameters of INOV observations.

Source (1)	Date yy.mm.dd (2)	ψ (%) (3)	*F1* (4)	*F2* (5)	Status (6)	*C1* (7)	*C2* (8)	Status (9)
1H 0323+342	12.01.24	12.69	1.90	1.74	V	1.38	1.32	NV
	12.01.25	—	1.41	1.36	NV	1.19	1.17	NV
	12.01.26	7.35	12.45	12.41	V	3.53	3.52	V
	12.02.02	—	1.766	2.15	NV	1.33	1.47	NV
	12.11.19	3.41	5.30	3.69	V	2.73	2.37	NV
	12.11.20	4.34	4.88	3.81	NV	2.23	1.77	NV
	12.12.09	35.74	279.81	276.54	V	16.63	16.63	V
SBS 0846+513	12.11.20	11.99	6.85	8.60	V	2.62	2.93	V
	12.12.09	24.37	48.78	47.33	V	6.98	6.88	V
	12.12.10	22.15	11.00	8.53	V	3.32	2.92	V
	12.12.25	41.30	20.67	20.32	V	4.55	4.51	V
	13.02.12	36.76	57.15	62.50	V	7.56	7.91	V
	13.03.11	33.27	62.53	58.38	V	7.91	7.64	V
PMN J0948+0022	26.01.12	51.92	114.43	107.99	V	10.70	10.39	V
	02.02.12	17.12	54.45	56.27	V	7.41	7.50	V
	11.03.12	33.13	168.34	161.50	V	12.98	12.71	V
	19.04.12	25.25	24.071	25.50	V	4.91	5.05	V
PKS 1502+036	18.04.12	6.49	3.26	3.913	V	1.81	1.98	NV
	22.05.12	3.58	21.74	23.75	V	4.66	4.87	V
	23.05.12	3.16	8.429	10.19	V	2.90	3.19	V
	24.05.12	10.09	93.04	86.51	V	9.65	9.30	V

Notes. Col.[1]: source name; Col.[2]: date of observation; Col.[3]: INOV amplitude in percent; Col.[4] and [5] *F*-values computed for the γ-NLSy1 galaxy DLCs relative to the steadiest pair of comparison stars on any night; Col.[6]: variability status according to *F*-statistics: V: variable, NV: non-variable; Col.[7] and [8] values of *C* for the two γ-NLSy1 galaxy DLCs relative to the two comparison stars; and Col.[9] variability status as per *C*-statistics.

4.2.1 1H 0323+342

To construct the broadband SED, first the long-term multi-frequency light curves of 1H 0323+342, covering from 2008 August 5 to 2013 September 15, are generated and shown in Figure 4.5. In this plot, *Fermi*-LAT data are weekly binned, whereas, *Swift*-XRT data corresponds to one point per observation ID. From the long term multi-wavelength light curves, a low activity (Q) and three flaring activity states (annotated as F1, F2, and F3) are selected for broadband SED generation and modeling. It should be noted that the simultaneous UVOT data corresponding to the XRT observations are also selected, though not shown in Figure 4.5. The fluxes over different wavelengths are averaged over each of the four time intervals considered for modeling.

The results of the SED modeling are shown in Figure 4.6 and the parameters are given in Table 4.5. In all the activity states, the optical-UV spectrum is dominated

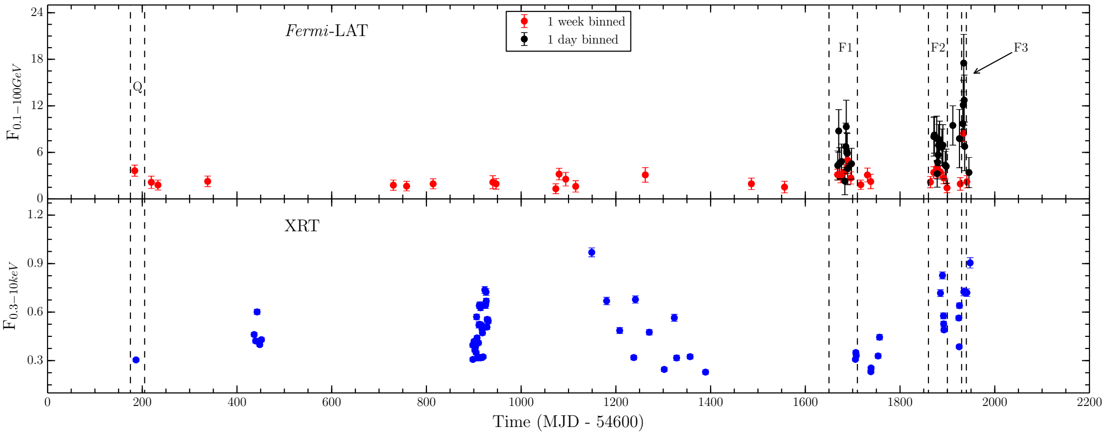

FIGURE 4.5: Flux history of 1H 0323+342 in high energy X-ray and γ-ray bands. Symbol Q corresponds to a quiescent state while F1, F2, and F3 are three flaring states when enhanced γ-ray emission is detected. *Swift*-XRT and *Fermi*-LAT data points are in units of counts s^{-1} and 10^{-7} ph $cm^{-2}\,s^{-1}$, respectively.

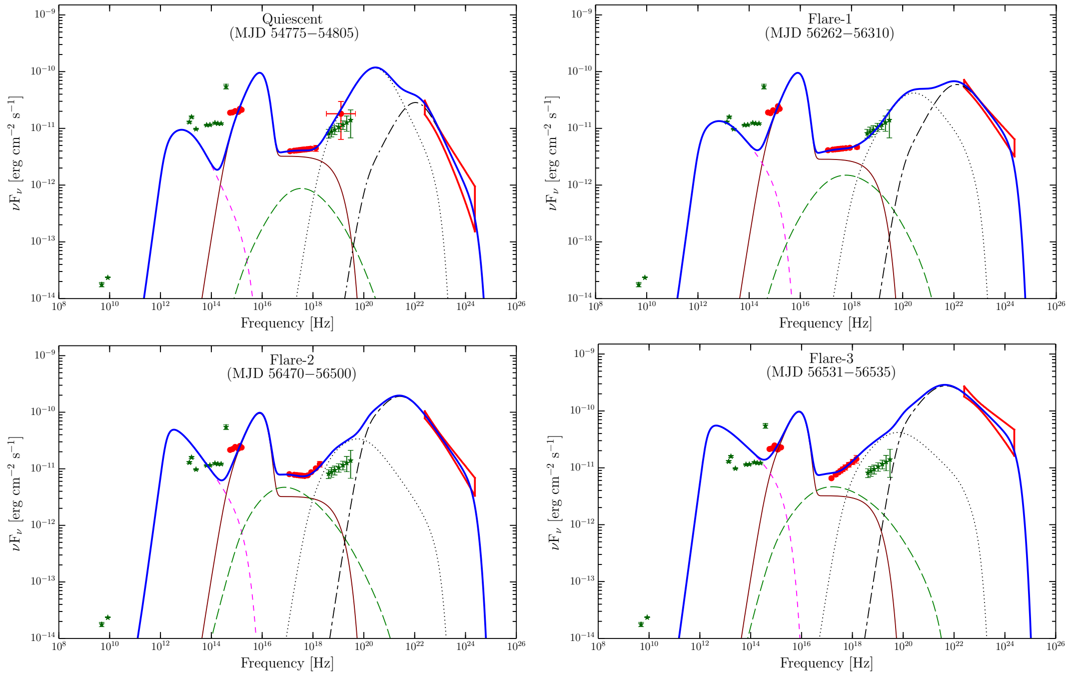

FIGURE 4.6: SEDs of 1H 0323+342 during different activity states. Simultaneous *Swift*-UVOT, XRT (filled circles) and *Fermi*-LAT (bow-tie plot) observations are shown by red color. Archival data are shown with dark green color. In the quiescent state SED, simultaneous 15−150 keV *Swift*-BAT observation is also shown. The 70 month averaged *Swift*-BAT spectrum is also displayed, though it is not used for modeling. Thin solid line (maroon color) shows thermal emission. The synchrotron (pink), SSC (green) EC-disk and EC-BLR (black) processes are shown with dashed, long dashed, dotted and dotted dashed lines, respectively. Blue continuous line is the sum of all radiative components.

Table 4.5: Summary of SED parameters for 1H 0323+342.

Parameter	Q	F1	F2	F3
log $L_{\rm corona}$ [1]	43.41	43.41	43.41	43.41
p	1.2	1.2	1.6	1.6
q	4.9	4.2	4.3	3.9
B	7	5.3	6.2	6.4
Γ	7	7	7	8
U'_e	1.95	1.12	1.53	1.63
$\gamma'_{\rm min}$	15	15	15	10
$\gamma'_{\rm b}$	150	150	75	70
$\gamma'_{\rm max}$	2000	2000	2000	2000
$\rm R_{diss}$	625 (1.2×10^{-3})	1096 (2.1×10^{-3})	1827 (3.5×10^{-3})	1463 (2.8×10^{-3})
P_r	41.29	41.36	41.74	41.62
P_p	44.06	44.22	45.03	45.14

Notes. The black hole mass and the disk luminosity are adopted as $2 \times 10^7\ M_\odot$ and 1×10^{45} erg s^{-1}, respectively. Accordingly, the size of the BLR is 0.03 pc. The symbols have the same units as given in Table 3.6.

[1] Corona luminosity in log scale.

by the accretion disk emission. The γ-ray emission can be well explained by EC scattering of BLR photons, thus, suggesting the location of the emission region to be within the BLR. A significant contribution from the X-ray corona is observed in the quiescent (Q) and first flaring (F1) states. However, during other two flaring states (F2 and F3), the X-ray spectrum is dominated by non-thermal jet emission. The X-ray spectrum of the second flare (F2) exhibits a break which can be explained as a dominance of SSC and X-ray corona in the soft X-ray band, whereas EC-disk takes over at hard X-rays. In the third flare (F3), the X-ray spectrum becomes completely dominated by jet. A hardening of the γ-ray spectrum in brighter state is also noted.

During flaring states, an increase in SSC emission is noticed, which is attributed to increase in the magnetic field. Assuming the equipartition between magnetic energy density (U'_B) and particle energy density (U'_e), increase in U_B leads to enhancement of U'_e (see Table 4.5). This explains the hardening of the γ-ray spectrum, as well as an increase of the EC-BLR flux, seen during the γ-ray flaring states. The EC-disk flux is found to be dominating over EC-BLR in the quiescent state SED, however, in all the three flaring states, the EC-BLR peak is higher than EC-disk. The relative dominance of EC-BLR and EC-disk processes depends on the relative energy densities of the disk ($U'_{\rm disk}$) and BLR radiation ($U'_{\rm BLR}$), measured in the comoving frame. These energy densities, in turn, are a function of the bulk Lorentz factor and the location of the emission region from the central source (see, Ghisellini & Tavecchio 2009, for a detailed discussion). The dependence of $U'_{\rm disk}$ and $U'_{\rm BLR}$ on the distance of the emission region from central engine is shown in Figure 4.7. In this plot, the location of the emission region during different

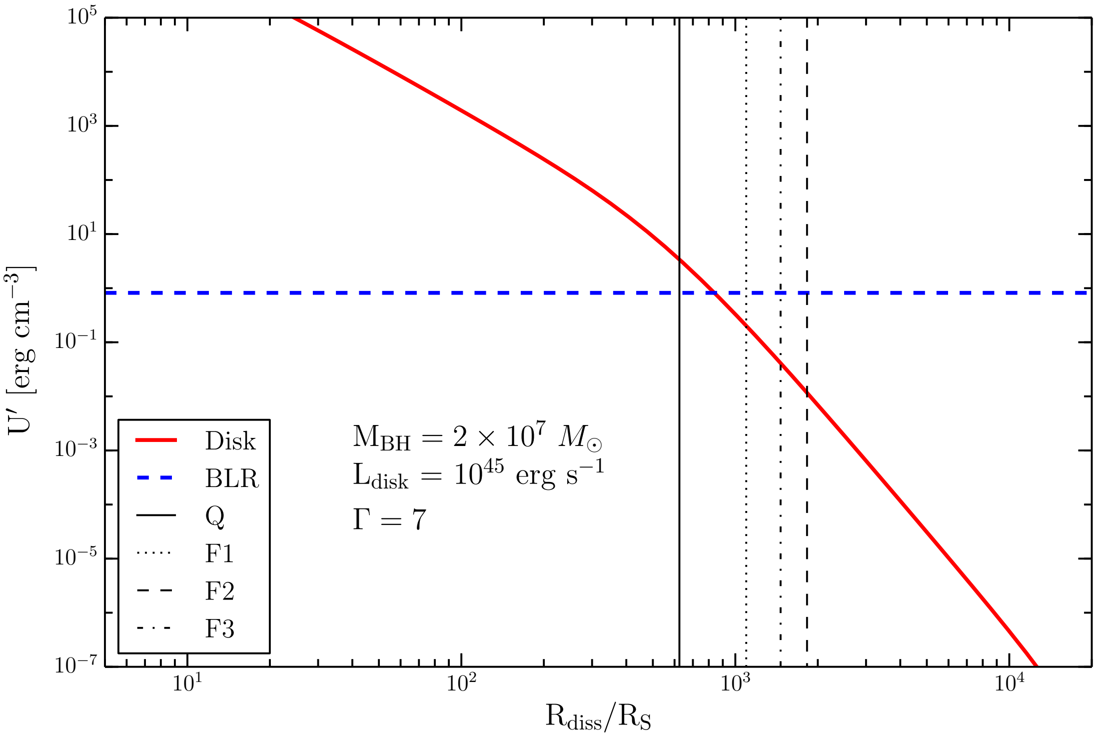

FIGURE 4.7: Variation of comoving frame disk and BLR energy densities as a function of dissipation distance (in units of Schwarzschild radius), for 1H 0323+342. Vertical lines show the location of the emission region for different activity states.

activity states are demarcated as vertical lines[3]. It is easy to understand from this figure that during the quiescent state $U'_{\rm disk}$ is higher than $U'_{\rm BLR}$, whereas, in all the three flaring states, $U'_{\rm BLR}$ dominates over $U'_{\rm disk}$. Therefore, the relative interplay of the two energy densities explains the dominance of EC-disk or EC-BLR during the different activity states of 1H 0323+342, as shown in Figure 4.7.

The 2013 September GeV outburst from 1H 0323+342 features a relatively hard γ-ray spectrum. Together with the large Compton dominance (see state F3 in Figure 4.6), this suggests that the bulk of the radiative energy is released prominently in the form of the high energy γ-rays. The 6 hr averaged isotropic γ-ray luminosity at the peak of the flare is derived as $L_{\gamma,iso} \simeq 4 \times 10^{46}$ erg s^{-1}. Correspondingly, the total power emitted in the γ-ray energy band, in the jet frame would be $L_{\gamma,em} \simeq L_{\gamma,iso}/2\Gamma^2 \simeq 3.1 \times 10^{44}$ erg s^{-1} (assuming bulk Lorentz factor $\Gamma = 8$, found from SED modeling). This is a significant fraction of the kinetic jet power ($\sim$ 23%; $P_{j,\ \rm kin} = 1.38 \times 10^{45}$ erg s^{-1}). This, in turn, implies that within a

---

[3] A negligible deviation in energy densities can be noted for $\Gamma = 8$, the bulk Lorentz factor considered for the SED modeling of state F3.

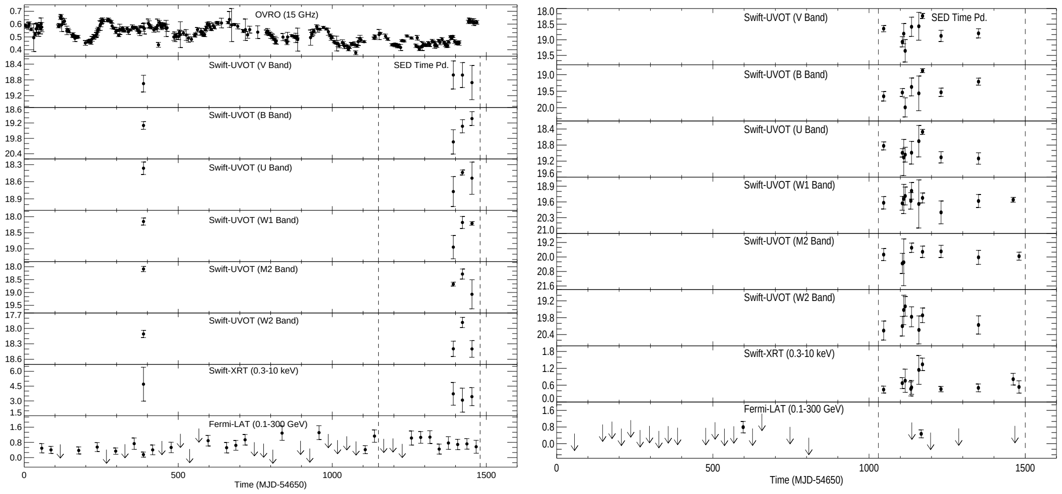

FIGURE 4.8: Multi-band light curves of PKS 1502+036 (left) and PKS 2004−447 (right). The OVRO data are in Jansky. UVOT data are in magnitude. XRT fluxes are in units of 10^{-13} erg cm^{-2} s^{-1} and 10^{-12} erg cm^{-2} s^{-1}, for PKS 1502+036 and PKS 2004−447, respectively. The *Fermi*-LAT data have the unit of 10^{-7} ph cm^{-2} s^{-1}. Downward arrows represent the 95% upper limits. The dashed vertical lines show the time interval selected for SED modeling.

few hours during this outburst, a considerable fraction of total kinetic luminosity carried out by the jet is transformed into radiation.

4.2.2 PKS 1502+036

The long-term multi-band light curves of the γ-NLSy1 galaxy PKS 1502+036 are shown in Figure 4.8. In the γ-ray band, flux values are obtained over 30 day binning, whereas, in the other bands each flux point corresponds to one observation of *Swift*. Though there are hints for the presence of variability in the multi-band light curves, a strong claim cannot be made due to sparseness of the data.

The broadband SED of PKS 1502+036 is generated using observations between MJD 55800 and 56130, as shown by vertical lines in Figure 4.8. Due to unavailability of good quality data and also due to faintness of the object, it is not possible to generate activity dependent SEDs. Therefore, only a time averaged SED is studied. The SED is modeled using the one-zone leptonic emission model described in Sahayanathan & Godambe (2012). The obtained results are shown in Figure 4.9 and the associated parameters are given in Table 4.6. As can be seen, the observed SED has a typical double hump structure similar to blazars. The optical-UV fluxes can be reproduced by synchrotron emission and the X-ray

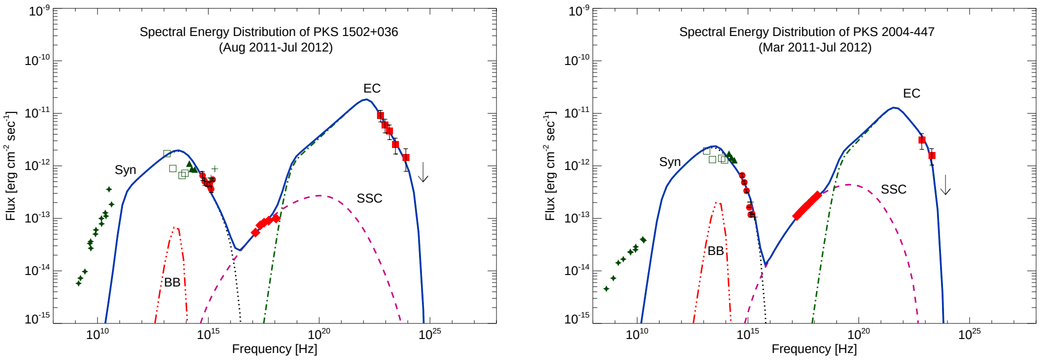

FIGURE 4.9: SEDs of γ-NLSy1 galaxies PKS 1502+036 (left) and PKS 2004−447 (right). Simultaneous flux from *Swift*-UVOT (filled circles), *Swift*-XRT (filled diamonds), and *Fermi*-LAT (filled squares) observations are shown with red symbols. The Vertical arrow depicts the 95% upper limit of γ-ray flux. Archival data are shown in green color: 2MASS (upward triangles Skrutskie et al. 2006), WISE (open squares; Wright et al. 2010), GALEX (plus sign; Martin et al. 2005), and Radio (filled star; NED). The dotted black line shows synchrotron emission. The SSC (pink) and EC (green) processes are shown by dashed and dotted-dashed line, respectively. The Blue continuous line is the sum of all radiative components. Around 10^{11} Hz, synchrotron self absorption is visible.

TABLE 4.6: Summary of the model parameters for the SED of PKS 1502+036 and PKS 2004−447.

Parameter	Symbol	PKS 1502+036	PKS 2004−447
Redshift	z	0.409	0.240
Particle spectral index (low energy)	p	2.22	2.10
Particle spectral index (high energy)	q	4.5	4.00
Magnetic field (equipartition)	B	0.60 G	0.72 G
Bulk Lorentz factor	Γ	12	9
Comoving emission region size	$R_{\rm blob}$	2.86×10^{16} cm	2.32×10^{16} cm
IR dust temperature in AGN frame	T^*	605 K	694 K
IR torus energy density in AGN frame	u^*	1.02×10^{-3} erg cm^{-3}	1.75×10^{-3} erg cm^{-3}
IR black body luminosity in AGN frame	L*	8.19×10^{43} erg s^{-1}	6.26×10^{43} erg s^{-1}
Particle energy density	U'_e	1.43×10^{-2} erg cm^{-3}	2.06×10^{-2} erg cm^{-3}
Minimum electron Lorentz factor	$\gamma'_{\rm min}$	30	60
Break electron Lorentz factor	$\gamma'_{\rm b}$	1870	1176
Maximum electron Lorentz factor	$\gamma'_{\rm max}$	1.8×10^4	7.5×10^3
Jet power	$P_{\rm j}$	3.1×10^{45} erg s^{-1}	8.5×10^{44} erg s^{-1}

flux by SSC process. The explanation of the γ-ray spectrum as an outcome of EC process requires the temperature of the external photon field to be 605 K. The spectrum of this external black body component, with luminosity of 8.19×10^{43} erg s^{-1}, is shown in Figure 4.9. The derived temperatures are consistent with that generally observed for the IR torus (Jaffe et al. 2004). The radio observation may be contaminated from the emissions from other extended region and hence do not satisfy the model curve.

4.2.3 PKS 2004−447

In the right panel of Figure 4.8, the multi-frequency light curves of PKS 2004−447 are presented. The *Fermi*-LAT data is monthly binned and *Swift* observations are one point per observation ID. Based on the availability of multi-wavelength data, the period MJD 55680−56130 is selected for SED generation and modeling. This period is shown with dashed lines in Figure 4.8 The modeled SED is shown in Figure 4.9 and the parameters associated to the modeling are presented in Table 4.6. Similar to other γ-NLSy1 galaxies, the SED of PKS 2004−447 also exhibit a double hump structure. The optical-UV spectrum of this object is dominated by synchrotron emission with no sign of the accretion disk radiation. The X-ray fluxes are well explained by SSC and an EC process is required to reproduce the γ-ray SED. Here, the seed photons for EC mechanism are assumed to be originated from a blackbody having a characteristic temperature of 694 K, which is typical to that of IR-torus.

The SED of the two γ-NLSy1 galaxies, PKS 1502+036 and PKS 2004−447, are further compared with that of blazars. Two well studied blazars, the FSRQ 3C 454.3 ($z = 0.859$) and the BL Lac object Mrk 421 ($z = 0.03$) are chosen for this purpose. The data analyzed for these two blazars are also taken for the same period as that used for the two γ-NLSy1 galaxies. The results of this comparison analysis are presented in Figure 4.10. It should be noted that during the period considered for spectral analysis, 3C 454.3 was in quiescence, while Mrk 421 was in an exceptionally bright state.

It is clear from Figure 4.10 that the synchrotron emission of 3C 454.3 peaks in the IR region, whereas the high energy EC emission peaks at MeV−GeV energies. On the other hand, for Mrk 421, the synchrotron emission peak lies in the UV−X-ray spectral band and the high energy SSC emission peaks in the GeV−TeV region. Though the optical-UV luminosities of the two γ-NLSy1 galaxies are similar to that of Mrk 421, their γ-ray luminosities are significantly higher than the flaring Mrk 421. This observation indicates that SSC alone cannot account for the high energy emission from these two γ-NLSy1 galaxies and that an additional mechanism (i.e., EC) is needed. Similar requirement is also noticed for the case of another γ-NLSy1 galaxy 1H 0323+342 (see Section 4.2.1). This suggests the similarity of γ-NLSy1 galaxies with FSRQs.

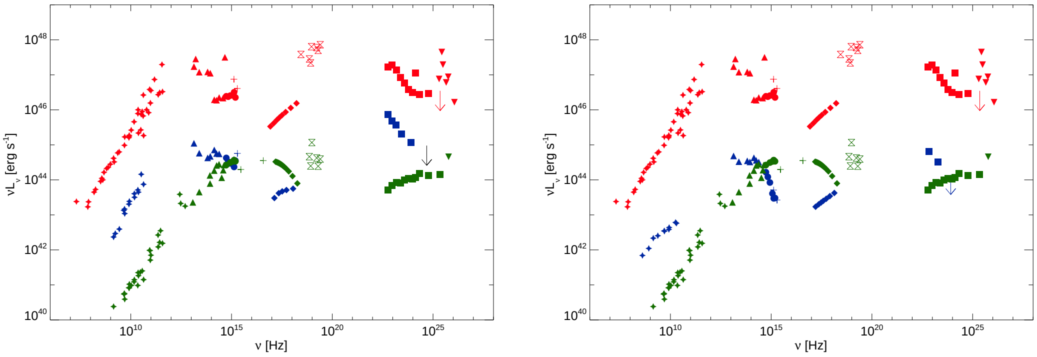

FIGURE 4.10: SEDs of γ-NLSy1 galaxies PKS 1502+036 (left panel) and PKS 2004−447 (right panel) along with that of 3C 454.3 and Mrk 421. Spectral data points of γ-NLSy1 galaxies are shown with blue colors, whereas, data points of 3C 454.3 and Mrk 421 are shown with red and green colors, respectively. *Fermi*-LAT data are shown with filled squares, while *Swift*-XRT and UVOT data are represented with filled diamonds and circles, respectively. Archival radio data are shown with filled stars, whereas, IR, UV and hard X-ray data are shown with filled upward triangles, plus sign, and hourglass, respectively. Filled downward triangles show the MAGIC (Anderhub et al. 2009) upper limit of 3C 454.3 and HAGAR Shukla et al. 2012 data of Mrk 421.

4.3 Gamma-ray Analysis of γ-NLSy1 Galaxies[4]

The observations of the rapid optical-IR flux variations and high and variable optical polarization from some of the γ-NLSy1 galaxies (Ikejiri et al. 2011; Liu et al. 2010; Paliya et al. 2013a; Jiang et al. 2012; Itoh et al. 2013) have strengthen the idea that these sources are similar to blazars. Moreover, modeling the SED of γ-NLSy1 galaxies also led to the similar conclusion. In this regard, a study of the γ-ray flux variability and spectral shapes of these sources will bring another dimension in understanding their physical properties. The motivation here is to see the similarities and/or differences in both the γ-ray flux variability and the γ-ray spectra of these sources with respect to the blazar class of AGN that emits copiously in the γ-ray band.

4.3.1 Long Term Gamma-ray Variability

The LAT light curves of the five γ-NLSy1 galaxies are presented in Figure 4.11. Based on the γ-ray brightness of the objects, different time binnings are adopted. The flux variations are quantified by calculating fractional rms variability and

---

[4] The results presented for γ-ray analysis of γ-NLSy1 galaxies are published in Paliya et al. (2015c).

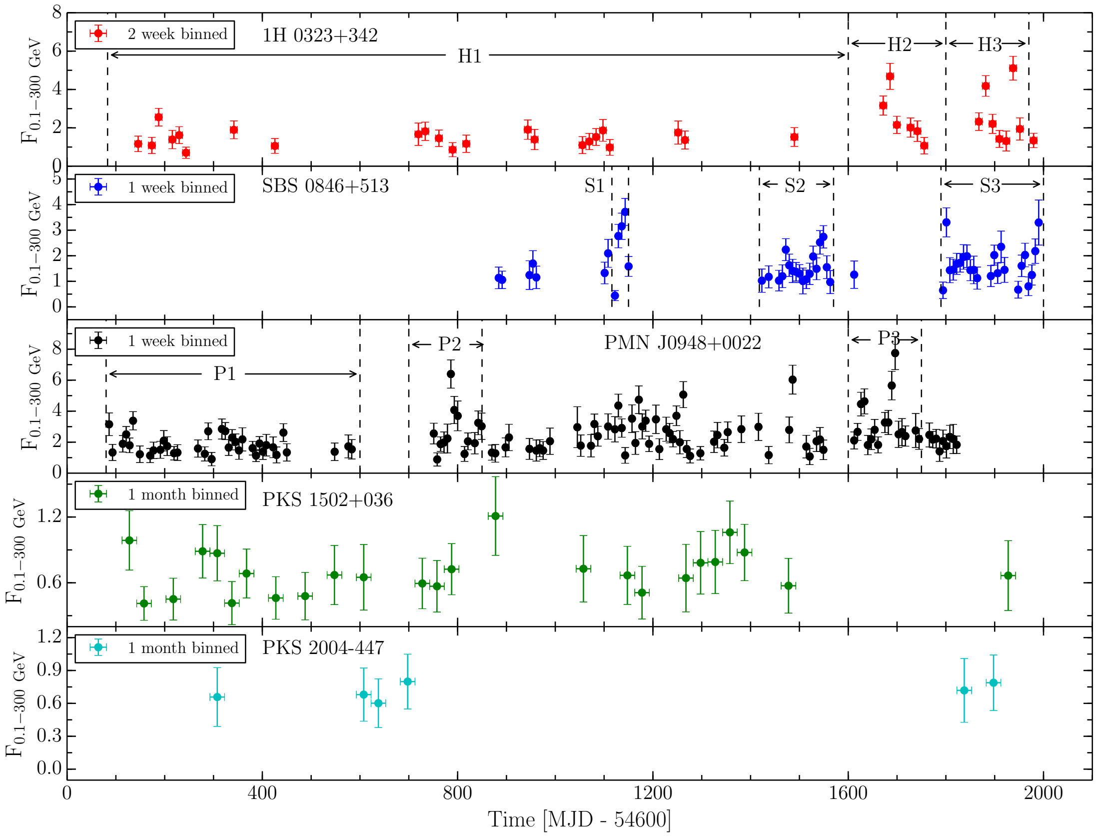

FIGURE 4.11: Long term γ-ray light curves of the γ-NLSy1 galaxies. Flux values are in units of 10^{-7} ph cm^{-2} s^{-1}. Different activity periods are marked with appropriate notations.

variability probability by means of a simple χ^2 test, following the prescriptions of Vaughan et al. (2003) and Abdo et al. (2010b), respectively. The obtained results are given in Table 4.7.

1H 0323+342:

1H 03232 was nearly steady in γ-rays during the first four years of the LAT observations, as can be seen in its bi-weekly binned γ-ray light curve in Figure 4.11. Later, it displayed flaring behavior at two epochs in 2013, one around MJD 56300 and the other around MJD 56500. These flaring periods are marked as H2 and H3 in Figure 4.11. The variability amplitude parameter $F_{\rm var}$ for this source is 0.498 ± 0.046 which is larger than that obtained for FSRQs ($\sim 0.24 \pm 0.01$) by Abdo et al. (2010b). The variability probability is >99% (Table 4.7), thus supporting the argument of substantial variability seen from this object.

TABLE 4.7: Fractional rms variability and variability probability for the γ-ray light curves (Figure 4.11) of the γ-NLSy1 Galaxies.

Name	Binning (days)	$F_{\rm var}$	Probability (%)
1H 0323+342	14	0.498 ± 0.046	> 99.0
SBS 0846+513	7	0.467 ± 0.042	> 99.0
PMN J0948+0022	7	0.443 ± 0.029	> 99.0
PKS 1502+036	30	–	34.5
PKS 2004−447	30	–	–

SBS 0846+513:

SBS 0846+513 was not included in the 2FGL catalog, thus, suggesting that it was in quiescence during the first two years of *Fermi* operation. A GeV flare observed by *Fermi*-LAT in 2011 led to the discovery of this NLSy1 galaxy in the γ-ray band (Foschini 2011). Later, multiple flaring episodes have been observed and they are annotated by S1, S2, and S3 in Figure 4.11. The probability that this source is variable is >99% and the $F_{\rm var}$ is 0.467 ± 0.042.

PMN J0948+0022:

PMN J0948+0022 is the first NLSy1 galaxy detected in the γ-ray band by *Fermi*-LAT. The weekly binned light curve reveals the peak flux value of $(7.74 \pm 1.07) \times 10^{-7}$ ph cm^{-2} s^{-1} observed during a GeV flare (D'Ammando & Orienti 2013). The source displayed many flaring activities and two of them are considered for further analysis (see period P2 and P3 in Figure 4.11). A $F_{\rm var}$ of 0.443 ± 0.029 is derived, which clearly indicates the existence of substantial flux variability in this object.

PKS 1502+036:

PKS 1502+036 has been frequently detected by *Fermi*-LAT, however, at a low flux level of $\sim 4.5 \times 10^{-8}$ ph cm^{-2} s^{-1}, as can be seen in the monthly binned light curve in Figure 4.11. The χ^2 analysis classifies the object to be a non-variable.

PKS 2004−447:

PKS 2004−447 is the γ-ray faintest member in the sample of γ-NLSy1 galaxies. No definite conclusion can be drawn about its flux variability behavior owing to the low photon statistics and no significant value of $F_{\rm var}$ could be obtained.

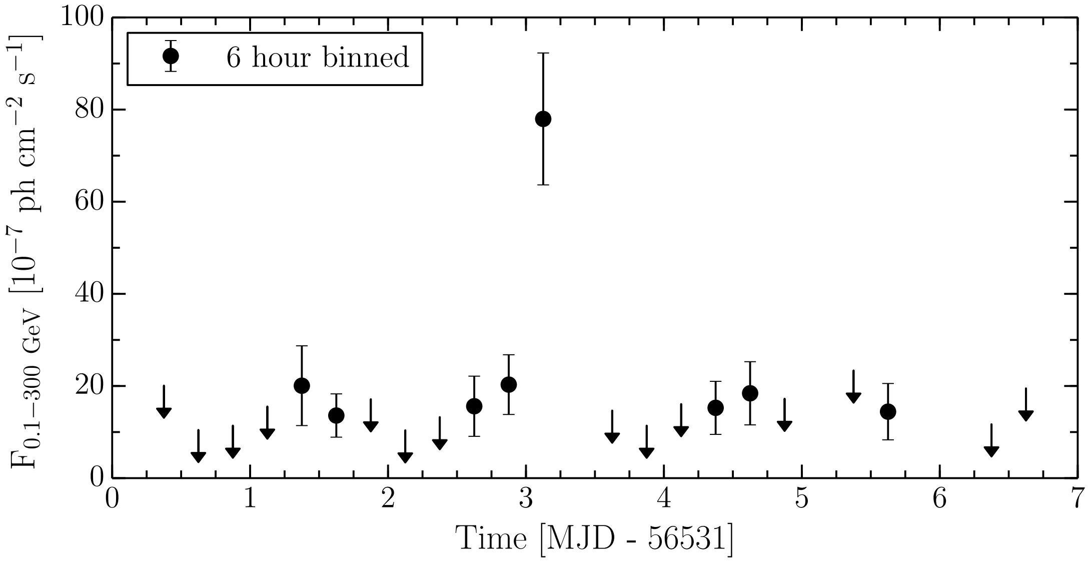

FIGURE 4.12: Six hr binned γ-ray light curve of 1H 0323+342 covering the period of GeV outburst in 2013 September. Upper limits, at 2σ level, are shown by downward arrows.

4.3.2 Short Term Gamma-ray Variability

The shortest timescale of flux variations constrains the size and the location of the γ-ray emitting region (see e.g., Tavecchio et al. 2010; Brown 2013). Therefore, it is important to search for the presence of flux variability over short timescales (of the order of hours) in the light curves of the γ-NLSy1 galaxies. Three out of five γ-NLSy1 galaxies, 1H 0323+342, SBS 0846+513, and PMN J0948+0022, have shown GeV outbursts. From the long term light curves of these objects, the epochs of high activities are selected and one day and 6 hr binned light curves are generated. The data are then scanned to calculate the shortest flux doubling/halving timescales.

1H 0323+342:

The good photon statistics during the epoch of GeV outburst from 1H 0323+342 in 2013 August-September (period MJD 56531−56535, in particular) has allowed to generate a 6 hr binned light curve (Figure 4.12). In contrast to the earlier reports where variability of the γ-NLSy1 galaxies were characterized over longer timescales ($\geqslant$1 day; e.g., Calderone et al. 2011; Foschini et al. 2012), this high activity period provides evidence of extremely fast variability observed from a γ-NLSy1 galaxy. A flux doubling time of 3.09 ± 0.85 hr is the fastest γ-ray variability ever observed from any NLSy1 galaxy. The highest flux in the 6 hr binned light curve is $(7.80 \pm 1.43) \times 10^{-6}$ ph cm^{-2} s^{-1}. This corresponds to an isotropic γ-ray luminosity

($L_{\gamma,\rm iso}$) of 2.82×10^{46} erg s^{-1}, which is ~100 times higher than the five year average value. The jet-frame γ-ray luminosity would be $L_{\gamma,\rm em} \simeq L_{\gamma,\rm iso}/2\Gamma^2 \simeq 2.20 \times 10^{44}$ erg s^{-1} (assuming a bulk Lorentz factor Γ=8; Paliya et al. 2014), which is ~16% of the Eddington luminosity adopting a black hole mass of 10^7 $M_\odot$ (Zhou et al. 2006).

SBS 0846+513:

Observation of a huge GeV flare in 2011 June led to the first time detection of SBS 0846+513 in the γ-ray band. During this period of high activity, a maximum daily averaged flux of $(8.20 \pm 0.08) \times 10^{-7}$ ph cm^{-2} s^{-1} is noticed, which is ~20 times higher than the five year average value. Further, re-binning the data into six hr bins resulted in the detection of even higher γ-ray flux of $(9.37 \pm 1.74) \times 10^{-7}$ ph cm^{-2} s^{-1}. Accordingly, the apparent γ-ray luminosity is $\sim 1.44 \times 10^{48}$ erg s^{-1}. Blazars, in general, and FSRQs in particular, are known to be emitters of such high power in the γ-ray band, thus supporting the argument made earlier regarding the similarity of the γ-NLSy1 galaxies with FSRQs. If a bulk Lorentz factor of 15 is assumed (D'Ammando et al. 2012), the total radiated power in γ-rays would be $L_{\gamma,\rm em}$ $\simeq$3.21 $\times$ 10^{45} erg s^{-1}, which is about 93% of the Eddington luminosity (assuming a BH mass of $10^{7.4}$ $M_\odot$; Yuan et al. 2008). There were many instances during this flaring period when the apparent isotropic γ-ray luminosity exceeds 10^{48} erg s^{-1} (e.g., MJD 55742 and 55745). The derived shortest flux halving time is $\sim 25.6 \pm 11.0$ hr.

PMN J0948+0022:

The brightest GeV flare from PMN J0948+0022 was observed in 2013 January (D'Ammando & Orienti 2013). During this flaring period, a maximum one day averaged flux of $(1.76 \pm 0.32) \times 10^{-6}$ ph cm^{-2} s^{-1} was observed on MJD 56293, which is about 14 times the five year average value and is similar to that noted by Foschini et al. (2012). On further dividing this active period into 6 hr bins, a maximum flux of $(2.40 \pm 0.83) \times 10^{-6}$ ph cm^{-2} s^{-1}is noticed. This corresponds to an isotropic γ-ray luminosity of 1.87×10^{48} erg s^{-1}, which is ~20 times its five year average. Accordingly, the total radiated power in the γ-ray band is $L_{\gamma,\rm em}$ $\simeq 4.16 \times 10^{45}$ erg s^{-1} (assuming $\Gamma = 15$). If the black hole mass of this object is assumed as $10^{7.5} M_\odot$ (Yuan et al. 2008), the radiated γ-ray power is about

TABLE 4.8: Details of the PL and LP model fits to the five year average LAT data of the γ-NLSy1 galaxies.

Name [1]	Model [2]	$F_{0.1-300\ \mathrm{GeV}}$ [3]	$\Gamma_{0.1-300\ \mathrm{GeV}}/\alpha$ [4]	β [5]	$L_{\mathrm{PL/LP}}$ [6]	TS [7]	$\mathrm{TS_{curve}}$ [8]
1H 0323+342	PL	7.54 ± 0.39	2.78 ± 0.05		44.4	732.3	
	LP	6.98 ± 0.40	2.66 ± 0.06	0.19 ± 0.05	44.3	738.3	17.36
SBS 0846+513	PL	4.35 ± 0.22	2.26 ± 0.03		46.7	1666.9	
	LP	3.73 ± 0.27	2.04 ± 0.07	0.09 ± 0.03	46.7	1660.4	15.03
PMN J0948+0022	PL	13.03 ± 0.36	2.62 ± 0.02		47.0	3299.8	
	LP	11.78 ± 0.37	2.35 ± 0.04	0.20 ± 0.03	46.9	3386.7	76.51
PKS 1502+036	PL	4.53 ± 0.35	2.63 ± 0.05		46.1	434.8	
	LP	4.29 ± 0.39	2.53 ± 0.10	0.06 ± 0.05	46.0	434.4	1.90
PKS 2004−447	PL	1.42 ± 0.24	2.38 ± 0.09		45.2	106.1	
	LP	0.91 ± 0.23	1.54 ± 0.36	0.42 ± 0.18	45.3	113.1	10.10

Notes. (1) Name of the object; (2) model used (PL: power law, LP: log-parabola); (3) integrated γ-ray flux (0.1−300 GeV), in units of 10^{-8} ph $\mathrm{cm^{-2}\,s^{-1}}$; (4) and (5): spectral parameters; (6) The PL and LP luminosities at logarithmic scale; (7) TS; and (8) TS of the curvature.

95% of the Eddington luminosity. The shortest variability timescale observed is 74.7 ± 27.6 hr.

4.3.3 Gamma-ray Spectral Shape

The analysis of the γ-ray spectral shape is done using a power law (PL) and a log parabola (LP) model. Following Nolan et al. (2012), the TS of curvature, $\mathrm{TS_{curve}} = 2(\log \mathrm{L_{LP}} - \log \mathrm{L_{PL}})$, is also calculated and the condition $\mathrm{TS_{curve}} > 16$ is applied to ascertain the presence of a significant curvature in the γ-ray spectra.

The results of the five year average spectral analysis of the γ-NLSy1 galaxies are given in Table 4.8. The γ-ray spectrum of two sources, 1H 0323+342 and PMN J0948+0022, are found to display a significant curvature. A $\mathrm{TS_{curve}}$ of $\sim$17 and $\sim$77 indicates that the LP model represents the data better than the PL model. A $\mathrm{TS_{curve}}$ of $\sim$15 also hints for the presence of curvature in the γ-ray spectrum of SBS 0846+513, though at a low significance. No significant curvature is noticed for the remaining two sources, probably due to low photon statistics. For better visualization of the spectral shape and to show the departure from a PL behavior, a binned likelihood analysis is performed on appropriately chosen energy bins covering 0.1−300 GeV. The results are presented in Figure 4.13. In this plot, the PL model is represented by the solid red line while the LP model is plotted by a green dashed line. It is evident from the residual plot (lower panel) of the PL model fits to the sources that the spectrum of 1H 0323+342 and PMN J0948+0022 show a clear deviation from the PL behavior, thus, confirming the $\mathrm{TS_{curve}}$ test. Additionally, hints for the presence of curvature can be seen in the residual plot of

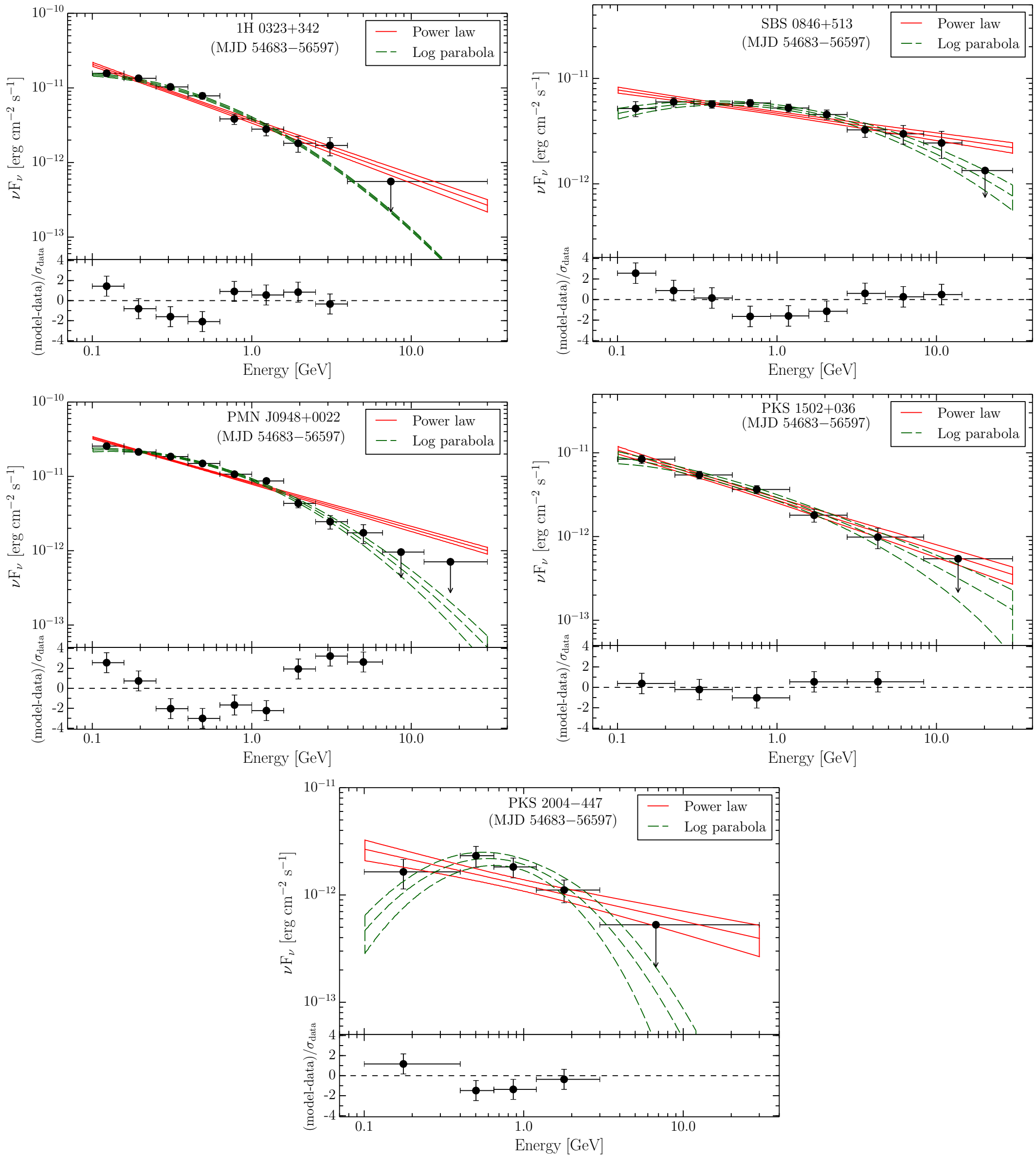

FIGURE 4.13: Five year average *Fermi*-LAT SEDs of the γ-NLSy1 galaxies. Solid and dashed lines represent PL and LP model fits with 1σ uncertainties, respectively. The residuals in the lower panels are with respect to the PL model.

SBS 0846+513. The derived curvature index β for PKS 2004−447 is found to be high and does not appear to be realistic because no significant curvature found in the γ-ray spectrum of this source. Thus, the unusual β value may be due to the poor photon statistics and hence unreliable.

Of the five γ-NLSy1 galaxies, three sources, 1H 0323+342, SBS 0846+513, and PMN J0948+0022, are relatively γ-ray bright and have shown flaring activities, thus, enabling to probe their spectral behavior during different activity states. For these sources, the periods of low and high states are selected and are marked in

Table 4.9: Details of the PL and LP model fits to the various brightness states of the γ-NLSy1 galaxies. The units are same as in Table 4.8.

Name [1]	Model [2]	$F_{0.1-300\ \mathrm{GeV}}$ [3]	$\Gamma_{0.1-300\ \mathrm{GeV}}/\alpha$ [4]	β [5]	$L_{\mathrm{PL/LP}}$ [6]	TS [7]	$\mathrm{TS}_{\mathrm{curve}}$ [8]
			1H 0323+342				
H1 (54,683–56,200)	PL	5.44 ± 0.46	2.83 ± 0.07		44.3	291.8	
	LP	4.89 ± 0.43	2.70 ± 0.09	0.34 ± 0.11	44.2	301.7	16.13
H2 (56,200–56,400)	PL	12.90 ± 1.23	2.67 ± 0.08		44.7	222.0	
	LP	11.60 ± 1.28	2.49 ± 0.12	0.21 ± 0.09	44.6	228.0	7.68
H3 (56,400–56,550)	PL	18.50 ± 1.51	2.68 ± 0.07		44.9	335.2	
	LP	17.80 ± 1.56	2.62 ± 0.09	0.08 ± 0.06	44.7	335.0	1.61
			SBS 0846+513				
S1 (55,716–55,746)	PL	21.90 ± 0.52	1.99 ± 0.01		47.6	608.6	
	LP	15.60 ± 0.22	1.21 ± 0.01	0.32 ± 0.01	47.8	634.8	29.53
S2 (56,018–56,170)	PL	12.20 ± 0.90	2.14 ± 0.05		47.2	917.0	
	LP	10.80 ± 0.95	1.92 ± 0.09	0.09 ± 0.03	47.2	919.3	6.87
S3 (56,390–56,597)	PL	12.20 ± 0.81	2.24 ± 0.05		47.1	983.9	
	LP	11.20 ± 0.87	2.08 ± 0.08	0.07 ± 0.03	47.1	981.5	5.20
			PMN J0948+0022				
P1 (54,683–55,200)	PL	11.70 ± 0.63	2.67 ± 0.05		46.9	842.9	
	LP	10.70 ± 0.62	2.40 ± 0.08	0.21 ± 0.05	46.9	866.0	21.72
P2 (55,300–55,450)	PL	14.40 ± 1.22	2.54 ± 0.06		47.1	323.2	
	LP	12.20 ± 2.13	2.14 ± 0.17	0.26 ± 0.06	47.0	331.2	12.02
P3 (56,200–56,350)	PL	24.00 ± 0.47	2.62 ± 0.01		47.3	756.9	
	LP	22.60 ± 0.19	2.44 ± 0.01	0.14 ± 0.01	47.2	764.5	7.65

Figure 4.11. PMN J0948+0022 has shown multiple episodes of GeV outbursts (e.g., D'Ammando & Orienti 2013) and the two brightest flares (P2 and P3) are chosen for further analysis. The time duration along with the parameters associated with the likelihood analysis are presented in Table 4.9. The spectra of the sources along with their best-fit model are also shown in Figure 4.14 and 4.15. A statistically significant curvature ($\sim 4\sigma$) is observed in the faint state spectrum of 1H 0323+342. However, the high activity states spectra are better represented by a power law model. A significant curvature ($\sim 5\sigma$) is also observed in the first flaring state (S1) of SBS 0846+513, similar to that reported by D'Ammando et al. (2012). However, no such feature is found in the other high activity state (S2) of this source. Further, the low activity γ-ray spectrum of PMN J0948+0022 exhibits a significant curvature. Interestingly, during the GeV outbursts, no curvature is observed (Table 4.9).

4.3.4 Gamma-ray Spectral Variations

The γ-ray spectrum of 1H 0323+342 is found to be harder in the high activity states. For example, in the bin centered at MJD 56285 (peak flux in the interval H2 in Figure 4.11), the photon index (2.51 ± 0.12) is significantly harder than the five year average value (2.78 ± 0.05). A hard photon index of 2.49 ± 0.11 is also observed during the 2013 August GeV outburst. The γ-ray spectra of

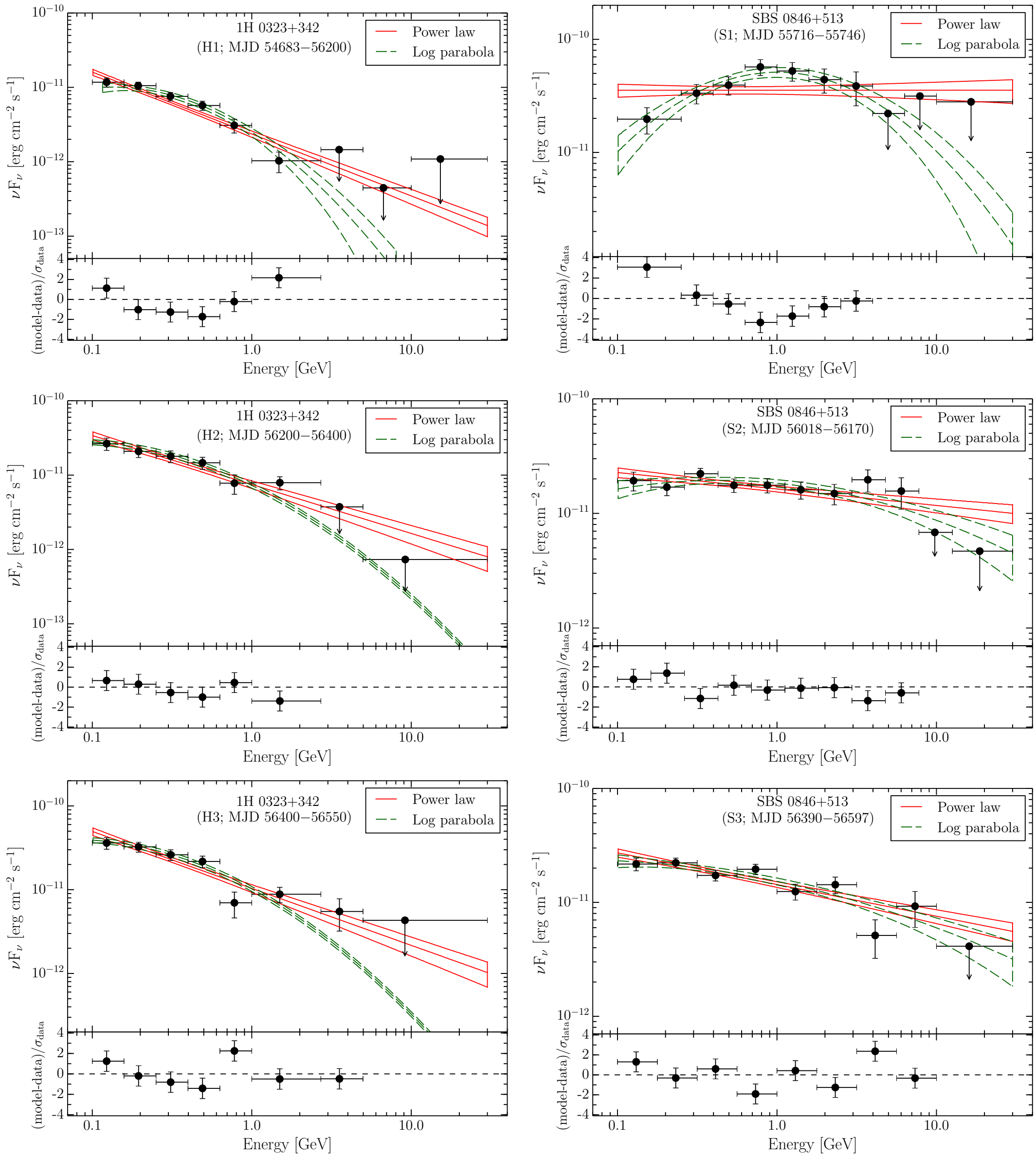

FIGURE 4.14: *Fermi*-LAT SEDs of 1H 0323+342 (left panels) and SBS 0846+513 (right panels) in their different brightness states. Other information are same as in Figure 4.13.

SBS 0846+513 also exhibit similar patterns. During its first GeV outburst, a hard photon index of 1.93± 0.09 is noticed, which is typical of high synchrotron peaked BL Lac objects (Ackermann et al. 2011). Similar “harder when brighter” trends have also been seen during the flaring periods of PMN J0948+0022. During its first γ-ray outburst in 2010 July, a photon index of 2.39 ± 0.12 is obtained which is significantly harder when compared to the five year average value of 2.62 ± 0.02. A maximum flux of (1.21 ± 0.36) × 10^{-7} ph $cm^{-2}\,s^{-1}$ is observed from PKS 1502+036 in the bin centered at MJD 55477 and the associated photon

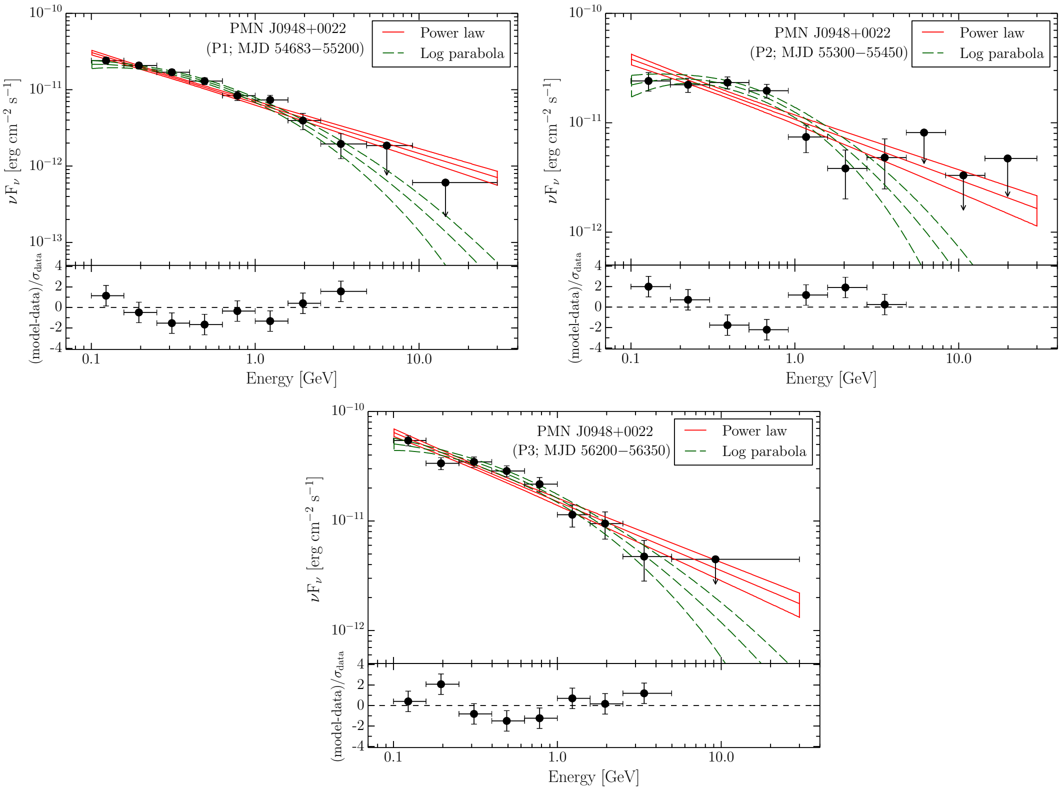

FIGURE 4.15: *Fermi*-LAT SEDs of PMN J0948+0022 during its different activity states. Other information are same as in Figure 4.13.

index is 2.83 ± 0.28 which is not significantly different from its five year average (2.63 ± 0.05). Spectral behavior of PKS 2004−447 could not be ascertained owing to its faintness.

To study the spectral evolution of the γ-NLSy1 galaxies, the photon indices are plotted against the fluxes in Figure 4.16. PKS 1502+036 exhibits a "softer when brighter" behavior whereas no conclusion can be drawn about PKS 2004−447 due to the small number of data points. Moreover, for remaining three sources, a "softer when brighter" trend is visible, up to a flux level of $\simeq 1.5 \times 10^{-7}$ ph cm^{-2} s^{-1}. Above this flux value, there is a hint for a "harder when brighter" trend. A Monte Carlo simulation, taking into account the dispersion in flux and photon index measurements, is adopted to statistically test these patterns. For each observed pair of flux and index values, a re-sampling is done by extracting the data from a normal distribution centered on the observed value and standard deviation equal to the associated 1σ error. This test is not performed on the data of PKS 1502+036 and PKS 2004−447 due to small sample size. For lower fluxes (i.e., $F_\gamma < 1.5 \times 10^{-7}$ ph cm^{-2} s^{-1}), the correlation coefficients (ρ) are found to be 0.21,

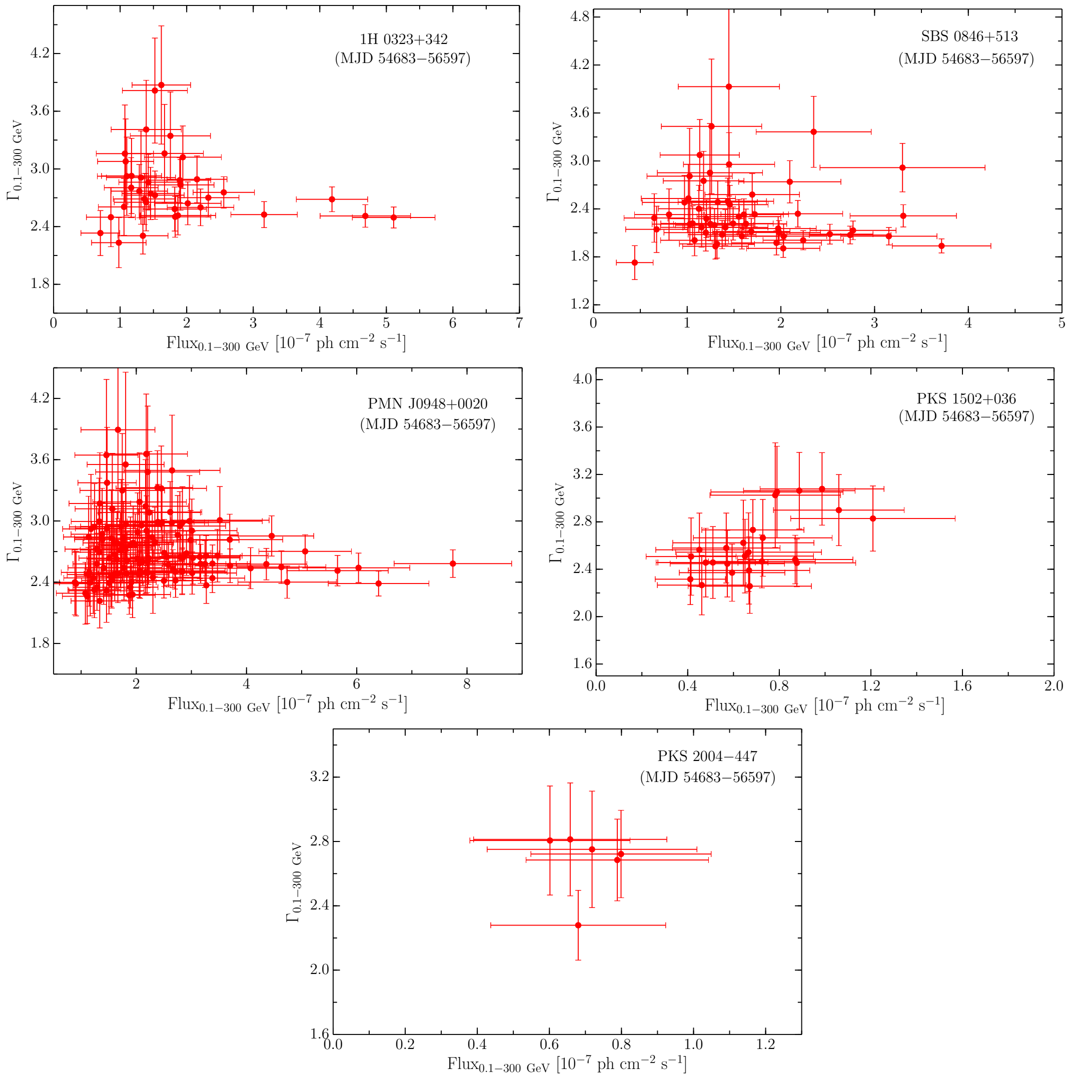

FIGURE 4.16: Photon index versus γ-ray flux plots of γ-NLSy1 galaxies obtained from the long term light curve analysis.

0.26, and 0.27 with 95% confidence limits of $-0.27 \leqslant \rho \leqslant 0.61$, $-0.03 \leqslant \rho \leqslant 0.51$, and $-0.05 \leqslant \rho \leqslant 0.54$, respectively, for 1H 0323+342, SBS 0846+513, and PMN J0948+0022. Moreover, for higher fluxes ($F_\gamma > 1.5 \times 10^{-7}$ ph cm^{-2} s^{-1}), the correlation coefficients are -0.32, -0.09, and -0.08 with 95% confidence limits of $-0.67 \leqslant \rho \leqslant 0.14$, $-0.48 \leqslant \rho \leqslant 0.33$, and $-0.27 \leqslant \rho \leqslant 0.12$, respectively, for 1H 0323+342, SBS 0846+513, and PMN J0948+0022. It is clear from the obtained parameters that a strong conclusion about the spectral behavior of γ-NLSy1 galaxies cannot be made based on the Monte Carlo analysis.

4.4 Summary of the Chapter: Gamma-ray loud NLSy1 Galaxies v/s Gamma-ray loud Blazars

4.4.1 Intra-night Optical Variability

Of the 5 sources in the sample of γ-NLSy1 galaxies, 4 have been observed to search for INOV over 21 nights. Using the widely accepted C-statistics, a DC of 55% is obtained which increases to 81% if F-statistics is considered. In most of the observations, the amplitude of variability is found to be >3%. Blazars are known to show such a high amplitude, high DC INOV. Therefore, the results of the INOV analysis of γ-NLSy1 galaxies clearly hints for their similarity with blazar class of AGN.

4.4.2 SED modeling

The SED of 3 γ-NLSy1 galaxies studied here show a typical double hump structure which is a characteristic feature generally observed in the SEDs of blazars. In all the cases, γ-ray emission could not be reproduced by SSC as it demands the parameters far from equipartition. The requirement of EC mechanism to explain the γ-ray emission in these sources indicate their similarity more with FSRQ category of blazars.

4.4.3 Gamma-ray Flux Variations

During the period 2008 August to 2013 November, a significant flux variation has been seen from three out of five γ-NLSy1 galaxies (1H 0323+342, SBS 0846+513, and PMN J0948+0022). However, due to the faintness and/or intrinsic low variability nature of the remaining two sources (PKS 1502+036 and PKS 2004−447), the same cannot be claimed. The derived $F_{\rm var}$ values for γ-NLSy1 galaxies are larger than that reported for FSRQs (0.24 ± 0.01) and BL Lac objects ($0.12 \pm 0.01, 0.07 \pm 0.02$, and 0.07 ± 0.02 for LSP, ISP, and HSP BL Lac objects, respectively; Abdo et al. 2010b). This gives another clear evidence that in terms of the γ-ray flux variations γ-NLSy1 galaxies are similar to the FSRQ class of AGN. Interestingly, during the 2013 September GeV outburst of 1H 0323+342, an extremely fast flux doubling time ($\sim$3 hr) is detected, which is the first time observation of hr scale γ-ray variability ever detected from any γ-NLSy1 galaxies. Such a short timescale flux variations are typically observed in powerful FSRQs (e.g., Abdo et al. 2011; Saito et al. 2013; Paliya et al. 2015b).

4.4.4 Shape of the Gamma-ray Spectrum

It is a well established fact that a curvature/break in the γ-ray spectrum is the characteristic properties of powerful FSRQs (e.g., Abdo et al. 2010c). The γ-ray spectra of three out of five γ-NLSy1 galaxies–1H 0323+342, SBS 0846+513 and PMN J0948+0022–show a clear departure from the power law and instead the log parabola model represents the data better. This observations gives another proof of the similarity of γ-NLSy1 galaxies with FSRQs.

4.4.5 Gamma-ray Luminosity and Spectral Indices

All the five sources studied in the thesis, exhibit steep photon indices and the average value is 2.55 ± 0.03. This is similar to the average photon index found for FSRQs (2.42 ± 0.17) in 2LAC (Ackermann et al. 2011) and is steeper than the value of 2.17 ± 0.12, 2.13 ± 0.14 and 1.90 ± 0.17 found for the low, intermediate and high synchrotron peaked BL Lac objects, respectively. Thus, in terms of the average γ-ray photon index these γ-NLSy1 galaxies are similar to FSRQs. The γ-ray luminosities of these objects are lesser compared to powerful FSRQs but higher than BL Lac objects (see Figure 4.17). As some of the γ-NLSy1 galaxies show evidence of the presence of spectral curvature and high flux variability, it can be argued based on the γ-ray properties that these sources show resemblance to FSRQs.

Positioning the blazars detected during the first three months of the *Fermi* operation on the γ-ray luminosity (L_γ) versus γ-ray spectral index (α_γ) plane, Ghisellini et al. (2009) have predicted the existence of low black hole mass FSRQs having steep α_γ and low L_γ. In the L_γ v/s α_γ diagram, the five γ-NLSy1 galaxies occupy a place where their spectral indices are steep and their L_γ values are intermediate

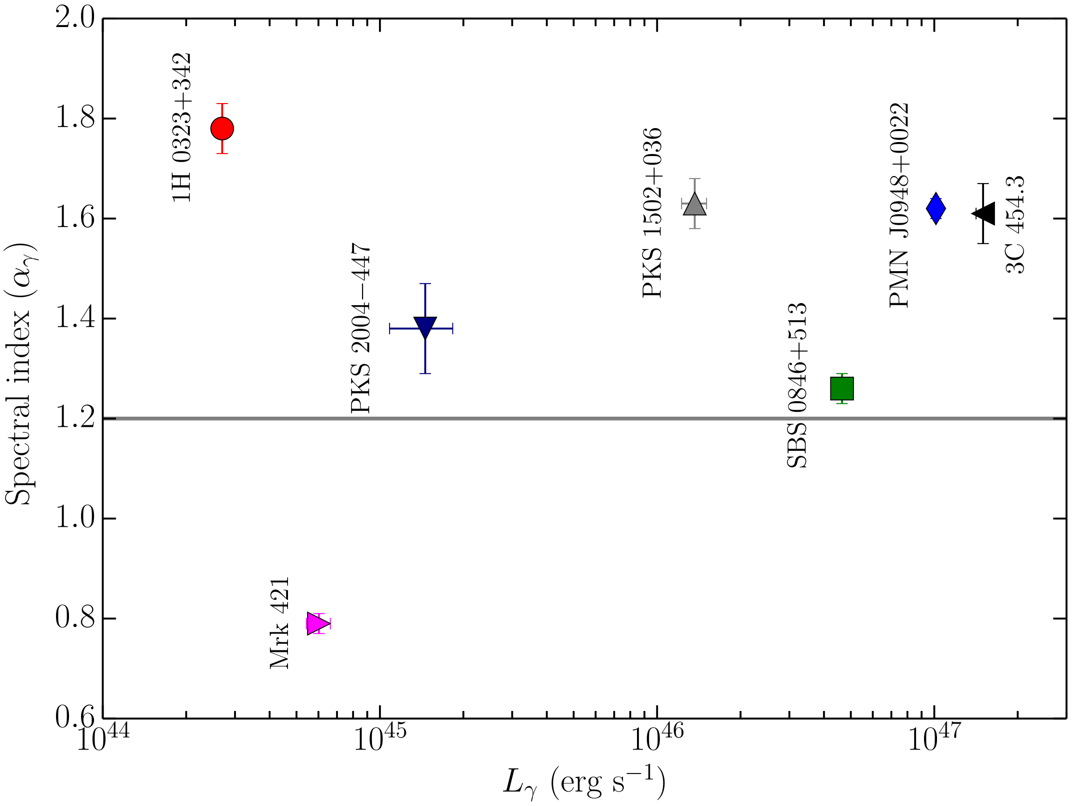

FIGURE 4.17: Variation of the spectral index (α_γ) against the γ-ray luminosity (L_γ). The horizontal grey line marks $\alpha_\gamma = 1.2$ (see Ghisellini et al. 2009).

to the FSRQ 3C 454.3 and the BL Lac object Mrk 421 (Figure 4.17). Further, from the estimates of black hole masses available in the literature, it is also apparent that these objects host low mass black holes (e.g., Zhou et al. 2006; Yuan et al. 2008; Oshlack et al. 2001). They appear to be on the higher side of the black hole masses known for NLSy1 galaxies in general (Komossa et al. 2006; Yuan et al. 2008), but lower than that known for powerful blazars (e.g., Ghisellini et al. 2010a). It is thus likely that these γ-NLSy1 galaxies are the low black hole mass FSRQs postulated by Ghisellini et al. (2009).

Chapter 5

Conclusions and Future Prospects

Blazars have been extensively studied for more than five decades and a significant progress have been made in our understanding of these objects. The emission from blazars is dominated by non-thermal processes, comprising the low energy radiation originates from synchrotron mechanism and the high energy emission primarily due to IC process. The origin of high energy γ-ray emission from blazars has always been an important problem in blazar physics. With EGRET, some progress were made to probe the MeV-GeV spectrum of a few blazars but the contemporaneous observations at other wavelength, closely matching with EGRET monitoring were done for ever fewer. The efforts in this direction got a major boost after the launch of *Fermi* Gamma Ray Space Telescope in the year 2008. Many programs were started as a support to *Fermi*-LAT monitoring[1] and this has allowed one to obtain near-simultaneous data from low energy radio band to high energy γ-rays. For the first time, a detailed fine time and energy resolved study of blazars is now possible, thanks to the excellent sensitivity of *Fermi*. This also led to the first time detection of significant γ-ray emission from about half-a-dozen RL-NLSy1 galaxies.

This thesis is an attempt to understand the radiative processes powering the relativistic jets in blazars. It also aim to characterize the multi-frequency properties of a new class of γ-ray emitting NLSy1 galaxies using both observational and theoretical modeling approaches and to compare them with that known from powerful blazars. Using the publicly available multi-wavelength data, a detailed

---

[1] `https://www.fermi.gsfc.nasa.gov/ssc/`

investigation of the possible correlation between various frequencies and also the determination of the shortest flux variability timescales, especially during the GeV outbursts, is done. A major emphasis is given on constraining the location of the γ-ray emitting region and ascertaining the dominance of various radiative processes for different activity epochs. A brief introduction and history about AGN, with a major emphasis on beamed AGN, is presented in Chapter 1. Chapter 2 is devoted to adopted data reduction techniques and the details of the developed leptonic model is also described in this chapter. The densely sampled multi-frequency observations of four blazars (S5 0836+71, BZQ J0809+5341, 3C 279, and Mrk 421) are investigated and the obtained results are discussed in Chapter 3. Chapter 4 of the thesis is devoted to the study of γ-NLSy1 galaxies.

5.1 Variability Studies

One of the important findings of this thesis is the discovery of extremely fast flux variability, both from low and high redshift blazars. A γ-ray flux doubling time as short as $\sim$1 hr is observed from 3C 279 during its 2014 April outburst, which is probably the shortest γ-ray flux variability ever detected from this source. Similar results are obtained for 2013 December and 2015 June flares.

The BL Lac object Mrk 421 underwent a violent X-ray flare in 2013 April and a deep study of *NuSTAR* observations has revealed the detection of minute scale hard X-ray flux variations. The derived flux doubling time ($\sim$15 minutes) is on the order of the light crossing time of the black hole's event horizon and thus possess questions on the validity of the conventional single zone radiative models. Moreover, a pattern of extremely fast variability events superposed on slowly varying flares is also noticed in most of the *NuSTAR* observations. Alternative hypothesis such as 'jet-in-a-jet' or magnetic reconnection model put forward by Giannios et al. (2009) can be used to explain this peculiar event. Though, minute scale flux variability has already been observed from many BL Lac objects at TeV energies (see, e.g., Albert et al. 2007; Aharonian et al. 2008), this is probably the first time detection of such a fast event at X-rays. High activities seen both at hard X-rays and VHE energies, thus, clearly support for a leptonic (plausibly SSC) cospatial origin of the X-ray and VHE γ-ray emission.

Hour scale flux variations have been detected from many nearby blazars, primarily due to availability of good photon statistics. However, high redshift objects also display similar features particularly during high activity states, and this is one of the unique finding of the thesis. The blazar S5 0836+71 showed high amplitude γ-ray flare at the end of 2011. A detailed analysis of this event discovered it as one of the most luminous γ-ray flare ever observed from any blazar. The derived shortest flux doubling time is $\sim$3 hr which is probably the fastest γ-ray flux variations ever seen from any blazar beyond redshift 2. The giant optical outburst of J0809+5341 was another surprising discovery. This is due to the fact that, in general, the optical emission from high redshift blazars is found to be dominated by the luminous accretion disk which is not expected to vary on short timescales.

The detection of hr scale γ-ray flux variability from the NLSy1 galaxy 1H 0323+342 during its 2013 September GeV outburst is the first measurement of such a fast flux variations from this class of AGN. Moreover, ground based optical monitoring of these sources resulted in the conclusion that they do show extremely fast brightness variations within the night. This, along with the detection of high duty cycle ($\sim$80%) of the optical variability, is another evidence that γ-NLSy1 galaxies are similar to blazars.

Overall, the following conclusions can be drawn from the variability study of different class of AGN, as done in the thesis.

- Short term flux variations are observed from all types of beamed AGNs, i.e., FSRQ, BL Lac objects, and γ-NLSy1 galaxies. This suggests the size of the emission region to be small and constrains the location of the emission region to be close to the central black hole, assuming a one zone emission model to be valid.

- This also hints at the similarity of the radiative processes powering the jets of γ-NLSy1 galaxies with that of blazars.

- Short term flux variation is possibly a common property of all types of beamed AGNs.

5.2 Radiative Mechanism Studies

The one zone leptonic emission model successfully reproduces the SEDs of both blazars and γ-NLSy1 galaxies, except the peculiar γ-ray flare of 3C 279 in 2013 December. On the other hand, 2014 April and 2015 June GeV flaring events of 3C 279 can easily be explained by this model. In both these outbursts, the modeling parameters indicate for the sudden increase in the bulk acceleration of the jet to be the most probable cause of the flare. Moreover, the location of the emission region at the time of the flares are found to be at the outer edge of the BLR where both BLR and IR torus provide the seed photons to produce γ-rays via IC scattering. A curved γ-ray spectrum, observed during these two flares, can be explained by adopting a broken power law particle energy distribution and due to Klein-Nishina effect. The 2013 December outburst of 3C 279, on the other hand, displayed an extremely hard γ-ray spectrum. Together with the observation of steeply falling optical spectrum, this suggests that a one zone leptonic emission model cannot reproduce the SED. An alternative approach, the two zone leptonic modeling, is then used. Multi-wavelength observations of 3C 279 during these three GeV outbursts, therefore, have clearly shown the dominance of various emission mechanisms at different epochs and hint for the complexity involved in understanding the jet properties.

The broadband SED modeling of the high redshift blazar S5 0836+71 has led to the conclusion that during all the activity states, the γ-ray emitting region lies inside the BLR where the primary mechanism of the γ-ray emission is the IC scattering of the BLR photons. Moreover, the high X-ray activity with less variable γ-ray counterpart, as seen in the multi-frequency light curves, can also be explained by the SED modeling. This can be due to the emission region being located relatively closer to the central black hole where the dominating energy density of the disk emission results in higher X-ray flux due to IC scattering of disk photons. The SED modeling of another distant blazar J0809+5341 indicate that, unlike other high redshift blazars, the optical-UV spectrum of this object is dominated by the non-thermal jet emission. The γ-ray spectrum of J0809+5341 is also unusually harder peaking at GeV energies. The black hole mass and the accretion disk luminosity derived from SDSS spectrum are significantly lower than that known in high redshift sources. All these properties point towards the unique nature of J0809+5341.

The broadband SED of γ-NLSy1 galaxies show the typical double hump structure similar to blazars. The γ-ray spectrum of these objects cannot be explained by SSC mechanism and an additional source of seed photons for IC scattering is required. The necessity of EC process, to reproduce the γ-ray window of the SED, hints for their similarity more with FSRQs than BL Lac objects. A prominent accretion disk radiation has been observed from couple of γ-NLSy1 galaxies and also some of them exhibit a pronounced curvature in the γ-ray spectra. In the γ-ray luminosity versus γ-ray spectral index plane, these objects occupy a region where their luminosities are lower than FSRQs but the spectral indices are steep and similar to FSRQs. All these features indicate that the γ-NLSy1 galaxies could be low black hole mass FSRQs, as predicted by Ghisellini et al. (2009).

The major findings from the SED modeling of the beamed AGN are as follows.

- The radiation from blazars could be dominated by a variety of emission mechanisms at different epochs, that also within a single source. The three GeV flares from 3C 279 are typical examples of this.
- The broadband modeling of the studied blazars suggests that the location of the γ-ray emitting region, at least in these objects, cannot be very far out from the BLR. This result could be true for other blazars also.
- The observed characteristics of J0809+5341 indicate that this object could be an exception among the family of high redshift blazars. Alternatively, there could be an entire population of such sources yet to be discovered.
- The radiative mechanisms working in the jets of γ-NLSy1 galaxies are similar to that known for FSRQs.

Finally, following are the overall conclusion of the thesis.

- **There is a diversity in the radiative processes operating in the relativistic jets of blazars. This reflects the level of complexity involved in understanding the blazar physics.**
- **γ-NLSy1 galaxies are low black hole mass FSRQs.**

5.3 Future Prospects

The recent developments in the field of high energy observational astronomy have significantly improved our understanding about beamed AGN. It is now well known that the bulk of the radiative output from powerful blazars (FSRQs, in particular) appears in the form of high energy γ-rays and a pronounced curvature in their γ-ray spectra is also seen. However, there are still a large number of unexplored problems such as the dominant emission mechanism in different class of γ-ray emitting sources, composition of the jet, location of the γ-ray emitting region, and role of external photon fields in γ-ray production. This thesis is a small effort to tackle some of these open issues and in the following few plans are discussed for future studies.

Apart from studying the flaring/low activity states of individual objects, a study of the broadband physical properties of a large sample of *Fermi* detected blazars will help in understanding the average physical properties of these sources and will also throw more light on few fundamental theories such as the blazar sequence. Availability of simultaneous observational data at all possible frequencies will be crucial in this regard. The currently operating satellites such as *Fermi*, *Swift*, *NuSTAR*, *XMM-Newton*, and *ASTROSAT* and also the upcoming missions, e.g., *ATHENA*, and *ASTRO-H* will definitely help in achieving this goal. Further, I plan to enhance the flexibility of the leptonic emission model developed during the thesis by including the hadronic processes and incorporate the Markov Chain Monte Carlo (MCMC) technique to calculate the uncertainties in the model parameters.

I plan to study the high energy GeV flares of blazars aimed at finding the shortest possible flux variations in them. For this purpose, a sample of those blazars will be prepared from which at least one GeV flare has been detected by *Fermi*-LAT. This will allow one to understand not only the pattern of GeV variations but also its possible dependence on the redshift. This problem is motivated by the discovery of hr scale flux variations from S5 0836+71, which suggests that even high redshift blazars can show the features which are generally seen in nearby objects.

Fermi-LAT has detected significant γ-ray emission from blazars upto redshift 3.1 and since the γ-ray detection is the most common fingerprint of the blazar nature of a source, one has to look at other physical characteristics to identify blazars beyond redshift 3.1. Two such features could be the high radio-loudness and a flat X-ray spectrum, which are the signatures of the beamed jetted emission. A sample of quasars detected by SDSS in its 12^{th} data release will be taken and radio-loud objects will be searched among them. A second filter of X-ray observation will be applied to those quasars which are significantly radio-loud (radio-loudness parameter $R > 100$). Following the blazar sequence, the IC hump of the high redshift blazars should lie at hard X-rays and thus they should be bright in this energy band. The data from currently operating hard X-ray mission *NuSTAR* and also upcoming *ASTRO-H* will be used to search for more blazars at high redshift. This will help not only in understanding the impact of powerful jets of blazars on the young Universe but also will throw light on the black hole evolution theories (see e.g., Volonteri et al. 2011).

The work on γ-ray emitting NLSy1 galaxies, which are good candidates to study the physical properties of relativistic jets at different mass and accretion rate scales, will be continued. The primary goal is to search for more RL-NLSy1 galaxies using the available optical spectrum databases, e.g., SDSS. The next step will be to search for significant γ-ray emission from them. As of now, only five γ-NLSy1 galaxies are known and therefore to enhance the understanding about these peculiar objects, the sample size needs to be enlarged.

Bibliography

Abdo, A. A., Ackermann, M., Ajello, M., et al. 2009a, ApJ, 699, 976

—. 2009b, ApJ, 707, L142

—. 2010a, Nature, 463, 919

—. 2010b, ApJ, 722, 520

—. 2010c, ApJ, 710, 1271

Abdo, A. A., Ackermann, M., Agudo, I., et al. 2010d, ApJ, 716, 30

Abdo, A. A., Ackermann, M., Ajello, M., et al. 2011, ApJ, 733, L26

Acero, F., Ackermann, M., Ajello, M., et al. 2015, ApJS, 218, 23

Ackermann, M., Asano, K., Atwood, W. B., et al. 2010, ApJ, 716, 1178

Ackermann, M., Ajello, M., Allafort, A., et al. 2011, ApJ, 743, 171

Aharonian, F., Akhperjanian, A. G., Barres de Almeida, U., et al. 2008, A&A, 478, 387

Akyuz, A., Thompson, D. J., Donato, D., et al. 2013, A&A, 556, A71

Albert, J., Aliu, E., Anderhub, H., et al. 2007, ApJ, 669, 862

Aleksić, J., Ansoldi, S., Antonelli, L. A., et al. 2015a, A&A, 576, A126

—. 2015b, A&A, 578, A22

Alexander, T. 2013, arXiv:1302.1508

Anderhub, H., Antonelli, L. A., Antoranz, P., et al. 2009, A&A, 498, 83

Arnaud, K. A. 1996, in ASP Conf. Ser., Vol. 101, Astronomical Data Analysis Software and Systems V, ed. G. H. Jacoby & J. Barnes (San Francisco, CA: ASP), 17

Asada, K., Nakamura, M., Inoue, M., Kameno, S., & Nagai, H. 2010, ApJ, 720, 41

Atwood, W. B., Abdo, A. A., Ackermann, M., et al. 2009, ApJ, 697, 1071

Baars, J. W. M., Genzel, R., Pauliny-Toth, I. I. K., & Witzel, A. 1977, A&A, 61, 99

Balanutsa, P., Denisenko, D., Lipunov, V., et al. 2014, The Astronomer's Telegram, 6096, 1

Barth, A. J., Ho, L. C., & Sargent, W. L. W. 2003, ApJ, 583, 134

Barthelmy, S. D., Barbier, L. M., Cummings, J. R., et al. 2005, *Space Sci. Rev.*, 120, 143

Baumgartner, W. H., Tueller, J., Markwardt, C. B., et al. 2013, ApJS, 207, 19

Beckmann, V., & Shrader, C. R. 2012, Active Galactic Nuclei

Begelman, M. C., Fabian, A. C., & Rees, M. J. 2008, MNRAS, 384, L19

Begelman, M. C., & Sikora, M. 1987, ApJ, 322, 650

Bessell, M. S., Castelli, F., & Plez, B. 1998, A&A, 333, 231

Blandford, R. D., & Königl, A. 1979, ApJ, 232, 34

Blandford, R. D., & Payne, D. G. 1982, MNRAS, 199, 883

Blandford, R. D., & Znajek, R. L. 1977, MNRAS, 179, 433

Błażejowski, M., Sikora, M., Moderski, R., & Madejski, G. M. 2000, ApJ, 545, 107

Blumenthal, G. R., & Gould, R. J. 1970, Reviews of Modern Physics, 42, 237

Boller, T., Brandt, W. N., & Fink, H. 1996, A&A, 305, 53

Bonning, E., Urry, C. M., Bailyn, C., et al. 2012, ApJ, 756, 13

Böttcher, M., & Chiang, J. 2002, ApJ, 581, 127

Böttcher, M., Mause, H., & Schlickeiser, R. 1997, A&A, 324, 395

Böttcher, M., & Principe, D. 2009, ApJ, 692, 1374

Böttcher, M., Reimer, A., Sweeney, K., & Prakash, A. 2013, ApJ, 768, 54

Breeveld, A. A., Landsman, W., Holland, S. T., et al. 2011, in AIP Conf. Proc., Vol. 1358, Gamma-Ray Burst 2010., ed. J. E. McEnery, J. L. Racusin, & N. Gehrels (Melville, NY: AIP), 373–376

Brown, A. M. 2013, MNRAS, 431, 824

Burrows, D. N., Hill, J. E., Nousek, J. A., et al. 2005, *Space Sci. Rev.*, 120, 165

Calderone, G., Foschini, L., Ghisellini, G., et al. 2011, MNRAS, 413, 2365

Cao, G., & Wang, J.-C. 2013, MNRAS, 436, 2170

Cellone, S. A., Romero, G. E., & Combi, J. A. 2000, AJ, 119, 1534

Celotti, A., & Ghisellini, G. 2008, MNRAS, 385, 283

Celotti, A., Padovani, P., & Ghisellini, G. 1997, MNRAS, 286, 415

Cerruti, M., Dermer, C. D., Lott, B., Boisson, C., & Zech, A. 2013, ApJ, 771, L4

Cortina, J., & Holder, J. 2013, The Astronomer's Telegram, 4976, 1

Crusius, A., & Schlickeiser, R. 1986, A&A, 164, L16

D'Ammando, F., & Orienti, M. 2013, The Astronomer's Telegram, 4694, 1

D'Ammando, F., Orienti, M., Finke, J., et al. 2012, MNRAS, 426, 317

de Diego, J. A. 2010, AJ, 139, 1269

Dermer, C. D. 1995, ApJ, 446, L63

Dermer, C. D., Cerruti, M., Lott, B., Boisson, C., & Zech, A. 2014, ApJ, 782, 82

Dermer, C. D., Finke, J. D., Krug, H., & Böttcher, M. 2009, ApJ, 692, 32

Dermer, C. D., & Menon, G. 2009, High Energy Radiation from Black Holes: Gamma Rays, Cosmic Rays, and Neutrinos, Princeton University Press

Dermer, C. D., & Schlickeiser, R. 1993, ApJ, 416, 458

Dermer, C. D., Schlickeiser, R., & Mastichiadis, A. 1992, A&A, 256, L27

Diltz, C., Böttcher, M., & Fossati, G. 2015, ApJ, 802, 133

Doi, A., Nagai, H., Asada, K., et al. 2006, PASJ, 58, 829

Doi, A., Nagira, H., Kawakatu, N., et al. 2012, ApJ, 760, 41

Donato, D., Ghisellini, G., Tagliaferri, G., & Fossati, G. 2001, A&A, 375, 739

Dondi, L., & Ghisellini, G. 1995, MNRAS, 273, 583

Dotson, A., Georganopoulos, M., Kazanas, D., & Perlman, E. S. 2012, ApJ, 758, L15

Errando, M. 2014, in AAS/High Energy Astrophysics Division, Vol. 14, AAS/High Energy Astrophysics Division, 106.11

Fan, J. H., Cheng, K. S., Zhang, L., & Liu, C. H. 1997, A&A, 327, 947

Fanaroff, B. L., & Riley, J. M. 1974, MNRAS, 167, 31P

Finke, J. D., & Dermer, C. D. 2012, ApJ, 751, 65

Finke, J. D., Dermer, C. D., & Böttcher, M. 2008, ApJ, 686, 181

Foschini, L. 2011, in Narrow-Line Seyfert 1 Galaxies and their Place in the Universe

Foschini, L., Ghisellini, G., Tavecchio, F., Bonnoli, G., & Stamerra, A. 2011, A&A, 530, A77

Foschini, L., Angelakis, E., Fuhrmann, L., et al. 2012, A&A, 548, A106

Fossati, G., Maraschi, L., Celotti, A., Comastri, A., & Ghisellini, G. 1998, MNRAS, 299, 433

Fossati, G., Buckley, J. H., Bond, I. H., et al. 2008, ApJ, 677, 906

Frank, J., King, A., & Raine, D. J. 2002, Accretion Power in Astrophysics (3rd ed,; Cambridge: Univ. Cambridge Press)

Gaidos, J. A., Akerlof, C. W., Biller, S., et al. 1996, Nature, 383, 319

Gehrels, N., Chincarini, G., Giommi, P., et al. 2004, ApJ, 611, 1005

Ghisellini, G. 2011, in American Institute of Physics Conference Series, Vol. 1381, American Institute of Physics Conference Series, ed. F. A. Aharonian, W. Hofmann, & F. M. Rieger, 180–198

Ghisellini, G., Guilbert, P. W., & Svensson, R. 1988, ApJ, 334, L5

Ghisellini, G., & Madau, P. 1996, MNRAS, 280, 67

Ghisellini, G., & Maraschi, L. 1989, ApJ, 340, 181

Ghisellini, G., Maraschi, L., & Tavecchio, F. 2009, MNRAS, 396, L105

Ghisellini, G., & Tavecchio, F. 2008, MNRAS, 386, L28

—. 2009, MNRAS, 397, 985

Ghisellini, G., Tavecchio, F., Foschini, L., et al. 2010a, MNRAS, 402, 497

Ghisellini, G., Tavecchio, F., Maraschi, L., Celotti, A., & Sbarrato, T. 2014, Nature, 515, 376

Ghisellini, G., Della Ceca, R., Volonteri, M., et al. 2010b, MNRAS, 405, 387

Ghisellini, G., Tagliaferri, G., Foschini, L., et al. 2011, MNRAS, 411, 901

Ghisellini, G., Nardini, M., Tagliaferri, J., G., et al. 2013, MNRAS, 428, 1449

Giannios, D., Uzdensky, D. A., & Begelman, M. C. 2009, MNRAS, 395, L29

Gillessen, S., Eisenhauer, F., Fritz, T. K., et al. 2009, ApJ, 707, L114

Goodrich, R. W. 1989, ApJ, 342, 224

Gopal-Krishna, Goyal, A., Joshi, S., et al. 2011, MNRAS, 416, 101

Gould, R. J. 1979, A&A, 76, 306

Grupe, D., & Mathur, S. 2004, ApJ, 606, L41

Gubbay, J., Legg, A. J., Robertson, D. S., et al. 1969, Nature, 224, 1094

Harpsøe, K. B. W., Jørgensen, U. G., Andersen, M. I., & Grundahl, F. 2012, A&A, 542, A23

Harrison, F. A., Craig, W. W., Christensen, F. E., et al. 2013, ApJ, 770, 103

Hartman, R. C., Bertsch, D. L., Fichtel, C. E., et al. 1992, ApJ, 385, L1

Hayashida, K. 2000, New A, 44, 419

Hayashida, M., Madejski, G. M., Nalewajko, K., et al. 2012, ApJ, 754, 114

Healey, S. E., Romani, R. W., Taylor, G. B., et al. 2007, ApJS, 171, 61

Healey, S. E., Romani, R. W., Cotter, G., et al. 2008, ApJS, 175, 97

Hovatta, T., Petropoulou, M., Richards, J. L., et al. 2015, MNRAS, 448, 3121

Hummel, C. A., Muxlow, T. W. B., Krichbaum, T. P., et al. 1992, A&A, 266, 93

Ikejiri, Y., Uemura, M., Sasada, M., et al. 2011, PASJ, 63, 639

Itoh, R., Tanaka, Y. T., Fukazawa, Y., et al. 2013, ApJ, 775, L26

Jaffe, W., Meisenheimer, K., Röttgering, H. J. A., et al. 2004, Nature, 429, 47

Jang, M., & Miller, H. R. 1997, AJ, 114, 565

Jiang, N., Zhou, H.-Y., Ho, L. C., et al. 2012, ApJ, 759, L31

Jones, F. C. 1968, Physical Review, 167, 1159

Jordi, K., Grebel, E. K., & Ammon, K. 2006, A&A, 460, 339

Jorstad, S., Marscher, A., Larionov, V., et al. 2013, in European Physical Journal Web of Conferences, Vol. 61, European Physical Journal Web of Conferences, 4003

Jorstad, S. G., Marscher, A. P., Lister, M. L., et al. 2004, AJ, 127, 3115

Jorstad, S. G., Marscher, A. P., Mattox, J. R., et al. 2001, ApJS, 134, 181

Jorstad, S. G., Marscher, A. P., Lister, M. L., et al. 2005, AJ, 130, 1418

Kaspi, S., Brandt, W. N., Maoz, D., et al. 2007, ApJ, 659, 997

Kellermann, K. I., Sramek, R., Schmidt, M., Shaffer, D. B., & Green, R. 1989, AJ, 98, 1195

Komossa, S., Voges, W., Xu, D., et al. 2006, AJ, 132, 531

Konigl, A. 1981, ApJ, 243, 700

Kuehr, H., Witzel, A., Pauliny-Toth, I. I. K., & Nauber, U. 1981, A&AS, 45, 367

Kushwaha, P., Sahayanathan, S., Lekshmi, R., et al. 2014, MNRAS, 442, 131

Leighly, K. M. 1999a, ApJS, 125, 297

—. 1999b, ApJS, 125, 317

Linford, J. D., Taylor, G. B., Romani, R. W., et al. 2012, ApJ, 744, 177

Lipunov, V., Kornilov, V., Gorbovskoy, E., et al. 2010, Advances in Astronomy, 2010, arXiv:0907.0827

Lister, M. L., Aller, M. F., Aller, H. D., et al. 2013, AJ, 146, 120

Liu, H., Wang, J., Mao, Y., & Wei, J. 2010, ApJ, 715, L113

Lobanov, A. P., Krichbaum, T. P., Witzel, A., et al. 1998, A&A, 340, L60

Lynds, C. R., Stockton, A. N., & Livingston, W. C. 1965, ApJ, 142, 1667

MAGIC Collaboration, Albert, J., Aliu, E., et al. 2008, Science, 320, 1752

Mannheim, K. 1993, A&A, 269, 67

Mannheim, K., & Biermann, P. L. 1992, A&A, 253, L21

Marinucci, A., Matt, G., Miniutti, G., et al. 2014, ApJ, 787, 83

Markwardt, C. B. 2009, in Astronomical Society of the Pacific Conference Series, Vol. 411, Astronomical Data Analysis Software and Systems XVIII, ed. D. A. Bohlender, D. Durand, & P. Dowler (San Francisco, CA: ASP), 251

Marscher, A. P., & Gear, W. K. 1985, ApJ, 298, 114

Martin, D. C., Fanson, J., Schiminovich, D., et al. 2005, ApJ, 619, L1

Massaro, E., Perri, M., Giommi, P., & Nesci, R. 2004, A&A, 413, 489

Mathur, S., Kuraszkiewicz, J., & Czerny, B. 2001, New A, 6, 321

Mattox, J. R., Bertsch, D. L., Chiang, J., et al. 1996, ApJ, 461, 396

Meegan, C., Bhat, N., Connaughton, V., et al. 2007, in American Institute of Physics Conference Series, Vol. 921, The First GLAST Symposium, ed. S. Ritz, P. Michelson, & C. A. Meegan, 13–18

Meier, D. L., Koide, S., & Uchida, Y. 2001, Science, 291, 84

Melia, F., & Konigl, A. 1989, ApJ, 340, 162

Miller, P., Rawlings, S., & Saunders, R. 1993, MNRAS, 263, 425

Moderski, R., Sikora, M., & Błażejowski, M. 2003, A&A, 406, 855

Monet, D. G., Levine, S. E., Canzian, B., et al. 2003, AJ, 125, 984

Mücke, A., Protheroe, R. J., Engel, R., Rachen, J. P., & Stanev, T. 2003, APh, 18, 593

Narayan, R., Mahadevan, R., & Quataert, E. 1998, in Theory of Black Hole Accretion Disks, ed. M. A. Abramowicz, G. Björnsson, & J. E. Pringle, 148–182

Nenkova, M., Ivezić, Ž., & Elitzur, M. 2002, ApJ, 570, L9

Nolan, P. L., Abdo, A. A., Ackermann, M., et al. 2012, ApJS, 199, 31

Oshlack, A. Y. K. N., Webster, R. L., & Whiting, M. T. 2001, ApJ, 558, 578

Osterbrock, D. E., & Pogge, R. W. 1985, ApJ, 297, 166

Otterbein, K., Krichbaum, T. P., Kraus, A., et al. 1998, A&A, 334, 489

Paliya, V. S. 2015a, ApJ, 808, L48

—. 2015b, ApJ, 804, 74

Paliya, V. S., Böttcher, M., Diltz, C., et al. 2015a, ApJ, 811, 143

Paliya, V. S., Diltz, C., Böttcher, M., Stalin, C. S., & Buckley, D. 2016, ApJ, 817, 61

Paliya, V. S., Sahayanathan, S., Parker, M. L., et al. 2014, ApJ, 789, 143

Paliya, V. S., Sahayanathan, S., & Stalin, C. S. 2015b, ApJ, 803, 15

Paliya, V. S., Stalin, C. S., Kumar, B., et al. 2013a, MNRAS, 428, 2450

Paliya, V. S., Stalin, C. S., & Ravikumar, C. D. 2015c, AJ, 149, 41

Paliya, V. S., Stalin, C. S., Shukla, A., & Sahayanathan, S. 2013b, ApJ, 768, 52

Paliya, V. S., Parker, M. L., Stalin, C. S., et al. 2015d, ApJ, 803, 112

Paneque, D., D'Ammando, F., Orienti, M., & Falcon, A. 2013, The Astronomer's Telegram, 4977, 1

Pâris, I., Petitjean, P., Aubourg, É., et al. 2014, A&A, 563, A54

Perucho, M., Kovalev, Y. Y., Lobanov, A. P., Hardee, P. E., & Agudo, I. 2012, ApJ, 749, 55

Peterson, B. M., McHardy, I. M., Wilkes, B. J., et al. 2000, ApJ, 542, 161

Petropoulou, M. 2014, A&A, 571, A83

Pian, E., Urry, C. M., Maraschi, L., et al. 1999, ApJ, 521, 112

Pier, E. A., & Krolik, J. H. 1992a, ApJ, 401, 99

—. 1992b, ApJ, 399, L23

Pittori, C., Verrecchia, F., Puccetti, S., Perri, M., & Tavani, M. 2015, The Astronomer's Telegram, 7668, 1

Poole, T. S., Breeveld, A. A., Page, M. J., et al. 2008, MNRAS, 383, 627

Pounds, K. A., Done, C., & Osborne, J. P. 1995, MNRAS, 277, L5

Poutanen, J., & Stern, B. 2010, ApJ, 717, L118

Punch, M., Akerlof, C. W., Cawley, M. F., et al. 1992, Nature, 358, 477

Rees, M. J. 1966, Nature, 211, 468

Richards, J. L., Max-Moerbeck, W., Pavlidou, V., et al. 2011, ApJS, 194, 29

Romero, G. E., Cellone, S. A., & Combi, J. A. 1999, A&AS, 135, 477

Rowan-Robinson, M. 1977, ApJ, 213, 635

Rybicki, G. B., & Lightman, A. P. 1979, Radiative processes in astrophysics

Sagar, R., Kumar, B., Omar, A., & Joshi, Y. C. 2012, in Astronomical Society of India Conference Series, Vol. 4, Astronomical Society of India Conference Series, 173

Sagar, R., Kumar, B., Omar, A., & Pandey, A. K. 2010, in Astronomical Society of India Conference Series, Vol. 1, Astronomical Society of India Conference Series, 203–210

Sagar, R., Stalin, C. S., Gopal-Krishna, & Wiita, P. J. 2004, MNRAS, 348, 176

Sahayanathan, S., & Godambe, S. 2012, MNRAS, 419, 1660

Saito, S., Stawarz, Ł., Tanaka, Y. T., et al. 2013, ApJ, 766, L11

Sambruna, R. M., Tavecchio, F., Ghisellini, G., et al. 2007, ApJ, 669, 884

Sanders, D. B., Phinney, E. S., Neugebauer, G., Soifer, B. T., & Matthews, K. 1989, ApJ, 347, 29

Schlafly, E. F., & Finkbeiner, D. P. 2011, ApJ, 737, 103

Schmidt, M. 1963, Nature, 197, 1040

Seyfert, C. K. 1943, ApJ, 97, 28

Shakura, N. I., & Sunyaev, R. A. 1973, A&A, 24, 337

Shen, Y., Richards, G. T., Strauss, M. A., et al. 2011, ApJS, 194, 45

Shu, F. H. 1991, Radiation: The physics of astrophysics, Vol I (Mill Valley, CA: Univ. Science Books)

Shukla, A., Chitnis, V. R., Vishwanath, P. R., et al. 2012, A&A, 541, A140

Shumkov, V., Balanutsa, P., Denisenko, D., et al. 2014, The Astronomer's Telegram, 6070, 1

Sikora, M., Begelman, M. C., & Rees, M. J. 1994, ApJ, 421, 153

Skrutskie, M. F., Cutri, R. M., Stiening, R., et al. 2006, AJ, 131, 1163

Smith, J. E., Robinson, A., Alexander, D. M., et al. 2004, MNRAS, 350, 140

Smith, P. S., Montiel, E., Rightley, S., et al. 2009, , arXiv:0912.3621

Spruit, H. C. 2010, in Lecture Notes in Physics, Berlin Springer Verlag, Vol. 794, Lecture Notes in Physics, Berlin Springer Verlag, ed. T. Belloni, 233

Stalin, C. S., Gopal Krishna, Sagar, R., & Wiita, P. J. 2004, Journal of Astrophysics and Astronomy, 25, 1

Stroh, M. C., & Falcone, A. D. 2013, ApJS, 207, 28

Tanihata, C., Urry, C. M., Takahashi, T., et al. 2001, ApJ, 563, 569

Tavecchio, F., Becerra-Gonzalez, J., Ghisellini, G., et al. 2011, A&A, 534, A86

Tavecchio, F., & Ghisellini, G. 2008, MNRAS, 386, 945

Tavecchio, F., Ghisellini, G., Bonnoli, G., & Ghirlanda, G. 2010, MNRAS, 405, L94

Thompson, D. J., Bertsch, D. L., Fichtel, C. E., et al. 1993, ApJS, 86, 629

Torrealba, J., Chavushyan, V., Cruz-González, I., et al. 2012, RMxAA, 48, 9

Urry, C. M., & Padovani, P. 1995, PASP, 107, 803

Vaughan, S., Edelson, R., Warwick, R. S., & Uttley, P. 2003, MNRAS, 345, 1271

Vercellone, S., D'Ammando, F., Vittorini, V., et al. 2010, ApJ, 712, 405

Véron-Cetty, M.-P., & Véron, P. 2010, A&A, 518, A10

Vestergaard, M., & Peterson, B. M. 2006, ApJ, 641, 689

Vlahakis, N., & Königl, A. 2004, ApJ, 605, 656

Volonteri, M., Haardt, F., Ghisellini, G., & Della Ceca, R. 2011, MNRAS, 416, 216

Wang, T., Brinkmann, W., & Bergeron, J. 1996, A&A, 309, 81

Wehrle, A. E., Pian, E., Urry, C. M., et al. 1998, ApJ, 497, 178

Woo, J.-H., & Urry, C. M. 2002, ApJ, 579, 530

Wright, E. L., Eisenhardt, P. R. M., Mainzer, A. K., et al. 2010, AJ, 140, 1868

Xu, D., Komossa, S., Zhou, H., et al. 2012, AJ, 143, 83

Yuan, W., Zhou, H. Y., Komossa, S., et al. 2008, ApJ, 685, 801

Zhang, Y. H., Treves, A., Celotti, A., Qin, Y. P., & Bai, J. M. 2005, ApJ, 629, 686

Zhou, H., Wang, T., Yuan, W., et al. 2006, ApJS, 166, 128